Reverse-Osmosis Desalination of Seawater Powered by Photovoltaics Without Batteries

by

A. Murray Thomson

A Doctoral Thesis

Submitted in partial fulfilment of the requirements

for the award of

Doctor of Philosophy of Loughborough University

30th June 2003

Certificate of originality

Abstract

The design, construction and testing of a photovoltaic-powered reverse-osmosis (PV-RO) desalination system is presented. The system operates from seawater and requires no batteries, since the rate of production of freshwater varies throughout the day according to the available solar power. Initial testing of the system, with the modest solar resource available in the UK, provided freshwater at approximately 1.5 m^3/day. Nearer to the equator and with a PV array of only 2.4 kW_P, a software model of the system predicts production of over 3 m^3/day throughout the year. The system employs a Clark pump brine-stream energy recovery mechanism and this, coupled with variable water recovery ratio, achieves a specific energy consumption of less than 4 kWh/m^3 over a broad range of operation. Standard industrial inverters, motors and pumps are employed and provide good energy and cost efficiency. Maximum power point tracking (MPPT) for the photovoltaic array is provided by a novel control algorithm, developed by the author. Instrumentation and data acquisition of the hardware test rig using LabVIEW is described. Testing and modelling of the system components in MATLAB-Simulink is presented, together with a discussion of the full system modelling and design procedure, in which the aim was to minimise the cost of water. This led to a capital cost estimate of £23,055 including the PV array, and an overall cost of water, including full maintenance, of £2.00 per m^3.

Acknowledgments

I wish to thank Tony Marmont for initiating and supporting CREST, the renewable energy research group at Loughborough University.

Also, I thank David Infield, Director of CREST, for giving me the opportunity to work in this area and for his guidance and encouragement throughout.

I thank Marcos Miranda for working with me during the earlier stages of this project. Marcos is now completing his thesis on *wind*-powered reverse osmosis. The reverse-osmosis test-rig at CREST is shared, and we both contributed to its development, as duly acknowledged in the chapters of this thesis. I have not seen Marcos's thesis but I imagine it will form a useful complement to this one for anyone seeking to further develop these systems.

I gratefully acknowledge financial support from the DTI through ETSU grant S/P2/00305.

Murray Thomson

June 2003

Contents

List of figures

List of tables

The new PV-RO test rig

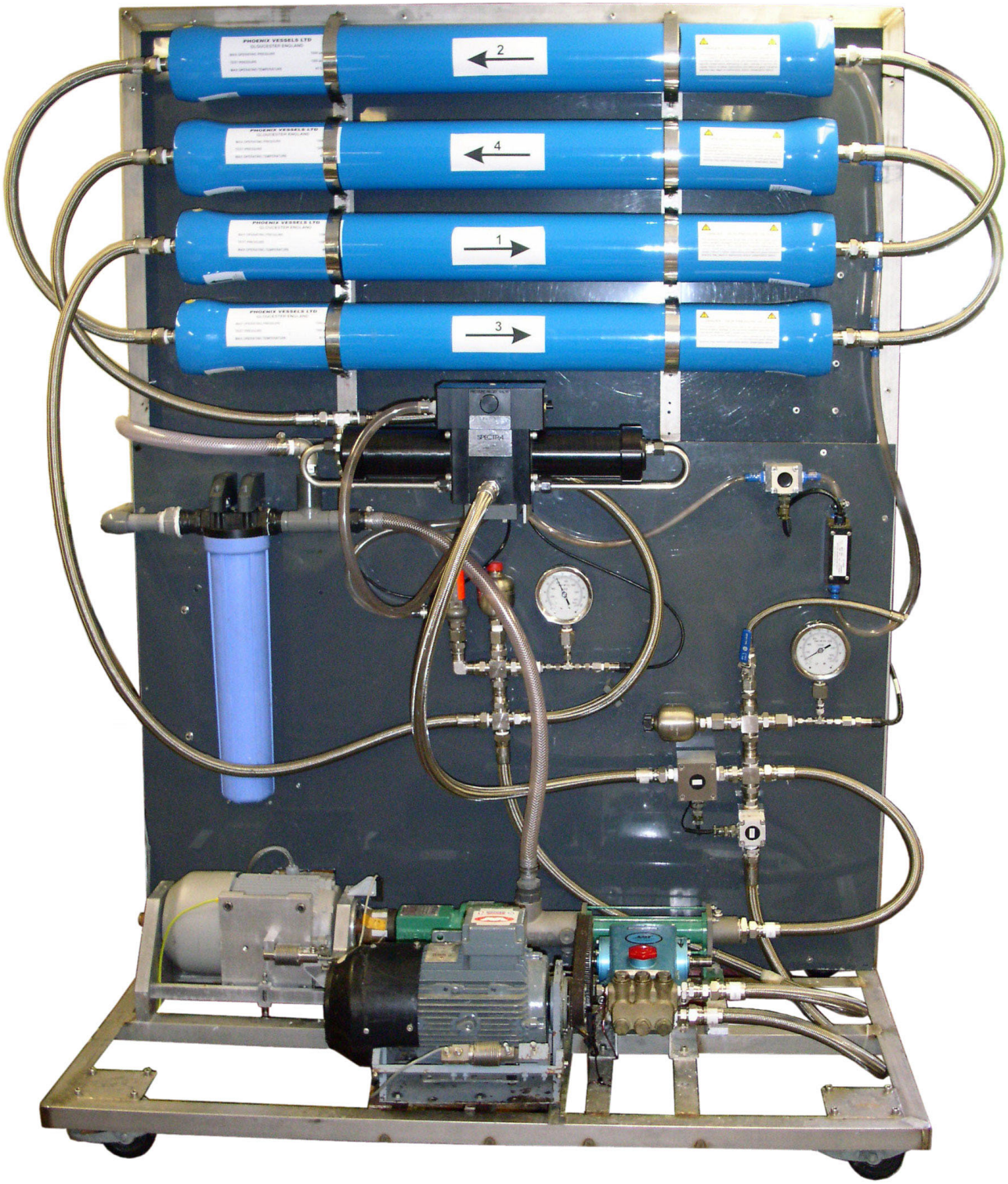

Chapter 1 Overview

1.1 Desalination and Renewable Energy

The desalination of seawater and brackish groundwater to provide fresh drinking water is an established and thriving industry. The most commonly used technologies are thermal distillation and reverse-osmosis (RO) filtration. Many towns and cities, particularly in the Middle East and the US, already rely heavily on large-scale desalination plants for their municipal water supplies. Small-scale desalination is also well-established, for example on ships.

Meanwhile, the world is facing a serious water crisis: 1.1 billion people (one-sixth of the world's population) have no access to improved drinking water, and *"All the signs suggest that it is getting worse and will continue to do so, unless corrective action is taken"* (UNESCO 2003). Desalination will undoubtedly play an increasing role in meeting worldwide water needs, but is limited by its cost, which is largely dominated by energy costs. Desalination intrinsically consumes a lot of energy, and this is quantified in the *specific energy*, which is the energy consumed in desalinating a unit volume of water, and is usually given in kWh/m^3. The theoretical minimum is around 0.7 kWh/m^3, when operating from seawater (Johnson et al. 1966 p. 357). In practice today, energy consumption many times greater than this is typical, which explains why the desalination industry exists mainly in countries with large fossil-fuel reserves.

The energy consumption of desalination also has an environmental impact, in particular the release of carbon dioxide (CO_2) into the atmosphere through the burning of fossil fuels. Prior to the industrial revolution in the 1760's, the concentration of CO_2 in the earth's atmosphere was around or below 280 parts per million (ppm), and had been for hundreds of thousands of years. Since the industrial revolution, mankind has raised this dramatically, as shown in Figure 1-1.

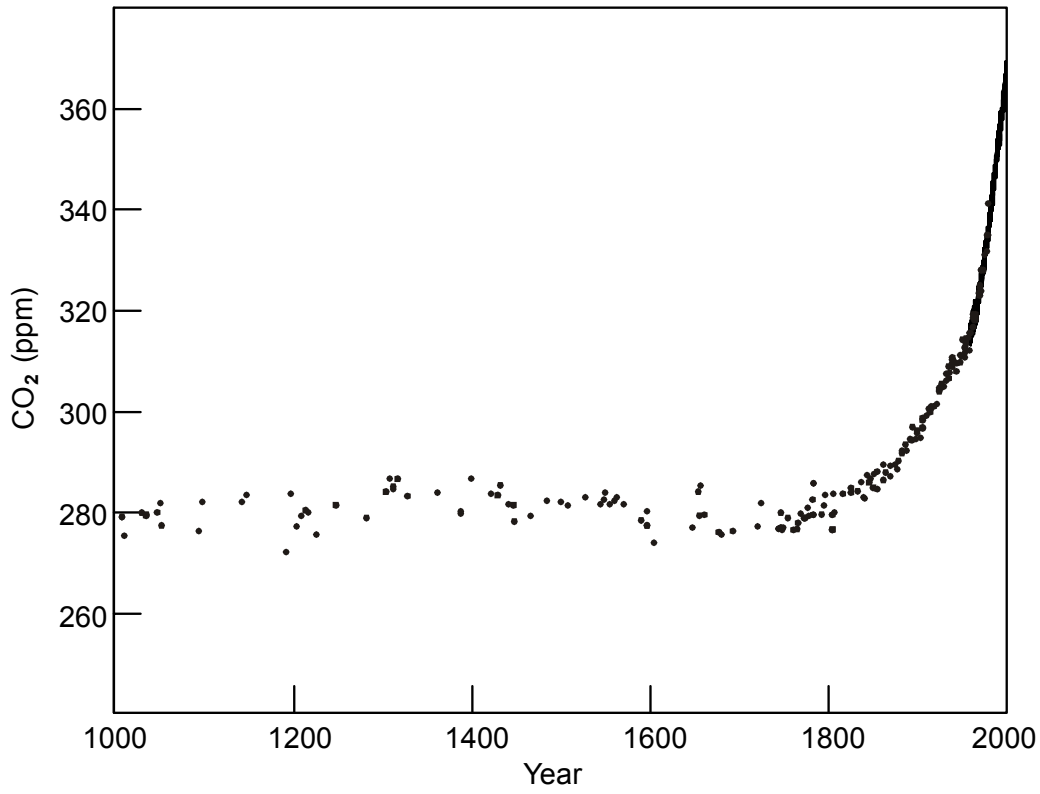

Figure 1-1 – Atmospheric carbon dioxide over the last 1000 years, illustrating the dramatic rise since the industrial revolution (IPCC 2001)

Graphs similar to Figure 1-1 exist for other greenhouse gases. The full consequences of making such significant changes to the earth's atmosphere are as yet unknown, but to continue to increase concentration levels seems foolhardy to say the least. Desalination is already a significant contributor to worldwide CO_2 emissions (see section 2.3.3), and this of course will increase as the industry grows.

CO_2 emissions can be greatly reduced through the application of renewable energy technologies, which are already cost competitive with fossil fuels in many situations. Good examples include large-scale grid-connected wind turbines, solar water heating and off-grid solar photovoltaics (PV). The use of renewable energy for desalination is, therefore, a very attractive proposition.

Renewable energy can come from a variety of sources and can be captured by a variety of technologies; likewise, desalination can be achieved by various methods. The numerous permutations combining these have been reviewed several times in recent years. Repeatedly, the combination of photovoltaics with reverse osmosis (PV-RO) has been considered one of the more promising, particularly for small-scale systems where other

technologies are less competitive. Indeed, PV-RO systems for operation from *brackish* water are now commercially available as discussed in section 2.9.1. Operation from seawater is more challenging from an energy perspective, and is the subject of this thesis.

1.2 Reverse Osmosis (RO)

Reverse osmosis is a form of filtration, in which the filter is a semi-permeable membrane that allows water to pass through, but not salt. When a membrane of this type has saltwater on one side and freshwater on the other, and in the absence of applied mechanical pressure, water will flow through the membrane towards the saltwater side, evening out the concentrations and reducing the quantity of freshwater. This is the natural process of osmosis, and is widely employed in the cells of all living species. In desalination, of course, the aim is to *increase* the quantity of freshwater and so a pump is employed to make the flow reverse, hence the name: reverse osmosis.

Osmosis is a surprisingly powerful phenomenon; the osmotic pressure of typical seawater is around 26 bar, and this is the pressure that the pump must overcome in order to reverse the flow. (26 bar also equates to the theoretical minimum energy consumption of 0.7 kWh/m^3, mentioned earlier.) In practice, a significantly higher pressure is used, typically 50-70 bar, in order to achieve a generous flow of freshwater, which is the *product*, also known as the *permeate*.

Of course, as freshwater passes through the membrane, the remaining saltwater becomes more concentrated and, for the process to continue, this *concentrate*, also known as the *brine*, must be continuously replaced by new feed water. To achieve this, the feed water is pumped *across* the membrane as well as through it; hence, RO is a *cross-flow* filtration process as depicted in Figure 1-2.

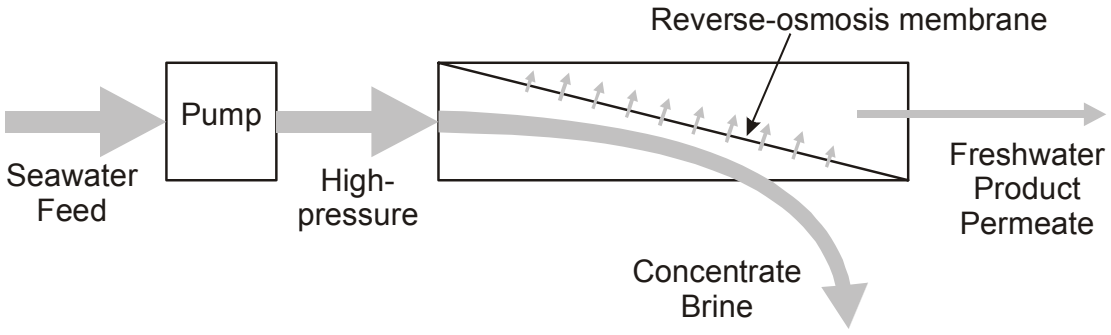

Figure 1-2 – Schematic of a simple reverse osmosis (RO) system

The ratio of product flow to that of the feed is known as the *recovery ratio*. With seawater RO, a recovery ratio of 30% is typical, meaning that the remaining 70% appears as concentrate, which is returned to the sea. However, this concentrate comes out of the reverse osmosis module at a pressure only slightly below that of the feed, meaning that it contains roughly two thirds of the total hydraulic power originally supplied by the pump. In large RO systems, this energy is usually recovered by way of a Pelton turbine and returned to the shaft of the main pump, allowing the motor size to be roughly halved and dramatically improving the overall system efficiency. This is known as *brine-stream energy recovery*. In small RO systems, brine-stream energy recovery is often omitted, which reduces capital costs but adds considerably to running costs (energy).

Reverse osmosis is a widely scaleable technology: the membranes found in small systems used on pleasure yachts to produce a few litres per day are virtually identical to those used in large municipal plants producing thousands of cubic metres per day. The balance of plant (pumps etc.) is, however, widely different and this usually leads to lower energy efficiencies in smaller systems, particularly when brine-stream energy recovery is neglected.

1.3 Photovoltaics (PV) and Batteries

Photovoltaic panels convert sunlight directly into electricity, and are already widely used in critical applications such as vaccine refrigeration, water pumping and battery charging for lighting and communications. PV is highly reliable and is often chosen because it offers the lowest life-cycle cost, especially for applications requiring less than 10 kW, where grid electricity is not available and where internal-combustion engines are expensive to maintain. PV is a rapidly developing technology with costs falling year on year, and this will soon lead to its broad application in systems requiring larger powers. Today however, it is clear that PV-RO will initially be most cost-competitive at the small-scale, perhaps for supplying remote villages or small hotels. The challenge then becomes the energy efficiencies in the balance of plant: pumps, motors and the critical brine-stream energy recovery mechanism.

Batteries are widely used in PV systems, storing the energy during the day and making it available through the night. Unfortunately, batteries are notoriously problematic in practice, especially in PV systems in hot countries. Experienced PV system designers

avoid batteries whenever possible. PV water pumping, for example, is usually designed without batteries, in which case the pump runs only during the day and the water is stored in a tank, if necessary. Likewise, PV refrigeration is possible without batteries, by virtue of storing the cold in the form of ice or other phase-change materials. From the outset, the project described in this thesis aimed to design a PV-RO system that would operate without batteries: desalinating water during the day and storing the product water in a tank. This seems straightforward, but is contrary to the normal 24-hour-a-day operation of mainstream RO systems.

Furthermore, in the absence of batteries, the power available from a PV array varies with the intensity of the sunlight, the *irradiance*, and, in order to make best use of this available power, a connected RO system must also operate at variable power. Again, this is contrary to the normal operation of mainstream RO systems. Also, the *efficiency* of the RO system must be maintained over a broad range of operating power; this is particularly challenging in the balance of plant.

1.4 Proposed PV-RO system

The aim of the project leading to this thesis was the design of a cost-effective PV-RO system that can desalinate seawater and does not require batteries. Such a system is presented in Figure 1-3. The design was developed by the author, with assistance from Spectra Watermakers Inc, Dulas Limited and Marcos Miranda, as specifically acknowledged in later chapters.

The chosen brine-stream energy recovery mechanism is the Clark pump from Spectra Watermakers Inc. It is a positive-displacement reciprocating pressure intensifier, and an animation of its operation can be viewed online at: http://www.spectrawatermakers.com/technology/overview.html (accessed: March 04) . Testing at CREST showed that the Clark pump is very efficient, typically above 90%, which is impressive indeed for any kind of pump on this scale.

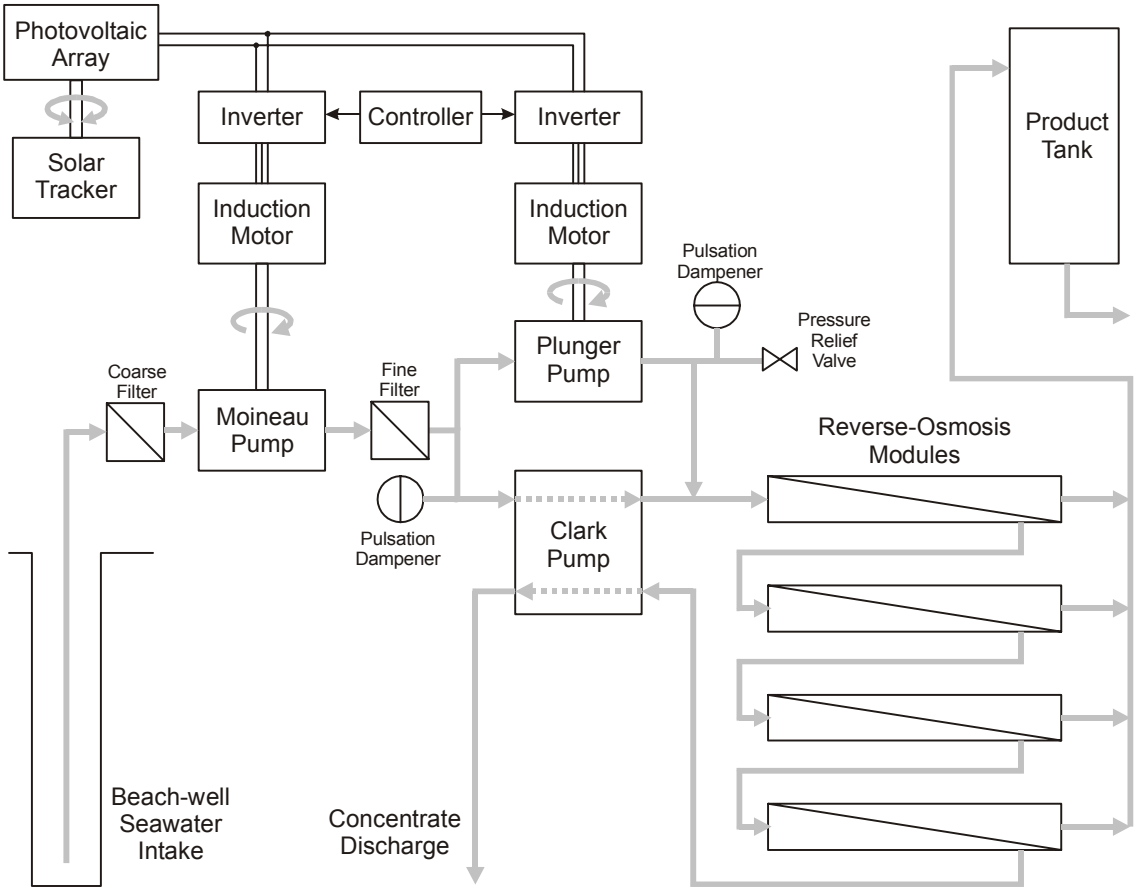

Figure 1-3 – System overview

Referring to Figure 1-3, the Moineau (progressing cavity) pump sucks seawater from a beach well and raises it to a medium-pressure (6 – 11 bar). A submersible version of the same pump is available, at extra cost, and could readily be substituted. The Clark pump raises its medium-pressure feed water to high-pressure (40 – 70 bar) by virtue of the energy it recovers from the concentrate. The flow ratio of the Clark pump is fixed by design, which normally gives a 10 % water recovery ratio at the membranes. However, the plunger pump injects an additional high-pressure feed, which increases the water recovery ratio to any desired value.

The controller Figure 1-3 in provides speed-set-point signals for the inverters and motors that drive the two rotary pumps. Firstly, this provides maximum power point tracking (MPPT), which ensures that the total power drawn from the PV array tracks the maximum available as the irradiance varies throughout the day. Secondly, the relative speeds of the two pumps are controlled in order to maximise the flow of product water. The controller algorithms are discussed in chapters 8 and 9.

1.5 Modelling

There are a vast number of possible configurations of motors, pumps, energy-recovery mechanisms and so on that can be used in a reverse osmosis system. The configuration outlined in Figure 1-3 was developed largely through computer simulation of numerous possibilities and an evaluation of their cost, performance and practicality. The simulation model was developed in Matlab-Simulink and includes everything from the solar irradiance striking the photovoltaic panels through to the water in the product tank. Each of the hardware components is modelled in detail and the critical sections are based on accurate measurements made in CREST's laboratory. The model fully represents the variations of flows and pressures throughout the system with respect to variations in irradiance and feed-water temperature. It can, for example, perform an hour-by-hour simulation of a whole year of operation.

1.6 System hardware testing

A test rig was constructed, with assistance from Marcos Miranda, and operated from a PV array at CREST to demonstrate and verify the design.

Of course, many other researchers worldwide have designed and built similar PV-RO systems, and these will be discussed in section 2.9. Many can work only from brackish water and most employ batteries or very large PV arrays or both. It is acknowledged however that many of these systems are operating in the field, whereas the system described here has, to date, only been tested in a laboratory.

1.7 Performance figures

To supply a remote village or small hotel, a freshwater production of 3 m^3/day was suggested by Dulas Limited, and was adopted as a design target.

1.7.1 Predictions from software model

Using solar irradiance data for a site in Eritrea, as an example, and taking seawater feed at 38,000 mg/L total dissolved solids (TDS) varying annually between 17 and 33 °C:

Annual freshwater production was predicted at 1424 m^3, which is an average of just over 3.9 m^3/day, and had a minimum monthly average of 3.3 m^3/day.

Specific energy consumption (photovoltaic-electricity) was typically between 3.2 and 3.7 kWh/m^3 depending on the solar irradiance and feed water temperature

Capital costs, including the PV array, were estimated (with assistance of Dulas Limited) at £23,055, with an overall cost of water of £2.00 per m^3, including full maintenance. The system has no fuel costs and no batteries.

1.7.2 Actual measurements

The completed test rig at CREST, achieved a specific energy consumption (DC-electricity supply, rectified mains) of between 3.5 and 3.8 kWh/m^3, with freshwater production adjustable between 181 and 488 L/h. Production was adjustable down to 17 L/h at lower efficiency.

PV-powered operation was demonstrated and, though limited by ambient UK irradiance levels coupled to an undersized PV-array (64% of design size), achieved freshwater production of 1.5 m^3/day.

Testing used NaCl solution at 32,800 mg/L, which is isosmotic with ASTM (1998) standard substitute ocean water, at 25 °C.

1.8 Global relevance

It may appear that a PV-RO system to produce 3 m^3/day is but a *drop in the ocean* compared to what is required to tackle the world's energy and water problems. Indeed it is, but the concept of matching variable loads, particularly RO desalination to naturally-varying renewable-energy sources, is valuable at a much larger scale. Renewable-energy sources, including solar, wind and wave power, are naturally varying, and often do not coincide with man's perceived energy requirements. Because of this, it is often assumed that very large-scale energy storage will be required in order to operate large electrical power systems from these sources. Certainly, energy storage is very valuable in the operation of power systems, but it is also very expensive. Batteries are expensive and problematic even at the small scale, pumped hydro is expensive both in civil engineering and environmentally, and other means of storing electrical energy are mostly at the development stage. The alternative to electrical energy storage is *demand-side management*. This is sometimes referred to as curtailment or use of deferrable loads. These expressions suggest that the customer will have to endure interruptions in their

supply, but this need not be the case. It is better to liken demand-side management to *making hay when the sun shines*, which, in the case of RO desalination, translates to making water when electricity form renewable energy is available. Demand-side management can also be readily applied to air conditioning, another major consumer of energy, through the use of ice storage. Systems doing exactly this are commercially available, but rarely applied. The low uptake of demand-side management, even in countries where it would be very advantageous, is largely due to split responsibilities: electricity generation, RO desalination and air conditioning are all operated by separate agencies. There are, however, some technical factors. In particular, RO desalination performs best when run at a constant flow 24-hours-a-day. Operation of large-scale RO desalination plants at variable flow to enable greater use of renewable energy sources will require significant changes to existing practices. It makes good sense to build up practical experience on small systems, such as that described in this thesis.

Another problem facing our planet is the general migration of people towards cities, driven partly by water and electricity shortages in rural areas. Small-scale renewable-energy powered systems providing these resources locally could perhaps reduce this trend.

Chapter 2 Technology and literature review

2.1 Desalination

2.1.1 A growth industry

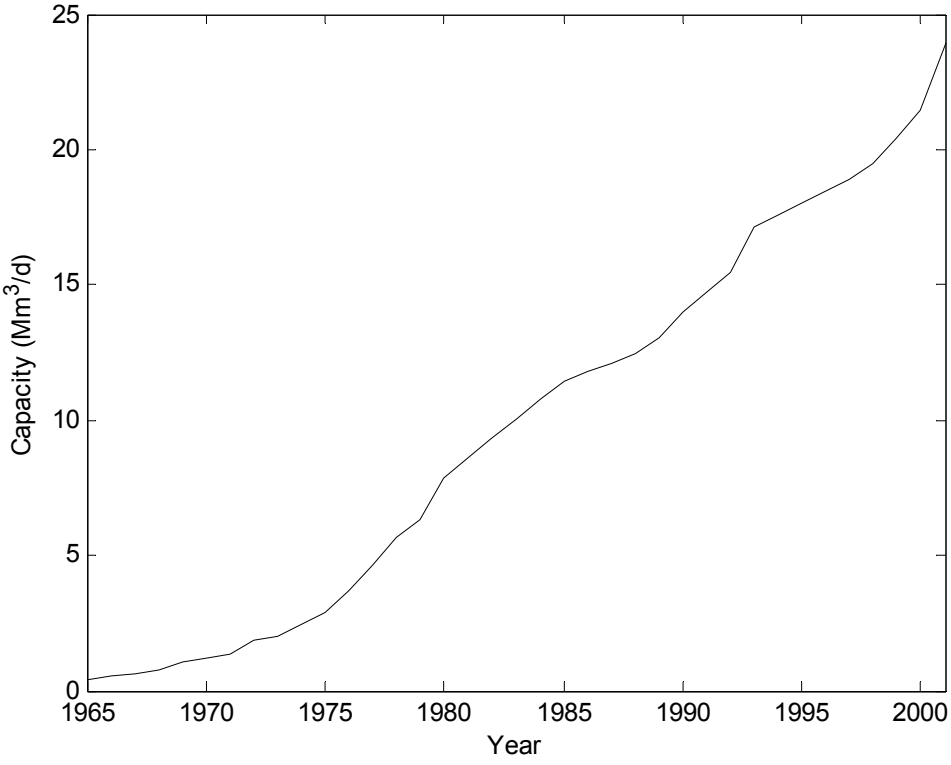

Figure 2-1 – Growth of worldwide desalination (Wangnick 2002; via Wiseman 2002)

The worldwide desalination industry now provides over 24 million cubic metres of freshwater per day. The growth of the industry over the last 37 years is shown in Figure 2-1 and can be expected to continue. The capacity shown is dominated by large-scale plants supplying large centres of population. In particular, the data includes only plants with capacities of 100 m^3/d and above; there are over 15,000 such plants worldwide. Additionally, there are many more thousands of smaller desalination units on ships, on islands and in remote areas.

2.1.2 Seawater versus brackish water

The desalination industry makes a distinction between seawater and brackish water (DOW 1995). Seawater typically has a salt concentration in the order of 36,000 mg/L total dissolved solids (TDS), while brackish water, usually from underground, might be between 3,000 and 10,000 mg/L TDS. Seawater intrusion of over-exploited groundwater supplies can blur the distinction, but still it is a useful starting point.

With desalination by reverse osmosis, the energy required to desalinate brackish water is considerably less than that for seawater. The system described in this thesis is specifically intended for seawater desalination; it could be used for brackish water but would be expensive. Also, brackish water tends to be more variable in terms of the proportions of salts it contains and this can complicate fouling and scaling considerations.

2.1.3 Product water specification

An important consideration for any desalination system is the quality required of the product water. Some systems provide very pure water for particular industrial processes, but the majority are designed to provide drinking water, and that of course is the aim of the PV-RO system in hand.

RO membranes are not perfect; they do allow some salt through. Seawater-RO membranes are generally designed to give product concentrations of 200 to 300 mg/L, when operating at full flow and pressure on the feed-water side. But, operation at significantly lower flow and pressure causes the product concentration to rise considerably. This is an important consideration when designing RO systems for best energy efficiency, since best energy efficiency usually occurs at flow and pressure well below maximum. The consideration has further importance in the case of a *batteryless* PV-RO system, because, when the available solar power is low, the system will operate at further reduced flow and pressure. The batteryless PV-RO system described in this thesis does at times operate at very low flow and pressure and, as expected, the concentration of the product is very high. Of course, this is concurrent with very low product flow and, once mixed in a tank with better quality water made earlier, may well be acceptable. Nonetheless, it is clearly important to establish an appropriate upper limit for the concentration of the water delivered to the consumer.

In desalination literature, it is often stated that the World Health Organisation (WHO) recommends a limit of 500 mg/L TDS, but the exact origin of this figure is unclear. The WHO is currently preparing the Third Edition of its Guidelines for Drinking-Water Quality and a draft (February 2003) is available on line (WHO 2003). It is a very comprehensive document, and includes notes describing the historical development of the guidelines with reference to guidelines given in previous editions. There is no evidence of a 500-mg/L limit within the WHO Guidelines.

The US Environmental Protection Agency (EPA), however, does set a guideline of 500 mg/L maximum TDS in their National Secondary Drinking Water Regulations (EPA 2004), and it is possible that this is source of the figure often attributed to the WHO in desalination literature. The following discussion is based on the WHO Guidelines.

The salt in seawater is primarily sodium chloride, NaCl, and unsurprisingly it is primarily sodium chloride that makes its way into the product.

Regarding sodium, the WHO Guidelines (Third Edition, 2003, chapter 8, page 248) say:

> *…no health-based guideline value is proposed. However, concentrations in excess of 200 mg/litre may give rise to unacceptable taste (see chapter 10).*

Likewise for chloride (chapter 8, page 236):

> *No health-based guideline value is proposed for chloride in drinking-water. However, chloride concentrations in excess of about 250 mg/litre can give rise to detectable taste in water (see chapter 10).*

And for total dissolved solids (TDS) (chapter 8, page 250):

> *…no health-based guideline value is proposed. However, the presence of high levels of TDS in drinking-water may be objectionable to consumers (see chapter 10).*

Apparently, the first edition of the guidelines (1984) did suggest a limit of 1000 mg/L for TDS, based on *taste*. This limit was removed in the second edition. There is no mention of any limit at 500 mg/L.

Chapter 10 of the Guidelines indicates that the *taste threshold* of sodium chloride is around 200 mg/L (pages 215 and 217). And regarding total dissolved solids (page 218):

The palatability of water with a TDS level of less than 600 mg/litre is generally considered to be good; drinking-water becomes significantly unpalatable at TDS levels greater than 1200 mg/litre.

In summary, the acceptable concentration of salt in RO-desalinated seawater is primarily a matter of taste, not health – assuming that the water is not so unpalatable as to encourage people to drink from less-safe sources (chapter 10, page 213). The acceptable taste will depend greatly on who the consumers are, what they are accustomed to and what their alternatives are. A product concentration of 500 mg/L remains a useful target, but in areas with no alternative supply, 1000 mg/L may well be perfectly acceptable, especially if this can be produced in greater quantity or with improved reliability.

The above discussion relies entirely on the WHO Guidelines. These are widely used as a basis for national and regional standards, and there is little variation from country to country. In the main, the WHO Guidelines assume a surface water or groundwater source; there are additional considerations for desalination systems (section 6.5 of the Guidelines), which are not specific to PV-powered systems and are not discussed further in this thesis.

2.2 Desalination techniques

The separation of freshwater from saltwater can be achieved in many ways and these are discussed at length in standard texts on desalination (Spiegler et al. 1994; El-Dessouky et al. 2002). A excellent overview is available on the internet (Buros 2000). The following section provides a brief introduction, intended only to set reverse osmosis in context.

2.2.1 Distillation

Heating water in a tank causes it to vaporise, leaving behind any salt. Cooling the vapour causes it to condense as freshwater, which may be collected in a separate tank. A *simple still* of this type is easy to construct, but very inefficient in energy terms. The heat energy required is the *latent heat of evaporation*, which is around 627 kWh/m^3, plus losses. A comparison of energy consumptions is given later in section 2.3.2.

2.2.2 Multi-Effect Distillation (MED)

Most of the heat energy consumed in a simple still ends up in the coolant of the condenser. Recycling this heat energy can improve efficiency several fold. Of course, the

temperature of the condenser is not high enough to heat the saltwater in the original tank, but it can be used to heat a second tank held at a lower pressure. Practical distillation systems often have many tanks, known as *effects*, hence the term *Multi-Effect Distillation* (MED).

MED was developed for desalination purposes during the first half of the twentieth century, but had a major practical problem with the build up of scale on the outside of the heating pipes, rather like the scaling of the heating element in an electric kettle (Arrindell et al. 2002).

2.2.3 Multi-Stage Flash (MSF)

In *flash* distillation, the water is heated under pressure, which prevents it from vaporising while being heated. It then passes into a separate chamber held at lower pressure, which allows it to vaporise, but well away from the heating pipes, thus preventing them from becoming scaled. Like MED, practical flash-distillation systems are divided into sections, but this time known as *stages*, hence the term *Multi-Stage Flash* (MSF).

When first introduced in the 1960's, MSF offered slightly lower energy efficiency than MED, but this was outweighed by scaling considerations and MSF became the industry standard.

2.2.4 Vapour Compression

Compressing water vapour raises its temperature, which allows it to be used at a heat source for the *same* tank of water that produced it. This allows heat recycling in a single-effect distillation process.

In *Thermal* Vapour Compression, the compressor is driven by steam, and such systems are popular for medium-scale desalination because they are simple, in comparison to MSF.

In *Mechanical* Vapour Compression, the compressor is driven by a diesel engine or electric motor.

2.2.5 Reverse Osmosis (RO)

Reverse Osmosis (RO) is a membrane filtration process and, in contrast to the distillation processes just described, does not involve vaporising the water. This generally leads to it being much more energy efficient. RO is the technology chosen for the system described in this thesis, and is described in sections 1.2 and 2.7.

2.2.6 Electrodialysis

Electrodialysis also uses membranes, but unlike RO, the salt ions are deliberately carried *through* the membranes, leaving behind the freshwater. Two types of membranes are required: one that lets anions through but not cations, and the other that does the opposite. These membranes are stacked alternately and held apart by spacers. The saltwater is fed into the spacer layers on one side of the stack, and a DC voltage is applied to the stack as a whole. The salt ions are attracted through one membrane or the other depending on their polarity, and by the time the water comes out of the other side of the stack, it is alternately freshwater and concentrate in the spacer layers. Reversing the polarity of the applied voltage reverses the freshwater and concentrate layers, and this can be done periodically (several times per hour) in order to reduce fouling, and is termed *Electrodialysis Reversal.*

Electrodialysis was commercialised during the 1960's and is widely used today for desalinating brackish water. The energy consumption depends very much on the concentration of the feed water and so electrodialysis is rarely used for seawater desalination.

2.3 Energy for desalination

2.3.1 Theoretical

It has already been stated that the theoretical minimum energy required to desalinate seawater is around 0.7 kWh/m^3. This is true, but is also a little misleading, because it assumes that the volume of seawater is infinite. Of course, the oceans are virtually infinite, in the scale of mankind's freshwater requirements, but practical desalination systems have to work with a finite flow of seawater, since it must usually be pumped from the sea.

The proportion of freshwater extracted from the seawater is known as the *recovery ratio*. Obviously, to minimise feed-water use and pumping requirements, it is best to use a high recovery ratio. On the other hand, in order to limit scaling and desalination energy, it is best to use a low recovery ratio.

The theoretical minimum energy required for desalination increases with recovery ratio as shown in Figure 2-2. The increase is readily explained in context of reverse osmosis, because, as freshwater is extracted, the remaining brine becomes more concentrated, which increases its osmotic pressure and the pump has to work harder to extract further freshwater.

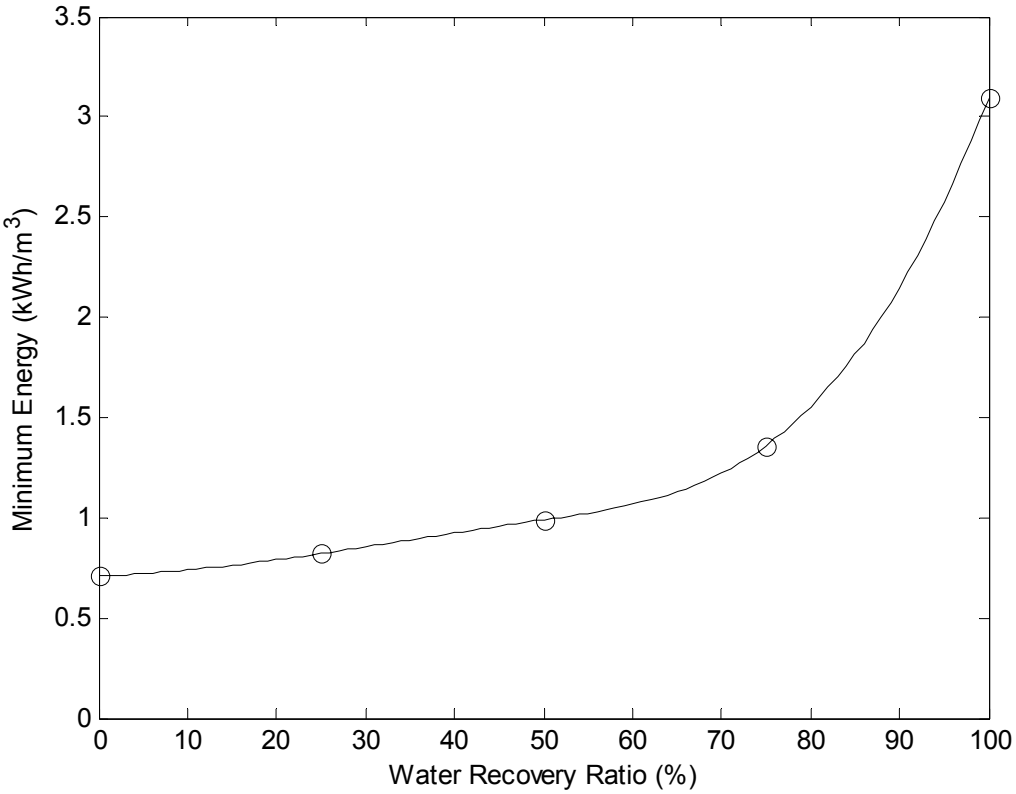

Figure 2-2 – Theoretical minimum energy required to desalinate seawater at 25ºC (Johnson et al. 1966 page 357)

The separation of freshwater from saltwater is a *reversible* process, in the sense that mixing them back together will release the same theoretical minimum energy that went into separating them. Thus, the process must obey the Second Law of Thermodynamics, meaning that the minimum energy required is the same regardless of the method used to achieve the separation. Therefore, the theoretical minimum energy shown in Figure 2-2

applies to *all* desalination techniques, including distillation and electrodialysis (Spiegler et al. 1994).

An appreciation of the theoretical minimum energy is useful in the design of reverse osmosis systems, but as we will see in the next section, practical desalination technology is, as yet, far from ideal.

2.3.2 In practice

It is common practice to couple large thermal desalination plants (MSF and MED) to electricity generating stations, since this provides better overall efficiency. The energy consumption for the desalination may then be quantified in terms of the electrical energy that could otherwise have been generated. This approach is taken in the IDA Worldwide Desalination Plants Inventory (Wangnick 2002) and leads to the data presented in Table 2-1.

	Electrical-equivalent energy consumption (kWh/m^3)
MSF	15.5
MED	6.5
Mechanical Vapour Compression	8 – 14
Reverse Osmosis (RO)	4 – 7

Table 2-1– Typical practical energy consumptions for seawater desalination (Simplified from Wangnick 2002, Table 4/2)

Comparing the figures in Table 2-1 against the latent heat of evaporation: 627 kWh/m^3, illustrates the considerable benefits brought to the thermal processes by heat recycling and by coupling MSF and MED to electricity generating stations. Despite these, it also illustrates that RO is currently the most energy efficient technology for seawater desalination. There are other considerations of course, particularly the capital and maintenance costs. Also, RO is a relative newcomer and is considered less reliable, particularly with regard to fouling caused by *difficult* feed waters (Wiseman 2002). Nonetheless, the attraction of RO for renewable-energy powered desalination is already apparent.

The data presented in Table 2-1 is typical for installed plants with capacities of 100 m^3/d and above. State-of-the-art RO plant can now achieve 2 kWh/m^3 (MacHarg 2001). But,

older and smaller RO systems, particularly those without brine-stream energy recovery, can easily consume up to 15 kWh/m^3.

2.3.3 Energy sources

Virtually all desalination today is powered by fossil fuels and nuclear energy; countries with large hydroelectric capacity do not generally require water through desalination.

It is tempting to estimate the total worldwide energy consumption for desalination, but this is almost impossible because it is so intertwined with electricity production. As already noted, many desalination plants are coupled to electricity generation stations, but also, the provision of water allows cities to grow thereby increasing electricity demand. Nonetheless, this calculation was attempted in 1996 (Rodriguez-Girones et al. 1996) and suggested that the total worldwide energy consumption for desalination at that time was 436 TWh/yr (37.5 Mtoe/yr), which was comparable to the gross energy demand of Sweden. Considering the growth of desalination presented earlier in Figure 2-1, it is safe to conclude that desalination is already a significant contributor to worldwide CO_2 emissions, and that this is set to increase considerably.

In addition to the consideration of CO_2 emissions, is the fact that many countries with water shortages simply do not have significant fossil-fuel reserves, and the import of such fuels places a tremendous burden on their economies.

2.4 Renewable energy for desalination

CO_2 emissions can be greatly reduced through the use of renewable energy, which is often abundant in countries with water shortages. This has led to great interest in using renewable energy for desalination. Indeed, many pilot demonstration plants have already been built and operated (See databases in: Rodriguez-Girones et al. 1996; CRES 1998; Wangnick 2002), and an even greater number of theoretical investigations completed.

Wind energy and solar energy have the biggest immediate potential for powering desalination. Wave power also has great potential, but a reliable means of capturing it has yet to be demonstrated. Tidal and geothermal energies may well be suitable, but are only available in a few locations. Hydropower and biomass are not widely available in arid regions.

2.4.1 Intermittency

Unfortunately, both wind and solar power are intermittent, which leads to three options:

a) Use fossil fuel to make up the gaps, so that the desalination plant can run continuously.

b) Store the renewable energy, so that the desalination plant can run continuously.

c) Run the desalination plant intermittently.

Option a) includes *grid-connected* systems, in which power from a large electricity grid is used to run the desalination plant whenever wind or solar power is not available. This greatly simplifies design and operation. Of course, the wind or solar power plant can be made large enough so that, *on average*, it supplies at least as much energy as is consumed by the desalination plant. This is commendable, since it offsets the burning of fossil fuel elsewhere, but it should be understood that the desalination plant is still reliant on the grid connection and therefore on the burning of fossil fuel. Considering an electricity grid as a whole, it is often found that the *penetration* of intermittent sources such as wind and solar is limited to around 20% of the total energy consumption (Jensen 2000 Table 1 page viii). In order to increase the allowable penetration requires either energy storage or demand-side management, which correspond to options b) and c) respectively, and which were discussed in section 1.8. In summary, use of a grid

connection, where available, greatly simplifies the operation of the wind or solar powered desalination plant today, but for the future, we must look to options b) or c).

Systems without a grid-connection are generally described as *stand-alone*, and can operate under any of the options a), b) or c). A system employing a diesel engine to cover periods when wind or solar power is not available comes under option a), and, in the absence of energy storage, the contribution from wind or solar is likely to be limited to about 20%, as before. In order to reduce the reliance on diesel requires a move towards options b) or c).

Dealing with intermittency, either through energy storage or intermittent operation of the desalination plant, is central to the development of the use of renewable energy for desalination.

2.4.2 Compatibility

The next few sections discuss the viability of some of the more promising combinations of renewable-energy and desalination technologies.

2.4.3 Simple solar stills

Simple solar stills are probably the oldest form of man-made desalination equipment, and the sheer simplicity of the concept gives it eternal appeal. A simple solar still comprises a glass-covered basin of saltwater. The greenhouse effect heats the water causing it to evaporate. It then condenses on the glass as freshwater and dribbles down into a container separate from the original saltwater. Unfortunately, simple solar stills yield very little water: 5 L/d/m^2 is a typical best, meaning that 3 m^3/d would require an area of 600 m^2. (The PV-RO system described in this thesis should achieve the same output with only 20 m^2 of PV.) The low productivity arises partly from the fact that a simple solar still uses *single-effect* distillation, meaning that it uses the latent heat of evaporation (627 kWh/m^3) and none of this heat is recycled. Also, having the solar collector and the evaporators as one unit leads to significant heat losses (Spiegler et al. 1994). Even if land is freely available, the maintenance of large solar stills (keeping the glass clean and vapour-tight) has repeatedly proved impractical (Delyannis et al. 2001).

2.4.4 Indirect solar thermal desalination

Innumerable attempts have been made to improve the performance of solar stills, and the more successful of these generally involve separating the solar thermal collector from the evaporator, which is known as *indirect* solar thermal desalination. Storage of the thermal energy in hot-water tanks is then possible, which allows production to continue through the night, and can improve efficiency by virtue of the condensing surface being cooler. Improved solar collectors may be used, such as parabolic-trough concentrators (mirrors) and evacuated-tube collectors. For further efficiency, it is usual to employ some recycling of the latent heat of evaporation, which moves the design towards multi-effect distillation (MED) or multi-stage flash (MSF).

A thorough discussion of the various solar-thermal desalination options is given by Kalogirou (1997) and a review of numerous demonstration plants is given by Garcia-Rodriguez (2002). A more detailed discussion of the economic feasibility of small solar MED seawater desalination plants for remote arid areas is presented by El-Nashar (2001).

Unfortunately, as shown earlier in Table 2-1 the heat energy demand of even the most efficient MED and MSF systems is considerable. Furthermore, to achieve these efficiencies, MED and MSF systems are complex to operate and therefore tend to be more successful at large-scale. In conclusion, indirect solar thermal desalination remains interesting at medium and large scale, but will face increasing competition from photovoltaic-powered reverse osmosis. However, there may be an alternative, at the small scale, in the form of Membrane Distillation.

2.4.5 Membrane Distillation

The membranes used in Membrane Distillation are unlike Reverse Osmosis or Electrodialysis membranes in that they are hydrophobic, meaning that they resist getting wet and therefore block the passage of both water and dissolved salts. They are, however, permeable to water vapour, rather like Gortex™. Membrane Distillation is primarily a heat-driven process and can achieve the recycling of the latent heat of evaporation without the complexity of multiple effects or a vapour compressor. This makes Membrane Distillation particularly interesting for small-scale application. Furthermore, since the membrane does not have to be selective between water and salt ions, the

effective pore size can be 1000 times larger than for RO, and this, coupled with the fact that it does not get wet, greatly reduces concerns regarding fouling. Membrane Distillation is still at the research stage but holds great promise for small-scale solar-powered application (Koschikowski et al. 2003; Cabassud et al. 2003).

2.4.6 Freezing

When saltwater is frozen the ice that forms is nearly pure and the salt is left in the remaining liquid. Freeze desalination was vigorously researched during the 1950's and 60's because it promised to be more energy efficient and have less scaling problems than thermal distillation processes (Snyder 1966). But, difficulties in the mechanical handling and separation of the ice from the water were never resolved and research was abandoned when reverse osmosis became available.

Meanwhile freezing has been commercially developed for the purpose of energy storage in association with air conditioning. Tanks containing eutectic aqueous solutions are frozen during the night using off-peak electricity and melted during the day to provide cooling (www.calmac.com accessed: March 04).

Observing that desalination is often employed in areas that also have a large air conditioning demand, one wonders if these two could not profitably be combined. This may be particularly interesting for wind-powered systems where the energy source is intermittent.

2.4.7 Wind-powered Reverse Osmosis

Wind power is now an established technology, in many situations providing electricity at a cost well below that of electricity derived from fossil fuels. Thus, the combination of wind-power and reverse osmosis appears very attractive, even for sites with a modest wind resource. The challenge lies in the variability of the wind.

Standing in a field, one might have the impression that a steady wind is blowing; measuring that wind with an anemometer and displaying it on an oscilloscope usually reveals that it is in fact highly variable. Dealing with this variability is one of the main challenges that faces wind-turbine designers. And, connecting an RO system directly to a wind turbine, without some form of energy storage buffer, brings that variability to the RO membranes. Most RO designers shy away from this, possibly with good reason, and

wind-powered RO systems often rely to some extent on fossil fuels: systems with an on-site diesel engine are often called *hybrid* systems; others rely on a grid-connection as discussed in section 2.4.1. Reverse osmosis systems relying solely on wind power are few and far between. The SDAWES project on Gran Canaria employed flywheel energy storage and switching on and off of eight sets of RO membranes (Rahal 2001). Enercon have a number of demonstration systems running, but reveal little about them (Lührs 2003). Vergnet are more open, but perhaps less successful (Fabre 2003). A full review of wind-powered reverse osmosis is doubtless contained in Marcos Miranda's thesis (2003).

A rather different form of wind-powered reverse osmosis, but worthy of mention if only for its sheer elegance, is the *Waterlog* (www.waterloginternational.com accessed: March 04). This is a device that can be dragged through the sea behind a sailing boat. It has a water turbine that operates a pump that feeds an RO membrane. The towline is hollow and carries the freshwater back to the boat.

2.4.8 Other studies

The foregoing sections discuss the viability of some of the more promising combinations of renewable-energy and desalination technologies. Several rather more comprehensive studies have been completed in recent years (Rodriguez-Girones et al. 1996; CRES 1998; Oldach 2001). A shorter discussion of the same subject is available online (Assimacopoulos et al. 2001) and, in broad agreement with the comprehensive studies, states: *"PV-RO (Photovoltaic powered-Reverse Osmosis) is clearly the favoured desalination combination for small stand-alone systems"*. PV-RO is of course the combination chosen for work described in this thesis, and will be discussed in section 2.9, after discussing PV and RO separately.

2.5 Photovoltaics (PV)

Photovoltaic cells convert sunlight directly into electricity. Green (1995) discusses their physics in detail. Roberts (1991), Wenham (1994) and Markvart (1999) include more of their application.

A typical cell is 10 by 10 cm and produces a few watts of DC electricity at around 0.5 volts. To achieve greater powers and voltages, cells are connected in series and assembled into modules, also called panels. A typical module comprises 36 series-

connected cells. This provides a voltage that is convenient for charging 12-volt lead-acid batteries, but such modules are also widely used in systems not employing batteries, including grid-connected systems. Modules are connected together to form arrays, the size of which is limited usually by cost.

2.5.1 Cost

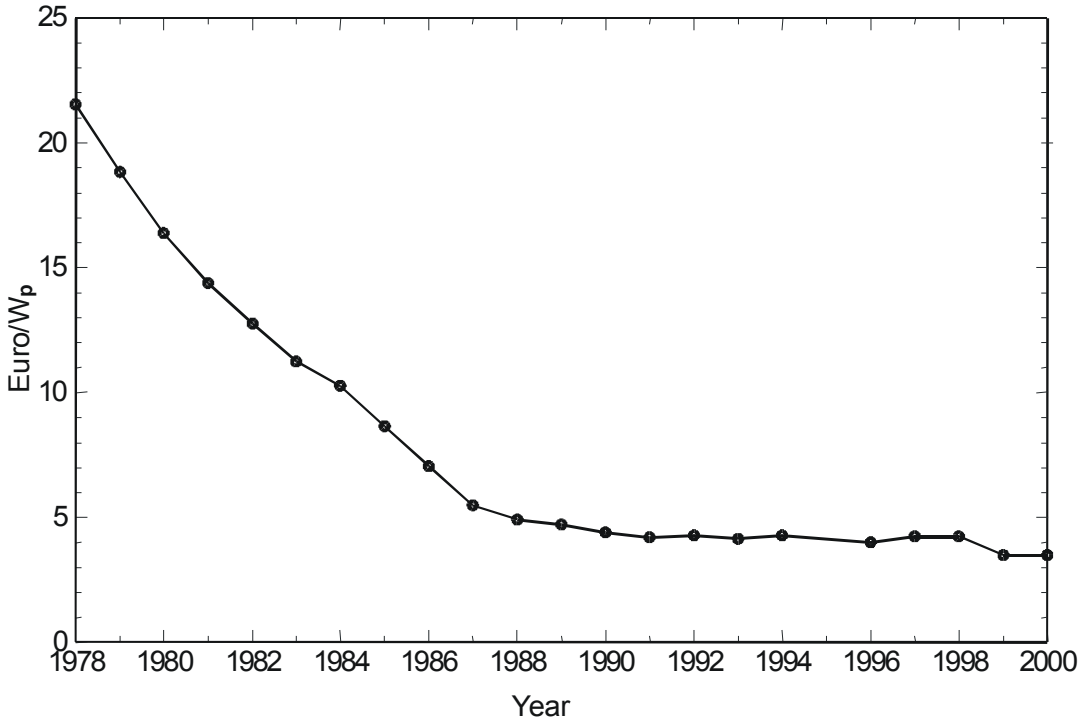

Figure 2-3 – Cost of PV (€/W_p) (Gottschalg 2001 page 254)

The cost of PV has fallen steadily, as shown in Figure 2-3, and this is expected to continue for several years yet. The cost today is still considerable, but there are many situations where PV already offers a cost-competitive solution, although, to make this apparent, it is usually necessary to consider the full lifetime costs of the alternatives. Life-cycle costing is a standard accounting technique and can readily be applied to PV systems (Markvart 1999 page 148).

Often the choice is between PV and diesel-fed internal combustion engines. The latter are typically very cheap to buy but expensive to operate, both in fuel and maintenance. The operating costs of diesel engines per kWh increase dramatically as the average demand (kWh/day) is reduced. In contrast, PV costs per kWh are almost constant, and thus, PV becomes competitive below a certain average demand (kWh/day). Parish (1999) showed that the crossover point can be between 2.5 and 5 kWh/day, depending on PV costs

($/W$_p$) and diesel costs. A far more detailed study, using data specific to India, showed a much higher crossover point: between 15 and 68 kWh/day (Kolhe et al. 2002). Both of these studies include substantial costs for batteries and battery replacement in the PV systems. For applications not requiring batteries, the crossover point is higher still. Nonetheless, there is still a crossover point, above which a diesel engine is more economic, excluding environmental considerations. In summary, PV is most competitive for systems with modest average demand, and thus PV-RO will be most competitive, initially at least, in small-scale.

Even using life-cycle costing, the PV often dominates the costs of a proposed system. This focuses attention on maximising the efficiency of the load to a far greater extent than might be pursued if operating from grid electricity or diesel. Indeed, much of the design effort described in this thesis relates to improving the efficiency of the load, in this case a small RO system.

2.5.2 Materials

Most PV is made of silicon, which itself is very cheap. The cost arises out of the need to purify it, the manufacture of the cells and their assembly into modules. Three forms of silicon are widely used: *mono-crystalline* silicon PV has the highest efficiency and the highest cost; *poly-crystalline* silicon PV is in the middle and amorphous silicon PV has lowest efficiency and least cost. Other materials, such as cadmium telluride, are also under development.

2.5.3 Watts-peak

The available power from a PV module or array is generally quoted in *watts-peak* (W_p), or *kilowatts-peak* (kW_p), and this is the maximum power available under standard test conditions (STC): 1000 W/m^2 irradiance, AM 1.5 spectrum and a cell temperature of 25°C. Under real operating conditions, the maximum power available can be higher than the quoted watts-peak, but is usually lower, and, of course, varies through the day.

2.5.4 Maximum Power Point Tracking (MPPT)

The current-voltage (*I-V*) curve and corresponding power-voltage (*P-V*) curve for a polycrystalline-silicon PV array operating at standard test conditions are shown in Figure 2-4.

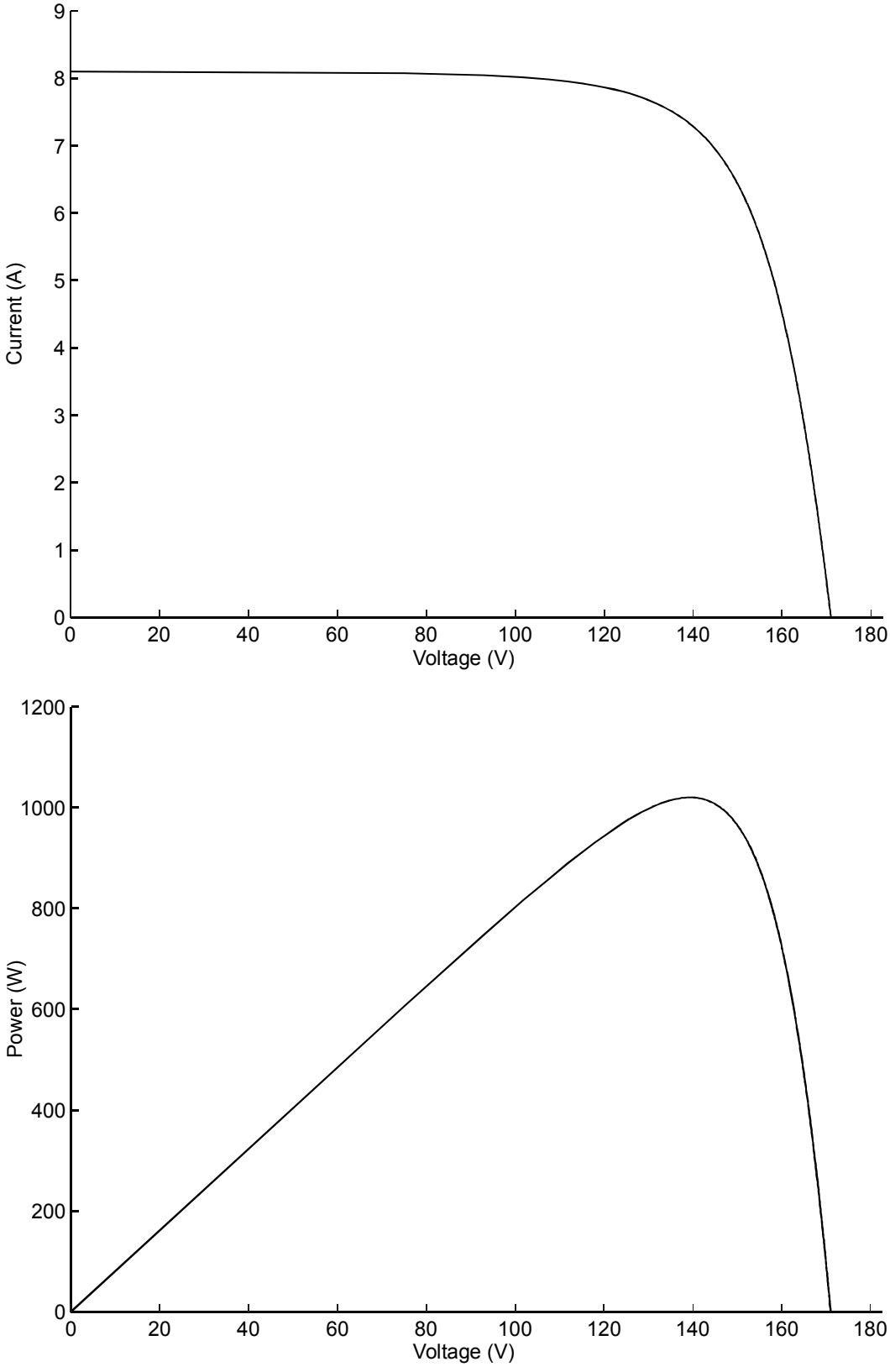

Figure 2-4 – Typical *I-V* and *P-V* curves for a polycrystalline-silicon PV array

In order to obtain maximum power from a PV array it must be operated at the peak of the power curve. In general, the connection of an arbitrary load to a PV array will not draw the maximum power available. This may be acceptable in small low-cost systems, but for large arrays, operating close to the maximum power point (MPP) is an economic necessity.

Furthermore, the natural variation of irradiance and temperature throughout the day and with passing clouds will cause the *I-V* curve to vary, and the *P-V* curve likewise, and thus, the MPP is not stationary. The control of voltage or current, in order to maintain operation close to the MPP is known as maximum power point tracking (MPPT) and is critical to the efficient operation of a PV-RO system, as discussed in Chapter 9.

2.6 Batteries

Rechargeable batteries are widely used in PV systems, mostly for storing the energy during the day and making it available through the night, but also sometimes for smoothing out variations due to passing clouds. Most batteries used in PV systems are *lead-acid*, because their size and weight can usually be accommodated, and because the alternative battery technologies (nickel-cadmium and so on) are usually considerably more expensive. Unfortunately, batteries are notoriously problematic in practice, especially in PV systems in hot countries:

When there is a problem it is usually to do with the lead-acid batteries (Roberts 1991 page 37).

The disadvantages of using batteries, however, are quite formidable (Green 1995 page 219).

The battery is the weakest part of a stand-alone PV system today (IEA 1999 page 6).

Numerous problems may arise in stand-alone PV systems. Premature battery failure is among the most common, and is a major concern throughout the PV industry and user groups. Although they are a relatively low fraction of a system's initial costs, batteries can be the most expensive component in the overall life cycle cost of stand-alone PV systems (Dunlop et al. 2001 page 1).

The electricity and telecommunications industries have been seeking reliable and long-life rechargeable batteries for well over a century (Kapp 1888; via Norris 1999). More recently, the PV industry and research community have also made considerable effort to improve the design and operating strategies of batteries for PV applications (Sauer et al. 1997; Dunlop et al. 2001; IEA 2002)

The need to use *deep-cycle* lead-acid batteries is well known throughout the PV industry and most professional PV system installers will specify batteries of this type. The common alternative: car and truck batteries, also known as SLI (starting, lighting and ignition) batteries, are designed to supply a large current for a short duration, and are totally unsuited to most PV applications. Despite this, SLI batteries are frequently used in PV systems in practice, because they are more readily available (Green 2003). SLI batteries are certainly not suitable for a PV-RO system, and the following discussion applies to deep-cycle lead-acid batteries.

Battery lifetime in PV systems in central Europe is typically 3 to 8 years (Sauer et al. 1997), but in hot countries, this reduces to typically 2 to 6 years (Gwillim 2001), since high ambient temperature dramatically increases the rate of internal corrosion. Even in temperate countries, batteries used for critical telecommunications are often kept in air-conditioned rooms, simply to extend the battery life. Such luxury is not economic for batteries in PV systems. Similar degradation can occur in transit and storage, and batteries may have lost a significant part of their potential lifetime before even being installed (IEA 1999 page 23). Also, batteries require regular maintenance and will degrade very rapidly if the electrolyte is not topped up. In practice, these factors combine and battery replacement costs often exceed original expectations.

Battery efficiency also has a significant cost, since the PV array must be oversized to cover the energy loss in the batteries. Typical battery efficiency is around 85% (Green 1995), but in hot countries, this reduces to below 75 % (Gwillim 2001).

In many PV applications, the use of batteries is almost unavoidable; hence, the research into improved batteries specifically for PV. In other applications, however, batteries are not required, PV-pumping being the obvious example. The requirement of batteries or not in PV-RO will be discussed in section 2.9.3.

2.7 Reverse Osmosis (RO)

Reverse osmosis was outlined fleetingly in the Section 1.2. Here the technology and its development will be discussed in a little more detail.

The early development of reverse osmosis is described by Merten et al. (1966) and the mainstream industrial application of the technology is discussed by Byrne (1995). Also, several of the membrane manufacturers provide comprehensive handbooks (DOW 1995; Koch 2000; Wagner 2001).

An RO membrane may be thought of, initially at least, as an extremely fine sieve that allows water to pass through, but not salt. However, microscopic study of an RO membrane reveals that it is not really a sieve, but rather that the water diffuses through the membrane while salt cannot. Such membranes are described as semi-permeable and were developed for the purpose of desalination during the 1950's and 60's. RO desalination was introduced commercially during the 1970's and now represents over 43% of installed desalination capacity worldwide (Wangnick 2002; via Wiseman 2002).

2.7.1 Membrane materials

The early commercial membranes were cellulose acetate, but since the 1980's, the desalination market has been dominated by thin-film composite membranes, comprising a thin semi-permeable polyamide (nylon) layer supported on a thicker porous polysulphone backing. The physical strength of the membrane and its support structure is critical for it to withstand the high pressures required in desalination.

2.7.2 Hollow-fibre permeators

The first commercial desalination membranes were made in the form of hollow fibres. The saltwater is pumped in at one end of the fibre, freshwater emerges through the membrane wall of the fibre, and the concentrate comes out of the other end. A large number of fibres are assembled into a bundle to form a *permeator*. Hollow-fibre RO permeators are still manufactured, but the market is now dominated by the *spiral-wound* arrangement.

2.7.3 Spiral-wound membrane elements

In the spiral-wound arrangement, the membrane is in sheet-form and has the feel of stiff coated paper. Two sheets are assembled to form a sandwich with a mesh spacer layer in the middle. The pressurised feed water will be on the outside and the freshwater will pass through the membrane into the spacer layer. The spacer layer is sealed on three sides and the fourth is joined to a freshwater collection tube.

In order to save space and cost in pressure vessels, the membrane sandwich is rolled on to the tube as illustrated in Figure 2-5 to form a membrane *element*. A second mesh spacer layer is required to carry the feed water, and, in practice, two or four sandwiches are wound onto each collection tube, which reduces the distance that the freshwater has to travel round the spiral into the tube. The feed water is pumped in at one end of the spiral element and the concentrate appears at the other.

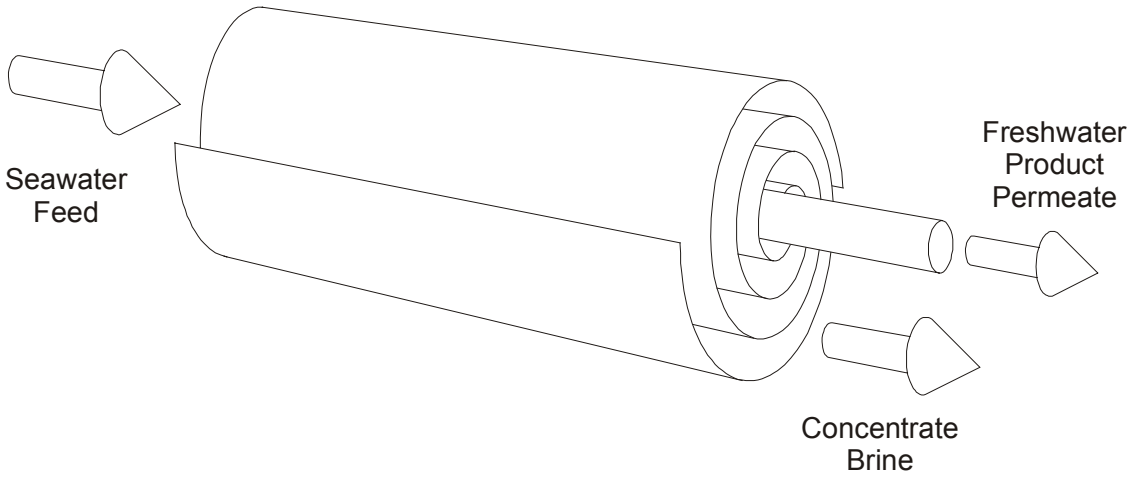

Figure 2-5 – Spiral-wound RO element

RO elements are usually 20, 40 or 60 inches long and 2½, 4 or 8 inch diameter (508, 1016 or 1524 mm long and 64, 102, or 203 mm diameter), the use of inches underlining the fact that most RO elements are manufactured, or at least designed, in the US. For use, the membrane elements are loaded into tubular pressure vessels. Typical pressure vessels hold between one and seven 40-inch elements and can be connected in series and parallel to achieve the desired plant capacity. Large-scale RO plants have hundreds of pressure vessels.

2.7.4 Fouling, scaling and membrane life

A major consideration in the design and operation of any RO system is the avoidance, or at least management, of fouling and scaling of the membranes, since this determines the frequency of required membrane cleaning and replacement. The rate of membrane fouling and scaling is very dependent upon feed-water quality and pre-treatment, and the membrane manufacturers' handbooks all devote substantial sections to these topics.

Scaling, in the context of RO, refers to the precipitation of sparingly soluble salts on the membrane surface when they become too concentrated. Scaling is commonly a limiting factor in systems using brackish feed water with high recovery ratios. Whereas with seawater, the osmotic pressure tends to limit the recovery ratio and scaling is rarely a major problem. With seawater, the main consideration is biological fouling, caused by bacteria.

Pre-treatment often includes the addition of chemicals to the feed water that control fouling and scaling of the membranes. However, there is a trend within the industry to reduce the use of chemical additives and to pay more attention to the design of the feed water intake, so as to obtain cleaner water in the first place (Koch 2000).

2.7.5 Temperature effect

The rate of diffusion of water through an RO membrane, and hence the product flow, is largely dependent on the driving pressure, but temperature is also a very significant factor. An increase in feed temperature of 4 °C will cause the product flow to increase by about 10 % (DOW 1995 section 6.7), *assuming* that other factors are kept constant. But, in systems employing efficient brine-stream energy recovery, the overall effect of temperature is greatly reduced.

2.7.6 High-rejection and high-flow membranes

RO membrane manufacturers typically offer seawater RO membrane elements in two grades: *High-rejection* elements provide low-concentration product, while *high-flow* elements provide a greater volume flow of product, but at slightly increased concentration. Even with high-flow elements, product concentration is usually perfectly acceptable in normal seawater desalination applications. The costs for the two grades are similar.

2.8 Brine-stream energy recovery

As noted in the introductory section 1.2, the energy efficiency of seawater RO is heavily dependent on recovering the energy from the pressurised concentrate (brine). This was recognised and investigated several years before RO became commercially viable (Bray 1966). With brackish water, much higher water recovery ratios are possible, meaning that there is much less energy in the concentrate, which makes brine-stream energy recovery less critical. The following discussion applies mostly to seawater RO.

2.8.1 Pelton wheel

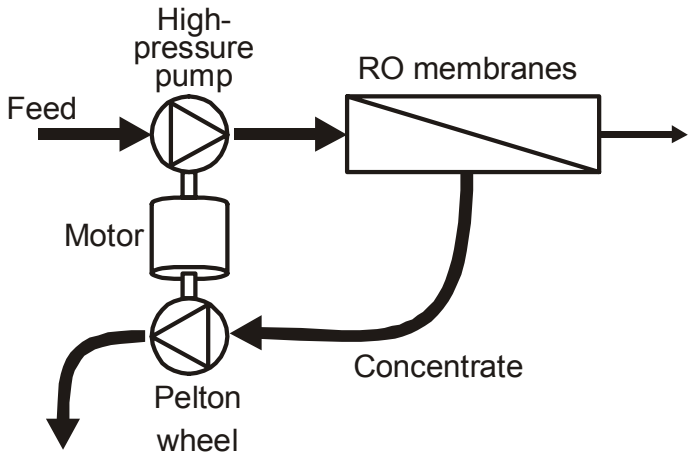

Figure 2-6 – Pelton-wheel energy recovery

In large systems, Pelton-wheel turbines are commonly employed. They are simple, reliable and very well proven in the field, but they are far from perfect. Their efficiency is usually significantly below what might be expected in a hydropower plant, first, because they are coupled to the shaft of the main high-pressure pump, which is really too fast, and second, because the buckets tend to be rough, due to cost-cutting in manufacture and corrosion in service (Doujak et al. 2003). Furthermore, seasonal variations of flow and pressure in a RO plant can be significant, due to variations in water demand, feed water temperature and the condition of the membranes. The efficiency of a Pelton wheel can be significantly reduced when operating away from the design flow and pressure. Lastly, the energy that is recovered then has to go back through the main pump, suffering a further loss before it can usefully be applied to the RO membranes.

In the light of the modest efficiency offered by Pelton wheels in RO systems, several manufacturers have developed alternative brine-stream energy recovery mechanisms.

Healthy competition in this market has led to a steady improvement in the energy efficiency of seawater RO. In no particular order, the leading technologies are the Hydraulic Turbo Booster, the Dual Work-Exchanger Energy-Recovery (DWEER) and ERI's Pressure Exchanger.

2.8.2 Hydraulic Turbo Booster

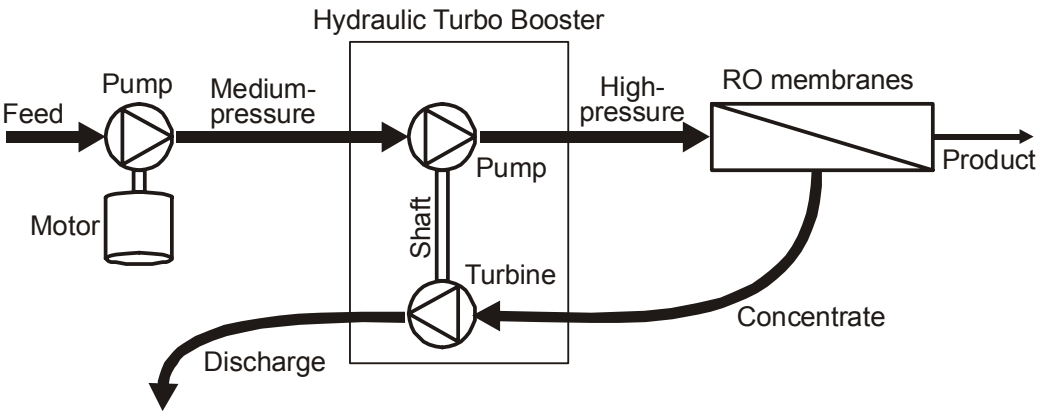

Figure 2-7 – Hydraulic Turbo Booster energy recovery

The Hydraulic Turbo Booster is manufactured by Fluid Equipment Development Co. (www.fluidequipmentdev.com accessed: March 04). It comprises a single-stage radial inflow turbine and a single-stage centrifugal pump on the same shaft, but totally independent of the motor-driven pump. This independence allows the rotational speed of the Turbo Booster to be chosen to optimise its efficiency rather than being fixed by the electric motor. It also facilitates throttling arrangements: control valves that are used to fine-tune membrane pressure. Furthermore, the Hydraulic Turbo Booster can discharge the concentrate at above ambient pressure.

2.8.3 DWEER Work Exchanger

The Dual Work-Exchanger Energy-Recovery (DWEER) is manufactured by DesalCo Ltd. (www.dweer.com accessed: March 04). It comprises two cylinders, each with a free piston. During one stroke, high-pressure concentrate water pushes the piston in one of the cylinders, which pressurises the feed water on the other side of the piston. At the same time, low-pressure feed water pushes the piston in the other cylinder, which pushes the old concentrate out of the system. On the other stroke, the pistons reverse roles. Automatic valves are used to control and coordinate the flows into the two cylinders, and their design is central to the DWEER technology.

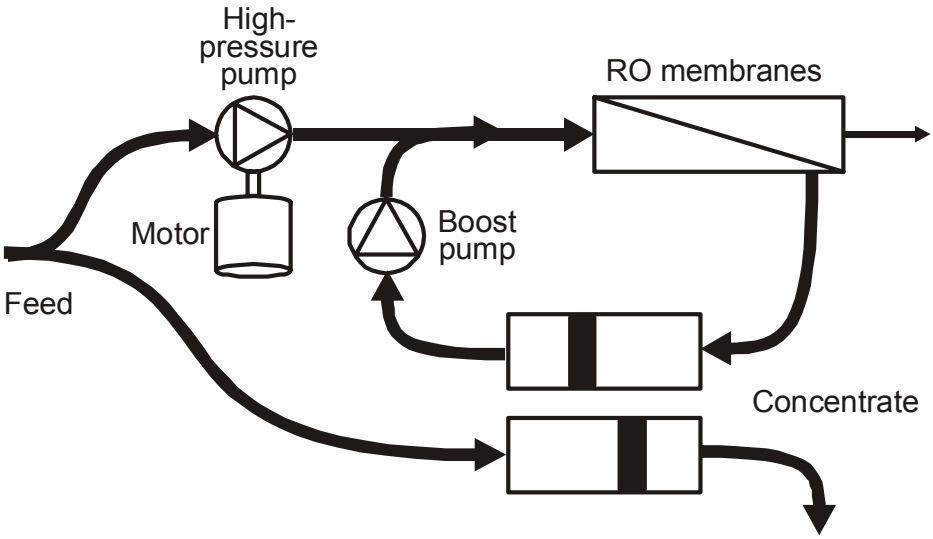

Figure 2-8 – DWEER Work Exchanger energy recovery

Notice, in Figure 2-8, that an additional (motor-driven) pump is required to make up for the small pressure loss that occurs to the concentrate in the membranes and the work exchanger.

An excellent review of large-scale work-exchanger energy recovery mechanisms, leading up to and including the DWEER, is presented by Andrews and Laker (2001).

2.8.4 ERI's Pressure Exchanger

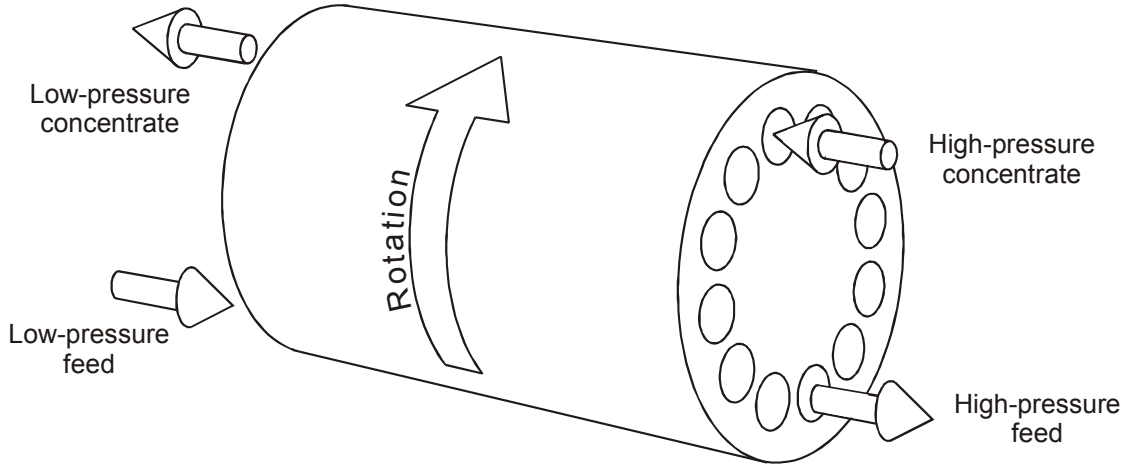

Figure 2-9 – ERI's Pressure Exchanger

The Pressure Exchanger (MacHarg 2001) is manufactured by Energy Recovery Inc. (www.energy-recovery.com accessed: March 04). It is a form of work exchanger, but has twelve *cylinders* with no pistons. The cylinders are co-axial around the circumference of

a ceramic rotor, rather like the holes in the magazine of a revolver. As with other work exchangers, high-pressure concentrate water pushes pressurised feed water through one cylinder, while low-pressure feed water pushes the old concentrate out of another. The absence of a piston allows the water to mix a little, which increases the concentration of the feed slightly but is acceptable in moderation. The automatic valve gear required in other work exchangers is replaced by the rotation of the cylinders past stationary inlet and outlet ports. The rotation is powered by the flow of water through the device, and the speed of rotation is critical to minimising the mixing.

2.8.5 Relative efficiencies

The relative efficiencies of the four energy recovery mechanisms just described are the subject of much debate. It is meaningless to compare the efficiencies of the mechanisms themselves since their outputs have different forms: The Pelton-wheel gives mechanical torque. The Hydraulic Turbo Booster raises the pressure of an arbitrary flow of water. The DWEER raises the pressure of a flow of water equal to that of the concentrate, and requires a further pump. ERI's Pressure Exchanger is similar, but involves some mixing of the flows.

In order to compare the efficiencies at all, the mechanisms must be considered within an RO system. The difficulty then is that parameters and efficiencies of all the other system components come in to play and, depending on these, any of the energy recovery mechanisms can appear in a favourable light (Andrews, Pergande et al. 2001; Oklejas 2002; MacHarg 2002). Losses in control mechanisms such as throttling valves and variable speed drives also need to be accounted for, as do seasonal variations in operating points (Manth et al. 2003).

2.8.6 Vari-RO

The Vari-RO combines water hydraulics with oil hydraulics. Three pistons are used to achieve the high-pressure pumping of the feed. These are driven by both the high-pressure concentrate and the oil hydraulics, which is powered by a motor. Computer controlled valves direct the high-pressure concentrate between three different cylinders. Importantly, they open and close at zero flow in order to minimise transients. A prototype was demonstrated (Childs et al. 1998; Childs and Dabiri 1999) and further developed for solar application (Childs, Dabiri et al. 1999; Childs et al. 2000).

2.8.7 Energy recovery in small-scale RO

Small reverse-osmosis systems are often built without any energy recovery mechanism. They have a manually-operated needle valve or pressure-operated relief valve to control the back-pressure in the concentrate. This keeps the capital cost down but is very wasteful of energy. Typically, 70 % of the input power is wasted in the valve and, consequently, such systems often consume more than 10 kWh/m^3, making them very expensive to run.

Turbines tend to have poor efficiency at small sizes. Gwillim (1996) looked into the possibility of using a Pelton wheel for energy recovery in a 3-m^3/d seawater RO system. It needed a jet size of less than 1 mm acting on a wheel of diameter ~300 mm. High windage losses were expected, together with high manufacturing costs, and in general, the approach was considered impractical.

For energy recovery in small-scale RO systems, positive-displacement devices generally offer much higher efficiencies. The DWEER Work Exchanger and ERI's Pressure Exchanger are positive-displacement devices but are not currently manufactured at small sizes. ERI did produce some small-scale Pressure Exchangers but found that they were prone to fouling (see also Kunczynski 2003); presumably this is less of problem in larger Pressure Exchangers with larger clearances. Other than ERI's Pressure Exchanger, most positive-displacement energy recovery mechanisms involve high-pressure valves that need to operate with precise timing to ensure a smooth flow of water. Combining this precision with corrosion-tolerance of concentrated seawater is very challenging, and many design concepts have failed in practice (Andrews and Laker 2001).

2.8.8 Energy recovery pumps

Integrated designs, combining brine-stream energy recovery with positive-displacement pumping, were developed by Bowie Keefer during the 1980's. He patented a hand-operated pump with energy recovery for application to seawater RO (Keefer 1980). The patent also suggested that the device could be operated by the reciprocating action of a traditional water-pumping wind turbine.

Later, he patented a shaft driven energy-recovery pump (Keefer 1984). This was based on a standard plunger pump, but with positive-displacement energy-recovery added between the crank assembly and the plungers. The plungers also served as spool valves

for the energy-recovery. Prototypes were built and demonstrated very good energy efficiency, including some that were operated from PV (Doman et al. 1982; Keefer et al. 1985). This work showed great promise, but unfortunately was not continued; perhaps the cost of manufacture was high.

2.8.9 Hydraulic motor

Oil-driven hydraulic motors are very widely used in many industrial applications; they are very efficient and very well-proven. Water-driven hydraulic motors are relatively new, but are used for example in the food industry, where risk of hydraulic oil leakage is not acceptable. Danfoss manufacture a range of small water-driven hydraulic motors for such applications. The Danfoss motors have axial pistons acting on a swash plate to rotate the shaft. They are lubricated by the driving water.

Dulas Limited (Gwillim 1996) demonstrated the use of a Danfoss hydraulic motor for energy recovery in a small seawater RO system. This reduced the specific energy consumption from 13 kWh/m^3, for a system using a needle valve, to around 5.6 kWh/m^3 – a vast improvement in the context of PV-RO. The work described in this thesis was founded on the success at Dulas and, in the early stages, employed a similar Danfoss hydraulic motor. However, testing at CREST indicated slightly lower efficiencies and corrosion problems, as discussed in Chapter 3, and the hydraulic motor was dropped from the design, in favour of the Clark pump. In contrast, Kunczynski (2003), who is also developing PV-RO, was using Clark pumps but has now switched to a hydraulic motor.

2.8.10 Clark pump

The Clark pump is a little like the dual work exchanger (section 2.8.3), except that the two cylinders are in-line and the two pistons are connected by a rod. The rod creates a difference in the effective areas on the two sides of each piston, which allows the relative flows to be adjusted by design. Furthermore, having the two pistons connected allows energy from the feed to be added to that of the concentrate, yielding an output pressure higher than that of the concentrate. Hence, the Clark pump is sometimes described as a *pressure intensifier*. A further description of its operation is presented below, but it is perhaps best understood from the animation at:
http://www.spectrawatermakers.com/technology/overview.html (accessed: March 04).

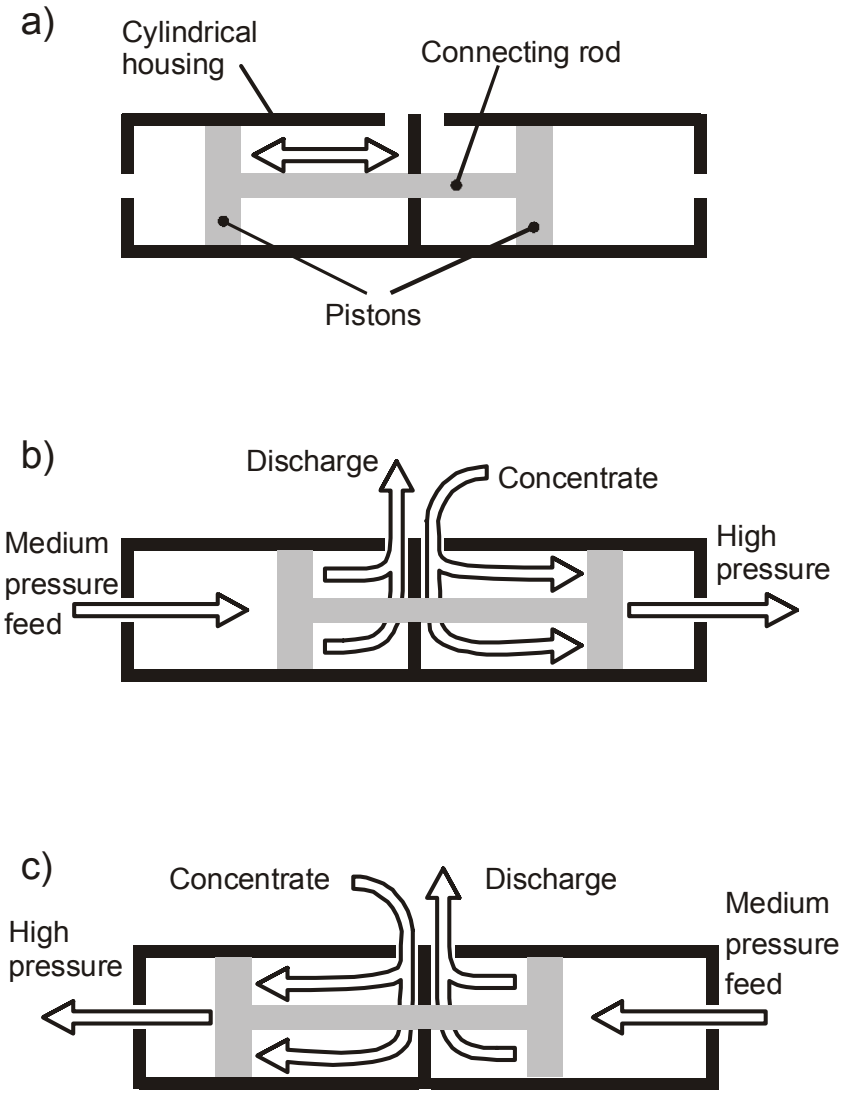

Figure 2-10 – Basic mechanics of a Clark pump

The basic mechanics of a Clark pump are shown in Figure 2-10a. The two pistons are solidly connected by the rod, and this assembly reciprocates inside the cylindrical housing. In Figure 2-10b the medium pressure and the concentrate pressure both act to push the piston assembly to the right, thus driving the high pressure, as shown. At the end of stroke, an internal mechanism reverses the ports, as shown in Figure 2-10c, and the piston assembly travels back to the left, until it again reverses.

The general arrangement of the two pistons and the rod, and its application to RO systems, was presented in patents many year ago (Pinkerton 1979; Wilson 1983). But, it was not until a practical valve-operating mechanism was developed and patented by Clark Permar (hence the name *Clark pump*) that the arrangement became commercially viable (Permar 1995). Permar licensed the design to Spectra Watermakers Inc. who

developed a commercial product during 1997. It was aimed at the yachting market and was sized to suit a single 2.5 by 40-inch spiral-wound seawater RO element.

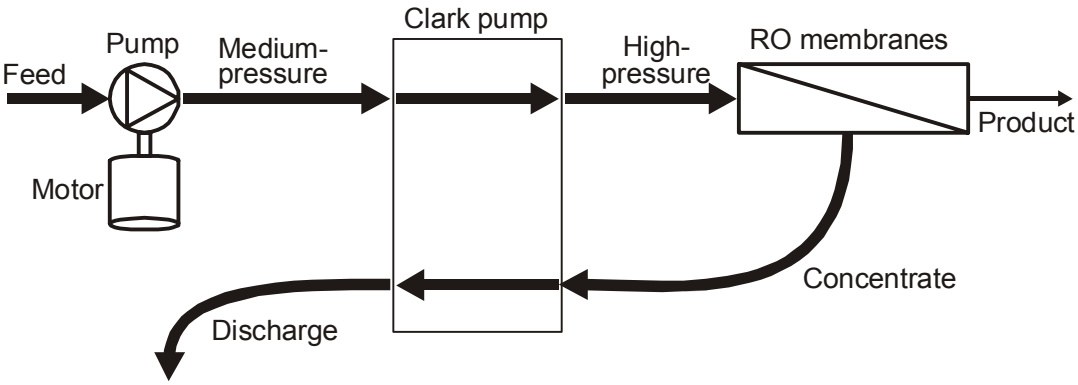

Figure 2-11 – Simple configuration of a Clark pump in an RO system

The simplest configuration of a Clark pump in an RO system is shown in Figure 2-11. It requires only one motorised pump and no pressure regulating mechanism: the water recovery ratio (product flow to feed flow) is fixed by the ratio of the cross-sectional area of the rod to that of the piston. This simple configuration is marketed by Spectra and achieves a specific energy consumption as low as 3.2 kWh/m^3 for seawater at 35,000 ppm, 25 °C (Smith 2000), which is excellent for a small system.

CREST obtained a Clark pump in August 2000 and tested its performance thoroughly. Its energy efficiency is excellent (see section 5.2) and, importantly, this is maintained over a very wide range of flow and pressure. The Clark pump is central to the PV-RO system presented in this thesis.

2.9 Photovoltaic-powered Reverse Osmosis (PV-RO)

As discussed in sections 2.2 to 2.4, photovoltaic-powered reverse osmosis (PV-RO) is considered one of the most promising forms of renewable-energy-powered desalination. And, as discussed in section 2.5.1, PV is currently most competitive in small-scale systems. Thus, small-scale PV-RO has received much attention in recent years and numerous demonstration systems have been built.

2.9.1 Brackish-water PV-RO systems

Brackish water has a much lower osmotic pressure than seawater and therefore its desalination requires much less energy, and therefore a much smaller PV array in the

case of PV-RO. Also, the lower pressures found in brackish-water RO systems permit use of low-cost plastic components. Thus, the total cost of water from brackish-water PV-RO is considerably less than that from seawater, and systems are starting to be offered commercially.

Location	References	Feed Water (ppm)	Capacity (m^3/d)	PV (kW_{peak})	Batteries (kWh)
Sadous, Riyadh, Saudi Arabia	(Alawaji et al. 1995) (Hasnain et al. 1998)	5800	15	10	264
Haifa, Israel	(Weiner et al. 2001)	5000	3	3.5 plus 0.6 wind	36
Elhamrawien, Egypt	www.nrea.gov.eg/pv.htm (accessed: March 04)	3500	53	18	200
Heelat ar Rakah, Oman	(Al Suleimani et al. 2000)	1000	5	3.25	9.6
White Cliffs, Australia	(Richards et al. 2003)	3500	0.5	0.34	NONE
Solarflow, Australia	(Mathew et al. 2001) (Maslin et al. 2003) www.sesltd.com.au (accessed: March 04)	5000	0.4	0.12	NONE

Table 2-2 – A selection of existing brackish-water PV-RO systems

Many of the early PV-RO demonstration systems were essentially a standard RO system, which might have been designed for diesel or mains power, but powered from batteries that were charged by PV. This approach tends to require a rather large PV array for a given flow of product, due to poor efficiencies both in the standard RO systems and in the batteries. Large PV arrays and regular replacement of batteries would tend to make the cost of water from such systems rather high.

The Solarflow system was developed at Murdoch University, Australia (Mathew et al. 2001). It has no batteries and the pump has been designed specifically for the application. The water recovery ratio is fixed at 16% or 25%, which is very low compared to most brackish-water RO systems. This greatly reduces scaling potential, which is a very important consideration with brackish water, less so with seawater. However, the low recovery ratio also gives a much higher flow of concentrate, and therefore energy in the concentrate. Thus, brine-stream energy recovery becomes worthwhile, which is unusual in brackish-water RO. The Solarflow system has energy recovery integrated into the

main motorised pump, along the lines of Keefer's designs mentioned in section 2.8.8. Furthermore, the Solarflow system requires no batteries, see section 2.9.3.

2.9.2 Seawater PV-RO demonstration systems

The osmotic pressure of seawater is much higher than that of brackish water, and therefore its desalination requires much more energy, and, unavoidably, a rather bigger PV array. Also, the higher pressures found in seawater RO systems require use of mechanically stronger components. Thus, the total cost of water from seawater PV-RO is likely to remain higher than that from brackish-water, and systems have not yet passed the demonstration stage.

Location	References	Feed Water (ppm)	Capacity (m^3/d)	PV (kW_{peak})	Batteries (kWh)
Lampedusa, Italy	(Sardi 1996; via CRES 1998)	Seawater	40	100	880
CRES, Laviro, Greece	(Tzen et al. 2003)	36,000	<1	4 plus 0.9 wind	44
ITC, Canaries (DESSOL)	(Herold et al. 1998) (Herold et al. 2001) (Espino et al. 2003)	Seawater	3	4.8	19
La Paz, Mexico	(Kunczynski 2003)	32,600	4 to 19	5 to 25	Yes

Table 2-3 – A selection of seawater PV-RO demonstration systems

The Lampedusa seawater PV-RO demonstration was a flagship project commissioned in 1990, with a very large PV array and battery bank. It includes an energy-recovery turbine of modest efficiency, and achieved a specific energy consumption of around 5.5 kWh/m^3. Since 1995, the PV has been supplemented by mains electricity.

The CRES and ITC projects are current. Neither have energy-recovery.

The project at La Paz is particularly interesting (Kunczynski 2003). It has included trial of three energy-recovery mechanisms: a small ERI's Pressure Exchanger, several Clark pumps and, most recently, the Danfoss hydraulic motor (Danfoss 2002). The test site has a large PV array and battery bank and the PV array size shown in Table 2-3 is based on the measured electrical power consumption of the RO system.

All known seawater PV-RO demonstrations employ batteries.

2.9.3 Batteries or not

As discussed in section 2.6 batteries are a necessary evil in many stand-alone PV systems. They are almost unavoidable in some applications, but anyone familiar with battery performance in real PV systems appreciates the great benefit of eliminating them wherever possible.

On the other hand, anyone familiar with RO desalination equipment appreciates the benefit of operating at constant flow 24-hours-a-day. Obviously, it maximises production and makes best use of the invested capital, but also, it maintains the quality of the product water and helps in the management of membrane fouling.

The reduction of product water quality (increase in salt concentration) may well be perfectly tolerable in some situations, see section 2.1.3, and, otherwise could be addressed through use of high-rejection (lower flow) membranes, as discussed in section 2.7.6, or diversion of the lower quality product, as discussed in section 10.6.

Thus, the main concern is the possible increase in membrane fouling caused by intermittent and variable-flow operation. As noted in section 2.7.4, the critical factor in membrane fouling is the quality of the feed water, which is very site specific and dependent on the intake arrangement. The vast majority of recorded experience of RO membrane fouling is with 24-hour-a-day operation. Systems that are operated intermittently, such as those on boats and ships, tend to be small and unrecorded. Hence, there is little data available to quantify any increase in membrane fouling.

Likewise, data quantifying battery failure in remote areas is very limited. And thus, the choice of using batteries or not within a PV-RO system depends on the relative lifetimes of batteries and membranes, neither of which is well quantified.

Kunczynski (2003) tried intermittent operation, but now favours using batteries. Most other PV-RO systems rely entirely on batteries. The notable exceptions are the two Australian brackish water systems shown in Table 2-2.

Abufayed (2003) reported on a 10,000 m^3/d seawater RO plant in Tajoura, Libya that was operated intermittently for over a year: *Cyclic operation with variable length operate/shut-down periods had no discernable quantitative adverse effects on plant efficiency*.

The University of Las Palmas de Gran Canaria recently set up a small RO rig for testing under variable conditions and have experienced no deterioration after 7000 hours of operation (Gotor et al. 2003). In more limited testing (Gocht et al. 1998), *nothing was observed ruling out a transient operation of the RO.*

These points perhaps support the decision made by CREST and Dulas Limited in 1998 to pursue the development of a batteryless PV-RO system.

2.9.4 Applications

The existing PV-RO demonstrations typically produce between 1 and 100 m^3/d, and, as noted at the beginning of this section 2.9, future systems are likely to be in the same range, initially at least.

At this scale, PV-RO is competing mainly with diesel-powered RO and water transported by tanker. The cost of diesel versus PV was discussed in section 2.5.1, although the comparison may be altered by the fact that a RO unit in a diesel-powered system will tend to be designed to minimise capital cost and therefore be less efficient than one designed to operate from PV. The cost of transported water is very site-specific, but a couple of examples are \$5-6/m^3 for supply by road-tanker to remote parts of Brazil (Laborde et al. 2001) and \$3.75/m^3 for supply by boat to small Greek islands (Avlonitis et al. 2003).

PV is already used to good effect in many developing countries, particularly for vaccine refrigeration, water pumping, lighting and communications. PV-RO will be added to this list, once its cost has reduced sufficiently, which may be fairly soon in the case of brackish-water PV-RO (Maslin et al. 2003). Seawater RO, the subject of this thesis, requires significantly more energy and the cost of PV may have to reduce a little further before seawater PV-RO can be widely applied in developing countries. The early adopters of PV-RO may well be in the luxury market: hotels or prestige dwellings in remote areas or on islands, particularly those keen to protect their environment.

Chapter 3 Initial test rig hardware and results

The work described in this thesis was founded on a previous project conducted by Dulas Limited (Gwillim 1996). In that project, Dulas had demonstrated the use of a Danfoss hydraulic motor for energy recovery in a small seawater RO system. This had reduced the specific energy consumption from 13 kWh/m^3, for a system using a needle valve, to around 5.6 kWh/m^3 – a vast improvement in the context of PV-RO. The Dulas test rig was re-commissioned and transported to CREST during 1999.

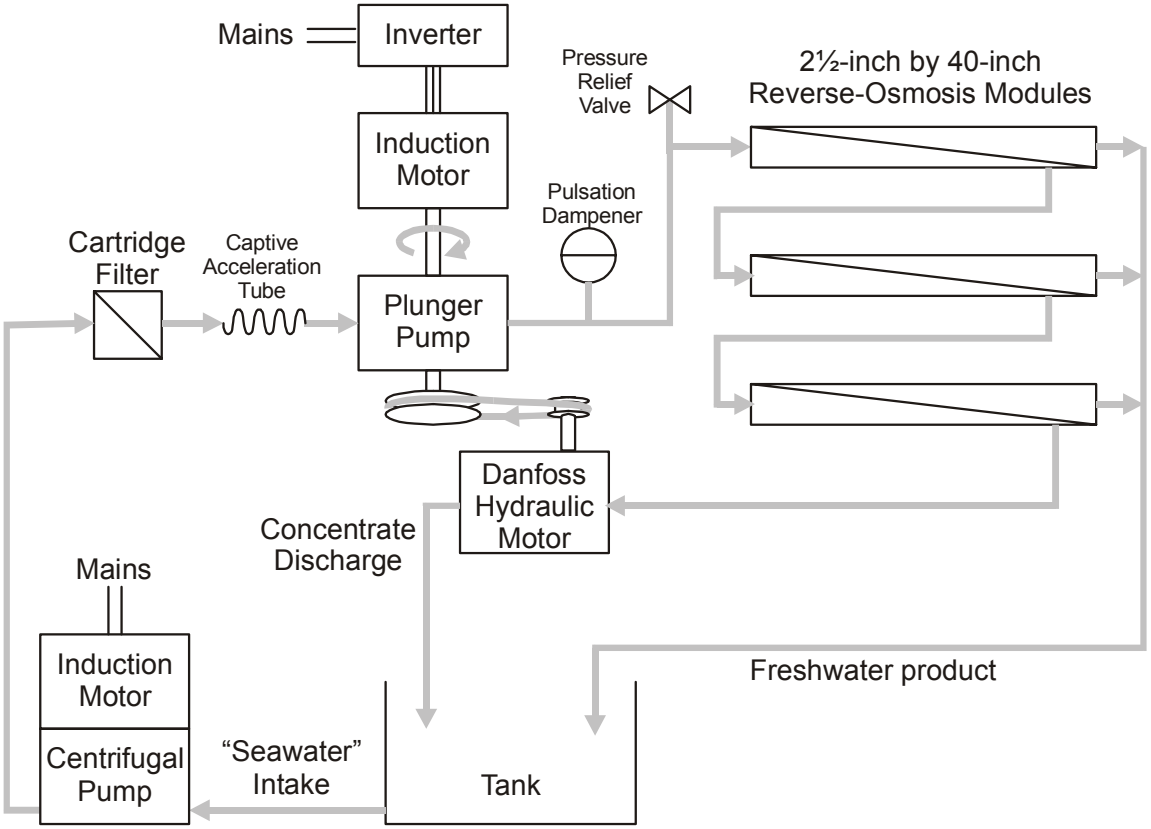

Figure 3-1 – Configuration of the initial test rig using a Danfoss hydraulic motor

Starting from the tank at the bottom of Figure 3-1, a constant-speed centrifugal pump raises the pressure to around 2 bar, at the inlet of the cartridge filter. The plunger pump operates at variable-speed, by virtue of the inverter, and raises the pressure to between ~40 and 69 bar, which feeds the RO modules. The high-pressure concentrate from the RO modules passes through the hydraulic motor and the energy is returned to the shaft of the plunger pump through the pulleys and a toothed rubber belt. Since both the plunger

pump and the hydraulic motor are positive-displacement devices, the water recovery ratio is fixed by the ratio of the pulley sizes. Thus, the recovery ratio could readily be adjusted on-site during commissioning to suit a particular feed water, or perhaps on a seasonal basis to allow for changes in the water temperature. Not all positive-displacement brine-stream energy recovery mechanisms have this flexibility.

The captive acceleration tube and the pulsation dampener, shown either side of the plunger pump in Figure 3-1, serve to smooth out the ripple in the flow created by the pump itself. The pressure relief valve is a safety mechanism.

3.1 Operational results

Surprisingly, the original membranes, which had been left unused and neglected for 3 years, were still functional and capable of producing water at less than 300 mg/L TDS, albeit at very reduced flow. It was decided that they should be used for the initial testing, particularly that of the other components and instrumentation.

The pulleys were configured to give a recovery ratio of around 10 % and the inverter was used to adjust the speed, between zero and maximum in a total of 38 steps. The feed flow, feed pressure and product flow all varied in keeping with the speed and no problems were experienced with the variable operation of the RO membranes. Details of the tests and results are provided in Appendix A and a summary is shown in Table 3-1.

Electrical input power (W)	502	997	1515
Speed (rpm)	494	864	1130
Electric motor torque (Nm)	6.9	8.7	10.3
Feed pressure (bar)	38.7	58.9	68.9
Concentrate pressure (bar)	37.7	56.4	65.1
Feed concentration (mg/L)	29000	29000	29000
Product concentration (mg/L)	550	283	262
Feed flow (L/s)	0.134	0.233	0.300
Product flow (L/s)	0.0075	0.022	0.0291
Specific energy (kWh/m3)	18.6	12.6	14.4

Table 3-1– Measurements from the initial test, using very old membranes

The high specific energy consumptions shown in Table 3-1 are primarily due to the use of very old membranes. Despite this, it was very instructive to consider exactly where the energy was being consumed.

3.2 Sankey diagram

Details of power flow and efficiency calculations are shown in section A.3 of Appendix A and are summarised here in the form of a Sankey diagram.

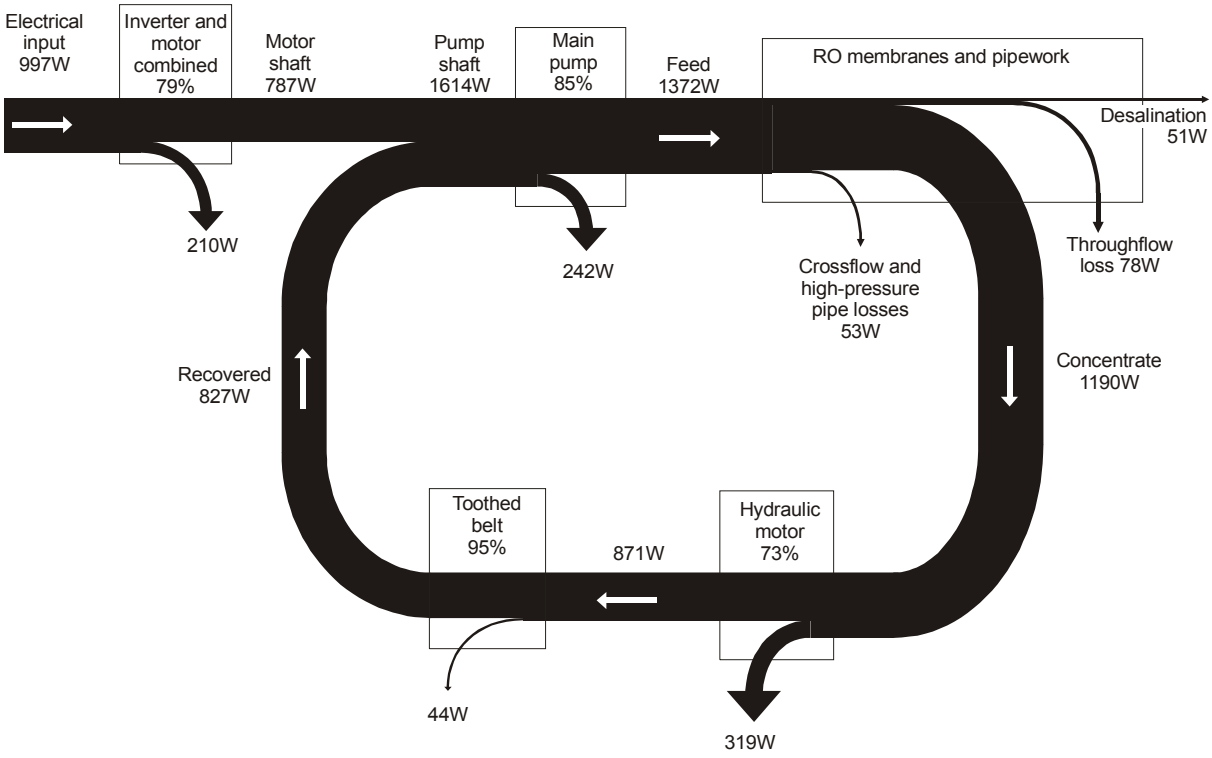

Figure 3-2 – Sankey diagram showing power flows in the initial test rig, using very old membranes

The line widths shown in Figure 3-2 represent the power flows corresponding to the middle column in Table 3-1. These powers can readily be converted to specific energy consumption (kWh/m^3) simply by dividing by 79, which is the product flow in L/h.

Starting on the left, 997 W is drawn from the mains supply. The combined losses in the inverter and the motor are 210 W, meaning that their combined efficiency is around 79%, which is as expected for a motor of this size.

The plunger pump is 85% efficient, which gives a loss of 242 W. Two losses are shown in relation to the RO membranes themselves. First, the 53 W represents the slight pressure drop found between the feed and the concentrate flows, and includes pressure drops in the interconnecting pipe work. Second, the 78 W represents the viscous losses associated with driving the product water through the membrane. The 51 W, on the far right of the diagram, represents the actual desalination power. (51/79 = 0.65 kWh/m^3,

which is a little lower than the theoretical minimum energy figures presented in section 2.3.1, because the concentration of the feed is a little lower.) The massive 1190 W, also emanating from the membranes, represents the energy contained in the pressurised concentrate water. The hydraulic motor recovers part of this energy and delivers it, through the toothed belt, back to the shaft of the pump.

The Sankey diagram, Figure 3-2, shows that the hydraulic motor is supplying more than half of the shaft power to the main pump. Without the hydraulic motor, the electric motor would have to supply the whole of the shaft power, and the electrical consumption would be more than double: ~2045 W, assuming the same motor efficiency. Rephrasing this, the hydraulic motor is reducing the energy consumption by 51%. The previous testing at Dulas (Gwillim 1996) had shown a reduction from 13 kWh/m^3 to around 5.6 kWh/m^3: a reduction of 57%.

3.3 Danfoss hydraulic motor

At this stage, early 2000, the Danfoss hydraulic motor appeared to be a good choice as an energy recovery device for a seawater PV-RO system. However, it was soon to be dropped from the design in favour of the Clark pump. Given that Kunczynski (2003) has recently switched in the other direction, our experience with Danfoss hydraulic motors is reviewed here.

As noted in section 2.8.9, water-driven hydraulic motors are relatively new, and were developed for use in the food industry for example, in which case the driving water is freshwater. For use in RO, as a brine-stream energy recovery mechanism however, the driving water is concentrated seawater, which is very corrosive.

The first Danfoss hydraulic motor, used at Dulas 1996, was a MAH-10. It did not survive the three-year standstill and was found to be totally unserviceable in 1999. The main high-pressure pump, a CAT 317, had endured similar abuse without ill effect. CAT pumps are widely used in small-scale RO systems, and are fully seawater compatible.

A new hydraulic motor, a MAH-5, was purchased from Danfoss in 1999, and at the time, Danfoss claimed that the design had been improved to give a greater resilience to corrosion. However, in mid 2000, after standing for approximately six weeks, some distinctly rust-coloured water emerged from the unit. Several days later, during routine

tests, the rig emitted sounds suggestive of an imminent component seizure and was immediately stopped. Turning the shaft of the hydraulic motor by hand strongly suggested that it was the cause – the torque was uneven and there was a noticeable grating in places. Nonetheless, the rig was restarted and, surprisingly, the problem disappeared. In conclusion, the long-term compatibility of the Danfoss hydraulic motor with concentrated seawater was in doubt.

Perhaps related to this, the hydraulic motor was occasionally reluctant to start. Because the hydraulic motor is coupled to the main pump via the toothed belt, and because initially there is no water pressure, the electric motor has to start both the pump and hydraulic motor. Any stiction in the system could well be a problem in a batteryless PV-RO system, particularly for early morning starting when the power available from the sun is low. A ratchet coupling could be employed but this would add mechanical complexity.

The Sankey diagram, Figure 3-2, shows the hydraulic motor operating with an efficiency of 73%. The toothed belt shows 95% and the main high-pressure pump 85%. Thus, the water-to-water efficiency of the complete arrangement is only 59%. Furthermore, when operating at reduced speed and pressure, as in the first columns of Table 3-1 and Table A-1, the efficiency of hydraulic motor reduced from 73% to 56%, giving an overall water-to-water efficiency of only 45%. In-house testing of the Clark pump, see section 5.2, showed water-to-water efficiency above 90% across a very wide range flow and pressure.

Danfoss now offer a new range of axial piston pumps, the APP range (Danfoss 2002), which are designed for use in seawater RO and can serve as hydraulic motors. These are the units now in use by Kunczynski (2003).

Chapter 4 Instrumentation and data-acquisition system

The early testing described in the previous chapter and in Appendix A also indicated the importance of accurate and reliable instrumentation and data-acquisition. In order to assess the energy efficiencies of the various system components, *with sufficient accuracy to compare different system configurations*, accurate measurements of flows, pressures, speeds, torques and so on are essential. Furthermore, in order to assess efficiencies over a broad range of operation, a computer-based data-acquisition system is required. The quality of the component models discussed in the next chapter is totally reliant on the quality of data from which they are constructed.

Instrumentation and data-acquisition is a major branch of science and engineering in its own right and this chapter is not intended to introduce the subject. Rather, it is intended to pass along particular experience related to the instrumentation of a small RO rig and to indicate the basis of data used in the modelling described later.

4.1 LabVIEW

LabVIEW software from National Instruments is perhaps the industry standard data-acquisition package. Several alternatives were considered at the start of the project in 1999, but overall it seemed that LabVIEW would be the most suitable and it was selected. Four years on, and with much experience in using LabVIEW, the choice still seems good.

LabVIEW is a *graphical* programming language, very different from the text-based languages that most programmers are familiar with. The data appears to flow simultaneously through different parts of the application program, and this, coupled with the fact that data-acquisition is inherently time-critical, can be off-putting, even to well-experienced text-based programmers. Data types (integers, reals, booleans, arrays and so on) are represented by line colours and thicknesses, and can seem awkward to programmers used to less strongly-typed languages such as Matlab, Basic or Perl. As with all programming languages, there are innumerable ways of tackling a particular problem. Used elegantly, LabVIEW can deliver impressive functionality with minimal

programming. Conversely, using LabVIEW as if it were text-based language leads to very clumsy and limited programs. National Instruments provide excellent documentation both for LabVIEW itself and for data acquisition in general. Careful study of this documentation has proved a very good investment of time throughout the course of this project.

4.2 Data acquisition hardware

Data acquisition cards that fit internal PC-computer slots provide cost-effective high-speed multi-channel analogue inputs. Initially an Advantech PCL-818HG card was used, with appropriate driver software to link it to LabVIEW. Various technical annoyances were encountered and, when more channels were needed, the card was replaced with a National Instruments PCI-6024E. Later, a second 6024E card was added and the two have performed impeccably throughout.

The 6024E has 16 single-ended analogue inputs, suitable for measuring voltages in ranges ±0.05 V to ±10 V. The strain gauges used within the pressure sensors and torque load-cells, discussed later, have a very low voltage output and require differential inputs. To accommodate these, National Instruments strain-gauge signal-conditioning boards SC-2043-SG are used. These convert 8 of the single-ended inputs on each of the 6024E cards into differential inputs with 10 times greater sensitivity. Again, the National Instruments hardware has performed impeccably throughout.

4.3 Acquiring data into LabVIEW

It was initially considered that acquiring data at a rate of 1 Hz would be perfectly adequate for the measurement of flows, pressures and so on in an RO rig. This would be mostly true, if the voltages from the sensors were clean DC signals. In the presence of power-electronic inverters, however, and even with diligent application of good distancing, screening and earthing practices, the signals suffer from significant electrical noise. This could be filtered in hardware, but was more readily dealt with in software. The data acquisition rate is set to 1 kHz and each 1000 samples is averaged in the software to give high-quality data at 1 Hz. A modest Pentium II PC handles these calculations with ease, for all 32 channels.

4.4 Signal processing

Once in LabVIEW, the voltage data for each channel is offset, scaled, linearised and so on to convert it to real-world units of flow, pressure and so on. In practice, it was found convenient to perform most of these calculations at 1 kHz, before any averaging. This allows the high-speed data to be viewed on-screen in real-world units, and again there is no problem with computation speed.

Numerous further calculations were implemented in LabVIEW, for example calculating the efficiencies of the various motors, pumps and so on. Viewing this data in real-time provides immediate indication of sensor failure or calibration problems.

4.5 Pulse inputs

The flow meters and speed sensors, described later, provide pulses to the data-acquisition system and were initially connected to dedicated *hardware counter* inputs of the 6024E cards. There are two ways to use such counter inputs to measure frequency.

The first, and most obvious, is to count the number of pulses over a fixed period of time; in our case, the obvious choice is 1 second. However, this gives very coarse results: for example, if the frequency is 9.9 Hz, the data will appear as 10 10 10 10 10 10 10 10 10 9 10 10 10 10 10 10 10 10 10 9 etc, which is correct on average, but is not good for viewing any dynamic effects.

The second approach is to measure the duration of one pulse. This is achieved by using the pulse signal to *gate* a high-frequency signal of known frequency. Counting the gated high-frequency pulses and taking the reciprocal gives the frequency of the unknown low frequency. This approach also gave problems, particularly when measuring frequencies below 2 Hz, because there are not necessarily two rising edges in a 1-second measurement period. This means that the data from the counter channels arrives in LabVIEW asynchronous to the other data on the analogue channels.

An additional, and unexpected, problem with counter channels was caused by electrical noise. Inspection of the pulse waveform on a fast oscilloscope showed a finite rise time as expected. It also showed that noise, during the rise, could cause the data-acquisition system to see *two* rising edges. Using the first method of frequency measurement described above, this led to an occasional extra count, which could easily have gone

unnoticed. Using the second method, the extra pulses were very prominent, because their short duration showed up as a ridiculously high frequency.

To sidestep the complications described above, the sensors with pulse outputs were connected instead to analogue inputs, along with the true analogue signals. Since these channels are sampled at 1 kHz, as mentioned previously, it is straightforward to locate the rising edges, with 1-ms precision, in LabVIEW. From this data, the software calculates the average frequency for every pulse and then rasterises this to give analogue data at 1 kHz. This data shows discrete steps at the pulse edges, but is generally very smooth compared to that available from the hardware counter.

The software approach also gets round the problem of measuring frequencies below 2 Hz, because it can wait for the next rising edge, which is achieved by buffering the data on the other channels, thus ensuring that final data is in perfect synchronism. This proved useful for viewing flow-pressure transients.

4.6 Data logging

The data is logged to disk, usually at 1 Hz, though several other rates have been used for particular investigations. The files are usually .csv and can be opened directly in either Excel or MATLAB.

4.7 Control

The data-acquisition system is also used to provide control of the RO system under test. In particular, it controls the motor speeds and the heating and cooling of the water. For many tests, simple sequencing programs were written to step through an array of test points automatically.

4.8 User interface

LabVIEW facilitates the construction of impressive user interfaces, and this has been exploited to provide real-time graphic display of the system variables and to allow manual control of the motor speeds and so on.

4.9 Flow measurement

4.9.1 Turbine flow meters

The initial test rig was fitted with turbine flow meters for the feed and product, as detailed in Appendix B, section B.1. These were carefully calibrated using a bucket and stopwatch, but repeating this calibration revealed drift of 4% and 13% respectively. Calibration drift of this magnitude renders the data useless for the study of efficiencies etc., and so the turbine flow meters were replaced with oval-gear flow meters.

4.9.2 Oval-gear flow meters

Three oval-gear flow meters are fitted to the new test rig. They measure the Clark pump feed flow, the plunger pump flow and product flow respectively. They are manufactured by Titan Enterprises Limited and offer a nominal accuracy of 0.5%. Titan provide traceable calibration certificates for each meter, as shown in Appendix B, section B.2, and claim repeatability of +/– 0.1%. Marcos Miranda used the data from the calibration certificates to create a polynomial for each meter and implemented these in LabView. Thus, the final accuracy is believed to be better than the nominal 0.5% and no further calibration was considered necessary.

4.10 Pressure sensors

The pressure sensors used are silicon-diaphragm type, PDCR 800 series, manufactured by Druck Limited. The datasheet (Druck 1997) claims a combined non-linearity, hysteresis and repeatability of ± 0.1% best-straight-line and a temperature effect of ± 0.5% within the range 0 to 50 ºC.

4.10.1 Medium-pressure sensor

For the medium-pressure feed to the Clark pump, a PDCR 810-0799 sensor rated at 15 bar is used. Its calibration sheet is in Appendix B, section B.3 and indicates a full-range output of 100.24 mV. However, the LabView data-acquisition system was set to the nominal specification value of 100.00 mV, increasing the overall error to around 0.25%.

4.10.2 High-pressure sensors

For the high-pressure feed to the RO modules and for the concentrate, two PDCR 810 sensors, rated at 60-bar, are used. Using them up to 69-bar is considered acceptable, although linearity may be slightly impaired. No calibration sheets were available for these sensors so they were checked, at least in their low range, by comparison against the medium-pressure sensor. This showed excellent agreement with the nominal specification and no further calibration of the absolute measurements was considered necessary. They were also checked against each other over the full range and this revealed a discrepancy of 0.44% at full range. In order to maximise the accuracy of the small delta pressure, which is calculated from the difference of the large high-pressure and concentrate pressure, this discrepancy was removed by adjusting one sensor up 0.22% and the other down by the same amount.

4.11 Concentration measurement

The concentrations of both feed and product water are calculated from conductivity measurements. In-line conductivity probes and industrial signal-conditioning units were fitted by the original manufacturers of the initial test rig. These had three problems.

First, the conductivity probes were wrongly orientated and poorly positioned in the pipe work. This can lead to lack of flow through the probe (dead space) and trapped air within the probe. Certainly, the data became much more consistent after the probes were refitted correctly.

Second, the 4-20-mA outputs from the signal-conditioning units were neither floating nor properly grounded. This gave errors when connected to single-ended inputs on the data-acquisition card. Connection to differential inputs seems extravagant for 4-20-mA signals, but did solve the problem.

Third, the temperature compensation included in the industrial signal-conditioning units was not accurate. To solve this it was disabled, and temperature compensation was implemented more accurately in LabVIEW.

With hindsight, it may have been better to connect the conductivity probes directly to the data-acquisition system. This would require a low-voltage AC supply to the probes to prevent electrolysis; the industrial units use 1 kHz.

The concentration is calculated from the conductivity in LabVIEW using a polynomial derived from data from DOW (1995 section 10.2), see Appendix B, section B.4.

For initial calibration, fixed resistors were used in place of the conductivity probes. For final calibration, water samples are periodically compared with accurately made solutions, and normally show good agreement.

4.12 Temperature measurement

Initially, a thermocouple temperature sensor was used, but this was very prone to electrical noise from the power-electronic inverters. It was replaced by a thin-film platinum element probe (RS part number: 237-1663), which provides a far better signal and is calibrated to BS 1904, Class B, DIN437860, 100Ω±0.1Ω at 0°C. This translates to ±0.3 °C and may be expected to rise to ±0.4 °C at 50°C (RS datasheet 249-4930).

National Instruments sell signal-conditioning units specifically for platinum resistance temperature sensors, but, to save cost, the sensor was connected in a Wheatstone-bridge configuration feeding one of the high-sensitivity differential inputs on the SC-2043-SG. A little circuit theory, programmed into in LabVIEW and including adjustment for the cable resistance, provides a measure of the sensor resistance, and implementation of the Callendar-Van Dusen equation, again in LabVIEW, provides the final temperature measurement.

4.13 Temperature control

The performance of RO membranes is very dependent on the water temperature, as discussed in section 2.7.5, and, in order to control this, the test rig is fitted with both an electric heater in the tank and a titanium-plate heat exchanger in the concentrate line for cooling. The cooling is provided by tap water, which is controlled by a solenoid valve. The heater and the solenoid valve are controlled through digital outputs from LabVIEW. The control uses pulse-width modulation, based on a saw-tooth at 0.05 Hz, coupled with a P-I controller. This arrangement normally holds the measured temperature within 0.1 °C of the setpoint.

4.14 Torque

In order to measure torque, each motor is mounted in a swinging cradle concentric with the shaft (gimbals) and fitted with a load-cell: Amber Instruments, model 355. The manufacturer's test and datasheet (for the load-cell only) is shown in Appendix B, section B.5.1, and presents data in terms of kilograms of "load" (mass). In theory, this could be converted to Newtons of force and then to Newton.metres of torque, but this approach would rely on accurate knowledge of the effective geometry of the load-cell mounting with respect to the motor shaft centre. In practice, measurement of this geometry would be awkward and error-prone. As an alternative, the complete mechanism (swinging cradle and load-cell) was calibrated by hanging mass on a horizontal arm of known radius, as detailed in Appendix B, section B.5.2.

The load-cells are prone to electrical noise, primarily because they are very close to their respective motors. The effect of the noise is repeatable to some extent and has been offset as far as possible within LabVIEW. In future, it may be better to remount the load-cells further from the motors.

4.15 Speed

The motor speeds are detected by a photocell in one case, and a magnetic sensor in the other. They both work very well, and provide pulses that are processed as described in section 4.5.

4.16 Voltage, current and electrical power

The measurement of electrical power consumed by the two inverters (variable-speed drives) is achieved through high-resolution measurements of the one voltage and two currents. In particular, the three signals are sampled at 10-kHz, then multiplied to give power, *before* being averaged. This ensures that non-sinusoidal and non-DC components are accurately measured.

4.17 Irradiance

The solar irradiance in the plane of the PV array was measured with a Kipp and Zonen CM11 pyranometer (Appendix B, section B.6), which is connected to a separate data logging system. It is logged at 10-second intervals and was aligned with the LabVIEW data by way of its timestamps.

Chapter 5 Component options, testing and modelling

There are innumerable possible configurations of membranes, pumps, energy recovery mechanisms and so on that could be considered for a PV-RO system. To assess the relative merits of different configurations, without building and testing them all in hardware, comprehensive and flexible software modelling was developed. The test rig and data acquisition system, already described, was used to construct models of the most critical components, and this was supplemented by data from manufacturers and so on to complete a set of models covering all the likely candidate components. These component models were then used to construct system models that allowed rapid assessment of numerous configuration options.

Of course, this strategy is pretty common throughout engineering, and there are various software packages that have a similar aim. In the field of RO system design, the membrane manufacturers generally offer software to system designers. DOW FILMTEC, for example, have a program called ROSA (DOW 2000), and KOCH Membranes have ROPRO (Koch-ROPRO 2000). These packages are similar in that they each include component models for all the membrane elements available from the respective manufacturer. The user can construct trains and arrays of these elements, and run simulations to predict overall performance. Both packages include detailed modelling of the chemical composition of the feed waters and provide chemical analysis predictions of the product. They model flows and pressures throughout the proposed system and can be used to estimate pump energy consumptions. Both of these programs were studied and used in the development of the modelling described here, but neither has the scope required for the design of a full PV-RO system. The main limitation in ROSA and ROPRO is that they only simulate operation at a single point, and have no facility for modelling *variable* flow, pressure, temperature and so on. Furthermore, they are only accurate within the normal working range of RO membrane elements; the batteryless PV-RO system described in this thesis sometimes operates at flow and pressure well below this range.

5.1 Modelling strategy – MATLAB-Simulink

MATLAB-Simulink is a general-purpose modelling and simulation package that is used throughout science and engineering research and design. MATLAB itself is a text-based programming language that is particularly intended for manipulation of matrixes (hence the name) and mathematical computing in general. Simulink is a graphical programming language that acts as a front-end to MATLAB and allows rapid construction of dynamic simulation models. MATLAB-Simulink was used extensively for the modelling of the PV-RO system. MATLAB (without Simulink) was used for much of the off-line processing of data from LabVIEW.

Simulink models are constructed as interconnected blocks that are structured hierarchically. The programmer has complete control over the structure, and the first challenge is to design an efficient structure for the task in hand.

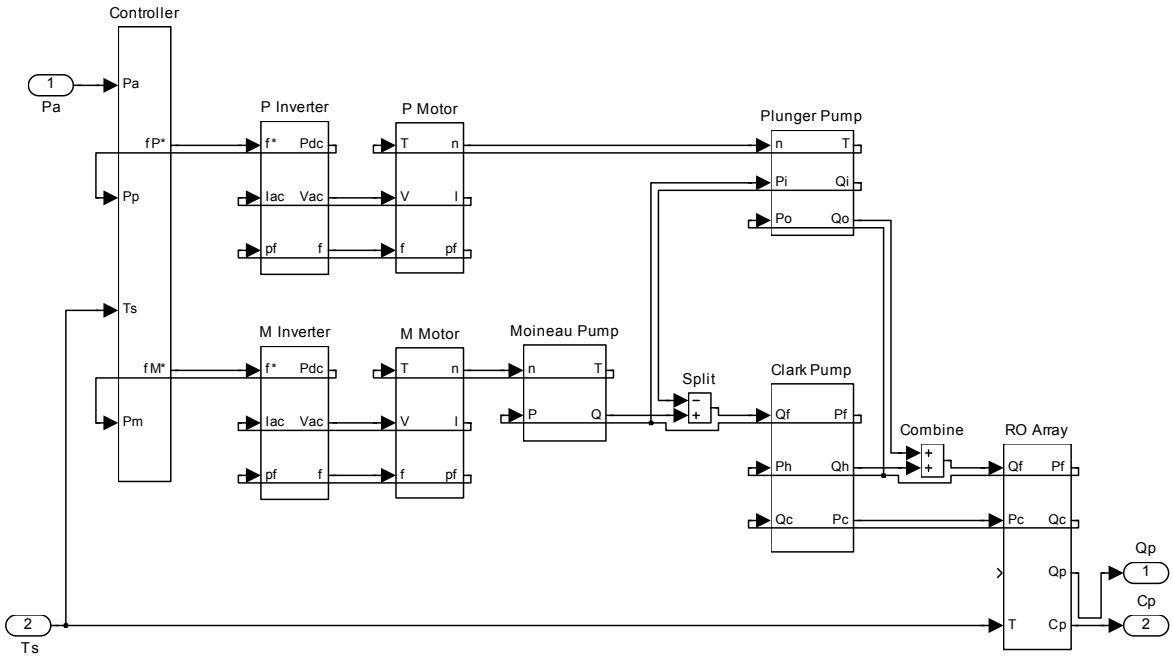

Figure 5-1 – Simulink model structure

The Simulink model shown in Figure 5-1 is presented here only to illustrate the general structure and interconnections between the component models; detailed discussion of the system model is deferred until Chapter 6, after the components have been discussed.

The structure of the model illustrated in Figure 5-1 may seem straightforward and obvious. Alternative RO system configurations can be modelled simply by dragging the blocks around and reconnecting the lines between them. Blocks can be copied and deleted and so on, and new blocks are fairly easy to construct. Achieving this apparent simplicity was not trivial.

The challenge in structuring a model of a physical system such as PV-RO is that *everything depends on everything else*, and it is very easy to end up with a mess of interconnecting lines, and blocks that are not identifiable with any particular hardware component. For example, consider one pump feeding one membrane element. The flow of water into the membrane element is a function of its pressure (and various other things). The flow can also be determined as a function of motor speed, and, assuming there are no leaks, the two can simply be equated to give an expression relating motor speed to pressure. The snag is that this expression is not associated with any one physical component. One could easily create a Simulink block to perform the calculation but its presence in the model would spoil the one-to-one relationship between the software blocks and the hardware components. The model could be perfectly good, in terms of performing the right calculations, but would be very poor for the purpose of trying out alternative RO system configurations. The blocks shown in Figure 5-1 are immediately identifiable as the physical components of the system being modelled.

Achieving the clean structure shown in Figure 5-1 is largely a matter of choosing the inputs and outputs of each block appropriately. For example, one might think that a motor outputs both speed and torque to a pump and propose a model such as that shown Figure 5-2 a). One quickly finds that this does not work, and the structure needs to be either b) or c). The choice between b) and c) is purely a matter of preference in this simple example, but for the full PV-RO system, which includes a loop by virtue of the energy recovery, membrane elements with three pipe connections and a Clark pump with four, the choices become more critical.

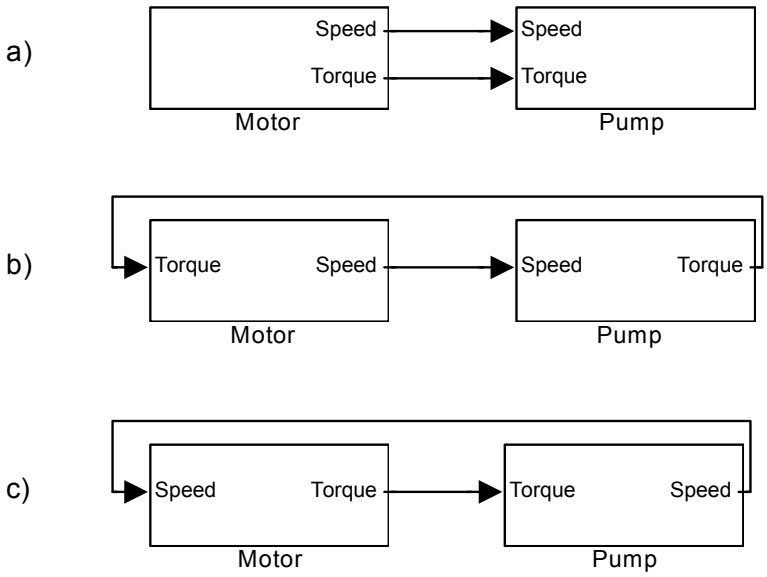

Figure 5-2 – Simulink structure possibilities

The structures shown in Figure 5-2 b) and c), and indeed in Figure 5-1, include quantities that are fed *backwards* (from right to left), implying that the model must know the answer before it can work it out. These *circular references* are a necessary feature of this type of system model. In Simulink, they are known as *algebraic loops* and are solved iteratively using Newton's method.

In conclusion, this section has introduced Simulink, which was used for modelling the components presented in the remainder of this chapter, and has indicated how the component models can be shaped such that they will be useful in the consideration of alternative PV-RO system configurations presented in the next chapter.

5.2 Clark pump

The Clark pump is central to the final PV-RO system design presented in this thesis. Its basic operation was described in section 2.8.10, but it is perhaps best understood from the animation at (http://www.spectrawatermakers.com/technology/overview.html accessed: March 04). Also available at that site is the Clark Pump Field Repair & Rebuild Manual (Spectra 2003), which shows the internal valve mechanisms.

The Clark pump was patented in 1995 and commercialised during 1997 as part of a complete RO system for use on yachts. The performance of the system as a whole had been measured and its excellent efficiency was, and still is, the main selling point.

CREST obtained a Clark pump in August 2000, at which time, there was no performance data available for the Clark pump itself, still less any published performance theory or model.

5.2.1 Theory

5.2.1.1 Ideal (lossless) Clark pump

An *ideal* Clark pump would have no leakage, pressure or frictional losses. The reversal (shift), at the end of the stroke, would be instantaneous and lossless. Thus, all flows and pressures would be perfectly constant (assuming constant external conditions). Also, due to symmetry, the flows and pressures of an *ideal* Clark pump can be fully understood by considering the pistons moving in only one direction.

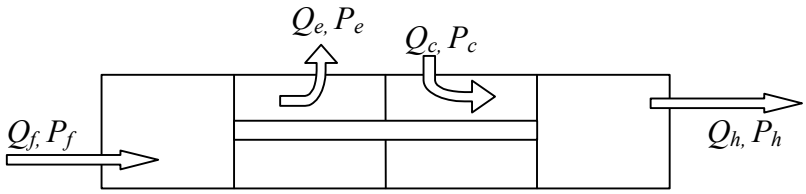

Figure 5-3 – Ideal Clark pump

Q is the flow and P the pressure. The suffixes stand for *feed, exhaust, concentrate and high-pressure*.

Flows

Equating the velocity of the pistons gives:

$$\frac{Q_f}{A_p} = \frac{Q_e}{A_p - A_r} = \frac{Q_c}{A_p - A_r} = \frac{Q_h}{A_p} \tag{1}$$

where A_p is the area of the piston and A_r is that of the rod.

Thus:

$$Q_f = \frac{Q_e}{1 - R_t} = \frac{Q_c}{1 - R_t} = Q_h \tag{2}$$

where R_t is the theoretical recovery ratio given by:

$$R_t = \frac{A_r}{A_p} \tag{3}$$

Rearranging equation 2 gives:

$$R_t = \frac{Q_f - Q_f(1 - R_t)}{Q_f} = \frac{Q_f - Q_c}{Q_f} = \frac{Q_p}{Q_f} \tag{4}$$

Where Q_p is the product flow.

Pressures

Summing the forces acting on the piston gives:

$$\sum f = P_f A_p - P_e(A_p - A_r) + P_c(A_p - A_r) - P_h A_p = 0 \tag{5}$$

So:

$$P_f + P_c(1 - R_t) = P_e(1 - R_t) + P_h \tag{6}$$

Powers

Combining equations 2 and 6 gives:

$$P_f Q_f + P_c Q_c = P_e Q_e + P_h Q_h \tag{7}$$

which simply confirms that:

$$\textit{Power in} = \textit{Power out} \tag{8}$$

as expected for a lossless system.

5.2.1.2 Leakages (flow losses)

Firstly, leakages past the pistons (Q_{fe} and Q_{hc}) and through the central rod seal (Q_{ce}) may be considered.

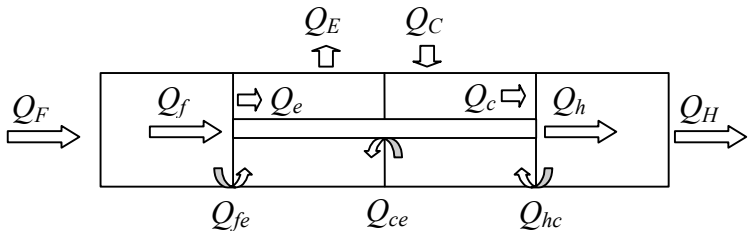

Figure 5-4 – Leakages

The lowercase suffixes indicate the net flows that act on the piston (the ideal flows, as before) and the uppercase suffixes indicate the total flows that may be observed at the external pipe connections. Thus, for example, the net feed flow acting on the piston would equal the total flow less the leakage: $Q_f = Q_F - Q_{fe}$.

In practice, various other leakages are possible, particularly through the valve gear, and, in general, it is possible that any one of the four chambers could leak into any other. This gives a total of six possible leakage flows and the following relationships.

$$Q_f = Q_F + Q_{hf} + Q_{cf} - Q_{fe} \tag{9}$$
$$Q_e = Q_E - Q_{he} - Q_{fe} - Q_{ce} \tag{10}$$
$$Q_c = Q_C + Q_{hc} - Q_{cf} - Q_{ce} \tag{11}$$
$$Q_h = Q_H + Q_{hc} + Q_{hf} + Q_{he} \tag{12}$$

The directions of the leakage flows, and hence the signs appearing in the above equations, are chosen such that positive flow is always from the higher pressure to the lower. Thus, all six leakage flows may be expected to be positive.

Effect on recovery ratio

Combining equations 2, 9, 10, 11 and 12 gives:

$$Q_F + Q_{hf} + Q_{cf} - Q_{fe} = \frac{Q_E - Q_{he} - Q_{fe} - Q_{ce}}{1 - R_t} = \frac{Q_C + Q_{hc} - Q_{cf} - Q_{ce}}{1 - R_t} = Q_H + Q_{hc} + Q_{hf} + Q_{he} \tag{13}$$

Where, as before, R_t is the *theoretical* recovery ratio.

Rearranging equation 13 gives:

$$\begin{aligned} Q_C &= \left(Q_F + Q_{hf} + Q_{cf} - Q_{fe}\right)\left(1 - R_t\right) - Q_{hc} + Q_{cf} + Q_{ce} \\ &= Q_F + Q_{hf} + 2Q_{cf} - Q_{fe} - R_t Q_F - R_t Q_{hf} - R_t Q_{cf} + R_t Q_{fe} - Q_{hc} + Q_{ce} \end{aligned} \tag{14}$$

And:

$$Q_H = Q_F + Q_{cf} - Q_{fe} - Q_{hc} - Q_{he} \tag{15}$$

Thus, the measured recovery ratio is given by:

$$R_m = \frac{Q_P}{Q_F} = \frac{Q_H - Q_C}{Q_F} =$$

$$\frac{Q_F + Q_{cf} - Q_{fe} - Q_{hc} - Q_{he} - Q_F - Q_{hf} - 2Q_{cf} + Q_{fe} + R_t Q_F + R_t Q_{hf} + R_t Q_{cf} - R_t Q_{fe} + Q_{hc} - Q_{ce}}{Q_F}$$

$$= R_t - \frac{Q_{he} + Q_{ce} + (1 - R_t)(Q_{cf} + Q_{hf}) + R_t Q_{fe}}{Q_F} \tag{16}$$

Or:

$$R_m = R_t - \frac{Q_L}{Q_F} \tag{17}$$

where Q_L is the combined leakages:

$$Q_L = Q_{he} + Q_{ce} + (1 - R_t)(Q_{cf} + Q_{hf}) + R_t Q_{fe} \tag{18}$$

Interestingly, Q_{hc} should have no effect on the measured recovery ratio.

Notice also that, the other five leakages will *all* serve to *reduce* the recovery ratio from its theoretical value (they are all positive in the expression for Q_L).

Also, from equation 17:

$$R_m Q_F = R_t Q_F - Q_L \tag{19}$$

In words this is:

measured product flow = theoretical product flow – leakages

The leakages may be expected to include two forms: Firstly, *pressure-driven* leakages that may be expected to increase with pressure. Secondly, *fixed-volume-per-cycle* leakages that may be expected to increase with frequency and, therefore, with flow.

Volumetric efficiency

The *volumetric efficiency* η_V of a Clark pump may be defined as:

$$volumetric\ efficiency = \frac{measured\ \ product\ \ flow}{theoretical\ \ product\ \ flow} \tag{20}$$

More specifically:

$$\eta_V = \frac{Q_P}{Q_F R_t} \tag{21}$$

Or:

$$\eta_V = 1 - \frac{Q_L}{Q_F R_t} \tag{22}$$

Useful flow relationships

$$Q_P = Q_F - Q_E = Q_H - Q_C = R_m Q_F = R_t Q_F - Q_L \tag{23}$$

$$Q_E = Q_F - Q_P = Q_F(1 - R_m) = Q_F(1 - R_t) + Q_L \tag{24}$$

$$Q_F + Q_C = Q_H + Q_E \tag{25}$$

5.2.1.3 Pressure Losses

The feed will experience a slight pressure loss due to its own viscosity in the pipes and valves on its way in to the chamber. Likewise, the high-pressure, on its way *out* of the chamber, and so on. These pressure losses are indicated: ΔP .

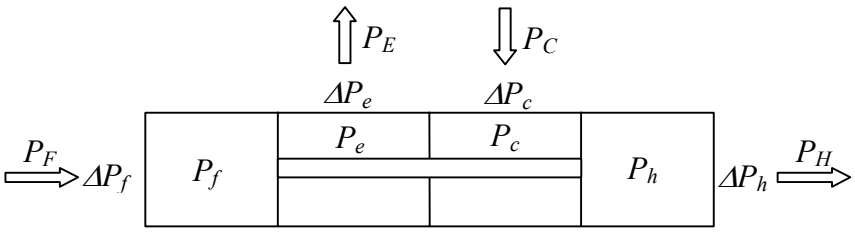

Figure 5-5 – Pressure losses

$$P_f = P_F - \Delta P_f \tag{26}$$
$$P_e = P_E + \Delta P_e \tag{27}$$
$$P_c = P_C - \Delta P_c \tag{28}$$
$$P_h = P_H + \Delta P_h \tag{29}$$

where lowercase suffixes indicate the pressures that act on the piston and uppercase suffixes indicate the pressures that may observed at the external pipe connections.

Friction F will also give rise to a pressure loss.

Thus, equation 6 becomes:

$$P_F + \Delta P_f + (P_C - \Delta P_c)(1 - R_t) = (P_E + \Delta P_e)(1 - R_t) + (P_H + \Delta P) + \frac{F}{A_p} \tag{30}$$

Or:

$$P_F + P_C(1 - R_t) - P_E(1 - R_t) - P_H = P_L \tag{31}$$

where P_L is the combined pressure losses:

$$P_L = \Delta P_f + (\Delta P_e + \Delta P_c)(1 - R_t) + \Delta P_h + \frac{F}{A_p} \tag{32}$$

The combined pressure losses, including the friction, may be expected to increase with flow, or perhaps flow squared.

Mechanical efficiency

The *mechanical efficiency* η_M of a Clark pump may be defined as:

$$mechanical\ efficiency = \frac{effective\ net\ input\ \ pressure}{net\ input\ \ pressure} \tag{33}$$

More specifically:

$$\eta_M = \frac{P_F - P_E(1 - R_t) - P_L}{P_F - P_E(1 - R_t)} = 1 - \frac{P_L}{P_F - P_E(1 - R_t)} \tag{34}$$

Useful pressure relationship

$$P_F = P_H + (1 - R_t)(P_E - P_C) + P_L \tag{35}$$

5.2.2 Testing

5.2.2.1 Hardware configuration

In order to characterise the Clark pump, the test rig was re-plumbed so that two manually operated valves were connected in place of the RO modules.

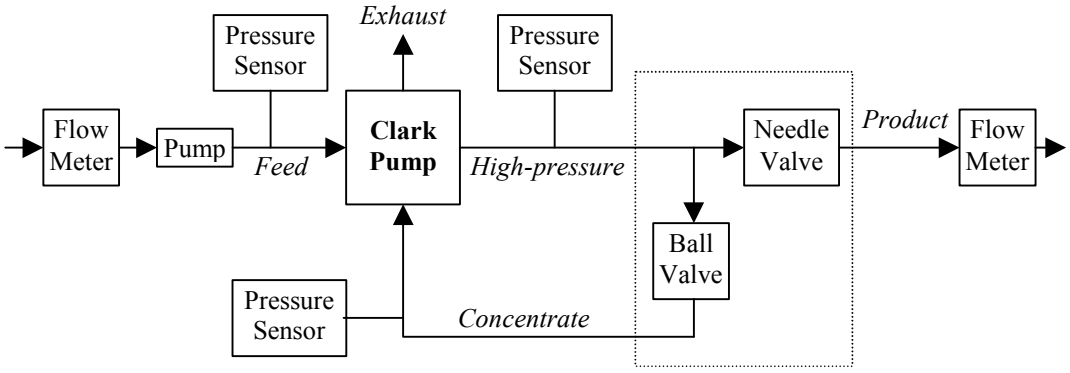

Figure 5-6 – Configuration used for Clark pump testing

The dashed box in Figure 5-6 indicates the usual location of the modules. Testing was carried out using freshwater, and the terms *Product* and *Concentrate* are retained simply to identify the various flows – obviously, no actual desalination is taking place.

The needle valve is used to simulate the pressure drop of water passing *through* the membranes. In practice, this pressure drop would be large (> 30 bar), since it includes both the osmotic pressure (around 26 bar for seawater) and the mechanical pressure required to force water through the semi-permeable membranes.

The ball valve simulates the *delta pressure*: the pressure drop of the water passing *across* the membranes along the mesh spacer layer described in section 2.7.3. In practice, this pressure drop would be very small (< 1 bar).

The pump used for the tests was a positive-displacement plunger pump (CAT 317). It was driven by an induction motor on a variable-speed inverter.

Thus, the test configuration allowed independent control of feed flow, high pressure and delta pressure.

5.2.2.2 Procedure

The rig was operated at a total of 55 discrete test points, including all combinations of:

- feed flow: 0.042, 0.127 and 0.211 L/s,
- high pressure: 20, 30, 40, 50 and 60 bar,
- delta pressure: 0, 2 and 4 bar.

The delta pressures chosen for testing were higher than those expected in practice, in order to exaggerate, and thus clearly identify, any affect of delta pressure.

Marcos Miranda adjusted the valves by hand to give the chosen test pressures and the speed setpoint on the motor inverter to give the chosen flows. Data was logged, at each test point, for at least one minute after steady operation had been achieved.

5.2.2.3 Data analysis and modelling

Off-line analysis of the data confirmed that the Clark pump is very efficient, and that this efficiency is maintained over a very wide range of flows and pressures. The detailed test results and analysis are presented in Appendix C. In summary, the data was analysed using regression calculations to determine the dominant causes of leakages and pressure losses, which were found to be as follows.

- The leakages are dependent mainly on the *product* of the high-pressure and the feed flow. The expectation had been that the leakages would increase with the *sum* of pressure and flow components.
- The delta pressure (up to 4 bar) has no significant effect on leakages.
- The pressure losses are dependent on the feed flow and feed flow squared. This was anticipated. Also, a dependence on delta pressure was observed.

The regression calculations also provided the following numerical expressions for the leakages and pressure losses respectively.

$$Q_L = 1.78 \times 10^{-4} \times Q_F P_H + 1.56 \times 10^{-5} \quad (36)$$

$$P_L = 49.2 \times Q_F^2 + 7.09 \times 10^{-2} \times \Delta P + 0.528 \quad (37)$$

In which, the units are litres/second and bar. And, $\Delta P = P_H - P_C$

Numerous alternative formulas to calculate leakages and pressure losses were reviewed, but equations 36 and 37 are considered to offer the most appropriate balance of precision and simplicity.

Equations 36 and 37 are used to estimate the leakages and pressure losses in the MATLAB-Simulink model of the Clark pump, presented next.

5.2.3 Modelling

The preceding theory and test results presented in Appendix C were used to build a software model of the Clark pump in the MATLAB-Simulink environment.

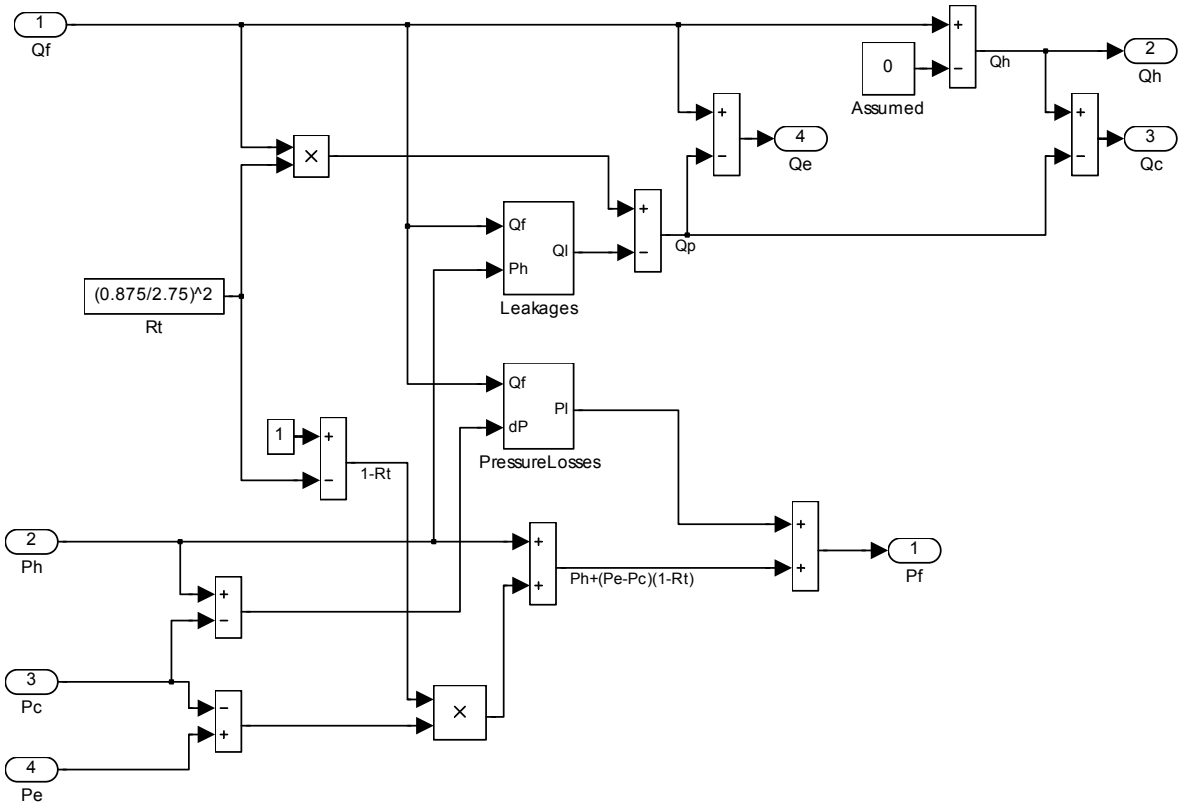

Figure 5-7 – Simulink model of Clark pump

The inputs to the model are on the left of the Simulink diagram in Figure 5-7.

Qf is the feed flow, previously denoted by Q_F (Simulink does not allow subscripts.)

Ph, Pc and Pe are the pressures of the high-pressure, the concentrate and the exhaust respectively.

Rt is a constant. It is the theoretical recovery ratio, calculated from the design dimensions of the pistons and the rod (see equation 3).

The boxes labelled Leakages and Pressure Losses are subsystems that implement equations 36 and 37 respectively.

The rest of the model shown in Figure 5-7 implements equations 23 and 31.

The zero shown in the box labelled Assumed represents the difference between the feed flow and the high-pressure flow. In an *ideal* Clark pump, there would be no difference, see equation 2. In practice, there probably is a slight difference but this was not measurable since the oval-gear flow meters on the test rig are limited to 20 bar. Fortunately, the overall efficiency is barely affected by this assumption as discussed in Appendix C, section C.4. Thus, very little of the precision of the model is lost.

The software model was tested by using the Q_F, P_H and P_C data collected during the original hardware testing as inputs to the model. The output data from the model was then compared against the original test results. Unsurprisingly, the match is very good.

5.2.4 Efficiencies and conclusions

There are various ways that the overall efficiency of an energy recovery mechanism may be defined, see section 2.8.5. The efficiency shown in Table 5-1 is calculated as the ratio of power delivered to the feed over that available in the concentrate.

$$\eta_{Clark} = \frac{Q_H P_H - Q_F P_F}{Q_C P_C - Q_E P_E} \tag{38}$$

High Pressure (bar)	Concentrate Pressure (bar)	Feed Flow (L/h)	Efficiency (%)
60	58	153	97.2
50	48	153	97.2
40	38	153	96.9
60	58	458	95.9
50	48	458	95.4
40	38	458	94.8
60	58	759	93.5
50	48	759	92.4
40	38	759	90.7

Table 5-1 – Clark pump measured efficiency

It is apparent that the overall efficiency shown in Table 5-1 decreases significantly with increased flow and, to a lesser extent, with increased pressure. The data analysis also showed that the volumetric efficiency, defined in section 5.2.1.2, is very high throughout,

and that the overall efficiency is dominated by the mechanical efficiency (pressure and frictional losses) defined in section 5.2.1.3.

Anyone familiar with typical efficiencies of pumps and turbines of this small scale will appreciate that the figures presented for the Clark pump in Table 5-1 are excellent. Comparing these results against the experience with the Danfoss hydraulic motor presented in Chapter 3 indicates that the Clark pump is far superior in terms of energy efficiency. It was selected for the PV-RO system.

5.3 Plunger pump

Plunger pumps, particularly those manufactured by CAT Pumps (www.catpumps.com accessed: March 04), are routinely used in small-scale seawater RO systems. There are few other contenders in seawater-compatible pumps that can raise the required pressure (up to 69 bar) in small sizes. They are mostly alternative brands of plunger and piston pumps similar to CAT's, and probably no better. Recently, Danfoss introduced a new range of axial piston pumps, the APP range (Danfoss 2002), which are designed for use in seawater RO and would be worth considering in the future.

The initial test rig, described in Chapter 3, included a CAT 317 triplex plunger pump, and this same pump was transferred to the new test rig; it has performed impeccably throughout and shows no sign of deterioration. The final system *design,* presented in section 6.4, also includes a CAT triplex plunger pump, in particular, a CAT 237.

	Bore (mm)	Stroke (mm)	Plungers	Geometric displacement (L/rev)
CAT 317	20	18	3	0.01697
CAT 237	18	7	3	0.00534

Table 5-2 – CAT plunger pump geometries

Table 5-2 shows the bore and stroke, taken from the manufacturer's datasheets, and the geometric displacement calculated using:

$$geometric\ displacement = \pi\left(\frac{bore}{2}\right)^2 \times stroke \times plungers$$

The CAT 237 was selected for the final system *design* because its smaller geometric displacement gives a higher shaft speed, which improves the efficiency of the motor driving it. The CAT 237 was modelled as follows.

5.3.1 Modelling

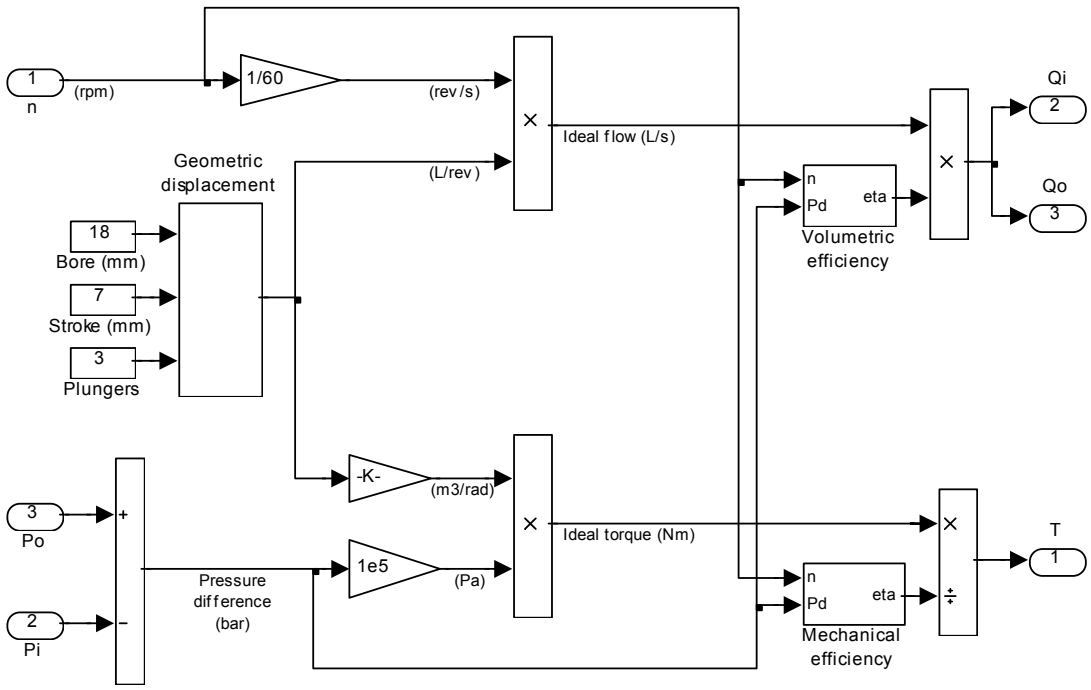

Figure 5-8 – Simulink model of CAT 237 triplex plunger pump

Starting at the top left of Figure 5-8, the input n is the shaft speed in rpm, which is converted to revolutions per second (rev/s). Multiplying this by the geometric displacement in litres per revolution (L/rev) gives the Ideal flow (L/s). A volumetric efficiency is then applied to provide the outputs Qi and Qo, which are the modelled flows through the pump inlet and outlet respectively. Qi and Qo are of course equal (assuming the pump has no external leak); they are provided as separate outputs from this Simulink component model only to provide consistency for the connections when it is used within the system model.

At the bottom left of Figure 5-8, inputs Pi and Po are the pressures at the pump inlet and outlet respectively. The Pressure difference (bar) is converted to pascals (Pa) and then multiplied by the geometric displacement in cubic metres per radian (m3/rad) to give the Ideal torque (Nm). A mechanical efficiency is then applied to provide the output T, which is the shaft torque that will be connected to the motor.

The expressions used for volumetric and mechanical efficiencies were based on measurements taken from the CAT 317 by Marcos Miranda. He performed regression calculations (similar to those presented in Appendix C) and provided:

$$volumetric\ efficiency = 1.00 - 8.75 \times 10^{-6} P_d + 0.000173n - 2.22 \times 10^{-7} P_d n$$

$$mechanical\ efficiency = 0.420 + 0.0225 P_d - 0.000430 P_d^2 + 2.91 \times 10^{-6} P_d^3 + 0.000138n - 6.97 \times 10^{-8} n^2$$

5.3.2 Modelled efficiency

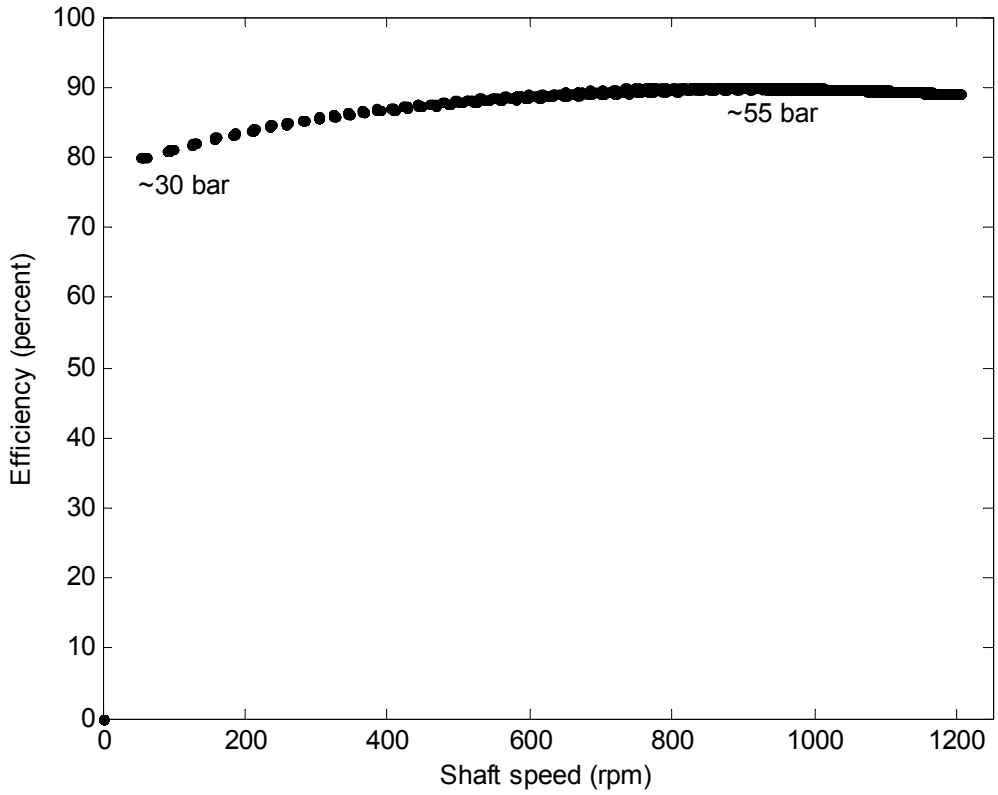

Figure 5-9 – Modelled efficiency of CAT 237 plunger pump

The efficiency of a plunger pump is dependent on the operating conditions: both flow and pressure. And, in the context of a batteryless PV-RO system, both flow and pressure are expected to vary with the available sunlight. It is the efficiency over a broad range of operation that is of importance.

The data shown in Figure 5-9 is taken from the complete system model presented in Chapter 6. Thus, it shows the efficiency calculated by the pump model presented in section 5.3.1, under the conditions expected in the complete PV-RO system.

The efficiency shown in Figure 5-9 is between 85 and 90 % for the majority of the expected operating range. This is very respectable for such a small pump. And, on this basis, the CAT 237 was selected for use in the final system *design*.

5.4 Moineau pump

The selection of a medium-pressure pump to feed the Clark pump is rather less straightforward. Obviously, efficiency is paramount and, unfortunately, plunger pumps are much less efficient at reduced pressure. Seawater compatibility is an obvious requirement, but additionally, the pump must be able to tolerate the occasional grain of sand, in order to minimise filtration requirements on its intake side.

A multi-stage centrifugal pump would seem to be a possibility, but, these offer very poor efficiency (less than 40%) at the required flow/pressure. Furthermore, to achieve optimum efficiency with a centrifugal pump, the rotor speed must be matched to the flow/pressure operating point. This is not straightforward in a system where both the flow and pressure must vary according to the available sunlight. Lastly, since a centrifugal pump does not offer positive displacement, balancing the water recovery ratio in the final two-pump system, Figure 1-3, would be rather difficult.

A wide range of diaphragm and vane pumps were also considered but finally a Moineau (progressing-cavity) pump was selected. These offer reasonable efficiency at the required duty and, importantly, this efficiency is generally maintained as the flow is reduced. Such pumps are often used in PV-powered systems.

Moineau (progressing-cavity) pumps were developed by a Frenchman, Rene Moineau, and his name has been Anglicised and Americanised by the manufacturers: Mono and Moyno respectively. Other manufacturers include Netzsch and Orbit. Moineau pumps are positive-displacement, employing a long metal screw rotor inside a rubber stator. They can tolerate the odd grain of sand but are quickly ruined if run dry.

Submersible Moineau pumps are widely used and could be used in this PV-RO application. However, if the well is shallow (less than 7 m) and the rig can be sited

nearby, an above-ground Moineau pump may be preferable, since this will permit use of a much higher efficiency motor. An above-ground Moineau pump was selected for the final design and performance predictions are based on this.

Moineau pumps can prime themselves if sufficiently wet, but can suffer from starting problems due to the static friction between the rubber stator and the metal rotor – once turning, the water being pumped acts as a lubricant. Starting difficulty was apparent during the commissioning of the final test rig, but was overcome by a software routine in LabVIEW that uses the inverter (variable-speed drive) to *wobble* the motor at start up.

Seeking a combination of seawater compatibility and energy efficiency, a Netzsch 021 (www.netzsch-pumps.com accessed: March 04) was selected.

5.4.1 Modelling data

Within this model, the inlet pressure of the Moineau pump is taken as zero (atmospheric pressure), representing the case where the pump is neither sucking nor being feed at positive pressure, which is in keeping with the arrangement of the final test rig. Thus, the *pressure* referred to below is equal to the outlet pressure.

The manufacturer's performance curves (Appendix D) show that, at zero pressure, the flow is directly proportional to shaft speed, as expected in a positive displacement pump, In particular:

$$geometic\ displacement = \frac{flow}{shaft\ speed} = \frac{3.7\ \mathrm{m^3/h}}{2500\ \mathrm{rpm}}$$

As the pressure is increased, leakage between the metal rotor and the rubber stator increases, which reduces the flow as illustrated in the performance curves and quantified in the second column of Table 5-3.

Pressure (bar)	Leakage: flow reduction (m^3/h)	Shaft power (kW)		
		at 250 rpm	at 1000 rpm	at 2500 rpm
4	0.0545	0.12	0.40	1.25
8	0.115	0.15	0.55	1.60
12	0.206	0.19	0.70	1.90

Table 5-3 – Netzsch 021 Moineau pump data extracted from manufacturer's performance curves (Appendix D)

Fitting a quadratic to the leakage data shown in Table 5-3 provides:

$$leakage = 0.000568P^2 + 0.0102P + 0.00121$$

where *leakage* is in m^3/h and P is the pressure in bar.

Using multiple regression (similar to that presented in Appendix C, section C.6) for the shaft power shown in Table 5-3 provides:

$$power = 0.0167 + 0.000186n + 0.00277P + 3.18\times10^{-5}nP + 7.11\times10^{-8}n^2$$

where *power* is in kW, n is the shaft speed in rpm and P is the pressure in bar.

5.4.2 Simulink model

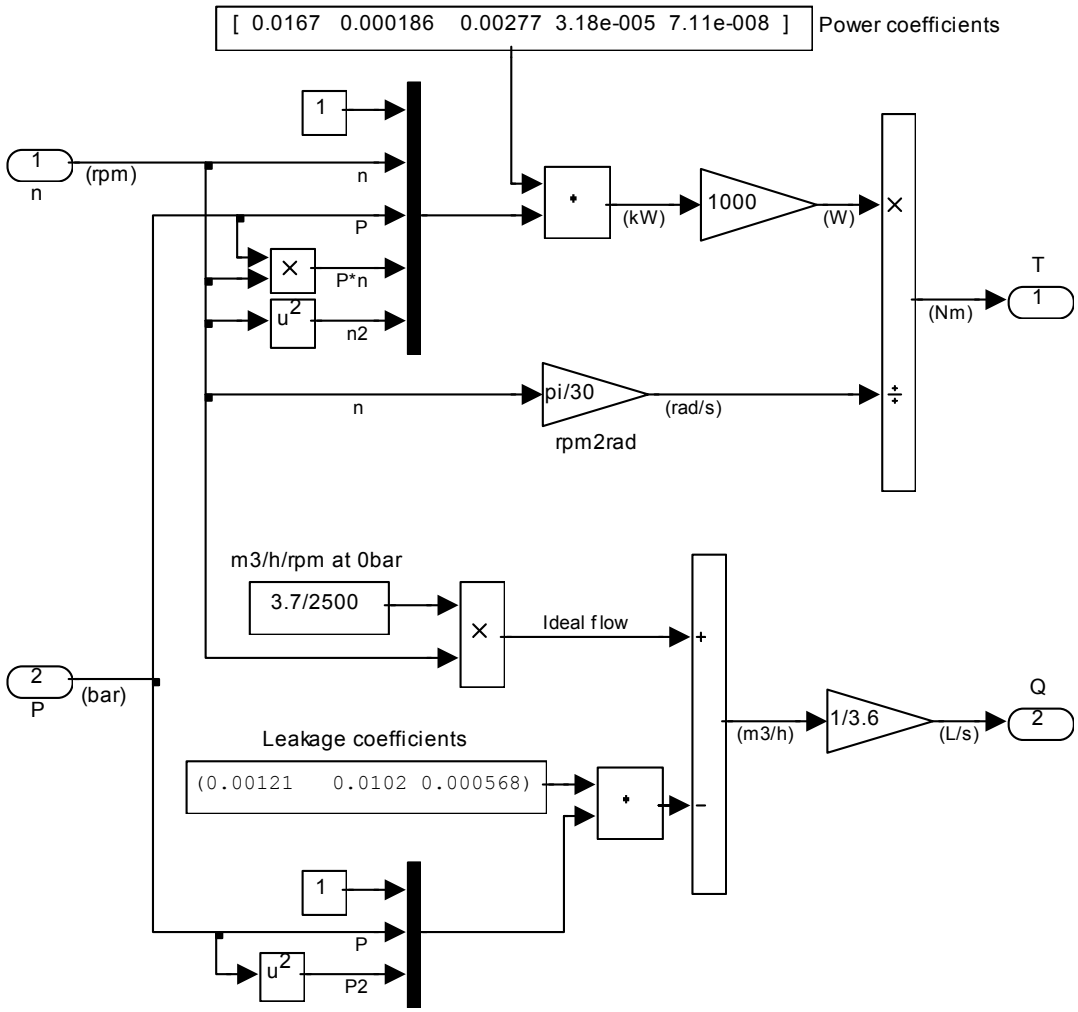

Figure 5-10 – Simulink model of Netzsch 021 Moineau pump

Figure 5-10 shows the structure of the Simulink model of the Netzsch 021 Moineau pump constructed from the equations presented in section 5.4.1. On the left of the figure, the inputs n and P are the shaft speed and the pressure respectively. On the right, outputs T and Q are the shaft torque and the flow respectively.

5.4.3 Modelled efficiency

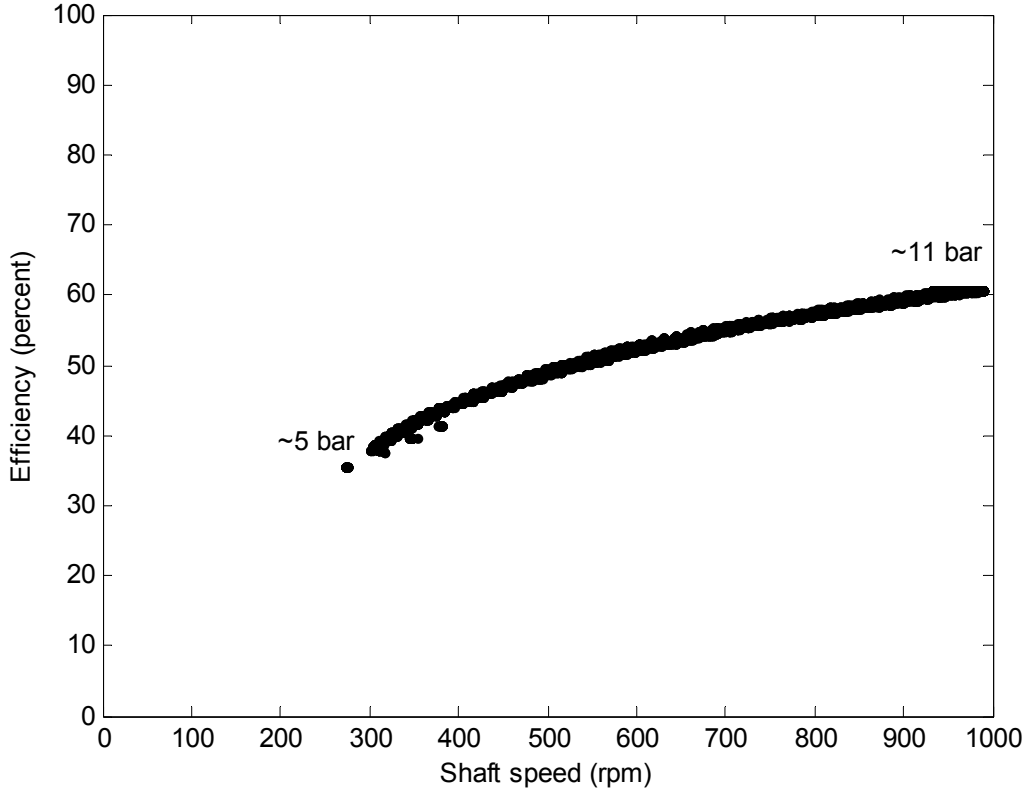

Figure 5-11 – Efficiency of Netzsch 021 Moineau pump modelled from manufacturer's performance curves

The efficiency of a Moineau pump is very dependent on the operating conditions: both flow and pressure. And, in the context of a batteryless PV-RO system, both flow and pressure are expected to vary with the available sunlight. It is the efficiency over a broad range of operation that is of importance.

The data shown in Figure 5-11 is taken from the complete system model presented in Chapter 6. Thus, it shows the efficiency calculated by the pump model presented in section 5.4.2, under the conditions expected in the complete PV-RO system.

Figure 5-11 may be compared against Figure 10-10, which shows the data measured in the new test rig.

5.5 Motors and inverters

In relation to PV pumping, it is often suggested that permanent-magnet motors (often DC, but sometimes AC) offer significantly higher efficiencies than AC induction motors (Wenham et al. 1994 page 212). However, improvements, over the last decade or so, in the efficiency of small induction motors and inverters for mainstream industrial application mean that this technology is now almost as efficient as any commercially available permanent-magnet motor system, AC or DC. The MATLAB-Simulink model of the complete PV-RO system showed that the higher cost of various alternative permanent-magnet motor drive systems that were considered was not justified, see section 5.6.4. Furthermore, the use of standard industrial components that can readily be replaced is very attractive for systems intended for use in remote areas. Thus, AC induction motors were selected.

Next, dedicated PV-pumping inverters were considered since they have the advantage that maximum power point tracking (MPPT, introduced in section 2.5.4) is built in. However, since it is a relatively small market, these inverters tend to be rather expensive and offer little flexibility in control strategy. In particular, the appropriate sharing of the available power between the two motors, which is necessary to optimise the water recovery ratio and hence maximise the product flow, would be difficult to implement with standard PV-pumping inverters.

The alternative, to dedicated PV-pumping inverters, is the standard industrial variable-speed drive inverter. These are far less expensive but have no MPPT, and require suitable selection of the PV modules so that the DC voltage falls in a relatively narrow range.

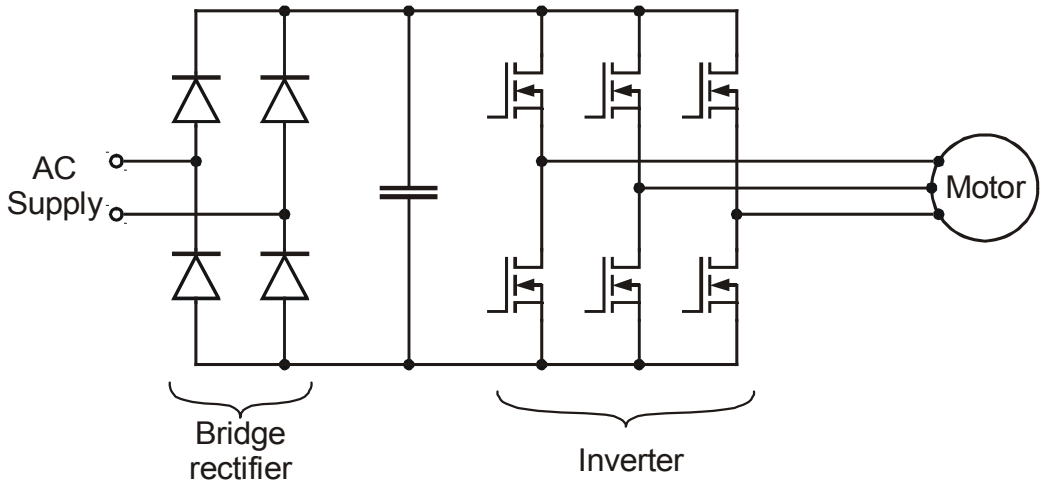

Figure 5-12 – Standard industrial drive circuit

Standard industrial drives are normally intended to operate from an AC mains supply as illustrated in Figure 5-12, but, *so long as nothing is internally connected prior to the bridge rectifier*, can usually be operated directly from DC (check with the manufacturer). Direct connection of a PV array to a standard industrial drive is a proven technique. It requires that the PV-array voltage range lies within the safe operational voltage range of the inverter. A typical rating is 230 VAC +/–15%, which translates to 276 to 374 VDC, but in practice, these boundaries can often be extended (check with the manufacturer).

Standard industrial motors and inverters were selected for the PV-RO system.

5.6 Induction motors

Induction motors are used throughout industry, and account for a considerable proportion of electricity consumption worldwide. Recognising that a general improvement in the efficiency of induction motors brings significant reduction in electricity consumption, many countries have introduced standards and regulations to encourage manufacturers to improve designs with regard to energy efficiency.

5.6.1 Modelling data

The motor chosen and modelled in Simulink during the design of the PV-RO system was the Toshiba Premium Efficient EQPIII B0026FLF2AYH, which is a 6-pole induction motor rated at 2-horsepower (~1.5 kW) on 230-V 60-Hz. Toshiba provided the data shown in Table 5-4, from which Table 5-5 is derived, assuming a linear torque-speed relationship.

Load (%)	Torque (Foot.Pounds)	Speed (rpm)	IEEE Efficiency (%)	Power Factor (%)
100%	8.96	1172	88.4	66.7
75%			87.7	58.1
50%			85.3	45.6

Table 5-4 – Toshiba motor data

Load (%)	Torque (Nm)	Speed (rpm)	Output Power (W)	Input Power (W)	Current (A)	Active Current (A)	Reactive Current (A)
100%	12.15	1172	1491	1687	6.35	4.23	4.73
75%	9.11	1179	1125	1283	5.54	3.22	4.51
50%	6.07	1186	754	885	4.87	2.22	4.33

Table 5-5 – Toshiba motor – derived data

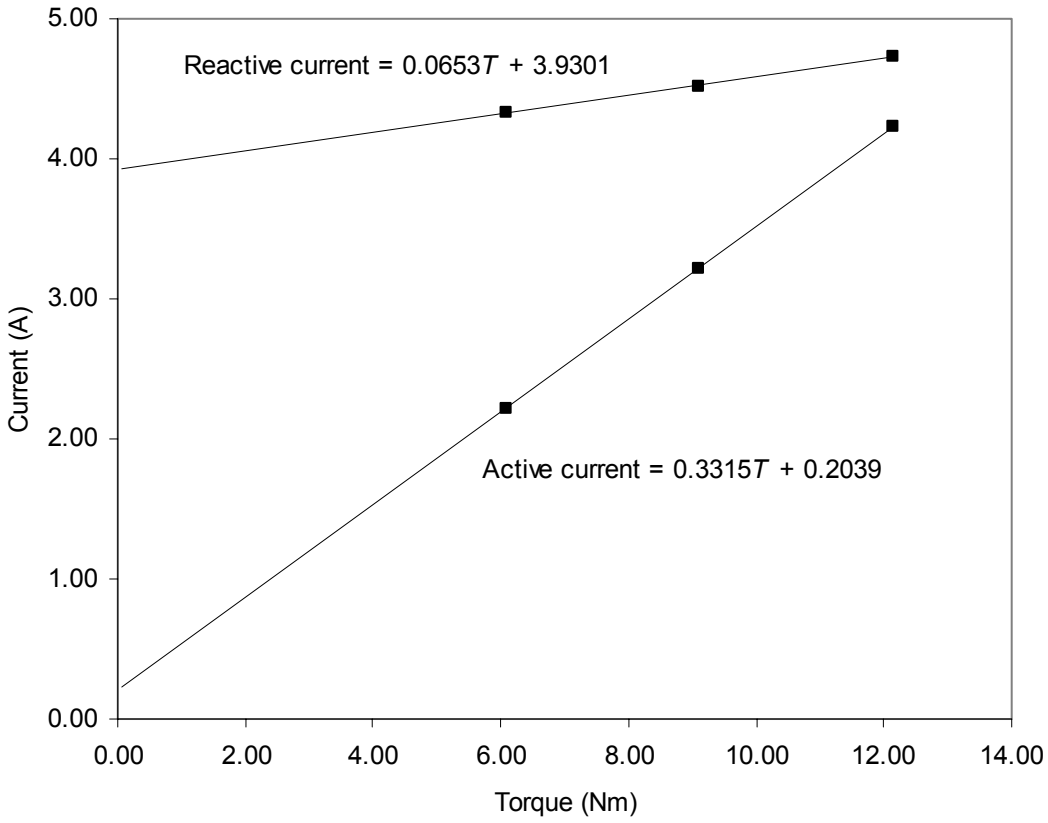

Figure 5-13 – Active and reactive motor currents versus torque

Figure 5-13 illustrates, as expected, that active current is proportion to torque, with an offset for friction and windage, while reactive current (magnetising current) is more constant.

5.6.2 Simulink model

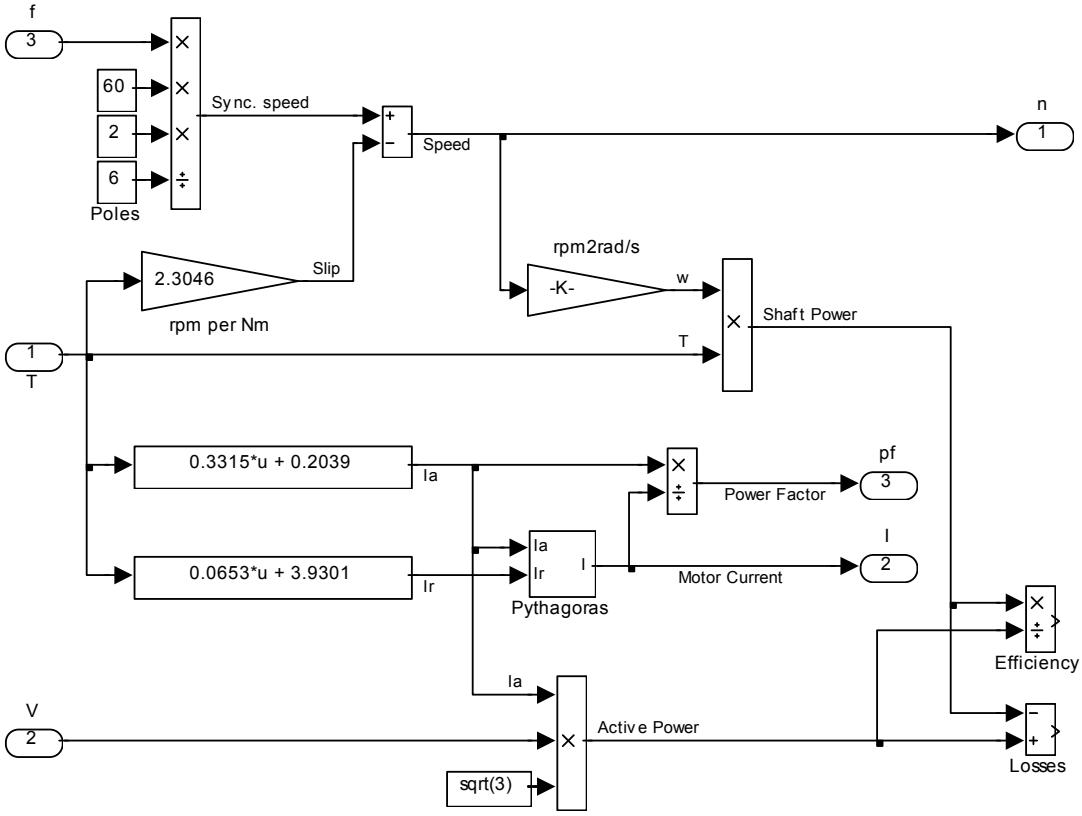

Figure 5-14 – Structure of Simulink motor model

Starting on the left of the motor model shown in Figure 5-14, the input f is the frequency of the ac voltage from the inverter. From this frequency in hertz, the synchronous speed in rpm is calculated, for a six-pole motor.

The slip (in rpm) is calculated from the torque T, using data from Table 5-5 and assuming a linear torque-speed relationship.

The synchronous speed less the slip provides the shaft speed n.

The active current Ia and reactive current Ir are estimated from the torque using the linear functions illustrated in Figure 5-13, and are combined to provide the motor current I and its power factor pf.

The remaining blocks in Figure 5-14 illustrate the calculation of motor input and output powers, losses and efficiency.

5.6.3 Induction motor efficiencies

The Toshiba Premium Efficient EQPIII B0026FLF2AYH, on which the modelling just described was based, is an American motor built to National Electrical Manufacturers Association (NEMA) standards. NEMA is based in the US and covers the US motor market. Motors for the US market must comply with the US Energy Policy and Conservation Act (EPACT), which uses the IEEE 112-1992 test method B to define the efficiency of small induction motors.

Elsewhere in the world, particularly in Europe, the efficiency of small induction motors is classified according to the European Committee of Manufacturers of Electrical Machines and Power Electronics (CEMEP) and is calculated according to an International Electrotechnical Commission (IEC) standard: IEC 60 034-2.

Siemens manufacture motors for both markets, and in some cases supply the same model to both markets. Their 1999 catalogue shows side-by-side specifications for the two markets. For example, the 1LA9 106-6KA (which is similar to the aforementioned Toshiba motor) is shown at 60 Hz for the US market and at 50 Hz for other markets.

50 Hz	1.5 kW	6-pole	945 rpm	IEC efficiency: 83%
60 Hz	2 hp	6-pole	1150 rpm	IEEE efficiency: 86.5%

Table 5-6 – Alternative specifications for the same motor (Siemens1LA9 106-6KA)

Table 5-6 shows that, for this example at least, the IEEE efficiency is some 3.5 % higher than the IEC efficiency, and illustrates the need for caution in comparing motor efficiencies.

5.6.4 Value of motor efficiency

In order to quantify the value of motor efficiency within the PV-RO system, and therefore provide a basis to compare motors of different costs and efficiencies, the final system model, presented in Chapter 6, was used as follows.

The efficiencies of the two motors in the system model were temporarily adjusted, first up 1 %, then down 1 %. In particular, multiplication factors of first 1.01 then 0.99 were inserted in the active current Ia line of Figure 5-14.

Motor efficiency	Active current factor	Annual water production (m^3)
Base case	1	1424
+ 1 %	0.99	1435
– 1 %	1.01	1413

Table 5-7 – Modelled results for motor efficiency changes

Table 5-7 shows that 1 % increase (or decrease) in motor efficiency gives an increase (decrease) in annual water production of 11 m^3, which is 0.77 %. The total capital cost of the PV-RO system, also estimated in Chapter 6, is £18272. Thus, the value of motor efficiency within the PV-RO system is 0.77 % × £18272 = 141 £/%.

5.6.5 Motor selection

By fortunate coincidence, the two selected pumps (Moineau described in section 5.3 and plunger described in section 5.4) have very similar shaft speed and torque requirements, and can be well served by two motors of the same type; in particular, a 6-pole 1.5 kW induction motor.

Various 6-pole 1.5 kW motors were considered during the system design, including those shown in Table 5-8.

Make and model	Cost (£)	Efficiency (%)			Adjusted cost (£)
		IEEE	IEC	Relative	
Toshiba B0026FLF2AYH	309	88.4		0	309
Siemens 1LA9 106-6KA	165	86.5	83.0	-1.9	433
WEG W21 HDA 100 B3	98		80.1	-4.8	775
FKI Marelli MA112M6	139		75.3	-9.6	1493
Baldor EM3664T	388	88.5	85.2	0.1	374

Table 5-8 – Costs and efficiencies of various 6-pole 1.5 kW induction motors

The cost shown in Table 5-8 for the Toshiba motor was based on its list price US$440 at the time (early 2001). The other costs were taken from specific quotations. The efficiencies shown are from the manufacturer's data and are a mix of IEEE and IEC as discussed in section 5.6.3. The *relative* efficiency shown takes the Toshiba as the base case, and takes into account the difference between IEEE and IEC efficiencies. The last column in Table 5-8 shows the cost adjusted according to the relative efficiency at 141 £/%. The minimum *adjusted* cost is clearly that of the Toshiba and illustrates why it was selected for the final design presented in Chapter 6.

5.6.6 Test rig motors

When the new test rig was being built, later in 2001, it was found that the selected Toshiba motor was not readily available in the UK and that importing it would inflate its cost to around £870. The next choice, according to *adjusted* costs in Table 5-8, would be the Baldor, but this has a high *unadjusted* cost (which was relevant for building a test rig) and had a long lead-time. Considering this the third choice, a Siemens 1LA9 106-6KA was purchased for the test rig. This has a quoted efficiency 1.9 % lower than the Toshiba; however, there is no guarantee that the efficiencies quoted by the two manufacturers can be compared with this accuracy.

The new Siemens motor drives the Moineau pump in the new test rig. The plunger pump is driven by 4-pole 3-kW motor left over from the earlier test rig.

5.7 Standard industrial variable-speed drive inverters

Various different industrial drive inverters were used throughout the project. There was little to choose between the manufacturers. One of the inverters included sensorless vector control. This gave more accurate speed control, which is largely irrelevant for PV-RO, but consumed power in a rather greedy and erratic fashion, particularly at low speeds, which is not good in a PV-powered system.

The inverters modelled and subsequently bought and fitted to the new test rig, were supplied by FKI Industrial Drives. In particular, a 1.5-kW FID1000 FKI-12150 is used for the Moineau pump on the test rig and for both pumps in the system model. A slightly larger 2.2-kW FID1000 is used for the plunger pump on the test rig. It is oversized only to allow flexibility in testing.

They are *V-over-F* type inverters, which means that the AC output voltage is directly proportional to its frequency, so that *V-over-F* is a constant. *V-over-F* type inverters are usually cheaper than those with vector control, and the FID inverters have performed well.

V-over-F type inverters often provide the option to apply slip-compensation. When selected, this option applies a slight increase to the frequency of the inverter's ac output voltage, to offset the estimated slip in the induction motor, so that the shaft speed more

closely matches the speed setpoint. Slip-compensation is of no benefit for the PV-RO system in hand and was turned off.

5.7.1 Modelling

With slip-compensation turned off, the frequency of the inverter's ac output voltage is directly proportional to the speed setpoint input. Thus, this input can be expressed as a speed setpoint n^* in rpm, as it is in Chapter 9, or as frequency setpoint f^* in hertz as it is in the Simulink model shown in Figure 5-15.

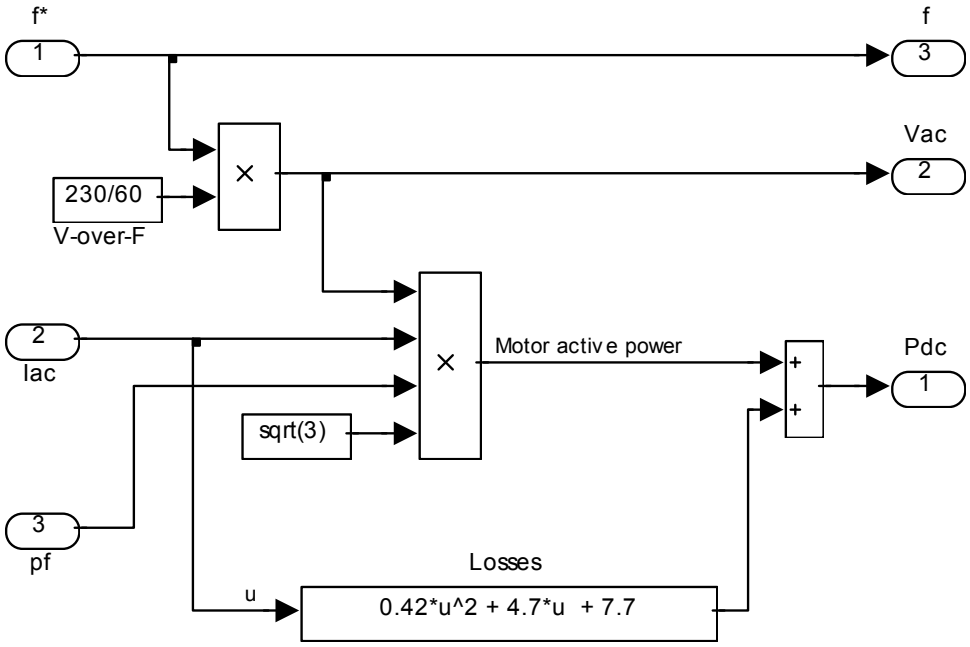

Figure 5-15 – Structure of Simulink inverter model

Starting at the top left of Figure 5-15, the input f* is the frequency setpoint and is passed straight through to the output f, which is the frequency of the inverter's ac output, as explained above.

Multiplying f by the constant V-over-F provides Vac, which is the voltage of the inverter's ac output. In this case, *V-over-F* = 230V/60Hz, corresponding with the Toshiba motor described in section 5.6.1.

Again on the left of Figure 5-15, inputs Iac and pf are the motor current and power factor respectively, which will be connected to the outputs from the motor model described in section 5.6.2.

The motor active power is simply the product of motor voltage, current and power factor, with further factor of root-3 because it is a three-phase motor.

The output Pdc represents the DC power drawn by the inverter and is the sum of the motor active power and inverter losses, which are modelled as follows.

FKI, the inverter manufacturers, provided measured loss data, for the 1.5-kW FID1000 FKI-12150, at three current levels and a curve was fitted as shown in Figure 5-16.

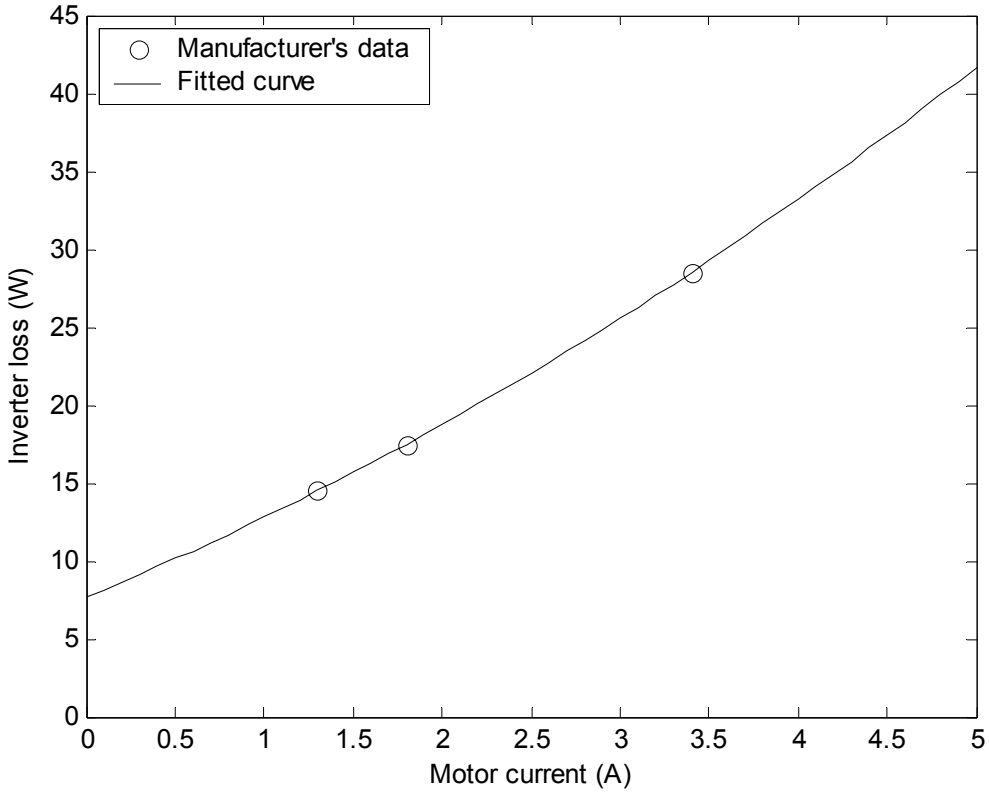

Figure 5-16 – Inverter losses versus motor current

The inverter losses were expected to include components in I^2 (resistive losses), I (switching losses) and a constant. The manufacturer's data was consistent with this and a 2nd order polynomial was fitted:

$$Inverter\ loss = 0.42\,I^2 + 4.7\,I + 7.7$$

where I is the motor current in Amps and the inverter loss is in Watts.

The maximum motor current shown in the complete system model was 4.9 A, which, as illustrated in Figure 5-16, required modest extrapolation of the data.

5.7.2 Parameter adjustments

During commissioning, it was found that the detailed settings of control parameters within the inverters can have a significant effect on energy efficiency. Since these inverters are normally used for industrial purposes and supplied by mains electricity, the instruction manuals tend to focus more on starting performance and speed control than on energy efficiency. Using the instrumentation and data-acquisition system attached to the test rig, it was possible to observe energy efficiency in real-time and make adjustments accordingly.

The first adjustment was to the *V-over-F* ratio. It was found that, for one motor, it was best left at the default: 230 V at 50 Hz (the test rig has 50-Hz nominal motors). But for the other motor, energy efficiency could be improved by ~2% by reducing the setting to 180 V at 50 Hz. This degraded the speed control due to the increased slip, but that is of little consequence in a PV-RO system.

Next, the *starting boost* was adjusted. This is a parameter commonly found on industrial inverters that increases the voltage at low frequencies in order to provide higher starting torque. This is useful in an industrial context because it ensures that machinery starts decisively at low speeds. However, it does consume extra power and, in the context of PV-pumping, including PV-RO, it can do more harm than good. Testing showed that for both the plunger pump and the Moineau pump the *starting boost* should be set to a minimal value in order to start the motors with minimum power. When commissioning an inverter with a Moineau pump, one might imagine that a generous *starting boost* should be applied in order to overcome stiction, but this is not the case; it is better to overcome stiction by *wobbling* the motor, if the software permits.

Next, the inverters used had a facility to *bend* the *V-over-F* characteristic, allowing the voltage at mid frequencies to be adjusted. This gave no efficiency improvement.

Lastly, different switching frequencies were tested. The default was 16 kHz. Changing this to 8 kHz, improved efficiency by ~1.2 %, because of the reduced switching losses, but the 8 kHz was highly audible, bordering on painful, and the setting was put back to the default 16 kHz for all further tests.

5.8 Solar irradiance

The main input to the PV-RO system model is of course the solar irradiance striking the PV array, which depends on the proposed location. Meteonorm (www.meteotest.ch accessed: March 04) is a software package that predicts irradiance at any chosen location. It uses algorithms, based on measured data from many sites around the world, together with some basic characteristics of the chosen location.

Meteonorm was used to provide data for a sample location at Massawa, Eritrea. The data is hourly and covers one whole year. Meteonorm aims to provide data for a *typical* year, as opposed to the long-term average for many years.

5.8.1 Solar-trajectory tracking

The system was modelled with a fixed PV array and with single-axis and dual-axis solar-trajectory-tracking arrays. Meteonorm provided global irradiance data in the plane of the array for both the fixed array and the array with dual-axis tracking. Rowbottom (Dulas Limited) then used PVSyst (www.pvsyst.com accessed: March 04) to adjust this Meteonorm data to provide the data for the array with single-axis tracking. Figure 5-17 shows the expected bell-shape daily profiles for these three sets of data averaged over the whole year.

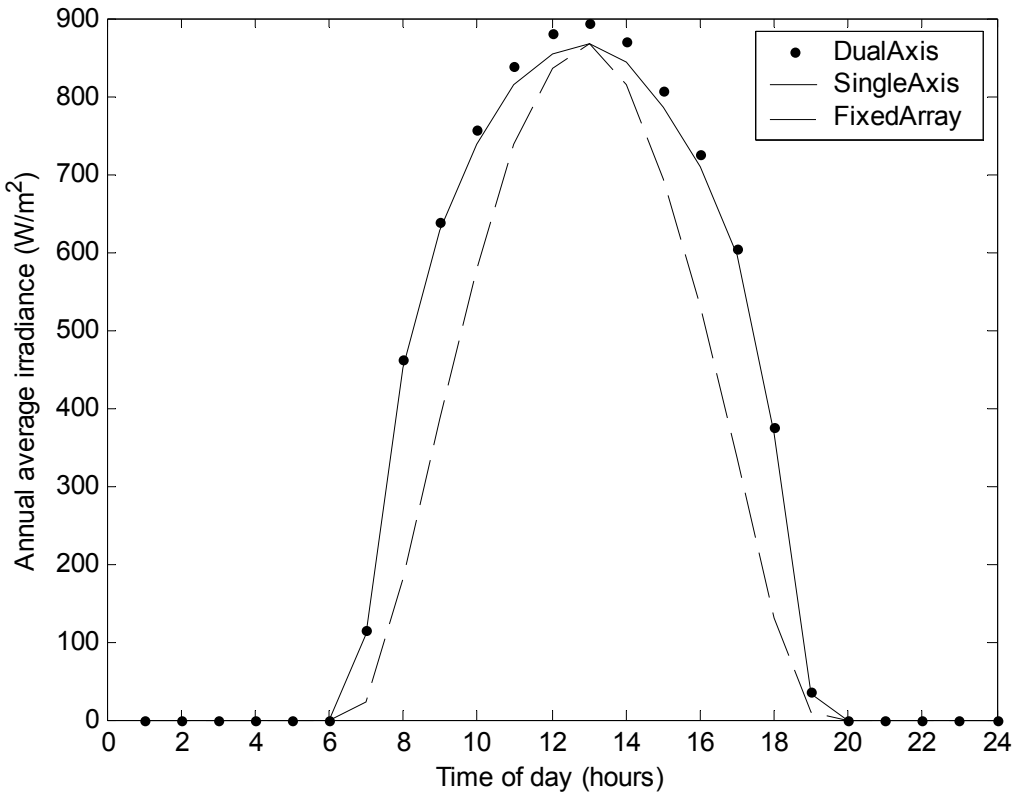

Figure 5-17 – Annual average global irradiance versus time of day for a fixed PV array and for single-axis and dual-axis solar-trajectory tracking arrays

Time of day (hours)	Annual average global irradiance in the plane of the fixed array (W/m^2)		
	Fixed	Single-axis	Dual-axis
6	0	0	0
7	23	109	114
8	182	451	461
9	386	627	637
10	577	738	755
11	738	815	839
12	837	855	881
13	867	868	893
14	814	843	869
15	694	786	807
16	531	709	725
17	336	595	605
18	131	367	376
19	9	33	34
20	0	0	0
Average	255	325	333
Percentage gain	27%	2%	

Table 5-9 – Data for Figure 5-24

The percentage-gain figures in Table 5-9 suggest that, at this location (Eritrea), the additional costs (both capital and maintenance) of a single-axis tracker may well be justifiable, but that the higher costs of a dual-axis tracker are probably not. And on this basis, a single-axis tracker was assumed throughout the design process. The figures in Table 5-9, however, represent the irradiance, which is the input to the PV-RO system; the choice of tracking arrangement was later checked with reference to the water production predicted by the final system model presented in section 6.5.1.

It should also be noted that the relative merits of single- and dual-axis tracking are very dependent on latitude.

5.8.2 Hourly irradiance

As noted earlier, Meteonorm aims to provide hourly data for a *typical* year, as opposed to the long-term average for many years. Thus, the data for a particular day is affected by local atmospheric conditions (particularly cloud cover) simulated within Meteonorm and may well differ from the bell-shaped average day.

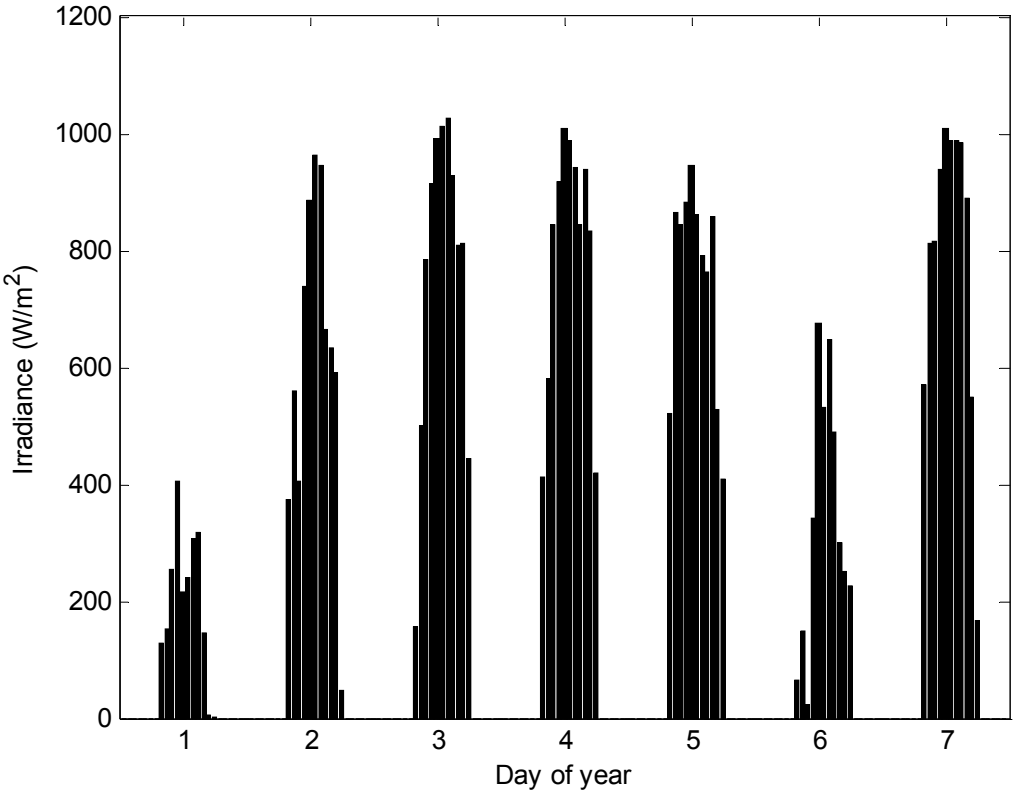

Figure 5-18 – Hourly global irradiance in the plane of a single-axis tracking PV array for the first week of the year-long data set

Figure 5-18 shows the hourly irradiance data for only one week of the year-long data set. The simulations of the PV-RO system were generally carried out on an hour-by-hour basis for the whole year (8760 hours). In order to present the input and results data here, they are averaged daily and monthly.

5.8.3 Average daily irradiance

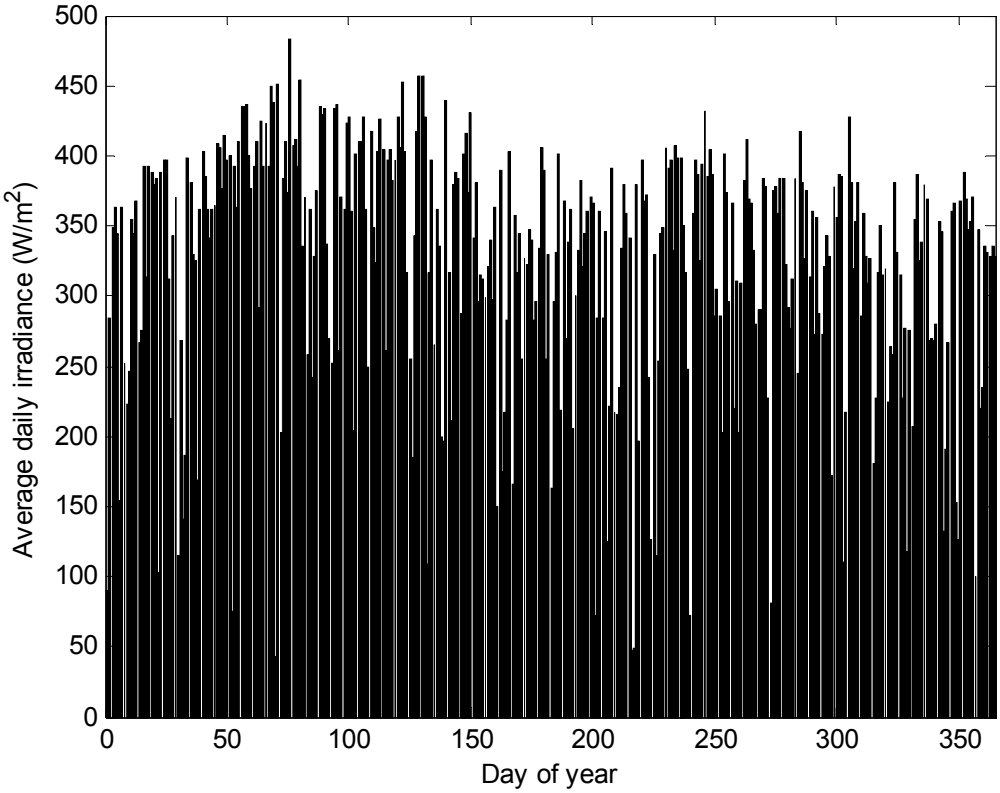

Figure 5-19 –Average daily global irradiance in the plane of a single-axis tracking PV array for the whole of the year-long data set

	Jan	Feb	Mar	Apr	May	Jun	Jul	Aug	Sep	Oct	Nov	Dec
1	90	141	376	337	406	381	330	379	326	376	428	338
2	284	187	392	270	452	296	163	359	395	379	381	379
3	349	399	410	252	403	314	297	341	431	359	319	369
4	364	381	291	433	316	313	331	47	386	384	353	268
5	344	329	424	436	255	300	401	49	404	384	381	269
6	154	325	393	261	185	322	218	380	387	322	286	268
7	363	168	424	370	343	340	367	197	287	292	358	280
8	252	362	392	362	418	297	270	397	304	277	328	353
9	222	403	450	423	456	364	339	367	285	312	309	345
10	246	385	437	428	457	149	362	373	202	384	327	132
11	354	362	43	361	428	389	205	241	401	246	180	191
12	344	342	451	203	110	175	301	126	373	417	228	267
13	368	362	203	402	317	217	333	330	296	382	316	360
14	267	365	384	410	396	283	382	115	366	327	350	366
15	275	409	410	411	266	403	320	254	220	375	315	153
16	392	405	373	427	361	166	344	345	311	314	319	126
17	314	377	483	362	335	358	360	348	202	361	225	368
18	392	414	408	249	199	317	371	406	309	273	265	388
19	388	397	411	418	196	345	367	392	382	357	258	369
20	379	399	392	349	440	254	72	397	412	287	381	347
21	383	75	454	324	317	327	284	333	370	272	331	354
22	103	392	336	403	211	323	361	407	366	321	315	371
23	388	363	370	426	379	347	284	398	332	343	228	100
24	398	410	259	405	388	339	346	398	279	328	277	348
25	397	434	361	261	384	282	125	350	290	172	118	220
26	313	435	242	398	287	295	222	316	290	378	275	235
27	213	436	329	404	401	334	392	248	383	356	206	336
28	343	399	375	382	415	405	217	72	378	386	355	330
29	370		435	397	374	389	215	358	227	386	387	329
30	114		429	428	430	255	235	397	81	110	326	335
31	268		434		342		334	387		217		328

Table 5-10 – Data for Figure 5-19

5.8.4 Average monthly irradiance

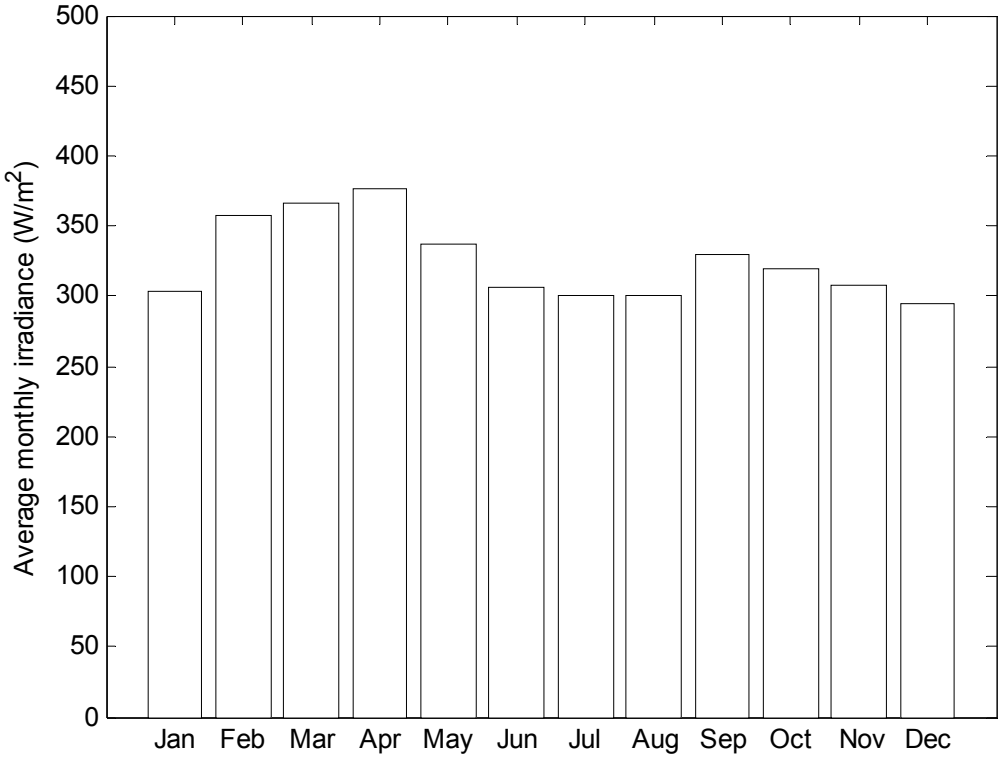

Figure 5-20 – Average monthly global irradiance in the plane of a single-axis tracking PV array

	Irradiance (W/m^2)
Jan	303
Feb	357
Mar	366
Apr	376
May	337
Jun	306
Jul	300
Aug	301
Sep	330
Oct	319
Nov	308
Dec	295
Annual Average	325

Table 5-11 – Data for Figure 5-20

The monthly averaging used to present Figure 5-20 and Table 5-11 (and for subsequent monthly figures and tables) is based on twelve equal months of 730 hours each. Thus, the figures shown in Table 5-11 will not exactly match the averages of the columns of Table 5-10. The annual average is of course consistent at 325 W/m^2.

5.9 Ambient temperature

Meteonorm was also used to provide ambient temperature data for the same site in Eritrea and for the same *typical* year. The data is hourly and was used within the Simulink model to estimate the hourly PV array temperature, as described in section 5.10.2.

5.9.1 Hourly ambient temperatures

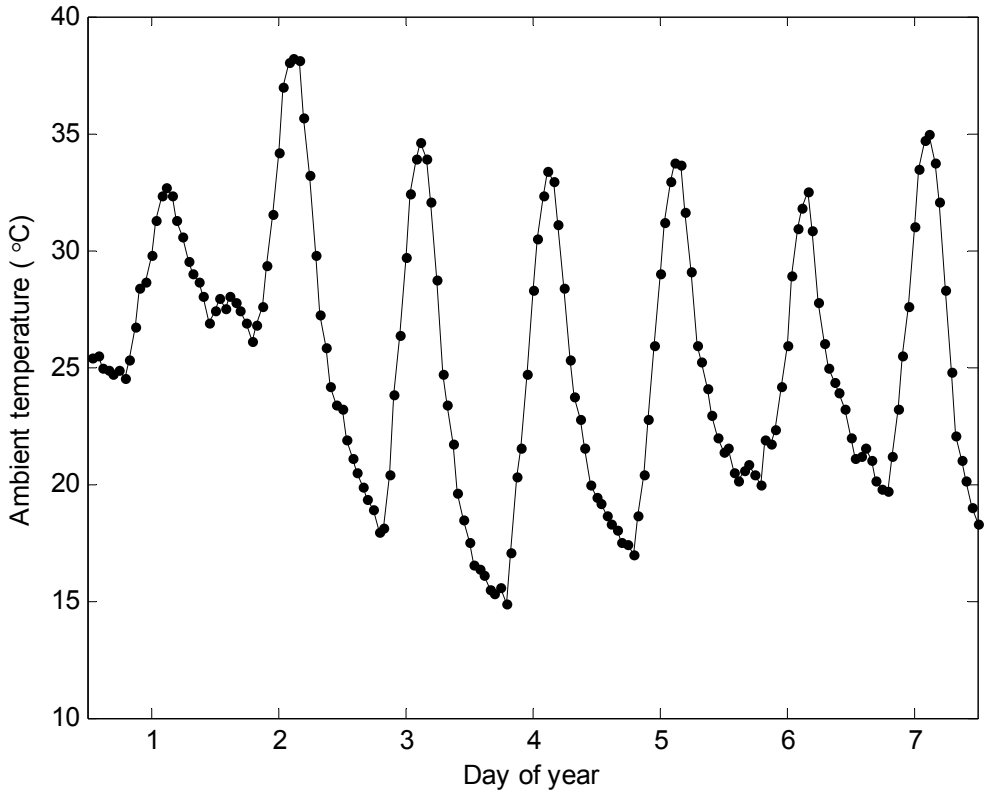

Figure 5-21 – Hourly ambient temperature for the first week of the year-long data set

Notice that the cloud cover (modelled within Meteonorm) that led to the low irradiance figures during days 1 and 6, shown in Figure 5-18, has also led to warmer nights, as shown in Figure 5-21.

5.9.2 Average monthly ambient temperatures

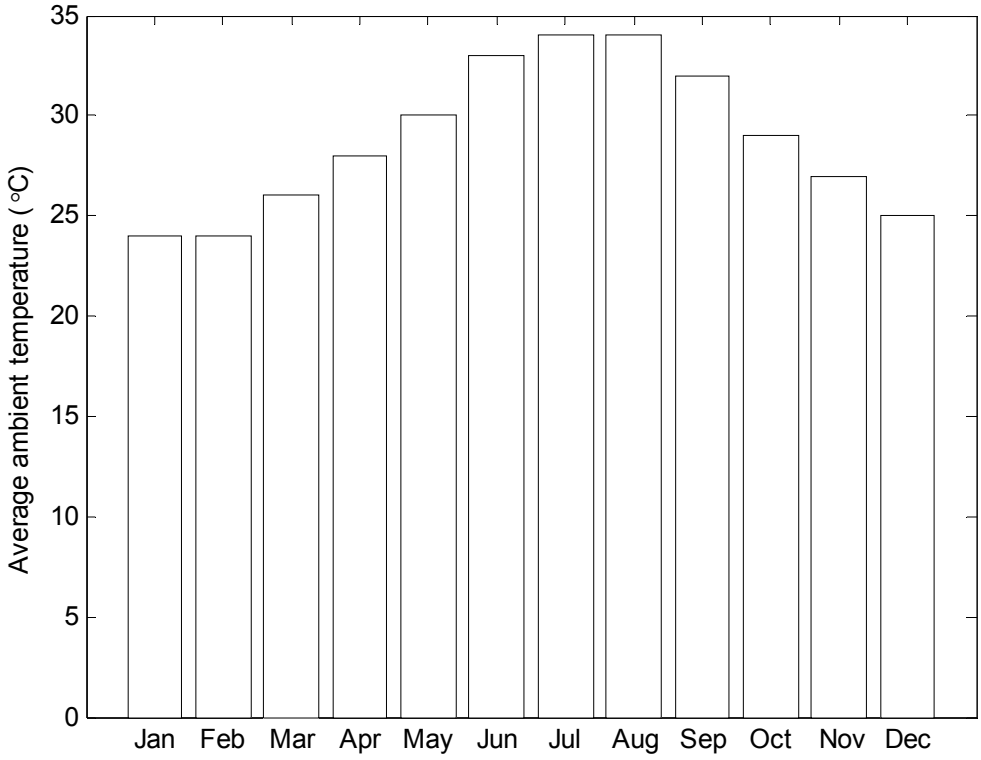

Figure 5-22 – Average monthly ambient temperature

	Average monthly ambient temperature (ºC)
Jan	24
Feb	24
Mar	26
Apr	28
May	30
Jun	33
Jul	34
Aug	34
Sep	32
Oct	29
Nov	27
Dec	25
Annual Average	29

Table 5-12 – Data for Figure 5-22

5.10 PV array

5.10.1 Two-diode model

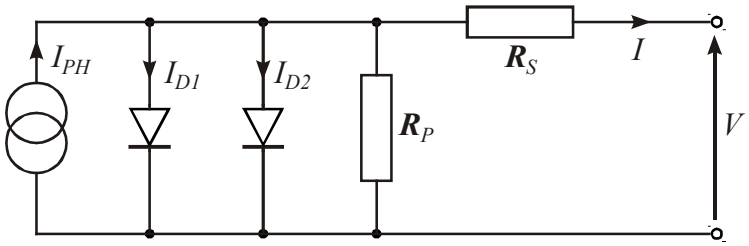

Figure 5-23 – Two-diode model of a PV cell (Gottschalg 2001 page 60)

The *two-diode model* shown in Figure 5-23 is commonly used to represent an individual PV cell. I_{PH} is the photo current, which is the part we actually want. The other components represent losses within the cell; in particular: I_{D1} represents recombination in the bulk material, I_{D2} represents recombination in the space charge region, R_P represents parallel leakage losses and R_S represents the series resistance. I and V are the terminal current and voltage respectively.

Applying Kirchoff's laws and exponential representations of the diodes yields:

$$I = I_{PH} - I_{01}(\exp\frac{e(V+IR_S)}{n_1 kT} - 1) - I_{02}(\exp\frac{e(V+IR_S)}{n_2 kT} - 1) - \frac{V+IR_S}{R_P}$$

(Gottschalg 2001 page 60)

in which:

$$I_{PH} = A_C(C_0 + C_1 T)G$$

$$I_{01} = A_C C_{01} T^3 \exp(-\frac{eV_{gap}}{kT})$$

$$I_{02} = A_C C_{02} T^{\frac{5}{2}} \exp(-\frac{eV_{gap}}{2kT})$$

T is the temperature of the cell in ºK.

A_C is the area of the cell and V_{gap} is the band gap voltage of the material. These and the other parameters were kindly provided by AstroPower (www.astropower.com accessed: March 04), describing their 120-W_p polycrystalline modules: AP-1206.

5.10.2 Simulink model

The two-diode model just described was implemented in Simulink, as shown in Figure 5-24.

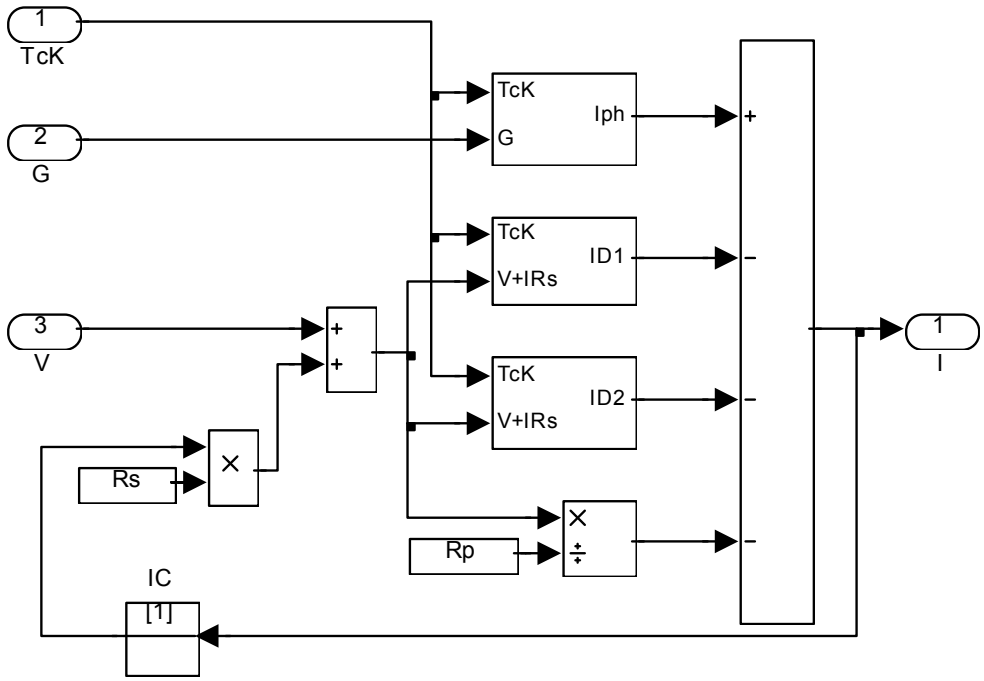

Figure 5-24 – Two-diode model of a PV cell in Simulink

In Figure 5-24, the input TcK is the temperature of the cell in ºK, previously denoted as T in section 5.10.1. The other symbols are defined as they were in that section.

The model requires an iterative solution, as indicated by the feedback of the current signal I. Simulink performs this almost transparently using Newton's method. The block labelled IC provides an initial value for the iteration.

Next, the PV cell model shown in Figure 5-24 was used to construct a model of a PV module as shown in Figure 5-25.

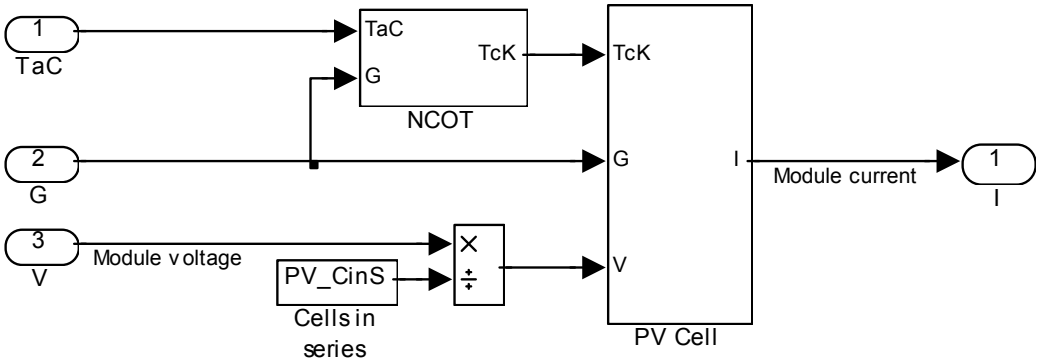

Figure 5-25 – Simulink model of a PV module

In Figure 5-25, the input TaC is the ambient temperature in ºC, as provided by Meteonorm discussed in section 5.9. Input G is the irradiance, also from Meteonorm, as discussed in section 5.8.

The cell temperature TcK is estimated from the ambient temperature and the irradiance using the *Normal Operating Cell Temperature* (NOCT) method (Markvart 1999 page 88).

Dividing the module voltage by the number of cells in series provides the cell voltage. A higher layer in the Simulink model hierarchy calculates the array voltage from the module voltage in a similar fashion. This approach makes no allowance for mismatch losses, which leads the PV-module model to give higher output predictions than those shown on the manufacturers' data sheet. It also means the array predictions are on the optimistic side. Measurements and modelling of PV arrays composed of undamaged production-run modules operating at uniform temperature and irradiance (totally unshaded) showed mismatch losses below 0.53 % (Chamberlin et al. 1995).

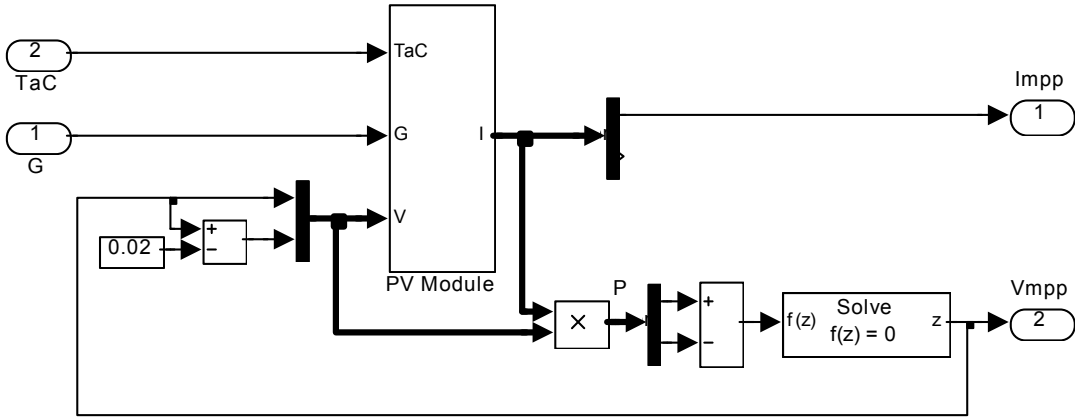

Figure 5-26 – Simulink programme to locate maximum power point (MPP)

Figure 5-26 illustrates how Simulink was used to locate the maximum power point (see section 2.5.4). The algorithm relies on the fact that, at the maximum power point, $dP/dV = 0$. The *Solve* block, towards the right of Figure 5-26, is a standard Simulink block and uses Newton's method to adjust its output z until its input f(z) equals zero. In this application, its output z is the module voltage and is fed back round to the left of the diagram. An arbitrary small constant 0.02 is subtracted from this voltage and the thick vertical bar combines the two signals into a vector of two voltages, indicated by the thick arrow line connected to the input V of the PV Module block. When presented with this vector input, the PV Module block simply produces a vector output I, which contains the two corresponding currents. Multiplying the two voltages by the two currents provides two powers in the vector P. The difference of these powers is fed to the solve block. The solve block locates the voltage where the difference of the two powers calculated at the two voltages is zero. This is where $dP/dV = 0$.

Since the I-V characteristic of the modelled PV module is smooth, the algorithm just described has no difficultly in locating the theoretical maximum power point. This again leads the model to be optimistic, since it makes no allowance for error in the maximum power point tracker. Chapter 9 will discuss maximum power point tracking in practice.

5.10.3 Electrical power available from PV

The irradiance and ambient temperature data, described in sections 5.8 and 5.9 respectively, was used as input to the Simulink model just described. The two-diode model parameters were kindly provided by AstroPower (www.astropower.com accessed:

March 04), describing their 120-W_p polycrystalline modules: AP-1206, and the results presented in this section are for an array of 20 modules, ie. a 2.4-kW_P PV array, which is the size chosen for the completed design shown in section 6.4.

The results presented here represent the *available* power from the PV; it is always possible, though wasteful, to use less than the available power.

The model performs the calculations on an hour-by-hour basis and gave an annual total of 5713 kWh.

5.10.3.1 Electrical power available – hourly

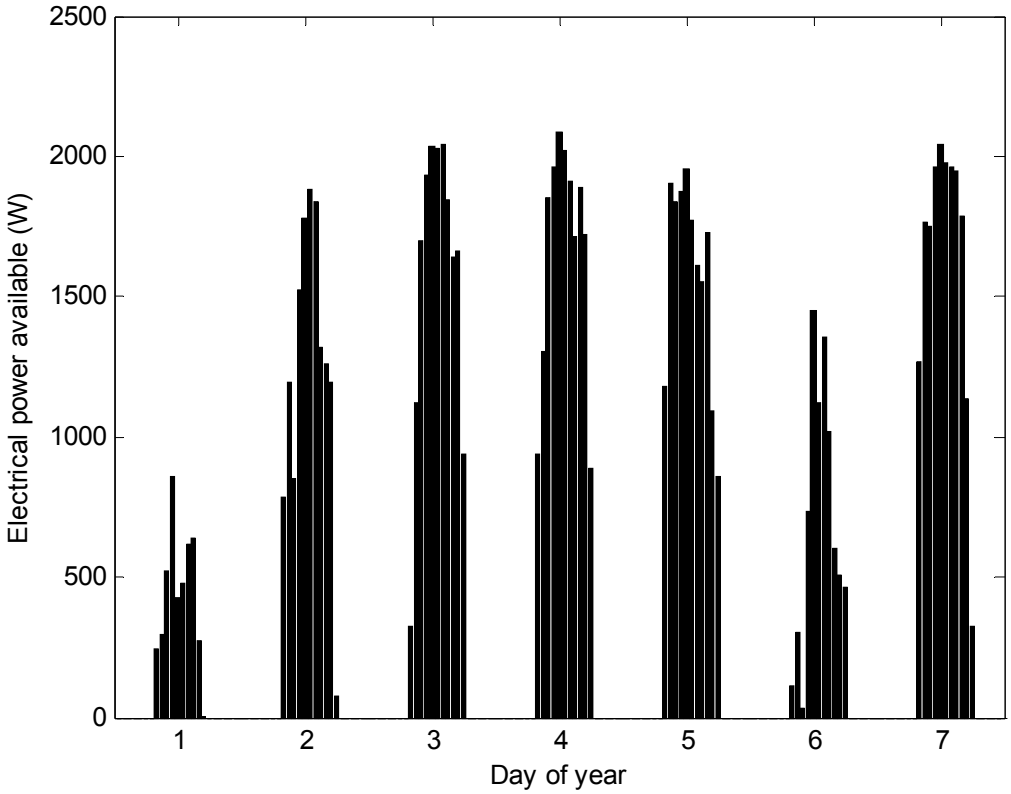

Figure 5-27 – Electrical power available – hourly for the first week of the year-long data set

The electrical power available from the PV array, shown in Figure 5-27, is a function of the irradiance, shown in Figure 5-18, and the ambient temperature, shown in Figure 5-21.

5.10.3.2 Power available versus irradiance

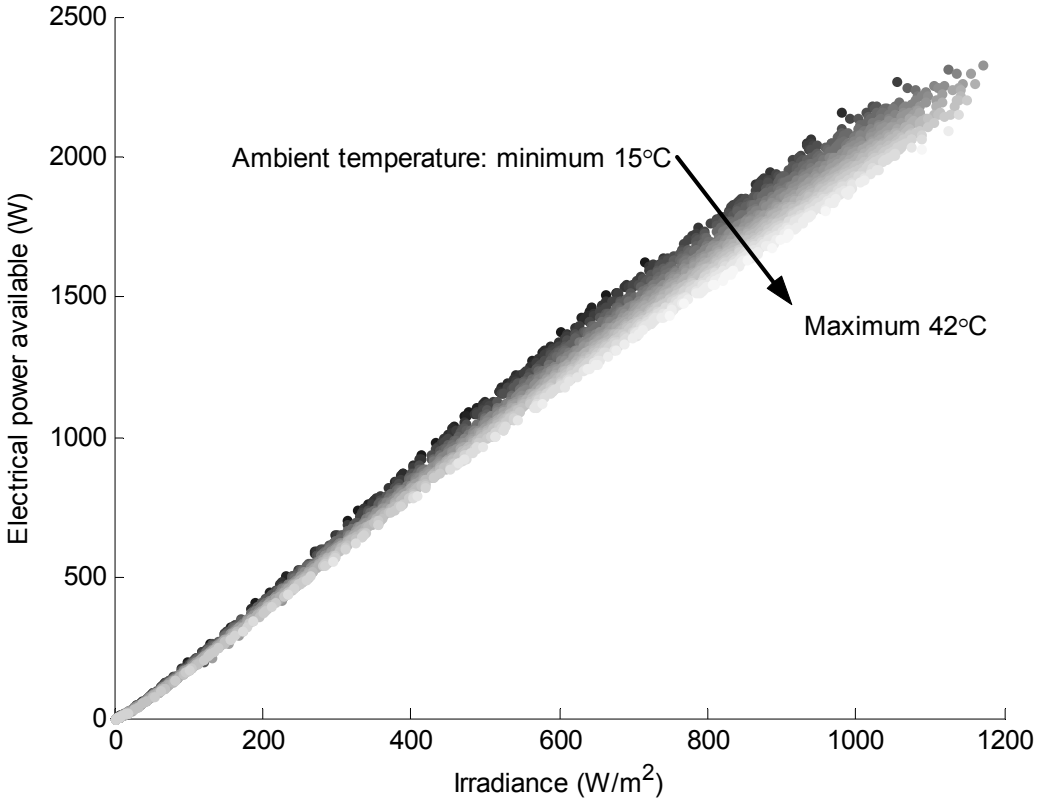

Figure 5-28 – Electrical power available versus irradiance

Figure 5-28 illustrates that power available from the PV is roughly proportional to irradiance, but decreases significantly as the ambient temperature increases.

5.10.3.3 Affect of ambient temperature

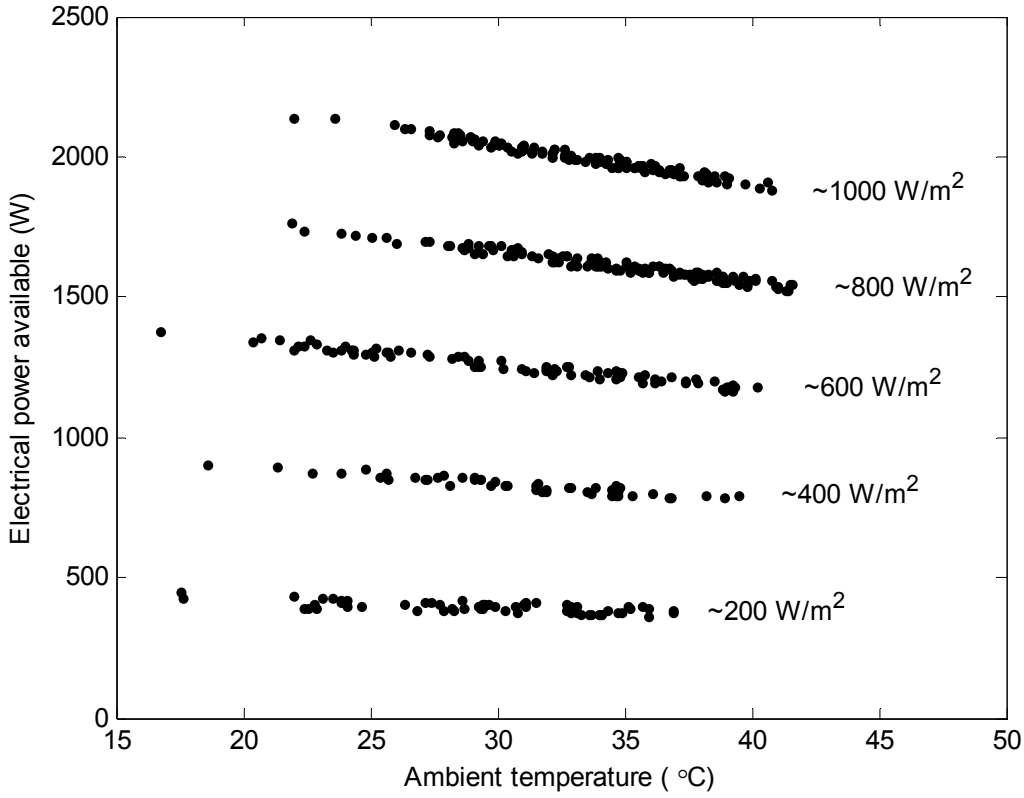

Figure 5-29 – Electrical power available versus ambient temperature

In Figure 5-29, the irradiance levels 200, 400, 600, 800 and 1000 W/m^2 are chosen for illustration only. The data plotted for each level includes +/– 10 W/m^2. Fitting a straight line to the 1000-W/m^2 data shows a temperature coefficient of around – 0.7 % per Cº.

5.10.3.4 Average monthly electrical power available

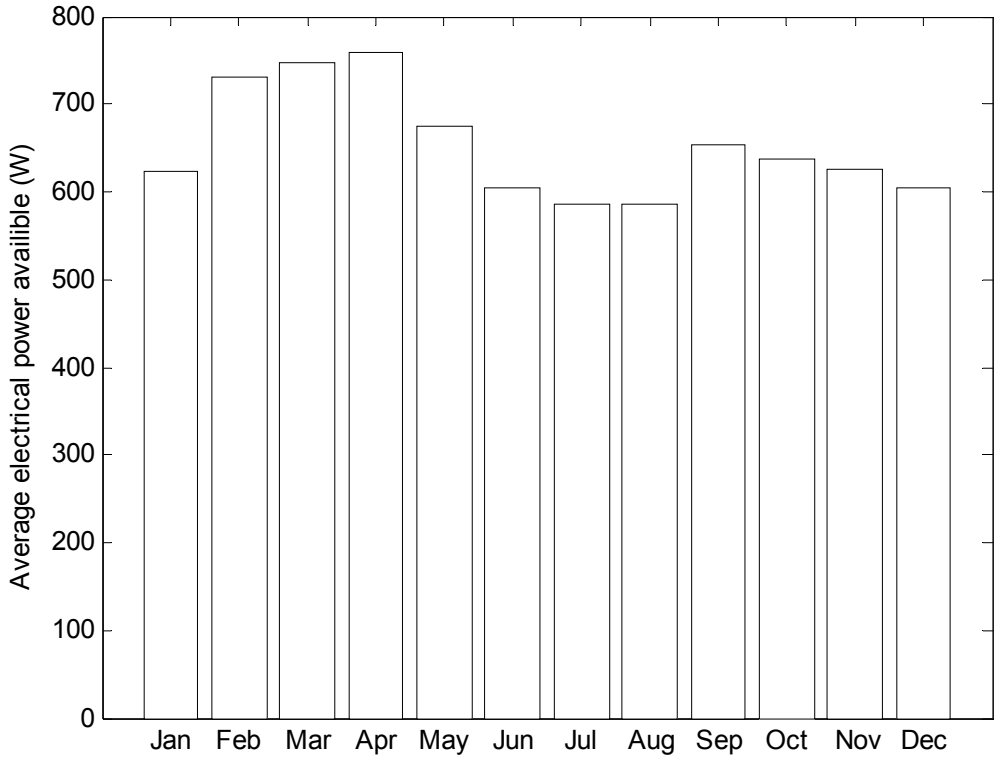

Figure 5-30 – Average monthly electrical power available from PV array

	Electrical power available from PV array (W)
Jan	623
Feb	730
Mar	747
Apr	759
May	674
Jun	605
Jul	585
Aug	585
Sep	653
Oct	638
Nov	625
Dec	605
Annual Average	652

Table 5-13 – Data for Figure 5-30

Figure 5-30 illustrates, as expected, that the monthly average power available from the PV is has a similar profile to the monthly average irradiance, shown in Figure 5-20, but is depressed during the summer due to the high ambient temperatures shown in Figure 5-22.

5.11 Seawater

The energy consumption of real-world seawater RO systems is affected by the concentration of the seawater feed, which varies from place to place and from time to time. Even in laboratories, the concentration of the seawater has no universally accepted standard, and is complicated by the variety of units employed.

5.11.1 Concentration: ppm versus mg/L

Oceanographers tend to express the concentrations of salts in seawater in weight-to-weight ratios, such as percent (%), parts per thousand (‰ or g/kg) or parts per million (ppm). Chemists, on the other hand, use weight-to-volume ratios, such as mg/L. The desalination industry uses both.

To convert from ppm to mg/L, one should multiply by the density (specific gravity), but, since the density of water is close to 1 kg/L, concentrations in ppm and mg/L are numerically similar, and the conversion is often overlooked. At low concentrations, associated with the product water, or even brackish feed water, the error is small and has little consequence in the field of desalination. With seawater however, the density is around 1.024 kg/L at 20 ºC (El-Dessouky et al. 2002 page 527), so for example 35,000 ppm is 35,840 mg/L. Interchanging the units without performing the calculation is perhaps acceptable when quoting ballpark figures to the nearest 1000, but for testing and modelling of energy efficiency the conversion should be done.

5.11.2 Salinity versus TDS

During the 1800's, *salinity* was defined as *the total amount of dissolved material in grams in one kilogram of seawater*. Because the units are in the definition, salinity is dimensionless, and is correctly written without units. Nonetheless, salinity *by this definition* is obviously numerically equal to the total dissolved solids (TDS) in parts per thousand.

Unfortunately, total dissolved solids is very difficult to measure directly, and so oceanographers have redefined salinity to suit available indirect measurement methods, and have done so several times over the last century as more accurate measurement methods have been developed (Stewart 2002). The result is that salinity is approximately 0.995 of TDS in ‰ (Millero 1996; Tonner 1999). Thus, seawater with 35,000 ppm TDS has a salinity of around 34.825. The difference between TDS and salinity is rarely a concern in desalination, and the word *salinity* is frequently used when discussing figures quoted in TDS.

5.11.3 Typical concentrations of seawater

The average salinity of the world's oceans is 34.72 (Snoke 2002), which equates to 35,750 mg/L TDS at 20 ºC, and the vast majority of seawater worldwide is close to this concentration: TDS between 35,300 and 36,100 mg/L. There are various descriptions of *standard seawater* in the literature (Millero 1996; Tonner 1999; DOW 1995; ASTM 1998), and most lie in this range. Costal waters can have significantly lower concentrations, particularly near rivers, but such areas are unlikely to need water through desalination. Some seas have significantly higher concentrations, notably the Red Sea and Arabian Gulf, which can be up to 45,000 mg/L (DOW 1995 section 3.2).

5.11.4 Composition of seawater

Although the *total* dissolved solids in seawater can vary significantly, as discussed above, the *relative* concentrations of the major constituents, shown in Table 5-14, are virtually constant throughout all of the world's oceans.

	g/kg	mg/l
Chloride	18.9799	19441.1
Sulfate	2.6486	2713.0
Bromide	0.0646	66.2
Bicarbonate	0.1397	143.1
Fluoride	0.0013	1.3
Sodium	10.5561	10812.6
Magnesium	1.272	1302.9
Calcium	0.4001	409.8
Potassium	0.38	389.2
Silica	0.00201	2.1
Strontium	0.0133	13.6
Orthoborsic Acid	0.026	26.6
Others	0.00135	1.4
Total Dissolved Solids	34.48496	35322.9
Water	965.51504	
Total	1000	1024.3
Salinity	34.325	
Specific Gravity @ 20°C	1.0243	

Table 5-14 – The major constituents of seawater (Lyman and Fleming via Tonner 1999)

5.11.5 Osmotic pressure

For the study of energy consumption in a reverse-osmosis system, the critical characteristic of the feed water is its osmotic pressure. Rudimentary texts suggest that osmotic pressure may be calculated by van't Hoff's equation:

$$\pi = nRT$$

where π is the osmotic pressure, n is the concentration, R is the gas constant, and T is the temperature. Unfortunately, this is only accurate at very low concentrations (Reid 1966). For stronger solutions containing mixed species, such as seawater, the calculations are more complex. ROPRO (Koch Membranes' RO systems design software: Koch-ROPRO 2000) uses experimentally determined osmotic pressure coefficients for each species. These are multiplied by the species concentration and summed to provide an estimate of the overall osmotic pressure of the solution. ROPRO was used to calculate the osmotic pressures of three *standard* seawaters and one other.

Lyman and Fleming's data (Table 5-14) is at the low-concentration end of typical seawater: TDS = 35323 mg/L and gives 25.4 bar.

Data for seawater at the other end of the range (Millero 1996) has TDS = 36121 mg/L and gives 26.0 bar.

Standard seawater according to DOW (1995) has TDS = 35617 mg/L and gives 25.6 bar.

Water from a particular borehole well in Massawa, Eritrea, off the Red Sea has concentration much higher than the average. It has a TDS of 40149 mg/L and gives 28.85 bar.

5.11.6 Straight NaCl solution

There is a recipe for the preparation of artificial *standard* seawater (ASTM 1998), but for the study of energy consumption in an RO system, it is sufficient to work with straight NaCl solution, *provided the concentration is adjusted accordingly*. Indeed, several of the manufacturers (Koch, Dow and Osmonics) specify their membranes in terms of straight NaCl solution. In particular, Koch Membranes are specified with NaCl at 32,800 mg/L, which is isosmotic with ASTM standard seawater.

Using ROPRO with NaCl at 32,800 mg/L gives 25.8 bar which lines up with the *standard* seawaters calculated previously.

To convert this to ppm, the density of straight NaCl solution (not seawater) at 20 ºC is given, by:

$$\rho = 0.6985 \times C + 0.99829$$

where ρ is the density in kg/L and C is the concentration in mg/L (Weber-Shirk 2003).

Thus for C = 32,800 mg/L, ρ = 1.021 kg/L, and 32800 mg/L / 1.021 kg/L = 32,125 ppm.

5.11.7 Summary

The average salinity of seawater is 34.72, which equates to 35,750 mg/L TDS at 20 ºC, and has an osmotic pressure of around 25.7 bar. For testing and modelling RO energy consumption, Koch use straight NaCl solution at 32,800 mg/L, which is 32,125 ppm and has a very similar osmotic pressure. Various concentrations have been used for testing and modelling of the PV-RO system and will be noted where appropriate.

5.12 Feed-water temperature

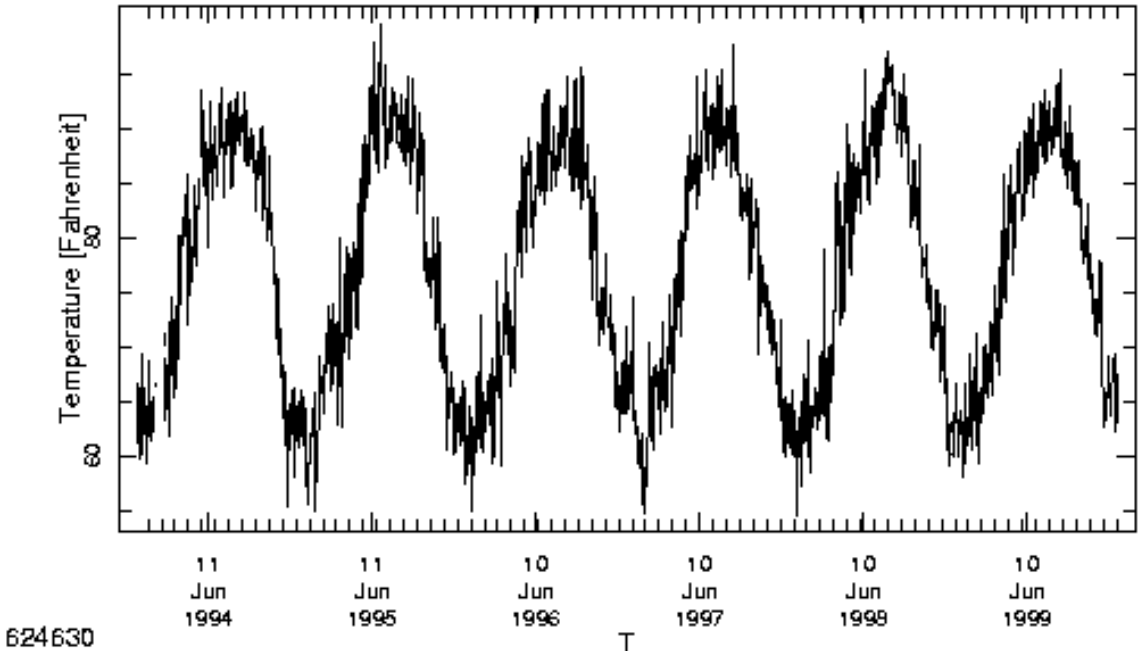

Figure 5-31 – Red Sea water temperature profile provided by Dulas Limited

A temperature profile for water in the Red Sea was provided by Dulas Limited in the form of the bitmap shown in Figure 5-31. This was converted to numeric data by treating the bitmap image as a matrix within MATLAB. Since the PV-RO system is designed to operate from a beach well, rather than an open-sea intake, it was assumed that the short-term temperature fluctuations would be smoothed out and that only the seasonal variations were important. The six years of data were superimposed and a sine curve was fitted, as shown in Figure 5-32.

$$Feed\ water\ temperature = 25 + 8\sin\left(2\pi\frac{day\ of\ year - 118}{365}\right)$$

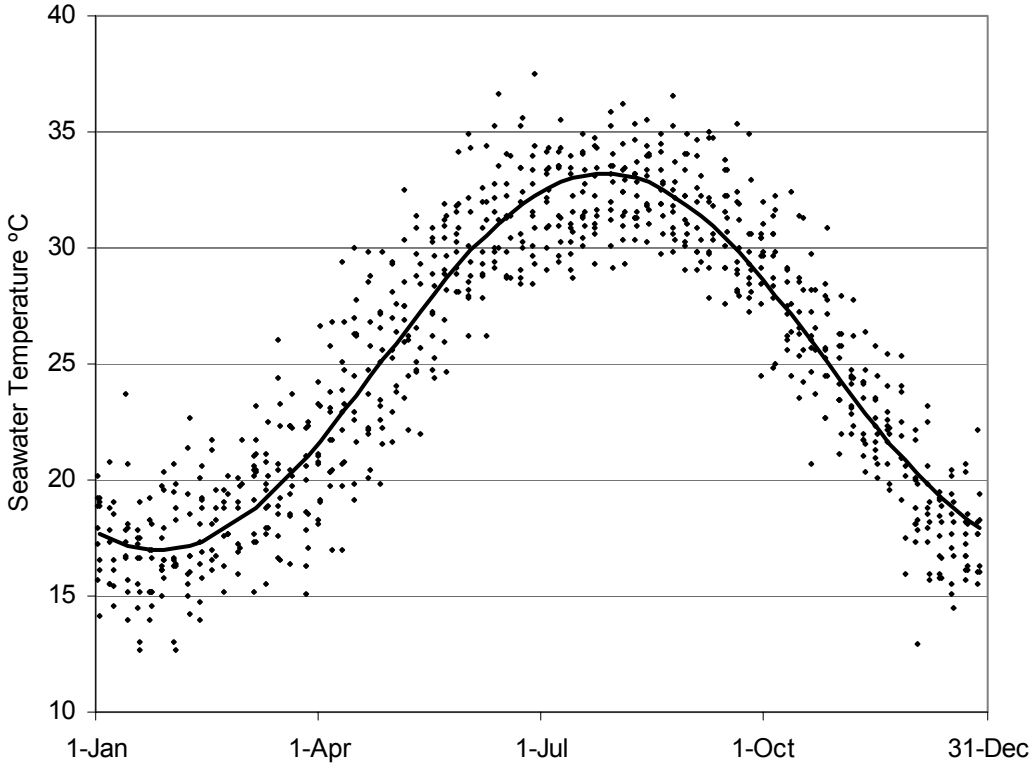

Figure 5-32 – Red Sea water temperature: data derived from Figure 5-31 and fitted sine curve

5.13 Reverse osmosis membrane elements

The general principle of reverse osmosis was outlined in section 1.2, and an introduction to the technology was presented in section 2.7. This section will discuss the development of a Simulink model for use in the design of the PV-RO system.

5.13.1 Model structure

In order to predict the flow and concentration of product water for the complete PV-RO system, a model of an RO membrane element is required. The required model is similar to those included in the membrane manufacturers' software packages such as ROSA (DOW 2000) and ROPRO (Koch-ROPRO 2000), except that it must fit within the complete Simulink PV-RO system model, so that operation at variable flow and pressure can be predicted. Also, it should be accurate over the full range of flows and pressures that occur in a batteryless PV-RO system.

The flow and concentration of product water from an individual membrane element is a function of the flow, pressure, concentration and temperature of the feed water, but, in order that completed membrane-element models can be connected together to model an array, care is required in selection of inputs and outputs of the Simulink block representing the RO element.

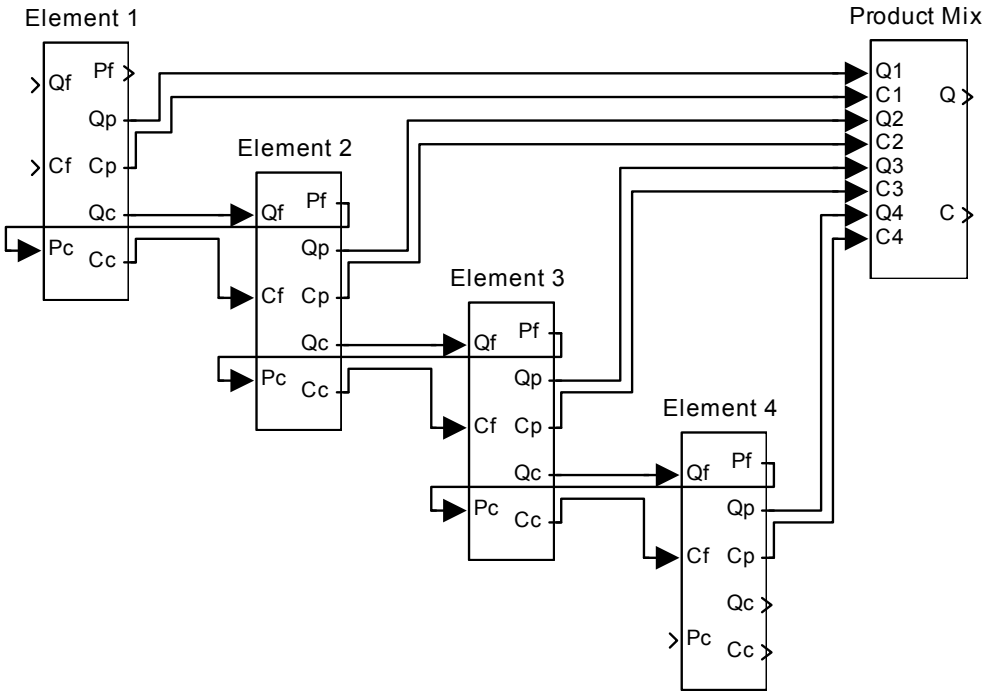

Capital letters	Q	Flow
	C	Concentration
	P	Pressure
Lowercase	f	feed
	p	product
	c	concentrate

Figure 5-33 – Structure of the Simulink model of the array of RO elements

The chosen structure is shown in Figure 5-33, and thus the RO element model has:

Inputs	
Q_f	Flow of the feed,
C_f	Concentration of the feed,
P_c	Pressure of the concentrate,

Outputs:	
Q_c	Flow of the concentrate,
C_c	Concentration of the concentrate,
P_f	Pressure of the feed,
Q_p	Flow of the product,
C_p	Concentration of the product.

The pressure of the product P_p and the temperature T are also inputs to the RO element model, but since they are global variables, they are not passed from one block to the next.

5.13.2 Calculations

Internally, the model follows the structure outlined in the equations set out by DOW(1995 section 4.11), and upon which ROSA is based. Initially, the model was constructed exactly according to those equations, but it was found that various adjustments were required, first, to make the results line up with ROSA, second, and more importantly, to match up with measured data obtained from the test rig. Throughout the project, the Simulink model has been refined, with assistance from Marcos Miranda. He tested various membrane elements over a very wide range of flows, pressures, temperatures and feed concentrations. Within normal flow and pressure ranges, the results lined up reasonably well with ROSA and ROPRO, but at very low flows and pressures, large differences were observed. The model used in the performance predictions presented in Chapter 6 is as follows.

All pressures are in bar, flows in L/s and concentrations in mg/L.

The model first calculates the small pressure drop in the feed/concentrate channel:

$$\Delta P = -0.26 + 7.61 Q_f/T + 11.3 Q_f^2 + 3.36\times10^{-6} C_f + 326(T\times P_c)^{-1} - 1.22\times10^{5}(T\times P_c)^{-2}$$

The pressure of the feed P_f is simply $P_c + \Delta P$, and the average pressure in the feed/concentrate channel is $P_{fc} = P_c + \frac{1}{2}\Delta P$. The osmotic pressure is calculated using:

$$\pi_f = \frac{0.002654 \times C \times (T + 273.15)}{1000 - C/1000}$$ (ASTM 1985).

In the early Simulink models, the calculation of C included C_c and concentration polarisation, following the DOW equations. But this creates an algebraic loop and it was found better to simply to calculate the osmotic pressure of the feed and to accommodate the concentration increase through extra terms in the product flow calculation. The net driving pressure (neglecting concentration increase) is then given by:

$$P_{nd} = P_{fc} - \pi_f - P_p.$$

The product flow is then given by:

$$Q_p = 0.00307 + 0.000193P_{nd} - 1.61\times10^{-7}C_f + 5.49\times10^{-5}T + 2.01\times10^{-5}P_{nd}\times T + 2.44\times10^{-5}P_{nd}\times Q_f\times T + 7.9\times10^{-7}C_f/T - 3.25\times10^{-10}P_{nd}\times T\times C_f$$

The salt passage through the membrane is the product of the product flow and its concentration and is given by:

$$Q_p\times C_p = 5.26 - 7.55\times10^{-5}C_f - 0.0209P_{nd} - 0.422T + 0.00551T^2 + 7.52\times10^{-6}C_f\times T + 0.00163P_{nd}\times T + 5.79Q_p/Q_f$$

Lastly, a simple mass balance is applied: $Q_c = Q_f - Q_p$ and $Q_f C_f = Q_p C_p + Q_c C_c$.

5.14 Product tank

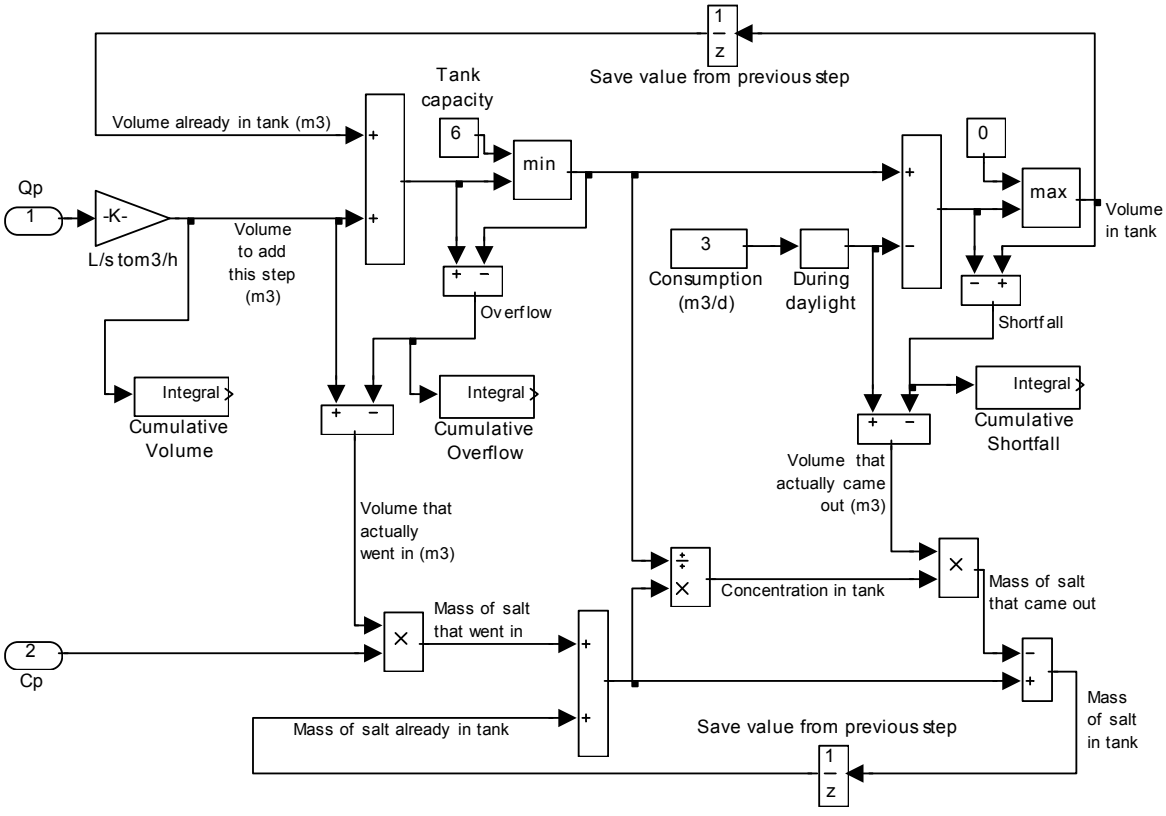

Figure 5-34 – Structure of Simulink model of product tank

Figure 5-34 illustrates the Simulink model used to represent the product tank. Starting on the left, Qp represents the flow of product water into the tank, in L/s. This is converted to m^3/h, which is numerically equal to the Volume to add this step in m^3, because the

time-step used to run the model is 1 hour. This volume is integrated, as the model runs, to provide the Cumulative Volume.

Next, the Volume to add this step is added to the Volume already in the tank from the previous step. If this exceeds the Tank capacity, ($6m^3$) an Overflow is calculated and this is also integrated to provide the Cumulative Overflow.

Continuing to the right of Figure 5-34, the Consumption shown is $3m^3$/day; the During daylight block simply doubles this between 8AM and 8PM and gives zero during the night. The consumption is then subtracted to give the (new) Volume in tank, and any shortfall is calculated.

The lower half of Figure 5-34 calculates the salt concentration in the tank and, therefore, supplied to the consumer. Starting again on the left, Cp represents the concentration of product water as it comes from the RO rig. Multiplying this by the volume of water that actually went in (after allowing for overflow) gives the Mass of salt that went in. And dividing this by the volume now in the tank gives the Concentration in tank, which is the concentration of the water consumed. Multiplying this by the volume of water that actually came out gives the Mass of salt that came out, allowing the remaining Mass of salt in tank to be calculated and saved for the next modelled time-step.

Chapter 6 System modelling, optimisation and performance predictions

6.1 System design strategy

The Simulink component models presented in the previous chapter were assembled into a complete system model, which will be discussed in this chapter. First, the structure of the completed model will be discussed, followed by an explanation of how it calculates the capital cost of the system and annual performance figures. These figures are used later in the chapter, in particular for optimising the RO and PV array sizes with respect to the capital cost.

6.1.1 System model structure

The general strategy for interconnecting the component models within Simulink was discussed in section 5.1. Now, the completed model will be discussed, starting with the top layer of the hierarchy shown in Figure 6-1.

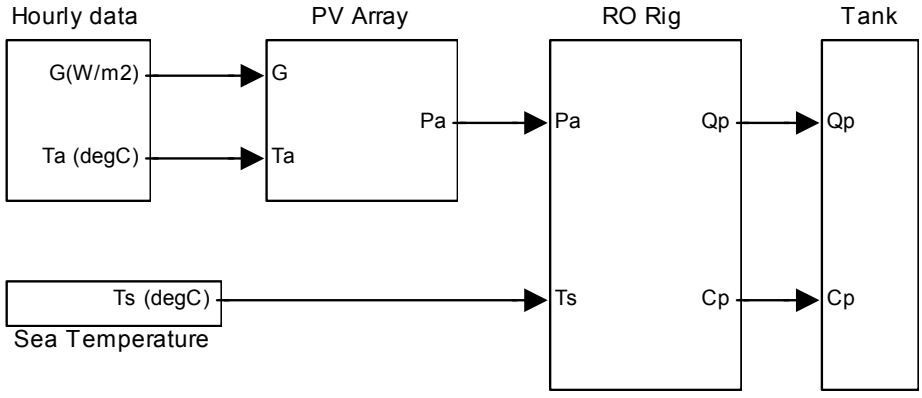

Figure 6-1 – Top layer of the hierarchical Simulink model of the complete system

In Figure 6-1, the Hourly data block includes the irradiance G and the ambient temperature Ta, both derived from Meteonorm as described in sections 5.8 and 5.9. This data feeds the PV Array model, described in section 5.10, which calculates the available power Pa. The seawater temperature Ts is modelled as described in Section 5.12. The RO Rig block uses the available power and the seawater temperature to predict the flow

of product water Qp and its concentration Cp. The tank integrates this flow of product water, taking into account the water consumption, as described in section 5.14.

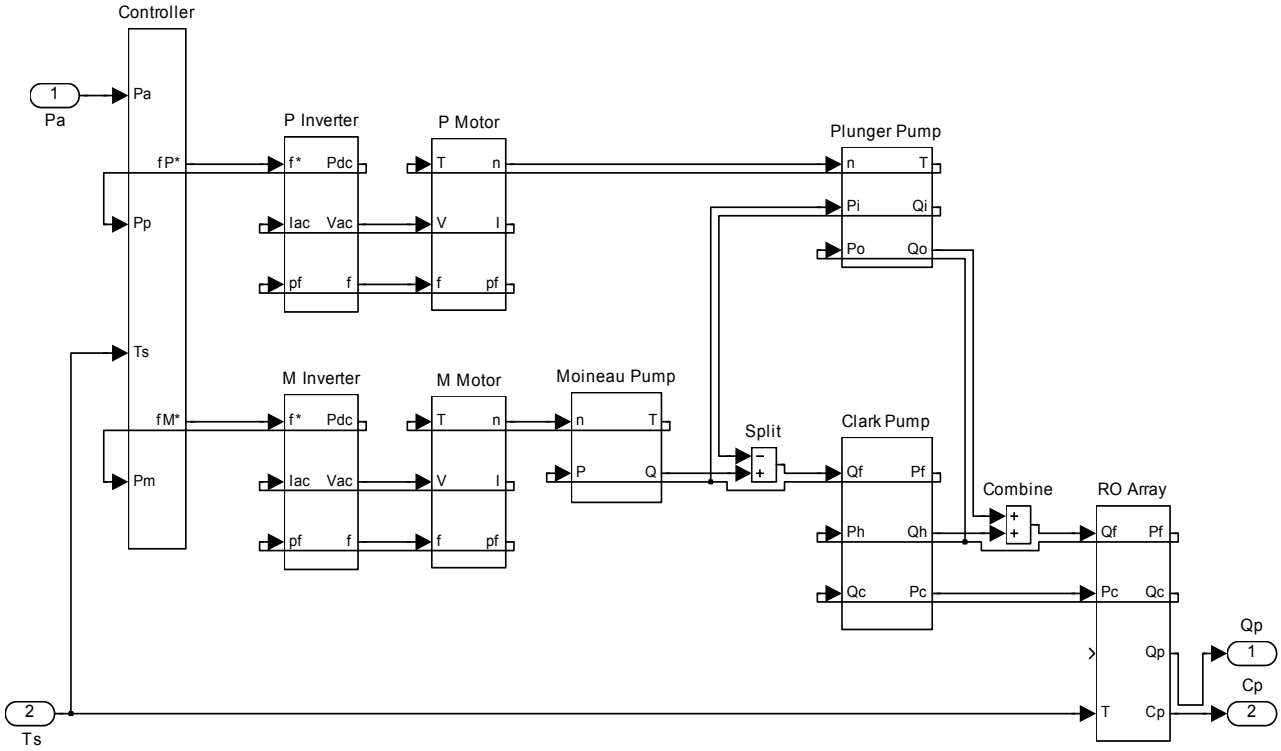

Figure 6-2 – Simulink model of the RO rig

Figure 6-2 shows the contents of the RO Rig block shown in Figure 6-1. The Controller shares the power available Pa between the two inverter/motor/pumps in order to maximise the water production, as described in section 6.2.3. It does this by providing a frequency setpoint signal f* to each of the two inverters. In return, the inverter models provide signals Pdc that represent the DC power drawn. The controller model ensures that the sum of these two equals the power available: Pp + Pm = Pa.

Each inverter is modelled as described in section 5.7.1 and provides signals Va and f representing the ac voltage and its frequency. These signals, together with the torque T from the respective pump, are inputs to the motor model blocks, which are as described in section 5.6.

Each motor block has an output n, which is the shaft speed and is fed to the respective pump. The motor blocks also provide outputs I and pf, which are the ac current drawn by motor and its power factor respectively, and are fed back to the inverter model blocks.

The Moineau pump, Plunger pump, Clark pump and RO Array are as shown in sections 5.4.2, 5.3.1, 5.2.3 and 5.13.1 respectively.

The blocks labelled Split and Combine may be understood with reference to Figure 1-3. In particular, the Split performs a simple subtraction, representing the fact that the feed flow to the Clark pump equals the flow through the Moineau pump less that through the Plunger pump. Likewise, the Combine block represents the addition of the Plunger pump outlet flow to that of the Clark pump.

6.1.2 Modifying the system model

The completed system model just described represents the *final* design, which was used for the performance predictions presented later in this chapter (section 6.5) and from which the new test rig was built. In order to develop this design, the system model was modified many times. A critical feature of the model structure is that components, such as pumps and RO modules etc., can be added, deleted and reconnected simply by manipulating the blocks and interconnections of the graphical interface. In order to assess the costs and benefits of alternative configurations, two additional MATLAB scripts (programmes) were written and linked to the Simulink model. The first deals with the capital costs, while the second provides annual performance figures and relates these to the capital cost.

6.1.3 Capital cost modelling

Since there are no fuel costs, the total cost of water in a PV-RO system is largely determined by the capital cost and the main aim of the optimisation presented in this thesis was to minimise the capital cost with respect to the predicted annual water production.

Each Simulink component model (each block in Figure 6-2 for example) contains a value representing its cost. Each time the model is run, a MATLAB script collates the costs for all the components in use and provides a summary table such as Table 6-1.

20 PV modules at £369 each	£7,380
4 RO membrane elements at £330 each	£1,320
4 pressure vessels at £369 each	£1,476
Clark Pump - Spectra	£1,200
Inverter (for Moineau) - FID 1.5kW	£94
Motor (for Moineau) - Toshiba PE	£309
Moineau Pump - Netzsch 021	£710
Inverter (for Plunger) - FID 1.5kW	£94
Motor (for Plunger) - Toshiba PE	£309
Plunger Pump - Cat 237	£380
Miscellaneous Costs	£5,000
Complete system capital cost	£18,272

Table 6-1 – Capital cost modelling estimates summary table

The data presented in Table 6-1 is that for the completed design. The costs shown were estimated in early 2001 as follows.

The estimated cost of the PV modules (£369 each) was obtained from Dulas Limited. It was for a typical 120 W_p module (no particular manufacturer) and includes an element to cover a single-axis solar-trajectory tracking system.

The cost shown for the RO membrane elements (£330 each) was based on a quotation for Koch Seawater High-flow TFC1820HF 4" by 40" elements. The price paid later in 2001 for elements of this type for the new test rig was £270 each plus VAT.

The cost shown for the pressure vessels (£369 each) was based on a quotation for 4" by 40" vessels. The price paid later in 2001 for four such vessels for the new test rig was £296 each plus certification, delivery and VAT. In the future, it would be well worth considering use of longer vessels that would hold either two or four membrane elements each, since they are much cheaper overall.

The cost shown for the Clark pump was based on discussions with the manufacturers Spectra Watermakers Inc. The Clark pump is not normally sold separately.

The cost shown for the inverters (£94 each) was based on a quotation for standard 1.5kW industrial drives, in particular the FID1000 FKI-12150. The price paid later in 2001 for an inverter of this type was £157 plus VAT.

The cost shown for the motors (£309 each) was discussed in sections 5.6.5 and 5.6.6.

The cost shown for the Moineau pump (£710) was based on a quotation for a Netzsch NM021SY02S12B in 316 stainless steel. The price paid later in 2001 for a pump of this type was £745 plus VAT.

The cost shown for the Plunger pump (£380) was based on a quotation for a Cat 237.

The £5000 shown in Table 6-1 for *Miscellaneous Costs* is an estimate provided by Dulas Limited and is intended to cover:

- pipe work, filters and interconnections,
- a frame on to which the components may be mounted,
- sensors, wiring and the controller,
- manufacture.

Lastly, Table 6-1 shows the *Complete system capital cost*, which is simply the sum of the above components. It was this figure that was minimised with respect to the predicted annual water production in the optimisation presented in this thesis.

6.1.4 Annual performance figures

In order to assess alternative system configurations and component sizes, the Simulink system model was run many times. Each run included hourly calculations for one whole year (8760 steps) of operation. The input data for all runs was that for Massawa, Eritrea, as discussed in sections 5.8 (irradiance), 5.9 (ambient temperature) and 5.12 (feed-water temperature), but with a feed concentration of 35,000 mg/L NaCl, as discussed in section 6.5. The output data includes hourly values for every input and output of every component (discussed in Chapter 5) and for the system as a whole. This data was summarised (by a Matlab script) after each run of the Simulink model, to provide a table of annual performance figures such as that shown in Table 6-2.

Annual energy available from the PV	5713	kWh
Annual energy consumption		
Insufficient to start	20	kWh
Excess (not used)	701	kWh
Losses		
Inverter (for Moineau)	163	kWh
Inverter (for Plunger)	153	kWh
Motor (for Moineau)	365	kWh
Motor (for Plunger)	369	kWh
Moineau pump	854	kWh
Plunger pump	200	kWh
Clark pump	330	kWh
Membranes	1446	kWh
Desalination	1113	kWh
Minimum monthly-average product flow	3.37	m^3/d
Annual-average recovery ratio	33	%
Tank concentration mean	300	mg/L
Tank concentration maximum	576	mg/L
Annual product volume	1424	m^3
Complete system capital cost	18272	£
Capital cost per daily water production	4685	£/m^3/day

Table 6-2 – Annual performance figures summary table

The data presented in Table 6-2 is that for the completed design. All other designs considered had a higher *Capital cost per daily water production* (last row).

The first row of Table 6-2 shows the annual energy available from the PV is 5713 kWh, which agrees with that shown in section 5.10.3.

The second section of Table 6-2 shows how this energy is consumed throughout the system. The 20 kWh recorded as *Insufficient to start* is the annual sum of the energy not used during the hours (typically at dawn and dusk) during which the power available from the PV is insufficient to run the RO rig. Likewise, the *Excess* recorded is the annual energy not used because the power available from the PV during some hours (typically around midday) is above the maximum that the RO rig can utilise, because pressure or flow limits are reached. The losses shown for the inverters, motors, pumps and membranes are those calculated from the component models presented in Chapter 5. And lastly, the figure shown for *Desalination* may be regarded as the useful output from the whole system; it is the theoretical minimum energy required to desalinate the predicted

volume of product water from seawater, as discussed in 2.3.1; it is calculated from the osmotic pressure of the feed and the flow of the product.

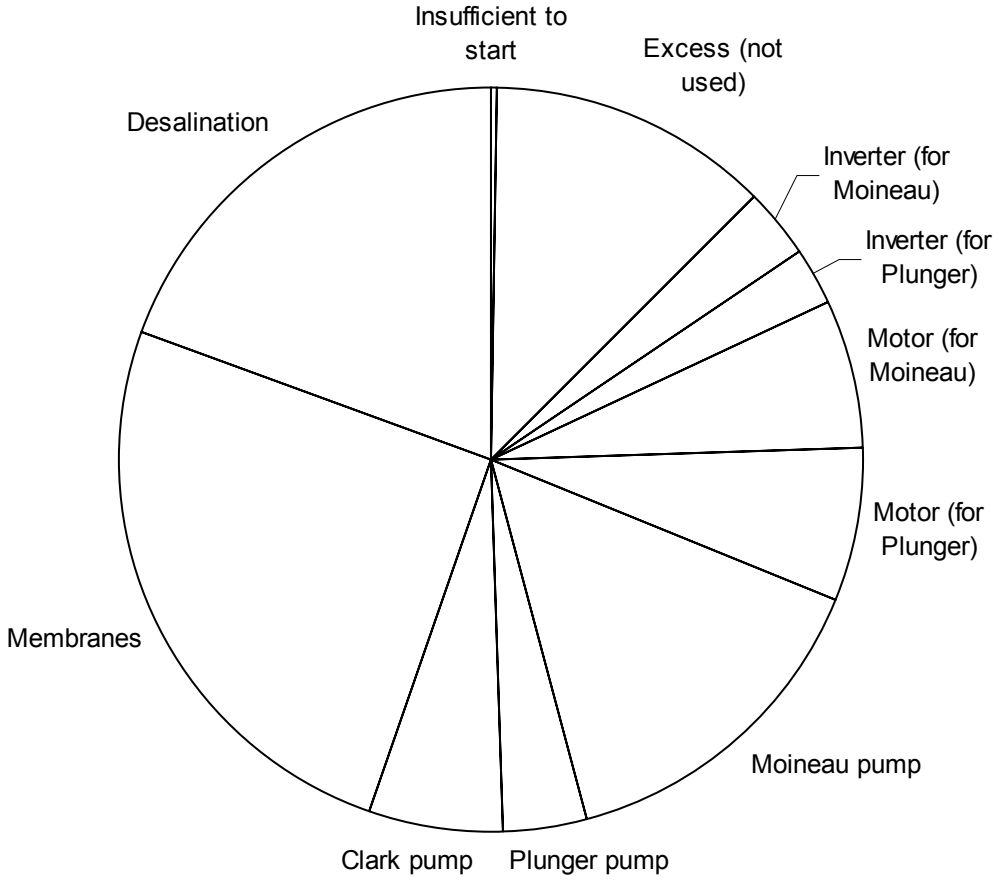

Figure 6-3 – Pie chart of annual energy consumption in the completed system design

The pie chart of Figure 6-3 illustrates the annual energy consumption data from Table 6-2 and clearly shows the proportions of the total available energy consumed in losses in the various components. Considering the data in this way gives a better view of component performance *within the system* than considering the individual component efficiencies.

Returning to Table 6-2, the next section includes: *Minimum monthly-average product flow, Annual-average recovery ratio, Tank concentration mean* and *Tank concentration maximum.* These parameters were not optimised during the design process but were checked, for each of the designs considered.

The last section of Table 6-2 shows the data that was used to optimise the system design. The *Annual product volume* is the sum of the hourly product flow data from the Simulink model discussed in section 6.1.1. The *Complete system capital cost* is calculated as

described in section 6.1.3. And lastly, the *Capital cost per daily water production* is given by: $\frac{Complete\ system\ capital\ cost}{Annual\ \ product\ volume/365}$. It was this figure that the design process sought to minimise.

6.2 Review of configuration ideas

The early designs were based on the Danfoss hydraulic motor as described in Chapter 3, but this was dropped in favour of the Clark pump, primarily because its water-to-water efficiency is substantially higher as discussed in section 3.3. Additional reasons were that its energy efficiency is maintained over a very wide range of operation, which is especially important in a batteryless PV-RO system, and that the Clark pump was designed for seawater compatibility from the outset. The configurations discussed in this chapter are all based on the Clark pump.

The Clark pump is a *high-tolerance precision machine* (Spectra 2003); its cost reflects this, and is a significant part of the final design cost, see section 6.1.3. Thus, the design process is largely a matter of building a system around a Clark pump that makes best use of that Clark pump. The Clark pump is manufactured in only one size, though it is now available with different diameter rods. The standard Clark pump has a rod-to-piston area ratio of 10 % and Spectra recommend that the feed flow should not exceed 3.5 US gallons per minute, which is 0.22 L/s.

6.2.1 Single feed pump

The simplest configuration of a Clark pump in an RO system was shown in Figure 2-11. It requires only one motorised pump, and a single 2.5-inch by 40-inch membrane element. A second similar membrane element may be added to increase water production, but given the 10 % fixed ratio and the feed flow limit mentioned above, the product flow is limited to 0.022 L/s, which is 1.9 m^3/day assuming 24-hour-a-day production. In a PV-powered system without batteries, production would typically be less than 0.6 m^3/day, assuming that the PV array is sized so that it is well utilised. A larger PV array would extend the average equivalent working day beyond 8 hours but would be under utilised around midday due to the flow limit. Referring to Table 5-9, the ratio of average irradiance to midday peak is around 0.26 for a fixed array and 0.37 for a tracking array. However, there will be reduction of pumping efficiency at dawn and dusk

and so an average equivalent of 0.33 (8 hours a the day) is a reasonable first estimate of best performance.

The sheer simplicity of the system in shown in Figure 2-11 is very attractive, but, in order to increase product flow per Clark pump and to achieve low specific energy consumption over a wide operating range, a second motorised pump is required.

6.2.2 Delayed injection – single motor

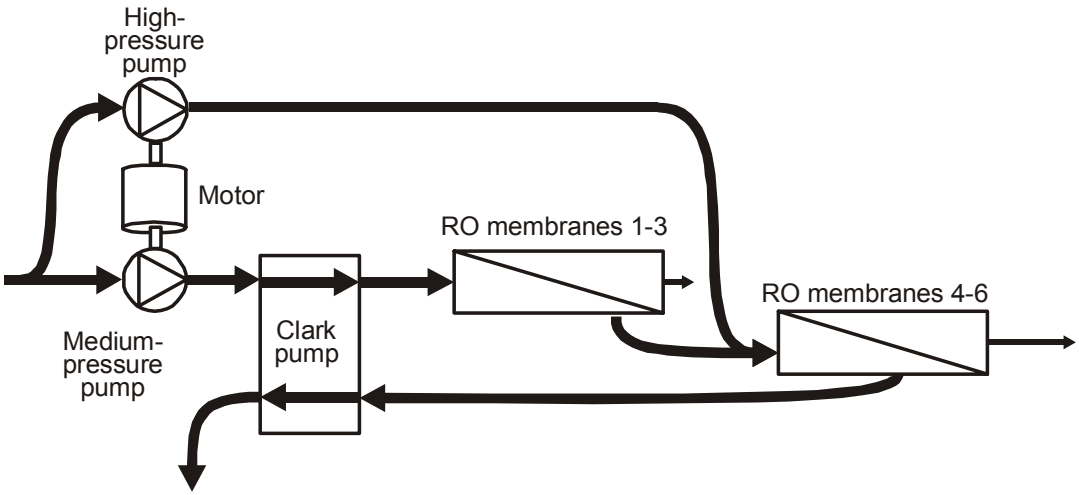

Figure 6-4 – Delayed injection – single motor

Recognising the need to increase product flow per Clark pump, Spectra proposed the configuration shown in Figure 6-4. The introduction of the second pump increases both the feed flow to the membrane array and the recovery ratio. The new recovery ratio can be adjusted by the ratio of the pump displacements, assuming they are positive-displacement pumps. The feed from the second pump in Figure 6-4 does not go to the first membrane element, but rather is delayed and injected before the fourth. The thinking here is that this reduces the build up of concentration through successive membrane elements.

The delayed injection arrangement was modelled in Simulink. The results presented here are for a system with a total of five 4” by 40” membrane elements.

	Annual product volume (m^3)	Annual average product concentration (mg/L)	Highest module recovery ratio	Lowest module concentrate flow (L/s)
Injection before 1st module	1409	308	12.8	0.22
Injection after 1st module	1408	311	16.4	0.21
Injection after 2nd module	1402	318		0.18

Table 6-3 – Delayed injection modelling results

The results shown in Table 6-3 illustrate that best overall performance, in terms of both the product volume and its concentration, is achieved with the injection before first module, that is at the beginning of the train, without any delay. The reduction of product volume and the increase of its concentration, caused by the delay of the injection until after the first module, is insignificant; but, the increase in highest module recovery ratio is not desirable, and is a direct result of the first module having reduced cross-flow. This undesirable reduction is also indicated by the reduction in lowest module concentrate flow. Delaying the injection until after the second model only worsens the situation. The concentration builds up more quickly in the first two modules, and, as far as the second three are concerned, it did not much matter whether the injected water has been through the first two modules or not. The idea of delaying the injection was dropped.

The model also showed that the fixed recovery ratio imposed by having the two pumps on the same motor was not ideal for optimising performance over a broad range. The model was modified to give each pump a separate motor. Being smaller, these two motors had lower efficiency than the previous one, but the ability to vary the recovery ratio allowed the overall efficiency, over a range of flows, to be improved.

The next alteration was to move the feed for the second pump to the outlet of the first. This gives the first pump the sole responsibility of getting water to the rig; it would allow the first pump to be a submersible borehole pump if necessary and simplifies filtering arrangements and so on.

It seems that Spectra had followed a similar course of development (Smith 2000 Figure 3).

6.2.3 Two motor – variable recovery ratio

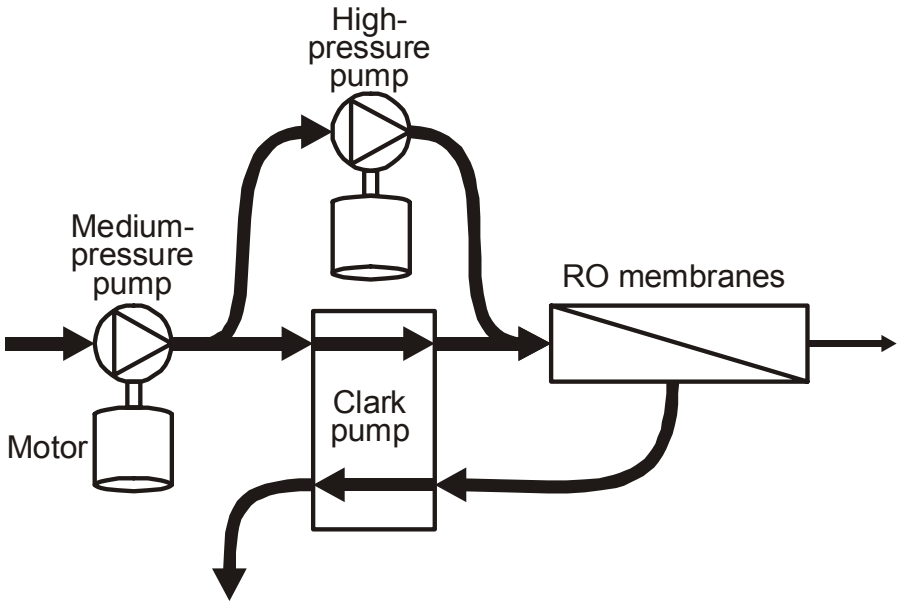

Figure 6-5 – Two motor – variable recovery ratio

A system using two variable-speed motors is shown in Figure 6-5, and this is the general arrangement finally adopted for the PV-RO system. The independent control of the two pump speeds provides control over the water recovery ratio, and this is especially valuable in a batteryless PV-RO system because it enables the water production to be maximised as the available sunlight varies through the day. The next step was to determine how the recovery ratio should be varied in order to achieve this maximum.

To investigate this, the Simulink model was programmed to step through a 3-D array of permutations of speeds, for the two pumps, and of feed-water temperatures. Sorting the results according to the product flow for a given electrical input power revealed that the recovery ratio should be varied as shown in Figure 6-6.

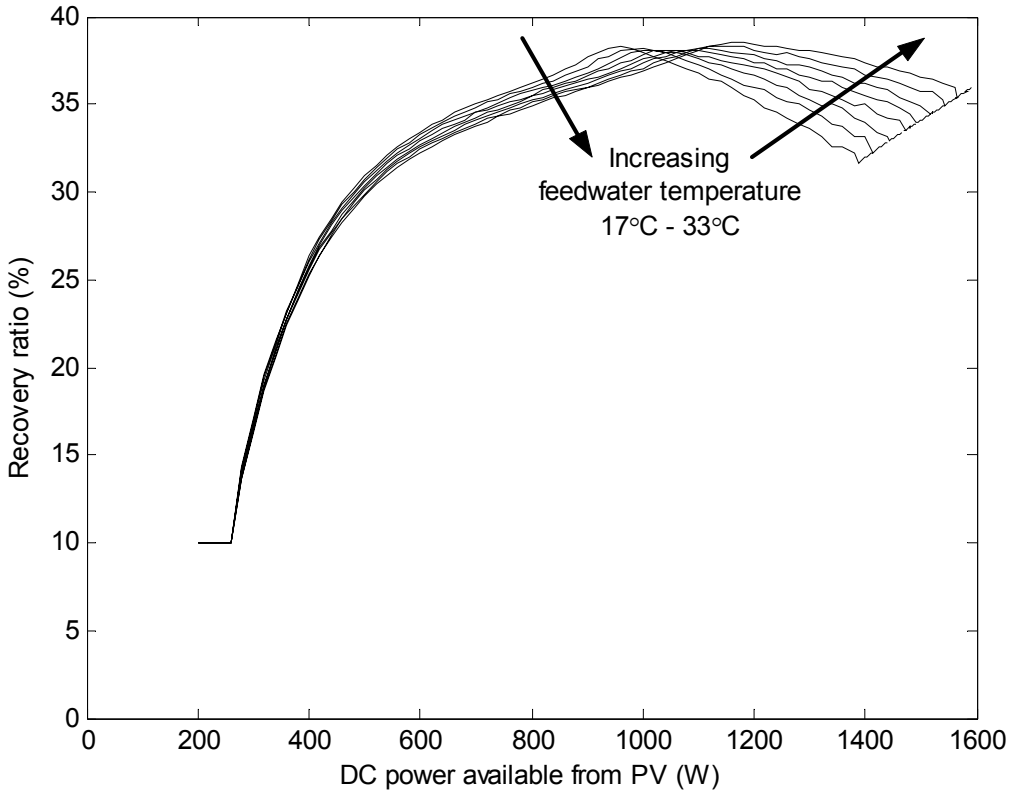

Figure 6-6 – Optimum recovery ratio versus DC power available from PV

Figure 6-6 shows how the water recovery ratio must be varied, in order to maximise the product water flow as the available power varies. When the available power is low, 200-300 Watts, the system operates with a low recovery ratio: 10 %. This is achieved by the running only the medium-pressure pump. As the available power increases, the high-pressure pump is started and its speed ratio, against that of the medium-pressure pump, is increased. The optimum recovery ratio also depends on feed-water temperature, as illustrated towards the right of Figure 6-6. Variation of feed-water concentration and membrane condition will have a similar effect.

6.2.4 Solar-thermal feed-water pre-heating

The final PV-RO design presented in this thesis does not include pre-heating of the feed water, but it was considered, as follows.

It is well known that the product flow of an RO system increases with an increase of feed water temperature (Byrne 1995 page 12). The product concentration also increases, but, if this can be tolerated, then pre-heating of the feed water can be useful. Indeed, pre-heating is a recognised technique in RO systems on boats, where waste heat from the

main engine may be used. With this in mind, the potential benefit of solar pre-heating of the feed water in a PV-RO system was considered. It was quickly apparent that a very large area solar collector would be required to significantly raise the temperature of the feed water. For example, to raise the temperature of 0.5 L/s of seawater from 15 °C to 35 °C requires:

$$0.5 \text{ L/s} \times 20 \text{ °C} \times 4.0 \text{ kJ/L°C} = 40 \text{ kW}$$

The 4.0 kJ/L°C is the specific heat of typical seawater (35,840 mg/L, 35,000 ppm) around 25 ºC (El-Dessouky et al. 2002 page 529).

To address this, a system of heat exchangers to recover heat from the concentrate and product flows was drafted and modelled.

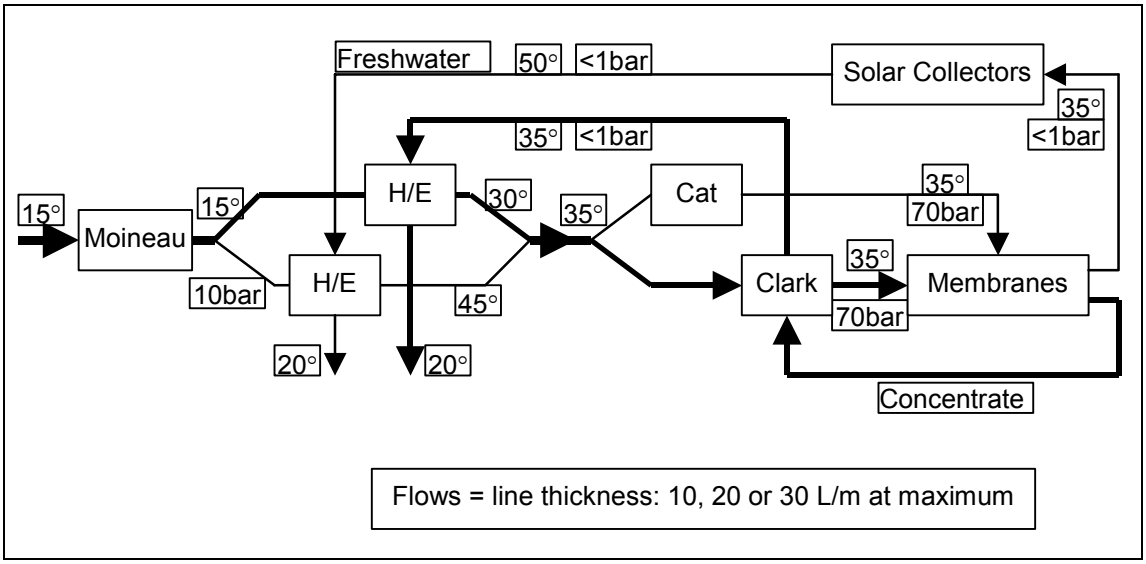

Figure 6-7 – A solar-thermal pre-heating configuration that was considered

In the absence of a brine-stream energy recovery mechanism, the model indicated that the quantity of product water would be increased by around 60 % by pre-heating the feed water from 15 °C to 35 °C. This suggested that the cost and additional complexity of the solar-water heater and heat exchangers would be justified. However, the improved efficiency occurs because the recovery ratio is increased and so less energy is wasted in the brine-stream. Once brine-stream energy recovery in the shape of the Clark pump was added to the model, the effect of feed water temperature was very much reduced, and it

became obvious that pre-heating of the feed water was much less significant. The effect of feed water temperature within the completed system design is shown in Figure 6-11.

6.3 RO and PV array sizing

Having selected the general arrangement shown in Figure 6-5, pumps and motors were chosen as described in sections 5.3 through 5.7. The remaining task was to adjust the sizes of the RO and PV arrays to minimise the cost of water.

6.3.1 RO array sizing

When designing an RO system that will operate on mains electricity or diesel power there is a tendency to specify the smallest number of membrane elements that will provide the required product flow. This keeps capital costs down but also leads to the specific energy (kWh/m^3) and hence energy costs being higher than they could be. Systems designed with energy efficiency in mind will usually have a greater number of membrane elements, because increasing the membrane area reduces the required driving pressure and therefore the energy consumption. When sizing an RO array intended to be PV-powered, the optimum size is larger still, because of the dominant effect of the PV array cost.

The Simulink model of the complete PV-RO system was used to predict the performance of systems with varying sizes of RO array. Starting with six 2½-inch by 40-inch membrane elements, the model showed that adding elements consistently reduced the *Capital cost per daily water production*, at least as far as eleven elements total. At this point it was clear that 4-inch by 40-inch membrane elements should be considered.

Number of 4” by 40” membrane elements	Annual product volume (m^3)	Complete system capital cost (£)	Capital cost per daily water production (£/m3/day)	Annual average product concentration (mg/L)
3	1189	17,573	5,397	250
4	1424	18,272	4,685	300
5	1482	18,971	4,673	376

Table 6-4 – RO array size modelling results

Table 6-4 shows that the *Capital cost per daily water production* is considerably lower with four 4-inch by 40-inch membrane elements than with three; the reduction is around 13 %. Whereas adding a fifth element gives almost no further improvement: ~ 0.25 %.

Table 6-4 also shows that adding membrane elements has a significant effect in increasing the concentration of the product water. This was not an overriding concern at the time because in-house membrane testing had always shown very good product quality in relation to the requirements discussed in section 2.1.3. Nonetheless, it clearly outweighed the minor cost reduction and an array of four 4-inch by 40-inch membrane elements was adopted for the design. It is roughly twice the size that would normally be selected to give the same maximum water production, in a petrol-powered or grid connected RO system.

6.3.2 PV array sizing

The required size of the PV array is obviously very dependent on solar irradiance at the site of installation. The data for Massawa, Eritrea, discussed in section 5.8, was taken as a specific example and the Simulink model was used to determine the size of PV array that would minimise the *Capital cost per daily water production*.

Number of 120-W_p PV modules	Annual product volume (m^3)	Complete system capital cost (£)	Capital cost per daily water production (£/m3/day)	Annual average product concentration (mg/L)
16	1275	16,796	4807	329
17	1322	17,165	4737	319
18	1362	17,534	4699	310
19	1396	17,903	4682	305
20	1424	18,272	4685	300
21	1447	18,641	4704	295
22	1466	19,010	4732	291
23	1484	19,379	4767	289
24	1499	19,748	4810	286

Table 6-5 – PV array size modelling results

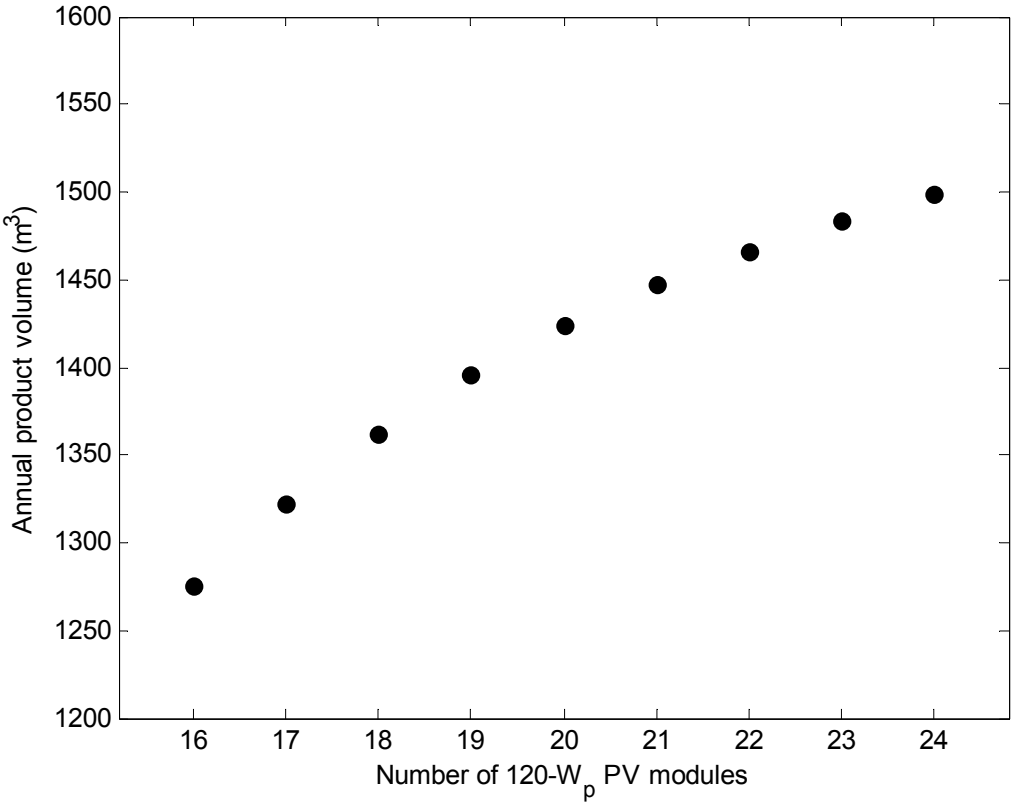

Figure 6-8 – Annual water production versus PV array size

Figure 6-8 shows, as expected, that increasing the PV array size increases the annual water production, but the curvature indicates a diminishing return.

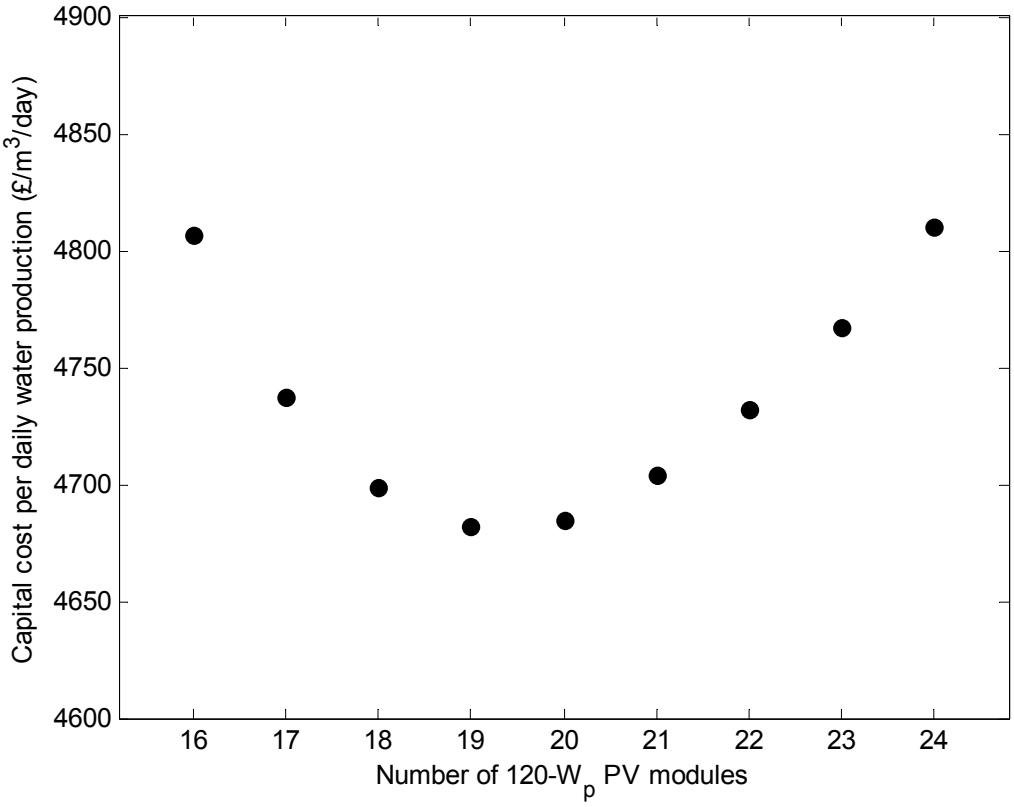

Figure 6-9 – Capital cost per daily water production versus PV array size

Figure 6-9 shows that the *Capital cost per daily water production* is minimised with an array of nineteen 120-W_p PV modules. The vertical scale is chosen to exaggerate the curve; the cost penalty for having a slightly under- or over-sized PV is actually very small. In particular the array of twenty modules chosen for the final design increases the *Capital cost per daily water production* by less than 0.1 %.

Having twenty modules, rather than nineteen, facilitates mounting, particularly when solar-trajectory tracking is employed. Also, it would allow modules to be configured in parallel strings, although, if standard industrial drives are to be employed, it is more likely that all modules would be in series; see the discussion on drive voltage requirements in section 5.5.

Even with the impressive efficiency improvements made by the Clark pump and throughout the RO system, the PV array remains the largest single cost in the PV-RO system, as shown in Table 6-8. It represents roughly one third of the total capital cost. It will, however, offset all fuel costs for the whole life of the equipment.

6.3.3 Life-cycle costing

The calculations just described, considered only the capital costs of the components. If full life-cycle costing were employed it is possible that the membrane area would be reduced slightly, but since the membrane life in an intermittently-operated system is unknown, section 2.9.3, accurate life-cycle costing is not possible.

6.4 Completed design

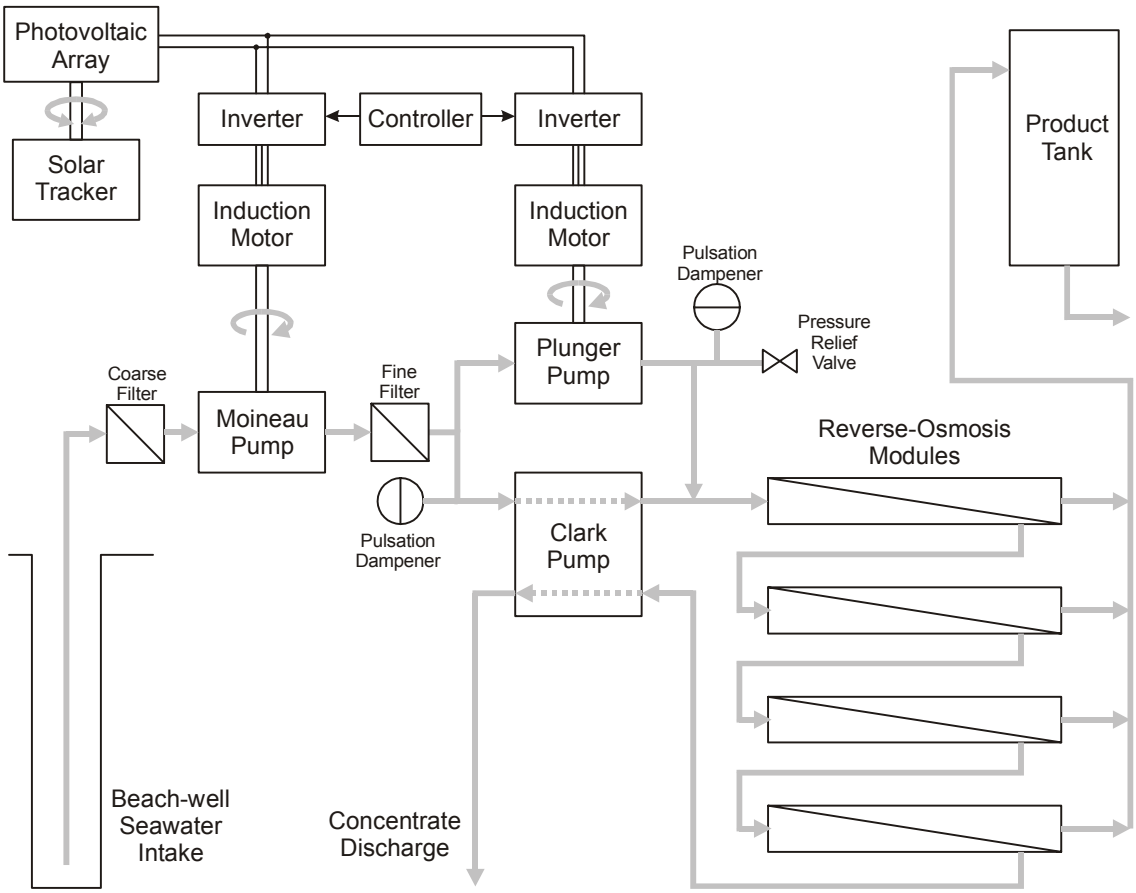

Figure 6-10 – Completed design

Photovoltaic array	2.4 kW_p, twenty AstroPower AP-1206 modules, with single-axis solar-trajectory tracking
Moineau pump	Netzsch NM021SY02S12B in 316 stainless steel Nominal 1.2 m^3/h at 900 rpm, 10 bar
Plunger pump	CAT 237 in nickel aluminium bronze Nominal 8.7 L/min at 1725 rpm, 105 bar (used up to 69)
Motors (both)	1.5-kW 6-pole high-efficiency induction motors, Siemens 1LA9 106-6KA10 or Toshiba B0026FLF2AYH
Inverters	1.5-kW standard industrial drives FID1000 FKI-12150
Reverse osmosis modules	Four 4” by 40” seawater RO membrane elements Koch TFC1820HF with 69-bar (1000-psi) pressure vessels
Clark pump	Spectra Watermakers
Product tank	> 6 m^3

Table 6-6 – Major parts list for completed design

6.5 Performance predictions

The performance of a PV-RO system is greatly affected by:

- the solar irradiance,
- the concentration of the seawater feed,
- the temperature of the seawater feed and
- the ambient temperature.

The correlation of the above factors is also important, particularly between the seawater temperature and the solar irradiance.

The site at Massawa, Eritrea was used to provide data for the following performance predictions. Hour-by-hour solar irradiance and ambient temperature data was derived from Meteonorm, as discussed in sections 5.8 and 5.9. The seawater was represented by straight NaCl solution at 35,000 mg/L, which is isosmotic with seawater at around 38,000 mg/L. This is significantly higher than typical seawater ~35,700 mg/L, but is still short of that measured at a seawater well in Massawa: 40,150 mg/L. An annual temperature profile for the Red Sea was used, showing a summer maximum of over 33 °C and a winter minimum of around 17 °C, as discussed in section 5.12.

6.5.1 Product water flow

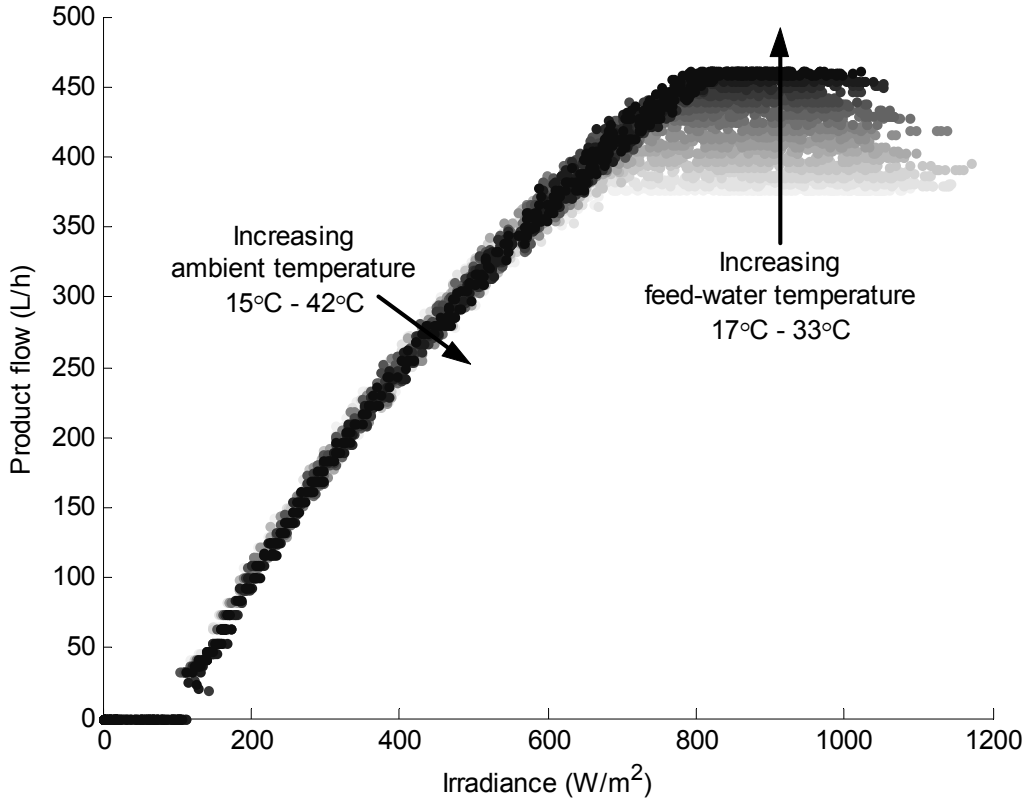

Figure 6-11 – Predicted product water flow versus irradiance

Figure 6-11 illustrates that the hourly product flow is broadly proportional to irradiance over a wide working range. According to the model, production starts at around 100 W/m^2 and increases steadily up to around 800 W/m^2. Above 800 W/m^2, production is limited by the pressure and flow limits of the Clark pump. The two temperature effects are also indicated in Figure 6-11. In the linear region, between 100 W/m^2 and 800 W/m^2, the ambient temperature has a significant effect on the power available from the PV, as discussed in section 5.10.3.3, and this causes the scatter in the data. In the region limited by pressure and flow, the feed-water temperature has the dominant effect. The data in Figure 6-11 is shaded according to feed-water temperature.

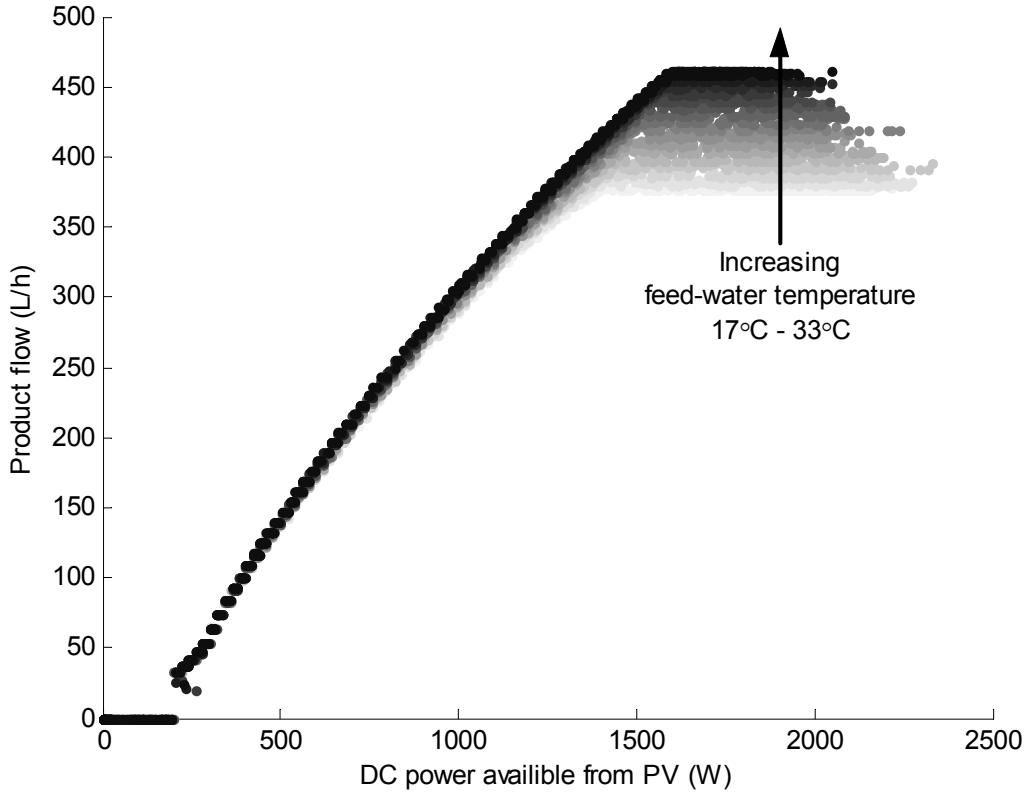

Figure 6-12 – Predicted product water flow versus DC power available from the PV

As discussed in section 5.10.3.2, the electrical power available from the PV is roughly proportional to irradiance, but decreases significantly as the ambient temperature increases. Thus, Figure 6-12 is similar to Figure 6-11 but with the scatter caused by the variation of ambient temperature removed.

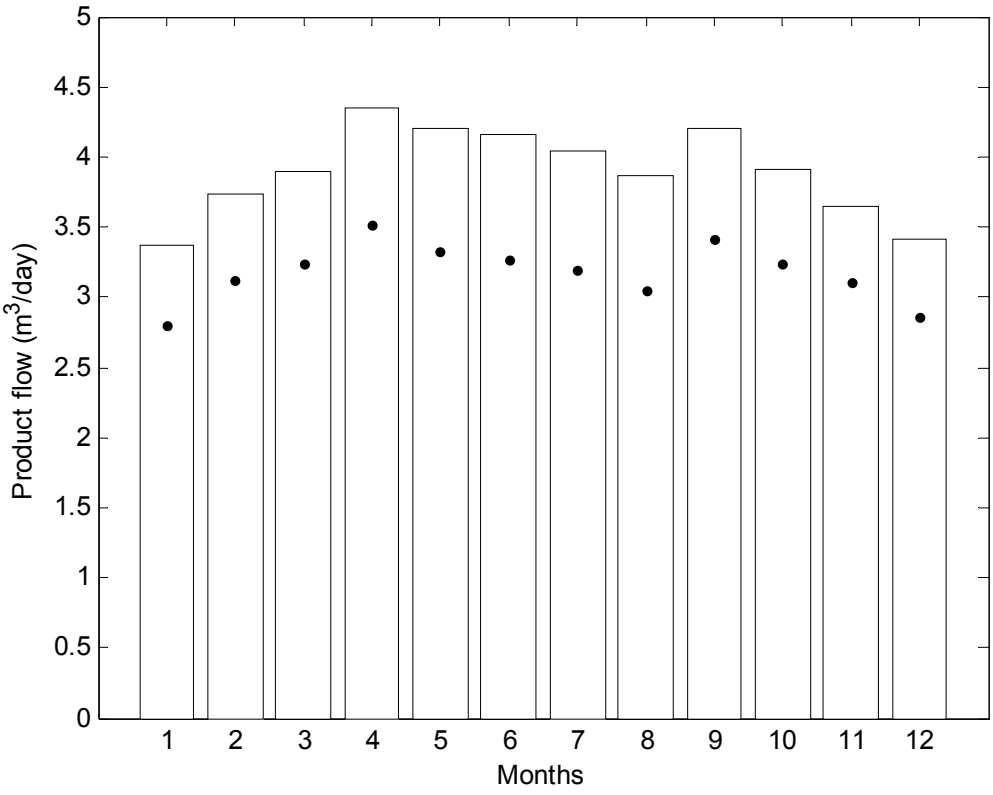

Figure 6-13 – Predicted product water flow – Monthly averages

The total annual predicted water production is 1424 m^3, which is an annual average of just over 3.9 m^3/day. The main bars in Figure 6-13 show how this is distributed though the year. The increase in the summer is due to the increase in seawater feed temperature, not solar resource.

The dots shown in Figure 6-13 are the results predicted with a *fixed* PV array; that is *without* the single-axis solar-trajectory tracking discussed in section 5.8.1 and which has been assumed throughout the design. The model was also run with dual-axis tracking and the results are presented in Table 6-7.

	Fixed	Single-axis	Dual-axis
Annual product volume (m^3)	1160	1424	1434
Percentage gain		23%	< 1%

Table 6-7 – Predicted annual product volume for a fixed PV array and for single-axis and dual-axis solar-trajectory tracking arrays

The annual water production shown in Table 6-7 is slightly less affected by the tracking arrangement than is the annual average global irradiance shown in Table 5-9. Nonetheless, the selection of single-axis tracking is confirmed.

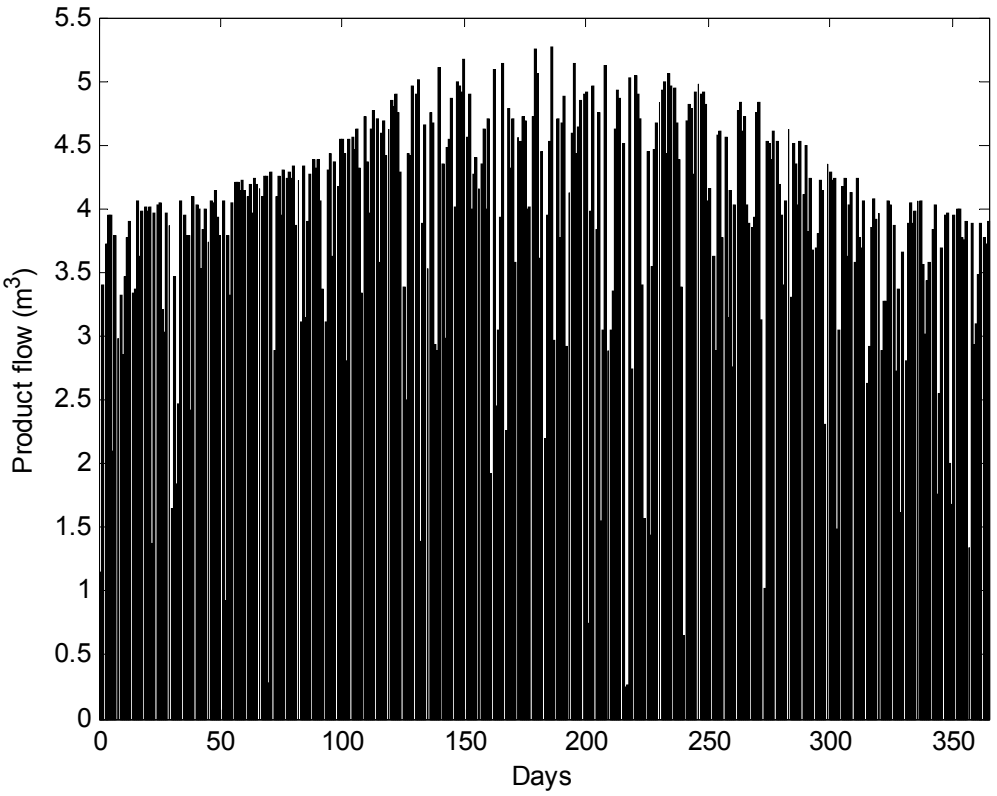

Figure 6-14 – Predicted product water flow – Daily totals

Figure 6-14 shows the same data, on a daily basis. There are occasional cloudy days on which very little water is desalinated and in order to meet a continuous demand, a generous product tank is required. By adjustment of the modelled tank capacity, shown in section 5.14, the simulations showed that a tank of at least 6 m^3 is required. In practice, it would be prudent to have a significantly larger tank to allow for even more erratic weather conditions, unplanned system downtime and variability in consumption.

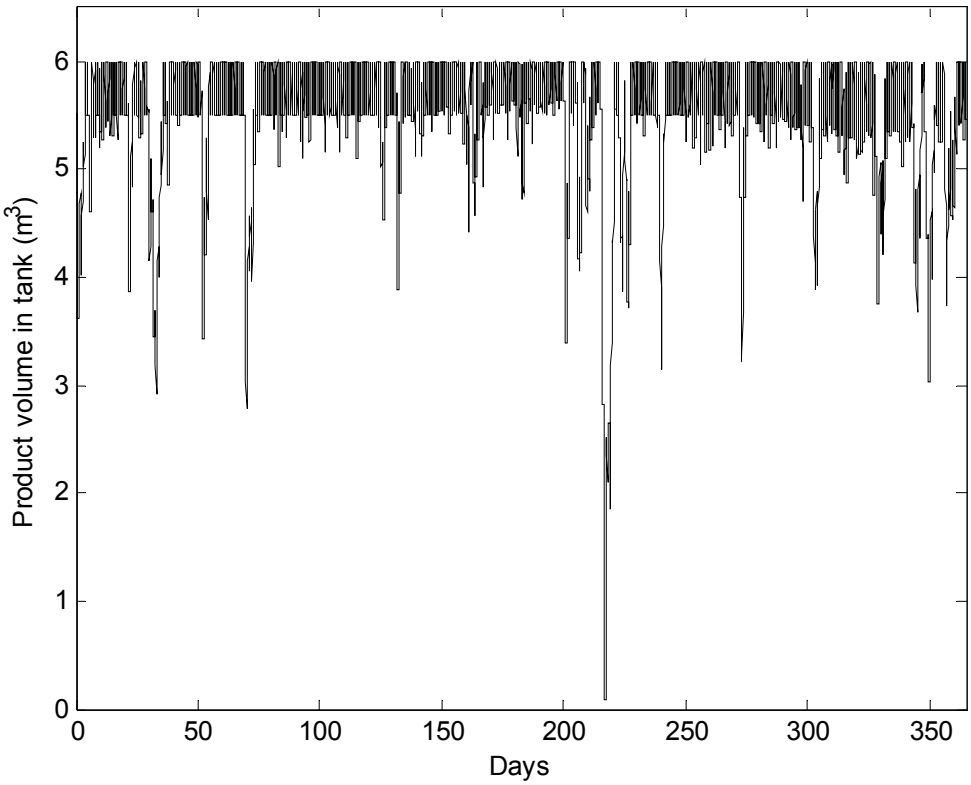

Figure 6-15 – Predicted volume in product water tank

Figure 6-15 predicts the volume of water in a product tank of 6 m^3, assuming that consumption is a constant 3.0 m^3/day. In practice, consumption is likely to be seasonal and could be influenced by the level in the tank.

6.5.2 Product water quality

At full power, the predicted product water concentration is in the range 170 to 330 mg/L, depending on the feed water temperature. As the available power reduces, the concentration of the product water is greatly increased, but, at the same time, the product flow is reduced. This small volume of poor-quality water will have little effect on the overall quality of water in a product storage tank.

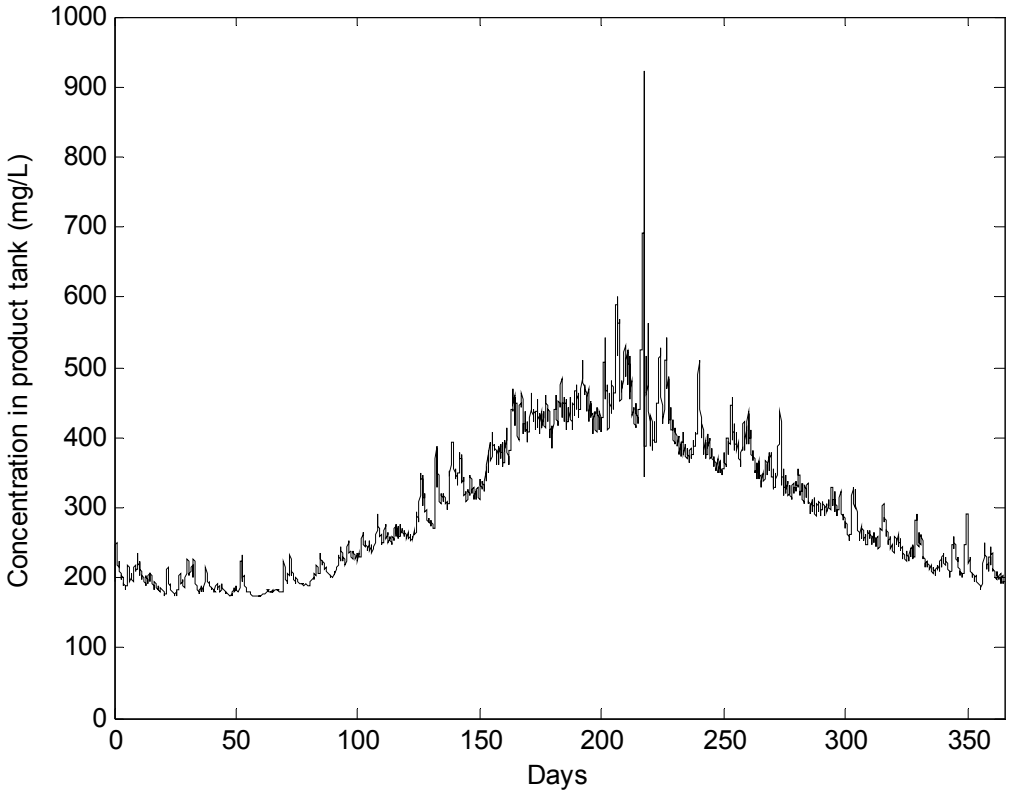

Figure 6-16 – Predicted salt concentration in product water tank

Figure 6-16 shows the predicted salt concentration in the same 6 m^3 product water tank and with the same constant 3.0 m^3/day consumption. This graph assumes that all of the product water is directed into the tank (no concentration-controlled diverter valve is included). It shows that the predicted quality of the water in the product tank is generally good, except after two consecutive cloudy days in August. The concentration of the product water can be expected to rise slightly as the membranes age. There are various straightforward techniques that could be used to limit the concentration in the product water tank, should this prove necessary as discussed in section 10.6.

6.5.3 Predicted energy flows – Sankey diagram

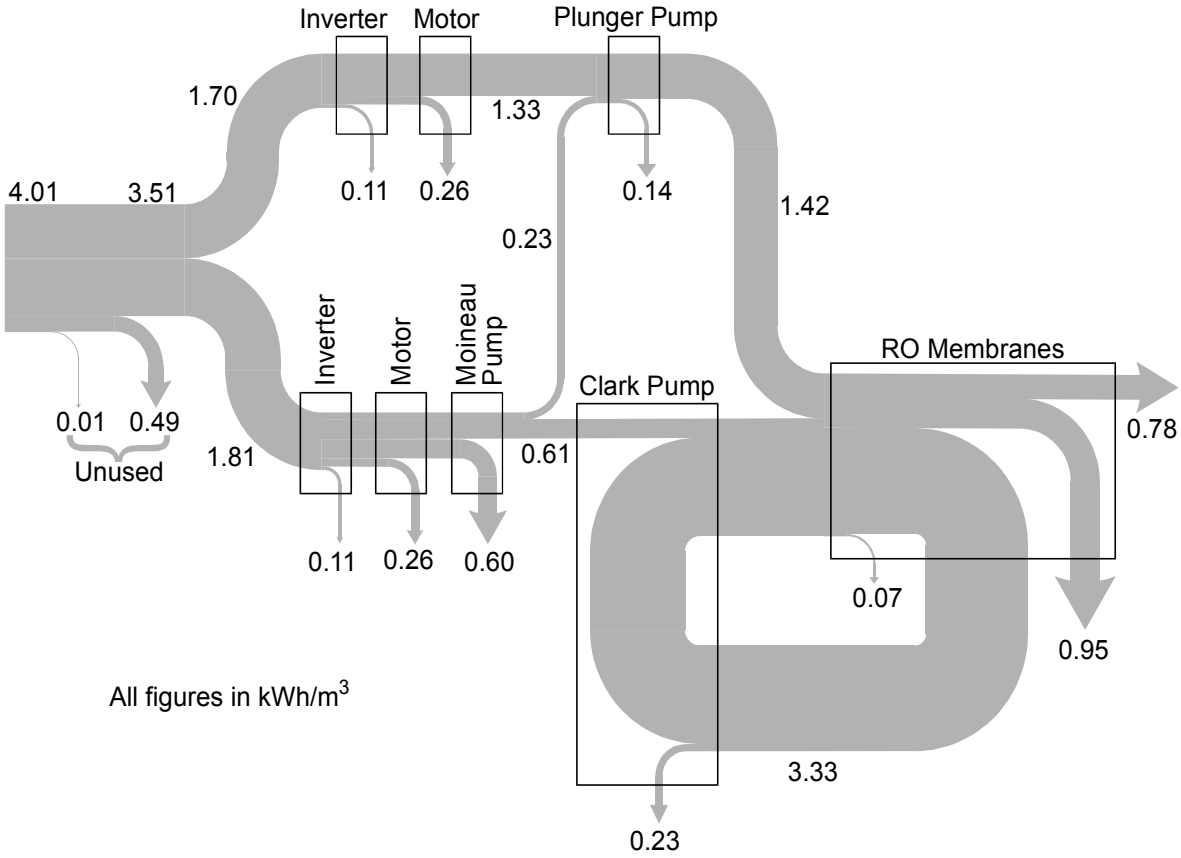

Figure 6-17 – Predicted energy flows – Sankey diagram

The numbers and line widths shown in Figure 6-17 represent the annual-average energy flow in kWh per m^3 of product water. These figures can readily be converted to annual kWh simply by multiplying by 1424 m^3, which is the predicted annual product volume.

Starting on the left, 4.01 kWh/m^3 (5710 kWh) is available from the PV array.

A tiny proportion of this, 0.01 kWh/m^3, is unused, representing the rare occasions when there is insufficient power available to start the rig.

Next, a further 0.49 kWh/m^3 is unused, representing the times when there is an excess of power available: the rig is operating at its maximum flow and pressure. A reduction in the size of the PV array would reduce this figure and so improve the annual-average energy efficiency; however, as already noted, the PV array size is chosen to minimise the overall cost of the water, which is a slightly different goal.

Neither of the above *unused* powers are necessarily *losses,* since they represent electrical power that is available for other purposes, such as battery charging for lighting.

Thus, the 3.51 kWh/m^3 may be regarded as the total electrical specific energy consumption for the desalination system.

Next, it can be seen that the inverter and motor efficiencies are good, particularly considering that these relate to very small induction motors, each delivering around 500 W on average.

The plunger pump is also very efficient. The additional 0.23 kWh/m^3 that feeds the plunger pump represents the work done by the Moineau pump in raising the feed water to medium pressure.

The Moineau pump itself is less efficient. Its selection is discussed in section 5.4.

Two losses are shown in relation to the RO membranes themselves. First, the 0.07 kWh/m^3 represents the slight pressure drop found between the feed and the concentrate flows. This includes pressure drops in the interconnecting pipe work. Second, the 0.95 kWh/m^3 represents the viscous losses associated with driving the product water through the membrane.

The 0.78 kWh/m^3, on the far right of the diagram, represents the actual desalination.

The massive 3.33 kWh/m^3, also emanating from the membranes, represents the energy contained in the pressurised concentrate water.

The Clark pump recovers this energy and delivers it directly back into the feed flow. It achieves an annual average of 93 % efficiency, which is excellent.

6.5.4 Power usage – average day

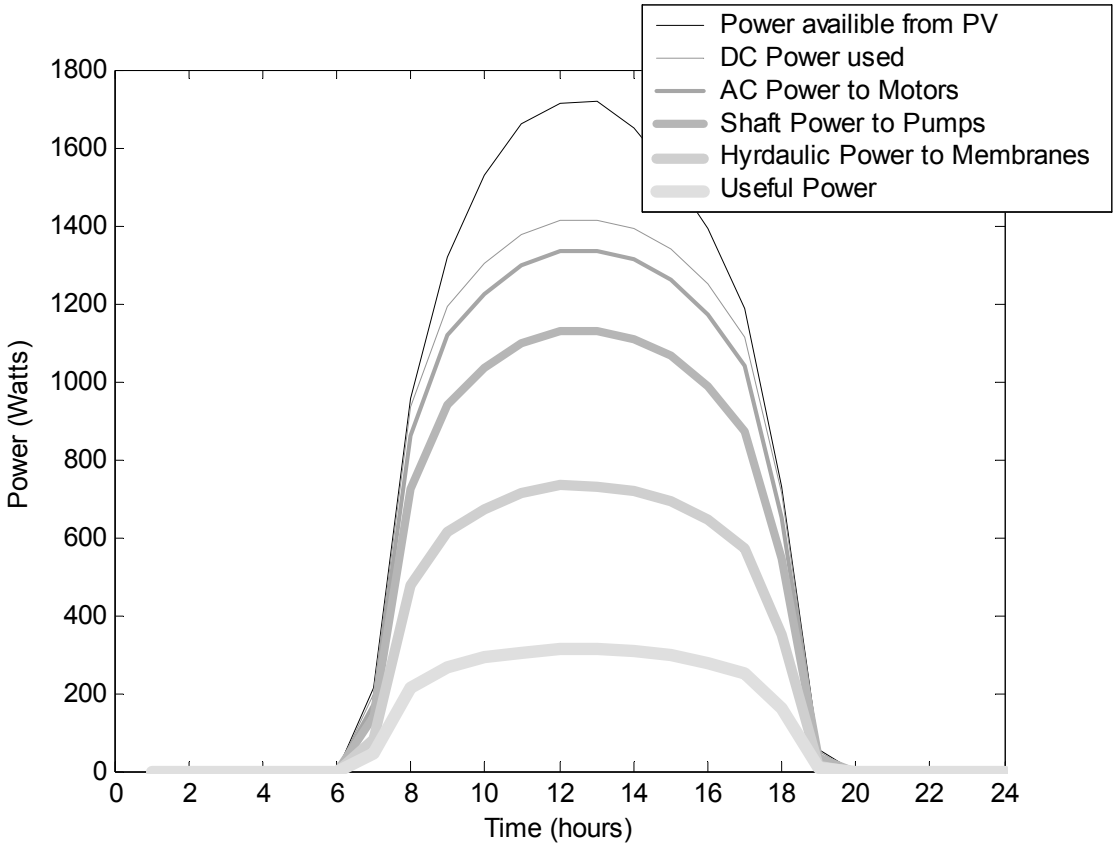

Figure 6-18 – Predicted analysis of power usage over an average day

Figure 6-18 illustrates how the power available from the PV array is used throughout an average day. The average is created from hourly values across the whole year.

As discussed under Figure 6-17, a proportion of the power available from the PV is unused: either it is insufficient to start the rig or it is in excess because the rig is operating at its maximum flow and pressure. Thus, the *DC Power used* in Figure 6-18 is significantly below that available. The *AC Power to Motors* is the sum of that going to the two motors and is below the *DC Power used* because of losses in the two inverters. Likewise, the *Shaft Power to Pumps* is the sum for the two motor-driven pumps, and is below the *AC Power to Motors* because of the losses in the two motors. The difference between the *Shaft Power to Pumps* and the *Hydraulic Power to Membranes* is due to losses in all three pumps: Moineau, plunger and Clark. Lastly, the *Useful Power* represents the actual desalination calculated from the osmotic pressure and the product flow. The difference between the *Hydraulic Power to Membranes* and the *Useful Power* is due to the losses in the membranes themselves.

6.5.5 Specific energy

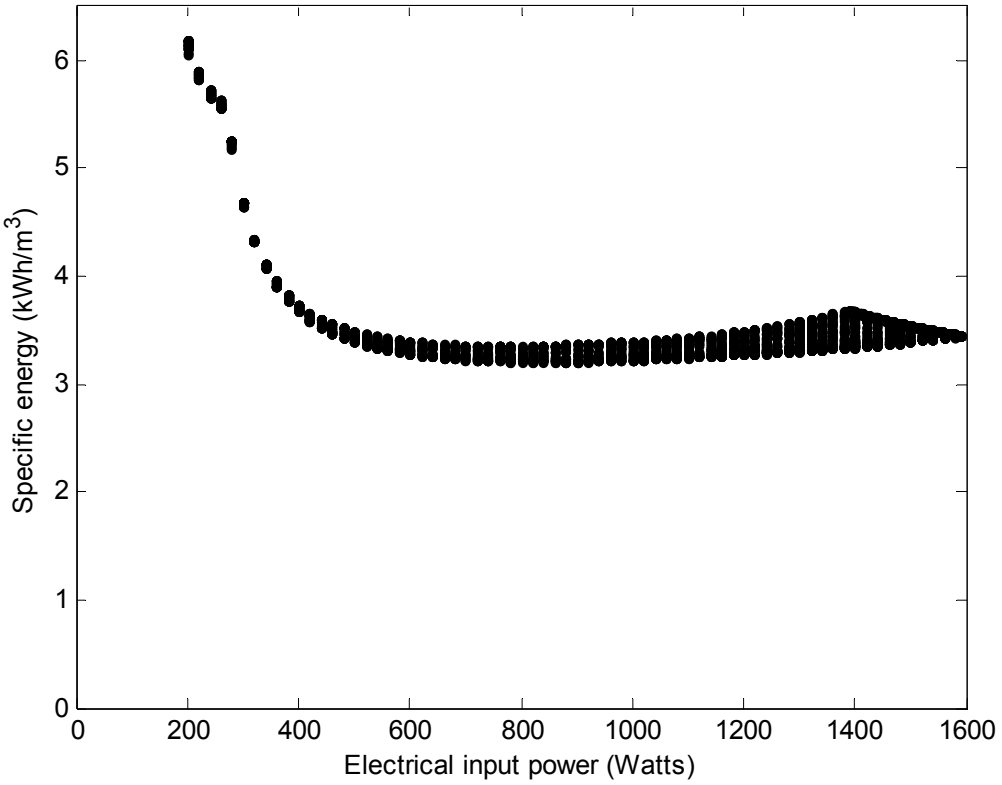

Figure 6-19 – Predicted specific energy vs. electrical input power

Figure 6-19 shows that the specific energy consumption is typically between 3.2 and 3.7 kWh/m^3. Moreover, it is near constant except under very low-power operation. Thus, the flow of product water is virtually proportional to the power available from the PV array over a very wide range.

These predictions are very impressive when compared to traditional reverse osmosis systems. The credit for this goes firstly to the Clark pump but also to the selection of all the other system components and the recovery ratio control strategy, discussed in section 6.2.3.

The slight spread of specific energy values for a given electrical input power (apparent in Figure 6-19) is due to the variation in feed seawater temperature (17 to 33 °C). This variation in specific energy is actually very small, again due primarily to the Clark pump.

6.6 Manufacturer's cost analysis

A full cost analysis of the completed design was conducted by Dulas Limited (Gwillim 2001). A summary was made public in a joint report (Thomson et al. 2001) and is repeated below.

Item	**Cost**
Photovoltaic (PV) Array	£ 7,319
Reverse osmosis elements and pressure vessels	£ 2,796
Pumps (all three)	£ 2,290
Motors and Inverters	£ 806
Miscellaneous	£ 2,537
Total Components and Materials	**£15,748**
Manufacturer's mark-up on Components and Materials	£ 3,150
Manufacturer's Labour at cost including overheads	£ 2,906
Mark-up on Labour	£ 872
Total	**£23,055**

Table 6-8 – Capital cost Dulas estimates summary table

The costs shown in Table 6-8 may be compared against those used in the modelling presented earlier in Table 6-1. The costs are very similar, except for the *miscellaneous* category: Table 6-1 showed £5000, while the sum of miscellaneous and manufacturing in Table 6-8 is £9465. This largely accounts for the difference between the modelled *Complete system capital cost*: £18,272 and final estimate: £23,055, stated in the abstract and introductory chapter.

In order to estimate the cost of water over the lifetime of the equipment, Dulas assumed a 20-year life for the system as a whole, with pump replacements at 5, 10 and 15 years. They also assumed that a complete new set of RO membrane elements would be required every 12 months. The estimated overall cost of water, including full maintenance and using an 8% discount rate, was £2.00 per m^3. This figure will reduce significantly if longer membrane lifetimes prove possible in practice.

A fuller discussion of these cost estimates was presented in the joint report (Thomson et al. 2001) and is repeated for convenience in Appendix E.

Chapter 7 New test rig hardware

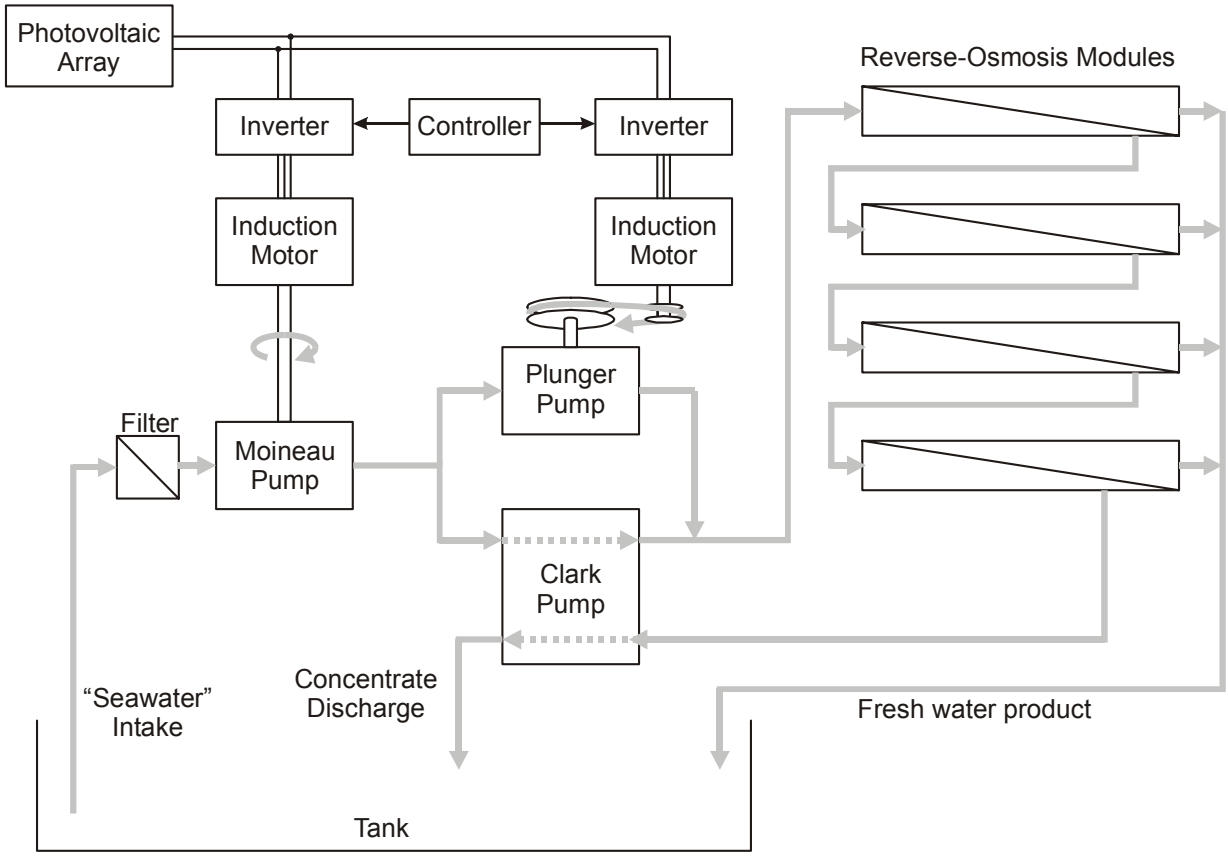

Figure 7-1 – Test rig configuration

The test rig described in Chapter 3 was inflexible and not suited to accommodating the new design presented in section 6.4. A new test rig was constructed during 2002, with much assistance from Marcos Miranda. The arrangement is shown in Figure 7-1, and is very similar to the design, except for the following details.

A tank holds the "seawater", which is actually straight NaCl solution. Both concentrate and product water are fed directly back into the tank so as to maintain the feed concentration during extended testing and the tank is continuously stirred to ensure that concentration is even. Despite this, the feed concentration does vary due to the variation of concentration of water held within the RO modules, which is affected by the recovery ratio. The new test rig has four 4-inch by 40-inch membrane elements, and these hold a

significant volume of water compared to the tank. (The volume of four 4-inch by 40-inch pressure vessels is 33 L; the tank held 75 L.)

The tank is fitted with a heating and cooling system, as discussed in section 4.13, to ensure that the temperature of the feed water to the reverse-osmosis membranes is held constant: 25 °C throughout the tests presented here.

The plunger pump is the CAT 317, taken from the earlier test rig. It is rather larger than the 237 called for in the design, and therefore, it revolves rather slowly at the required flow. The motor is a 4-pole induction machine, again left over from the earlier test rig, and would be very inefficient at such low speeds. So, the test rig employs pulleys and a toothed rubber belt to allow the motor to run faster. Ideally (as in the design), a smaller plunger pump would be used, directly connected to a 6-pole induction motor.

The PV array used for testing was the BP Saturn array on the CREST building at Loughborough. It is a fixed array (no tracker) comprising thirty-two 85 W_{peak} BP Solar Saturn BP585F mono-crystalline silicon modules, but only eighteen were used, as discussed in Chapter 9.

The *Controller* shown in Figure 7-1 was implemented in LabVIEW, alongside the data acquisition system. It provides the speed setpoint signals for the two inverters, and the development of the control algorithms is described in the next two chapters.

Chapter 8 Recovery-ratio control algorithm

The requirement to operate the batteryless PV-RO system with a variable recovery ratio so as to maximise the water production was discussed in section 6.2.3, and is to be achieved through the control of the two pump speeds. The *Controller*, shown in the completed design Figure 6-10, provides speed setpoints to the two inverters connected to the two pump motors.

Likewise, in the new test rig Figure 7-1, the controller provides the speed setpoint signals. The controller for the test rig was implemented in LabVIEW, alongside the data acquisition system, and this chapter describes the design of the recovery ratio control algorithm.

The design of the algorithm was based on measurements taken from the test rig while using mains electricity. These measurements characterised the system in terms of product flow in response to the two speed setpoints.

8.1 System characterisation

Using mains electricity for the test (unlimited power supply), the two pumps can be run at any speed from zero up to their respective maximums. However, the other system components impose limits as indicated in Figure 8-1. The pressure limit is 69 bar (1000 psi) and is imposed primarily by the rating of the pressure vessels that house the RO membranes. The Clark pump flow limit is 795 L/h (3.5 USgal/m). We will see later that these limits are rarely encountered if the system is operated for best efficiency. LabVIEW was employed to implement a test procedure that stepped through allowable combinations of the two pump speed setpoints, whilst respecting the pressure and flow limits. Operation at each test condition was maintained until the key system variables had stabilised. The steady-state results were then logged and the test moved to the next point.

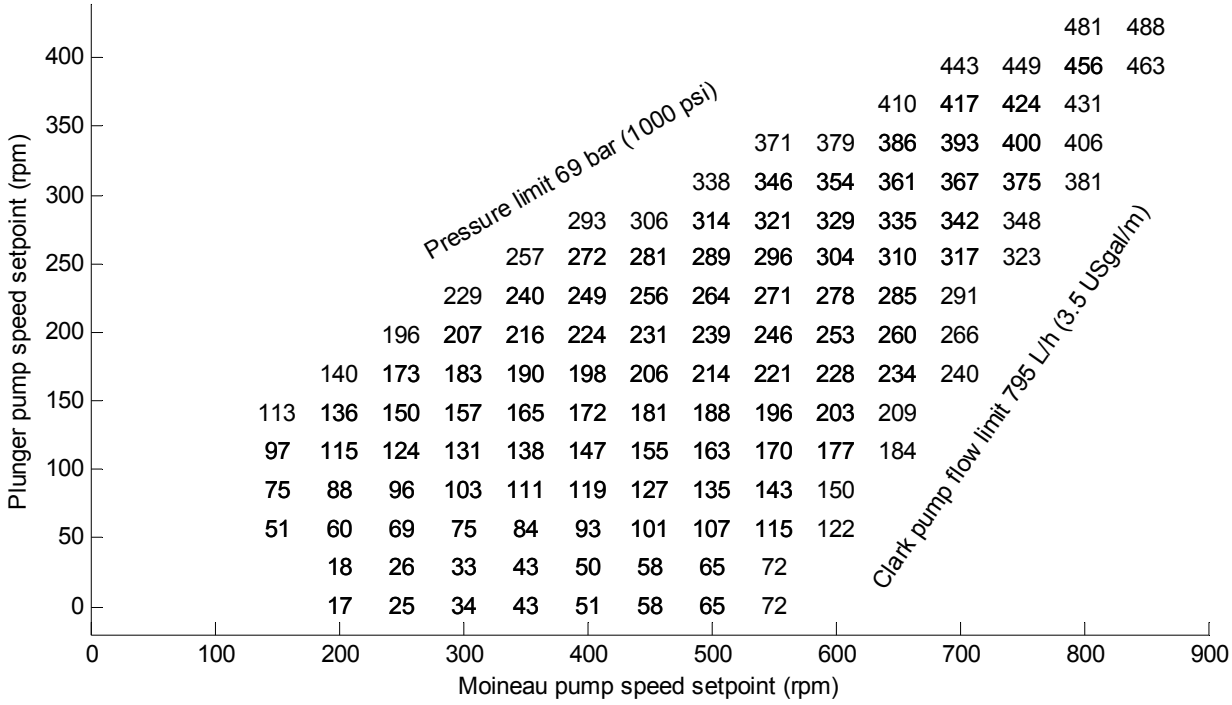

Figure 8-1 – Measured product flow (L/h) against pump speed setpoints

Inspection of Figure 8-1 confirms that increasing the speed setpoint of either pump increases the product water flow. Note that these are the speed *setpoints*, not the actual speeds, which will be lower due to slip in the induction motors. In particular, this accounts for the second row up, where the plunger pump speed setpoint is 28 rpm but the motor is stalled. It is perfectly possible to start the motor at this speed by introducing a *voltage boost* in the inverter settings; however, this can reduce efficiency and may or may not provide an overall benefit, as discussed in section 5.7.2.

8.2 Control strategy

Figure 8-1 shows that the maximum water production is around 488 L/h, and that the system can be operated over a wide range of pump speeds. But, Figure 8-1 does not provide any obvious means of optimising the two pump speeds to maximise the water production with respect to the power consumed. With this in mind, it is interesting to look at the specific energy consumptions (kWh/m^3) shown in Figure 8-2.

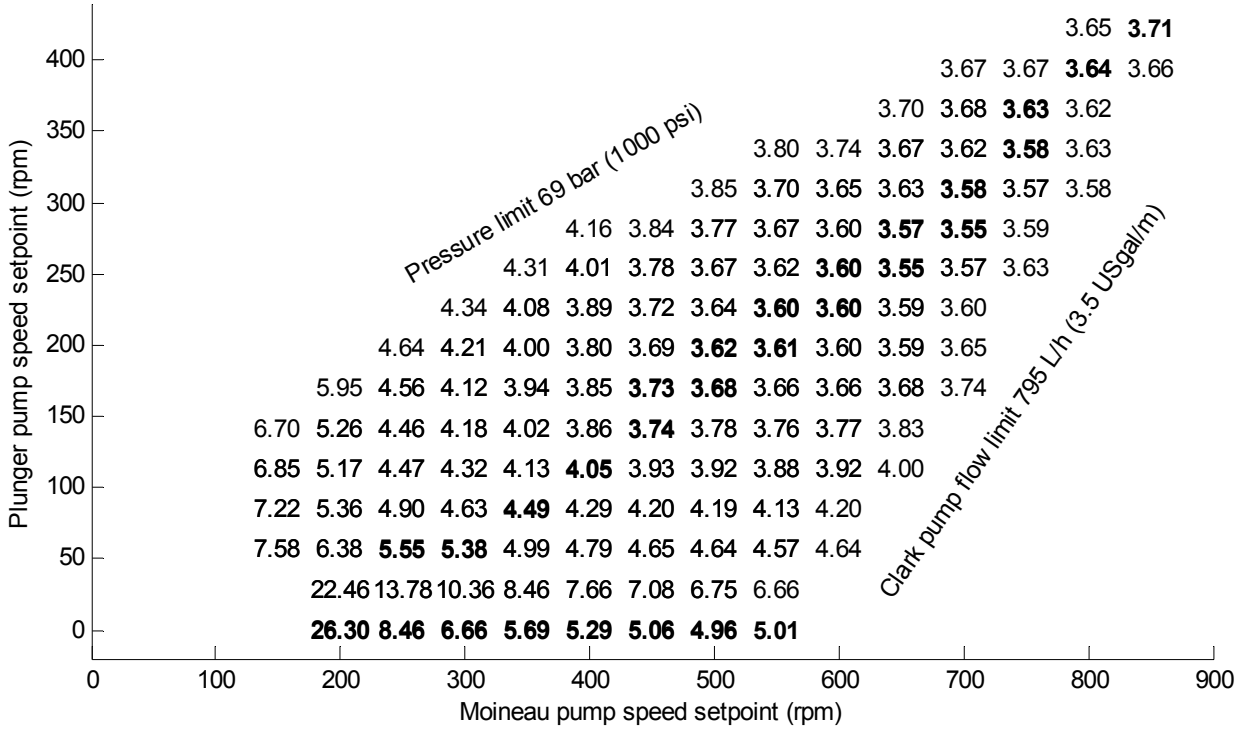

Figure 8-2 – Measured specific energy consumptions (kWh/m^3) against pump speed setpoints

In Figure 8-2 it can be seen that efficient operation (less than 5 kWh/m^3) is available over most of the area set by the pressure and flow limits, and that the *most* efficient operation is obtained in the central region, well away from those limits. Imagining this data in three dimensions, one can picture a *valley* of best efficiency, as indicated by the bold diagonal. Further plots (not presented here) and manipulation of the data confirmed that following this valley provides a good control strategy for maximising water production at powers between 400 and 1800 W. For powers less than 400 W, it is best to use the Moineau pump alone, as indicated in bold across the bottom of Figure 8-2.

This simple control strategy was implemented in LabVIEW. In particular, the speed setpoint for the plunger pump was derived from the Moineau pump setpoint, and thus, the two independent speed setpoints were reduced to one.

8.3 Measured performance

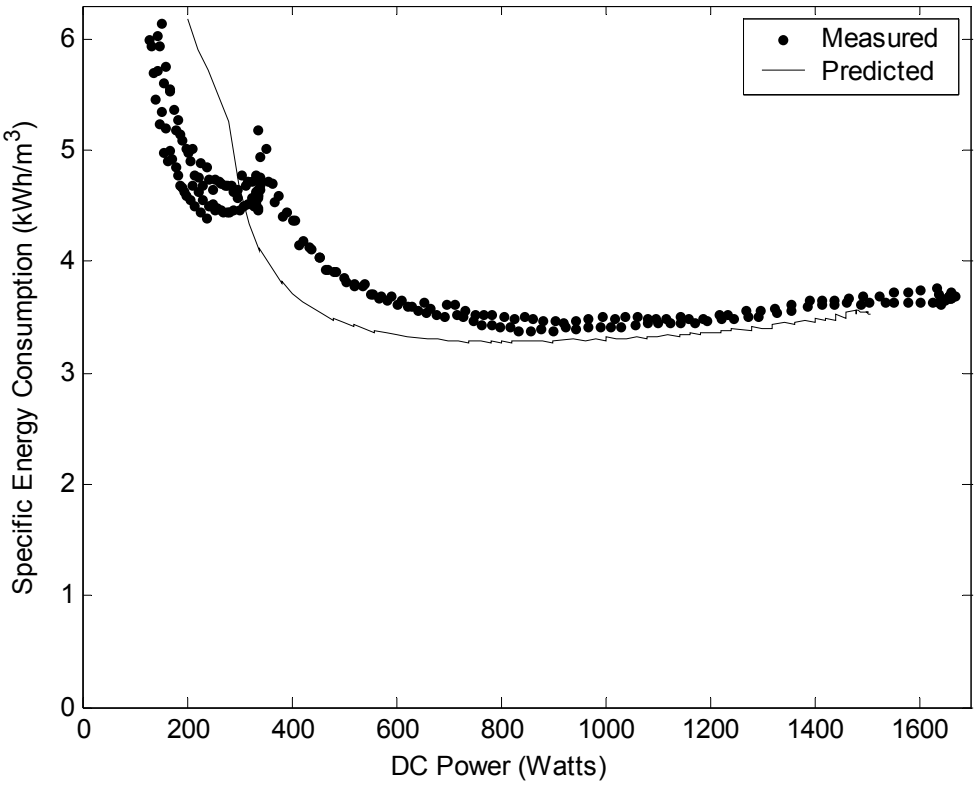

Figure 8-3 – Measured specific energy consumption against DC power

Slowly sweeping the Moineau speed setpoint, with the plunger speed under control as described above, gave the results plotted as *points* in Figure 8-3. The *line* is the predicted characteristic from the model described in section 6.5, and, in particular, derived from the data in Figure 6-19, but with the spread caused by temperature removed. Clearly, the measured results align very closely with the predicted. A discussion of differences is presented in section 10.4.

Chapter 9 Maximum power point tracking (MPPT) algorithm

The tests described in the previous chapter were conducted using mains electricity to power the system. The next stage was to operate the rig from the real PV array.

As outlined in section 5.5, the strategy was simply to connect the standard industrial variable-speed drive inverters directly to the PV array. The first step was to configure the PV array to provide a suitable voltage. The inverters used in the experimental rig specify a maximum DC-bus voltage of 400 VDC and this allows use of a maximum of 18 of the BP-Saturn PV modules available on the roof of the CREST building to be connected in series. Since the individual Saturn modules are rated at 85 W_p, 18 modules provide a total array power of 1530 W_p, which is only 64 % of the design value for the PV-RO system. Other brands of PV modules are readily available that have similar voltage but more power, and could normally be chosen to provide a better match to the RO system.

Connection of a PV array to a standard industrial inverter is common practice – the challenge lies in achieving maximum power point tracking (MPPT) as introduced in section 2.5.4. The next section will outline some of common MPPT algorithms used in PV systems, and after that, the implementation of MPPT with standard industrial inverters will be discussed

9.1 Common MPPT algorithms

9.1.1 Constant voltage

Perhaps the simplest way to get close to the MPP is to control the current drawn from the PV array such that the voltage remains constant.

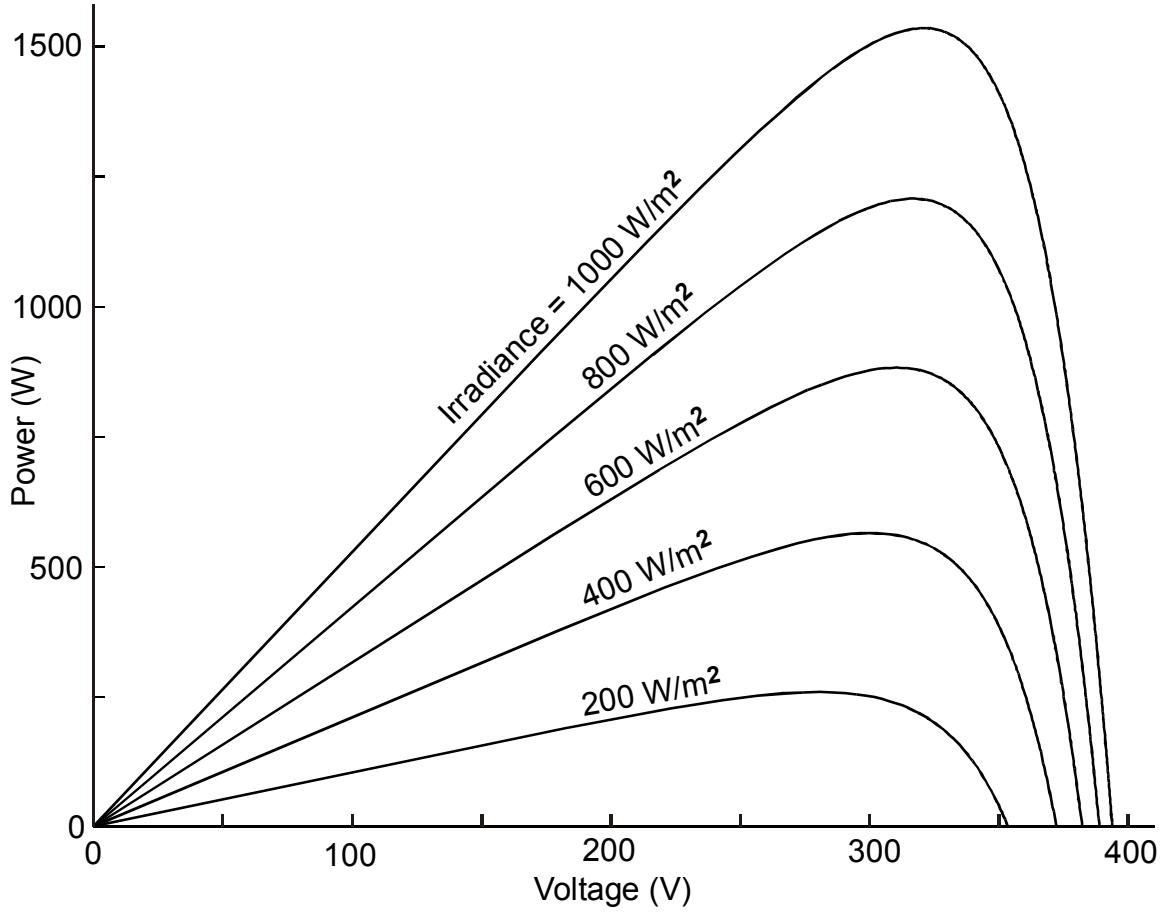

Figure 9-1 – Indicative power curves for a PV array at 25°C

Inspection of Figure 9-1 suggests that operation at a constant 310 volts will ensure operation close to the MPP, regardless of variations in irradiance. Indeed it will, but it will not perform well when the cell temperature changes, as illustrated by Figure 9-2.

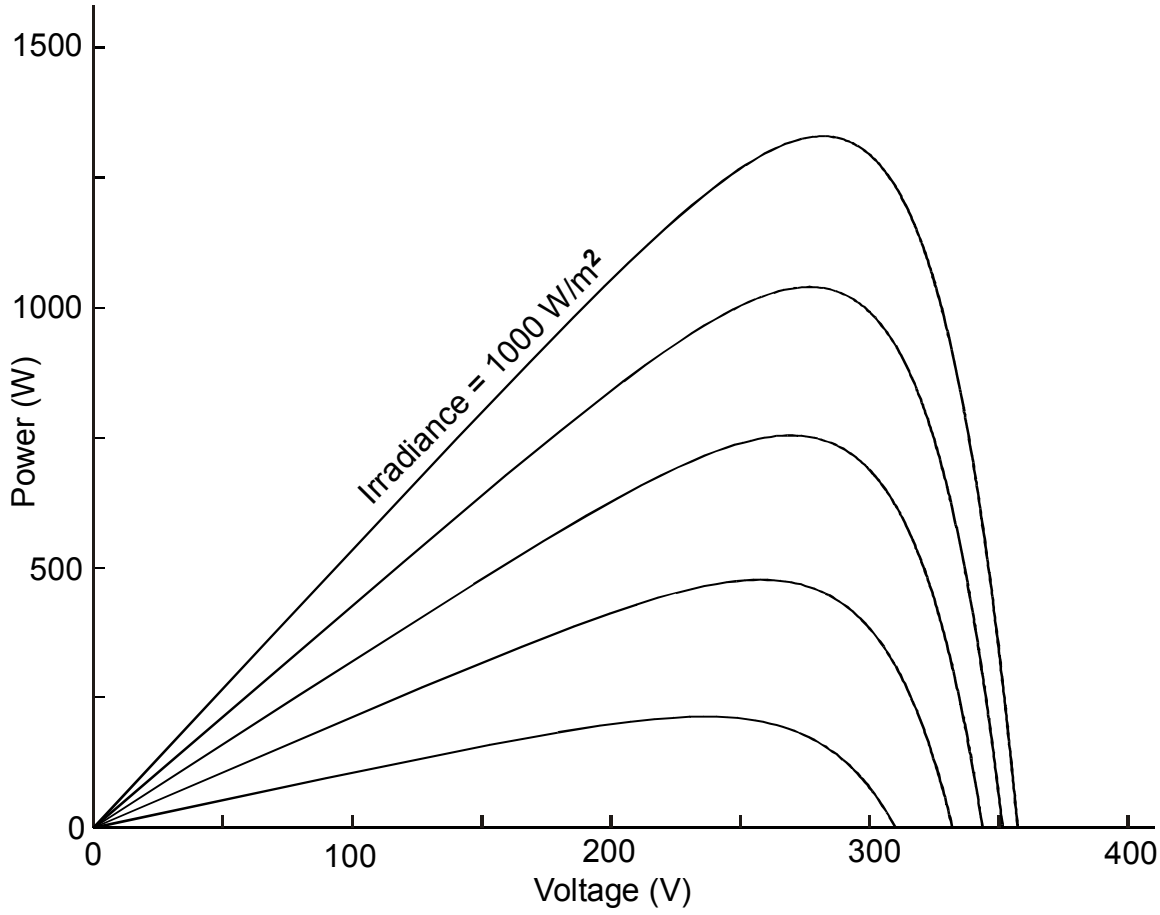

Figure 9-2 – Indicative power curves for a PV array at 50°C

9.1.2 Constant voltage with temperature compensation

The addition of a temperature sensor attached to one of the modules and wired into the controller allows the voltage setpoint to be adjusted and makes a useful improvement to the basic system.

9.1.3 Percentage of open-circuit voltage

When MPPT is implemented in a microprocessor, it is fairly straightforward to briefly open-circuit the array at regular intervals and to measure the open-circuit voltage. A fixed percentage of this voltage, usually around 79 %, is then used as the operating voltage setpoint until the next measurement is made. This technique allows for variations in cell temperature without need of a sensor.

9.1.4 Perturb and observe (hill climbing)

A basic hill-climbing maximum power point tracker requires feedback of the power being drawn from the PV array; usually this is derived by multiplying measured current and voltage. The tracker perturbs (makes a small change to) the array voltage (or current) and observes any change in the power; if the power has increased, it adjusts the voltage (or current) a little further in the same direction; otherwise, it adjusts it in the opposite direction. Thus, the tracker steps towards the MPP regardless of which side it starts. Once it reaches the MPP, it will move back and forth about the MPP, but remain close to it. If the MPP should move, the tracker will follow it.

9.1.5 Incremental conductance

The incremental conductance method is an alternative implementation of hill climbing. Instead of multiplying the measured current and voltage together at each end of the perturbation, the incremental conductance method compares $\mathrm{d}I/\mathrm{d}V$ against I/V in order to decide which way to go (Wilamowski et al. 2002).

9.2 Standard industrial variable-speed drive inverters

In the preceding descriptions of MPPT algorithms, it was assumed that the MPPT controller had direct control of the current drawn from the PV array, and through this, it could control the voltage. Direct control of the voltage would serve equally well, but with a standard industrial variable-speed drive inverter, we have neither. All we have is the *speed setpoint* input, which provides some control of the current drawn from the PV array, but not complete control.

Consider a standard industrial inverter and induction motor driving a pump, with the speed setpoint held constant. If the supply voltage is reduced slightly, *either* the voltage to the motor will be reduced, *or* the inverter will draw more current from the supply in order to maintain the voltage to the motor. Most modern industrial inverters will do the latter, at least by default, and this creates a problem for operation from PV. The problem turns into an opportunity, but we will come back to that later.

Consider that the standard industrial inverter, motor and pump are operating from a PV array. As the speed setpoint is gradually increased, the motor will accelerate and the current drawn from the PV array will increase, and as it does so, the voltage will fall

slightly as dictated by the *I-V* curve. The operating point will move upwards and leftwards along the *I-V* curve, and similarly along the *P-V* curve, as indicated by the arrows in Figure 9-3.

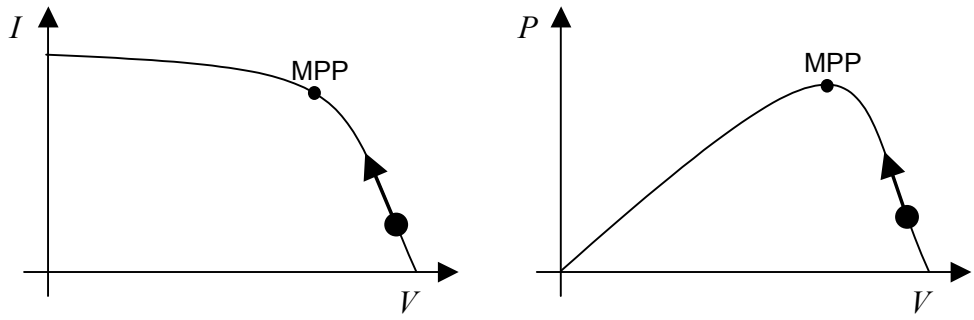

Figure 9-3 – *I-V* and *P-V* curves

All is well, until the operating point reaches the MPP, which obviously corresponds to the maximum available speed and is exactly the point at which we wish to be.

But, if the speed setpoint is increased slightly further, the extra current drawn by the inverter will cause an excessive reduction in voltage, and the power (the product of *I* and *V*) will be reduced, as indicated to the left of the MPP in the *P-V* curve. The inverter will respond to the reduction in voltage, (no more increase of setpoint is necessary) by again increasing the current drawn, which will reduce the voltage further, and so on, causing the voltage to collapse.

Thus, an industrial inverter of this type is only stable while operating on the *right* of the MPP. It is possible to operate on the left by rapid control of the speed setpoint, and this was demonstrated during commissioning of the PV-RO rig, but since the objective is to be *at the MPP*, neither left nor right, an alternative strategy was pursued.

9.3 New MPPT algorithm

If the voltage is steady, gently increase the speed setpoint.

If the voltage is falling, rapidly reduce it.

Thus, the problem of voltage collapse is turned into an opportunity to locate the MPP.

The word *new*, in the title of this section is perhaps an overstatement, but it does reflect the fact that this particular strategy has not been found in the literature. There are hundreds of academic papers describing MPPT algorithms, many of them claiming to be *new*. On close inspection, most of them turn out to be subtle variations of the approaches outlined earlier in section 9.1. Indeed, the algorithm presented here can be described as a hill-climber, in which one side of the hill is sheer cliff, so perhaps it should be called the cliff-hanger algorithm.

An important feature of the algorithm is that it requires only the voltage as an input signal; the hill-climbers outlined in section 9.1 require the current as well.

9.4 Basic implementation

The algorithm was implemented in LabVIEW using a 100 ms program loop. On each cycle of the loop, the program measures the PV array voltage v, which is the DC bus voltage of the inverter, and gives a new speed setpoint n^* to the inverter.

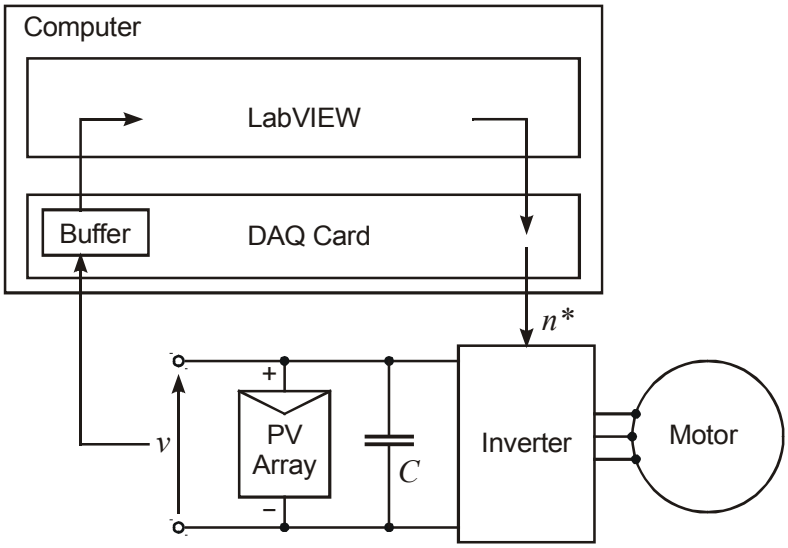

Figure 9-4 – MPPT hardware/software arrangement

Practical note: As described in section 4.16, the voltage is actually sampled at 10 kHz. The 100 ms program loop takes 1000 samples at a time, and averages these to provide good quality data at 10 Hz. In common with other hill-climbing algorithms, good-quality data is essential. Speeding up the program loop would have little benefit.

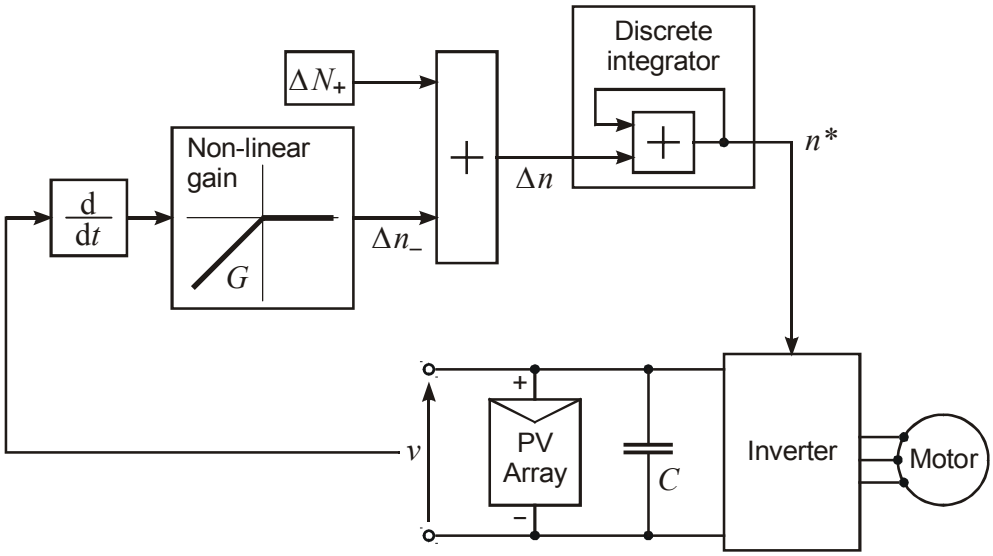

Figure 9-5 – MPPT basic implementation

Figure 9-5 shows the structure of the software used for a basic implementation of the algorithm, which was previously stated:

> *If the voltage is steady, gently increase the speed setpoint.*
>
> *If the voltage is falling, rapidly reduce it.*

ΔN_+ is a constant that defines the rise rate, while the voltage is steady. The integrator turns this constant into a ramp, and provides the speed setpoint n^* that is applied to inverter. Thus, the speed ramps up.

The voltage v is fed back and differentiated in software. If dv/dt is zero (steady voltage) or positive (rising voltage), it has no effect. But if it is negative (falling voltage), it is passed through to the integrator, which reduces n^*, and prevents the voltage from collapsing.

The *if statement* is implemented by the non-linear gain box, in which the G represents the gain when the input is negative. This defines by how much n^* is reduced.

Ideally, ΔN_+ should be set as large as possible, so that the controller ramps up quickly to the MPP. Meanwhile, G should be set as small as possible, just high enough to prevent the voltage from collapsing. If G is set too large, the controller becomes too cautious and stays a little to right of the MPP. To understand this, bear in mind that the voltage is

never perfectly steady; each time it dips a little, the controller reduces the speed setpoint a little.

In practice, the controller shown in Figure 9-5 did work, but was not ideal. In particular, it became apparent that *G* needed to be set to different values under different operational conditions. When the irradiance was high, *G* needed to be set to a high value so that speed setpoint would be reduced sufficiently to prevent voltage collapse. But when the irradiance was low, such a high value of *G* made the controller too cautious. Setting *G* by trial-and-error was not succeeding and a more rigorous approach was sought.

9.5 Enhanced implementation

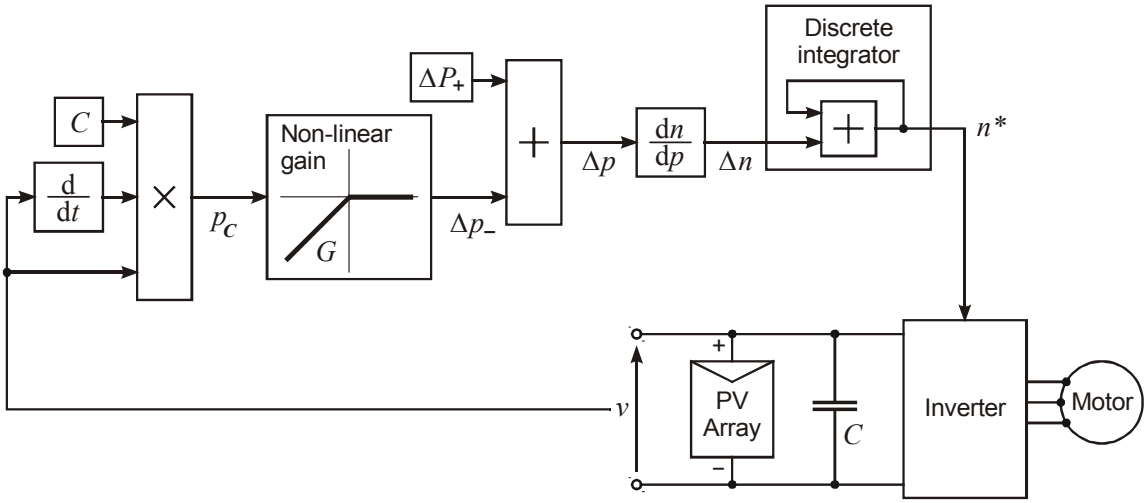

Figure 9-6 – MPPT enhanced implementation

The rate at which the voltage collapses is dependent on the capacitance *C*, illustrated between the PV array and the inverter in Figure 9-6. This capacitance includes the capacitance built in to the industrial inverter and any external capacitance added.

The voltage collapses when the inverter draws more power than the PV can supply. During the collapse, the additional power is supplied by the capacitor, and calculating this power will indicate by how much the inverter power must be reduced.

To maintain familiar sign conventions, power *into* the capacitor is treated as positive and is given by: $p_C = v\, i_C$. We also know that $i_C = C\frac{\mathrm{d}v}{\mathrm{d}t}$, and thus $p_C = v\, C\frac{\mathrm{d}v}{\mathrm{d}t}$. This calculation is implemented on the left of Figure 9-6.

So, the inverter power must be adjusted by an amount theoretically equal to p_C, but the inverter has a *speed* setpoint input, not power. To provide the conversion, $\frac{\mathrm{d}n^*}{\mathrm{d}p}$ is required, and this of course depends on the load, in our case, the RO rig.

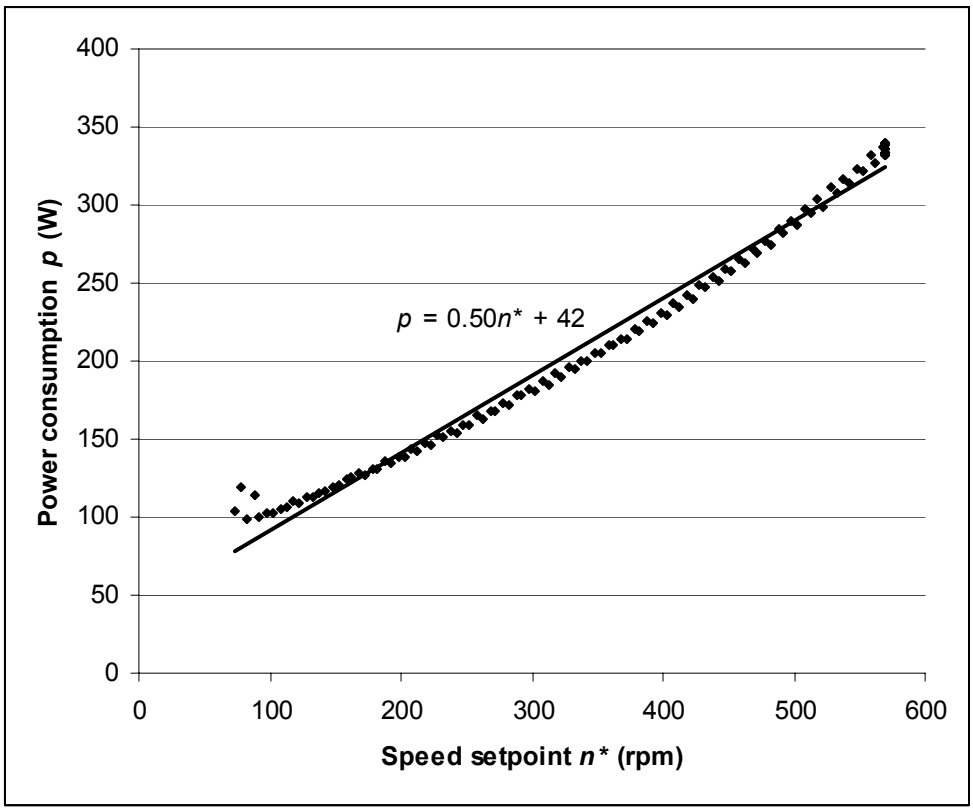

Figure 9-7 – Inverter power consumption vs. speed setpoint

The power consumption of the RO test rig was measured: first, running only the Moineau pump, and second, running both pumps as discussed in Chapter 8. Mains electricity was used for the test and the data for the Moineau pump only is shown in Figure 9-7.

The linear trendline in Figure 9-7 shows that $\frac{\mathrm{d}p}{\mathrm{d}n^*} = 0.50$, and thus, $\frac{\mathrm{d}n^*}{\mathrm{d}p} = 2.0$.

Alternatively, a quadratic trendline may be used. In which case, $\frac{\mathrm{d}p}{\mathrm{d}n^*}$ is a function of n^*, but it is sufficient to use n^* from the previous control-program cycle. This was demonstrated during commissioning of the PV-RO rig, but gave no discernible performance improvement, and was dropped. It would be worth reconsidering, if the

algorithm were being applied to a centrifugal pump, for example, where the power-speed characteristic was more curved.

Returning now to Figure 9-6, the components are complete and, in theory, G may be set to unity to ensure that the operating point is brought back to the MPP, whenever the voltage starts to collapse. In practice, a safety margin is required and setting G to 2 gave good performance.

9.6 Two inverters

In the interest of clarity, the preceding sections have described the MPPT algorithm with respect to a single inverter. Of course, the RO rig has two inverters, and their speed setpoints are to be coordinated as discussed in Chapter 8. The overall arrangement of the two inverters and their control is shown in Figure 9-8.

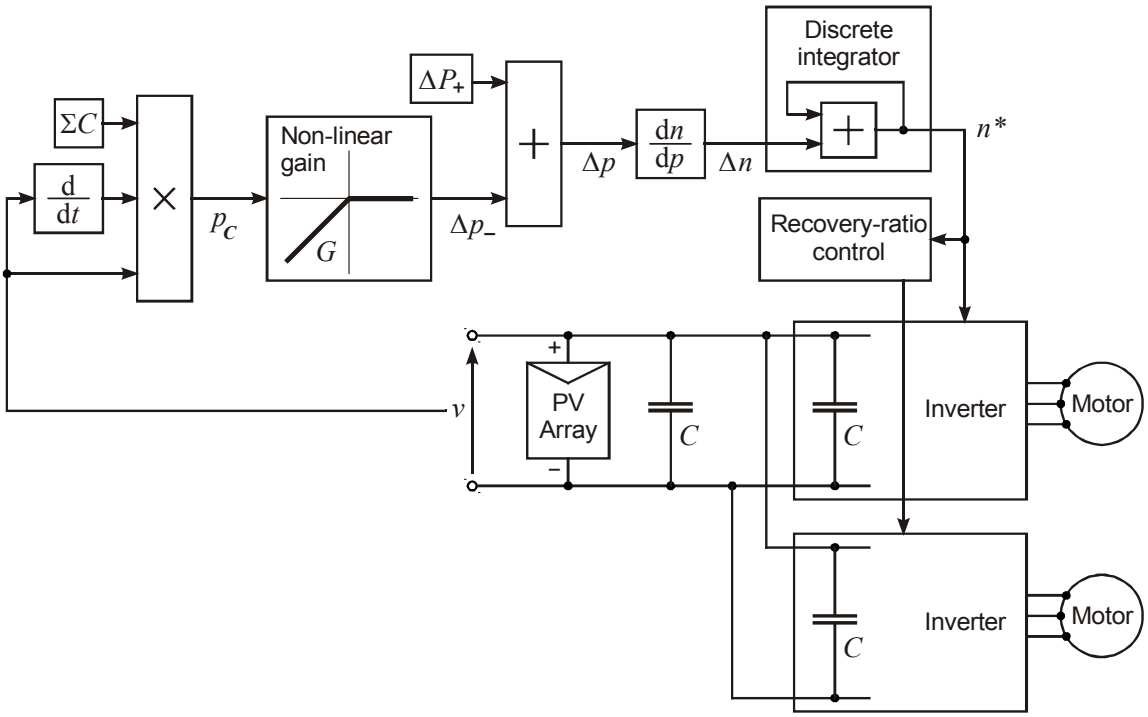

Figure 9-8 – Complete two-inverter MPPT control system structure

9.7 In practice

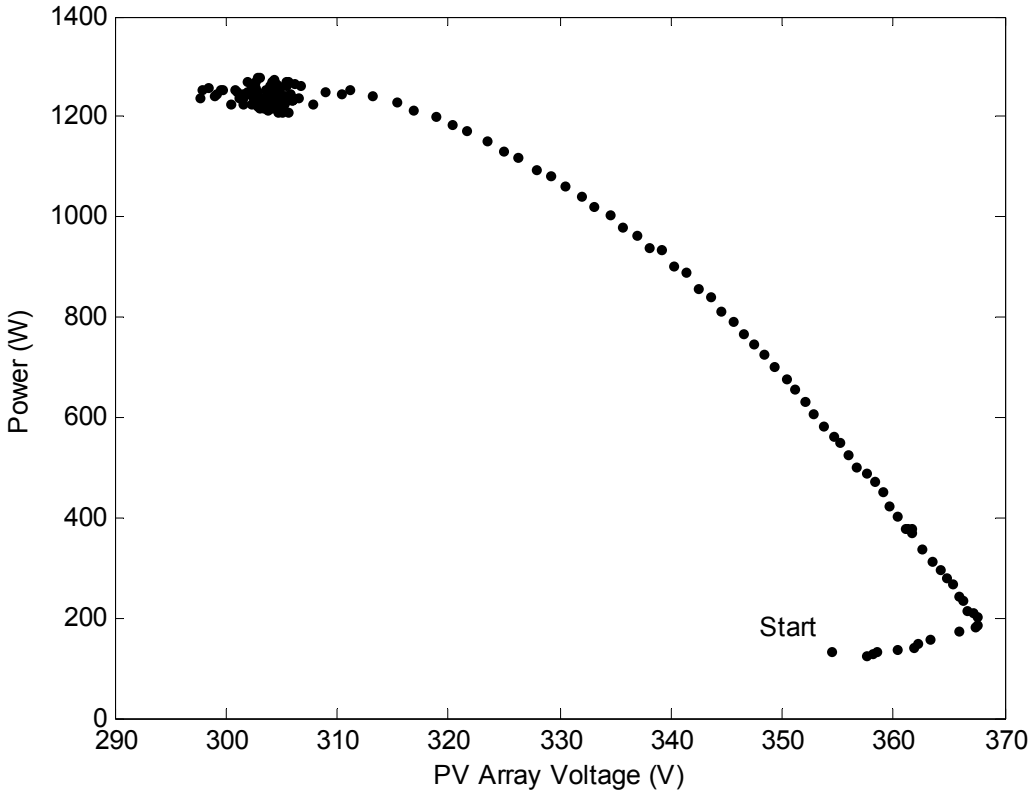

Figure 9-9 – Trajectory of MPPT operation, power vs. voltage

To illustrate the operation of the MPPT algorithm, a 3-minute period of 1-second data is shown in Figure 9-9. At the start of the period the sun was behind a cloud, and less than 200 watts was available from the PV array, just enough to run the Moineau pump. Then the sun came out and the voltage rose from 354 V to 368 V in just over 10 seconds. The tracker recognised this immediately, and started to ramp up the speed. The trajectory followed the classic *P-V* curve until the MPP was reached and then tracker stayed close to the MPP for the rest of the 3-minute period. The same data is plotted against time, in Figure 9-10.

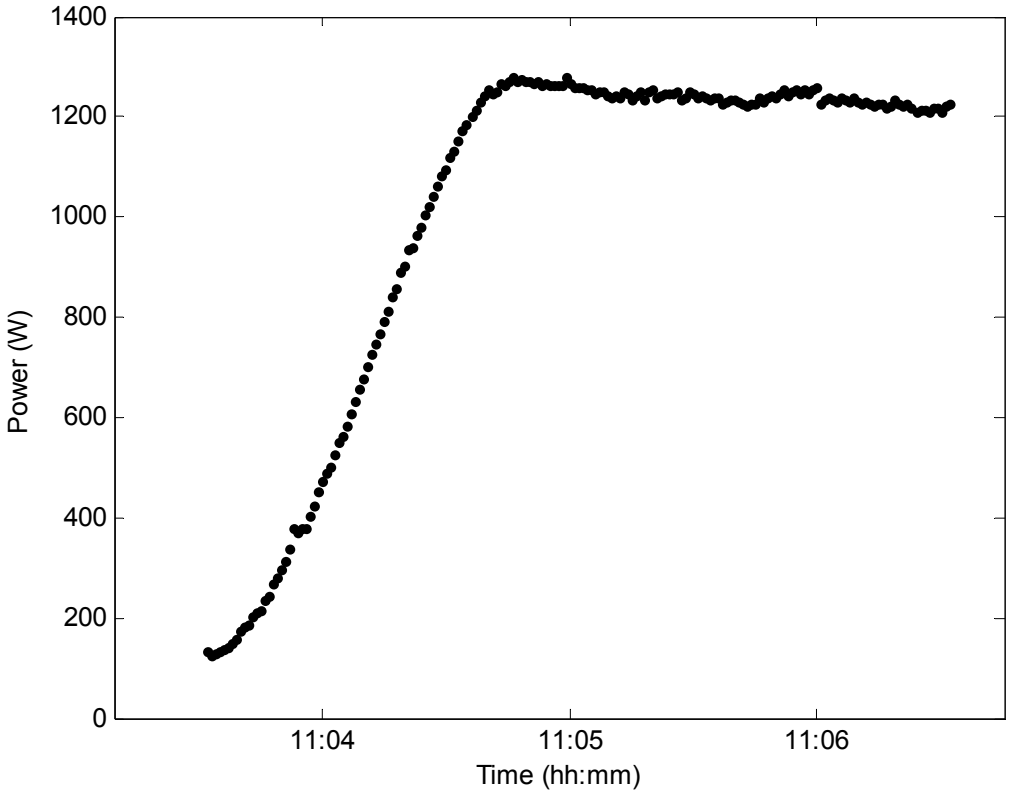

Figure 9-10 –MPPT operation, power vs. time

Close inspection of Figure 9-10 reveals a slightly soft (curved) start to the ramp. This is partly due to the 10 seconds taken for the sun to come out, but also due to a slight modification to the algorithm, whereby ΔP_+ is deliberately reduced at low powers to improve stability.

A slight pause is apparent, just below 400 W. This is where the plunger pump is started.

At the top of the ramp, there appears to be a slight overshoot, but in fact, this effect is due to the heating of the PV array.

The 3-minute section of data presented above was selected because it so cleanly demonstrates the operation of the controller. It shows the controller's response to an almost step change in irradiance, followed by a steady condition. The sun is rarely so obliging, and a more typical period of operation is shown in Figure 9-11.

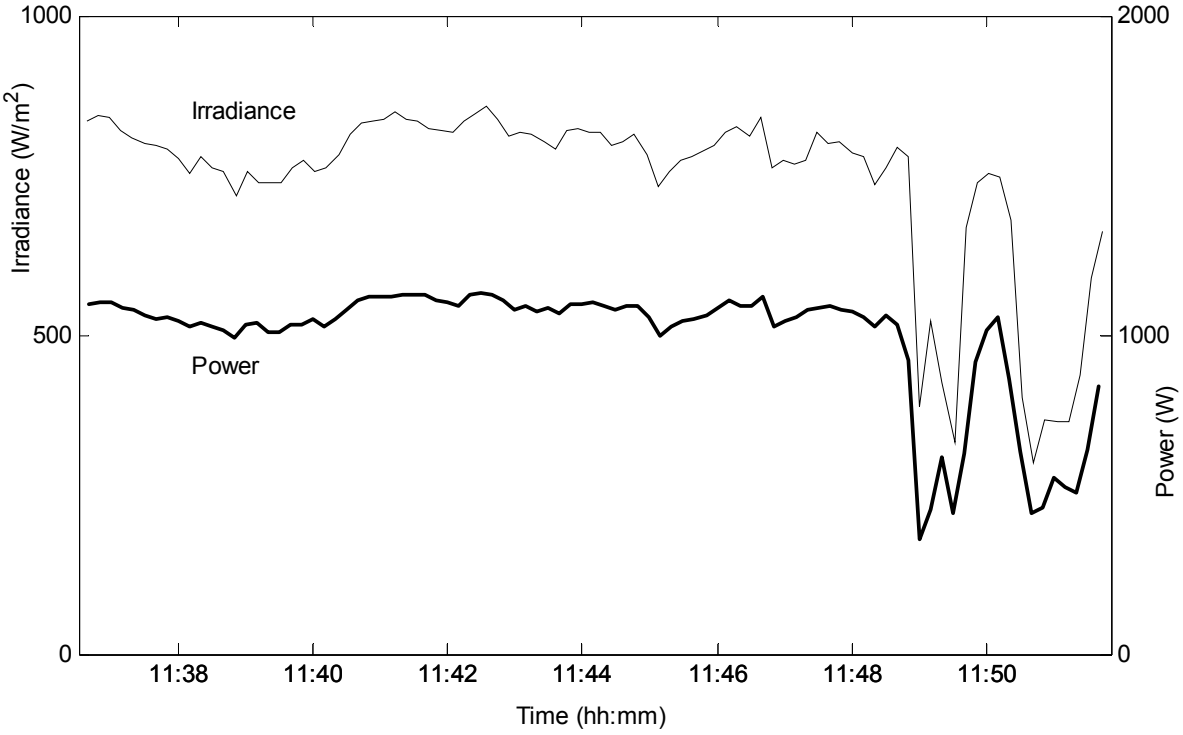

Figure 9-11 – MPPT operation over a 15-minute period

The performance of the tracker over a 15-minute period is shown in Figure 9-11. The thin trace is the irradiance in the plane of the PV array, measured with a pyranometer, as described in section 4.17. The thick trace is the DC power extracted from the array, measured at the input to the inverters. Some clouds passed over towards the end of the period shown and the tracker responded effectively to track the changing power available.

9.8 Discussion

No quantitative assessment of the tracker was attempted, but its operation under varying conditions was carefully observed over many hours and under different weather conditions. In particular, an X-Y plot in LabVIEW allowed on-line observation of the trajectory of the operating point in the power-voltage plane, rather like Figure 9-9. This indicated, for example, whenever the controller was being too cautious and operating to the right of the MPP. The following discussion is based on those observations.

For the most part, the tracker did appear to sit very close to the MPP. Two observations support this.

First, looking again at Figure 9-9, it is clear from the shape of the curve that the tracker is sitting at the top of the hill, where $dP/dV = 0$. The on-line LabVIEW display regularly showed similar behaviour. Furthermore, disabling the tracker and ramping the speed setpoint down over a period of a few seconds caused the operating point to cleanly trace out the right-hand side of the classic *P-V* curve, again showing that it had been tracking at the very top.

Second, when close to the MPP, the operating point could be seen looping around it. The looping is caused by the capacitor, and the fact that the power displayed includes the external capacitor power, which allows the displayed power to deviate transiently from the static *P-V* curve. The looping indicates that the voltage is starting to collapse, and that the controller is acting as intended.

Once the controller parameters G and ΔP_+ were suitably adjusted, the tracker was effective over a full range of steady-sun conditions: irradiance = 150 to 1100 W/m^2, but the rise time remained a concern.

Figure 9-10 showed that the tracker took approximately 1 minute to respond to a near step change in irradiance. During this time, the tracker was not at the MPP and power was being wasted. This is a natural characteristic of hill-climbing algorithms. The total energy loss that it causes over a long period of operation depends largely on the type of clouds. During the testing of the PV-RO system at Loughborough, there were periods of patchy clouds, during which some energy loss was apparent. Such loss may well be significant in many implementations of hill-climbing MPPT, but go unnoticed. In the case of the RO system, the sound of the motors running is a give away.

The rise time can be reduced by increasing the setting of ΔP_+. This pushes the operating point up the *P-V* curve more rapidly, but also tends to push it too far, causing the voltage to collapse. If the voltage does collapse, the controller resets and then has to climb the curve again, incurring further energy loss. Use of a *variable* ΔP_+ within the controller improved the performance of the demonstration system, as mentioned in discussion of Figure 9-10. Developing this approach further could substantially reduce the overall rise time.

9.9 Pros and cons

The MPPT algorithm described in this chapter works directly with standard industrial variable-speed drive inverters, which have much lower cost than specialised PV inverters.

LabVIEW was used for the demonstration, but the algorithm is simple, and could readily be implemented in a very low-cost micro-controller.

The algorithm requires feedback of only the PV voltage, or the inverter DC-bus voltage, which is virtually the same. Many industrial inverters can be configured to provide this as a ready-conditioned analogue signal. No feedback of the PV current is required. The algorithm tracks array temperature changes, without requiring a temperature sensor or periodically open-circuiting the array.

The performance of the demonstration MPPT was critically dependent on the careful adjustment of several control parameters and required an estimate of the load characteristic dp/dn*. With experience, these adjustments could be rationalised, possibly to a point that no manual commissioning is needed. No particular knowledge of the PV characteristics is required, and the algorithm should perform equally well with amorphous-silicon PV, provided the lower MPP voltage is within the range acceptable to the industrial inverter.

The algorithm appeared to perform well under steady sun, but needs further refinement to track unsteady conditions more rapidly.

The algorithm could be immediately applied to solar pumping applications, and it would be interesting to compare its performance with more traditional techniques.

Chapter 10 Batteryless PV-RO demonstration system measured performance

The PV-RO test rig outlined in Chapter 7, coupled with the recovery-ratio control of Chapter 8 and the MPPT algorithm just described in Chapter 9, was tested for two complete days, and some of the measured results are presented and discussed here.

The feed water was straight NaCl solution nominally at 32,800 mg/L, which is isosmotic with ASTM standard seawater, as discussed in section 5.10.3. The concentration varied by plus and minus 500 mg/L (±3% of the feed water concentration) during the tests because of variation of concentration of water held within the RO modules, which is affected by the recovery ratio.

The temperature was held at 25 ºC, plus and minus 0.1 ºC for most of the duration.

10.1 Irradiance and product flow

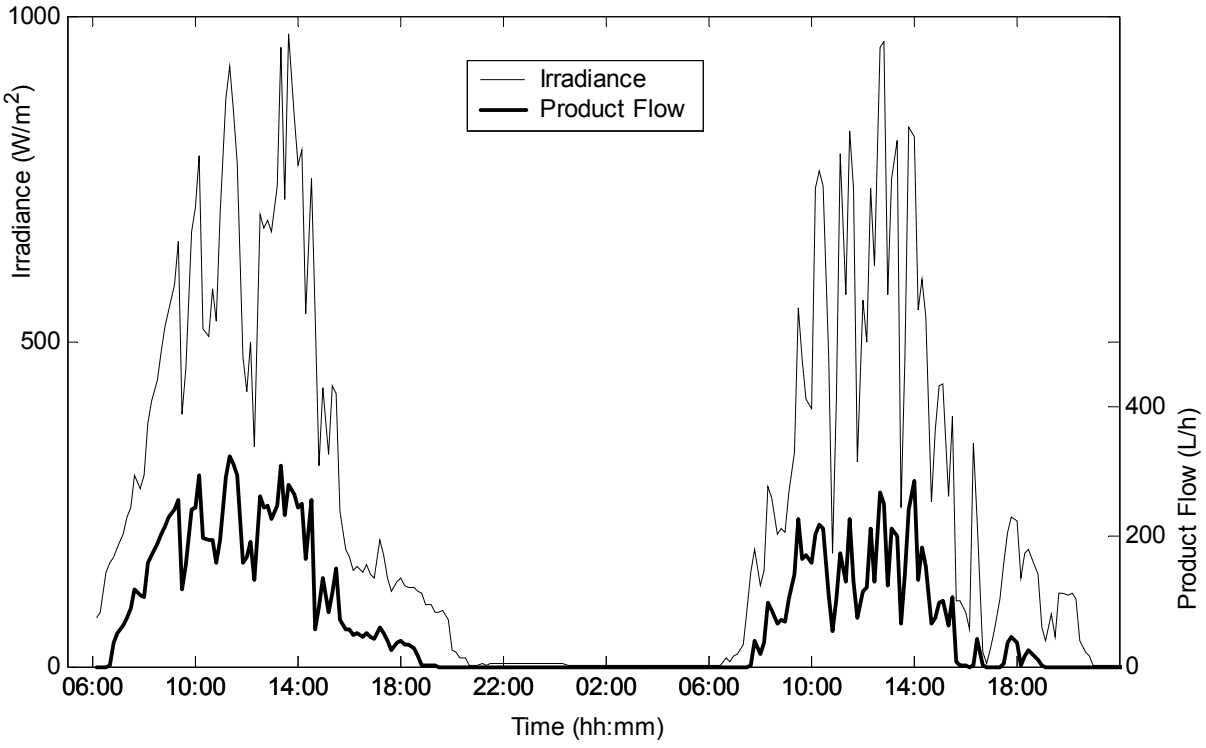

Figure 10-1 – Measured irradiance and product flow June 9th and 10th 2003

The thin trace in Figure 10-1 is the irradiance in the plane of the PV array, measured with a pyranometer, as described in section 4.17. The thick trace is the product flow, which totalled 2.93 m^3 over the complete two-day test.

The system is intended to produce more than twice this amount, but bear in mind that this testing was performed in the UK, with many passing clouds, and that the PV array is just 1530 W_p, which is only 64 % of the design value.

10.2 Product flow versus irradiance

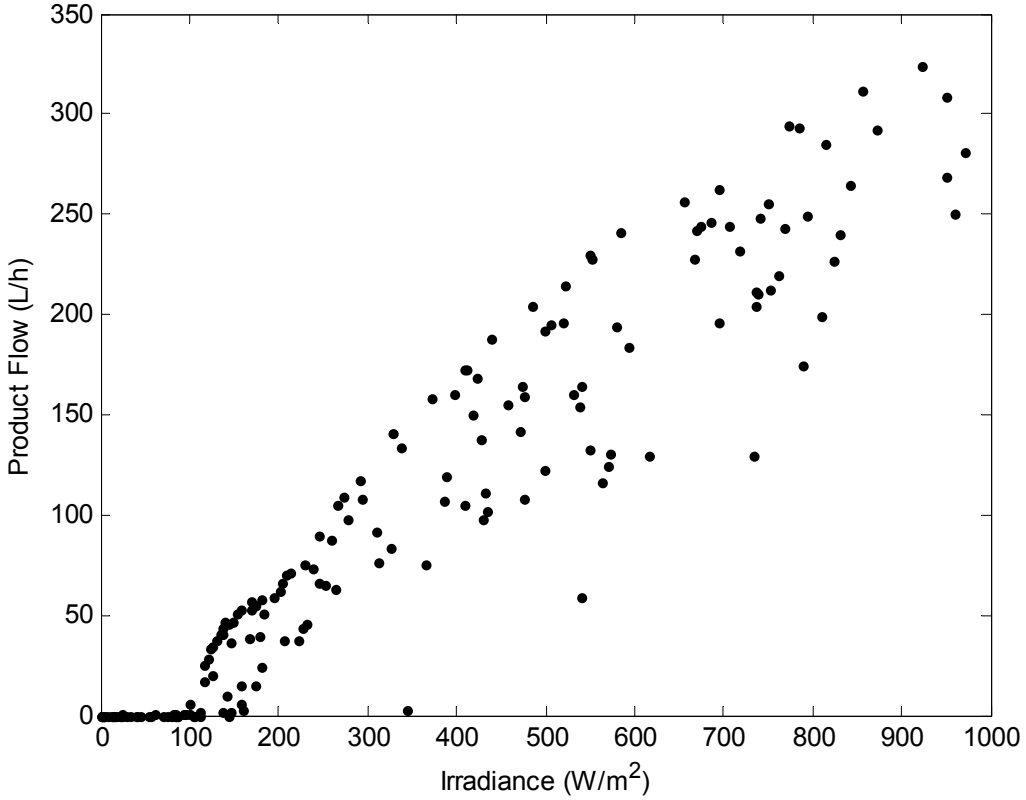

Figure 10-2 – Product flow versus irradiance

Figure 10-2 uses the same data as Figure 10-1 and shows that water production is roughly proportional to irradiance, and, importantly, that it starts at very low irradiance. This graph uses data averaged at 10-minute intervals, and shows considerable scatter. Looking ahead to Figure 10-3 shows that the scatter in Figure 10-2 occurs primarily in the conversion from irradiance to DC power. There are two likely causes. First, the temperature of the PV array, which varies during the day and with passing clouds, will have an effect on the DC power available from the array for any given irradiance. In particular, the measured array temperature varied by up to 26 ºC, at 200 W/m^2, which

was the worst case. This will affect the power available by approximately 13%, taking the coefficient of power at 0.5% per Cº (BP-Solar 2002). The scatter in Figure 10-2 is clearly much greater than 13% and is caused mainly by the maximum power point tracker, and in particular its slow rise time, as discussed in section 9.8. Assuming that this can be resolved by further development of the tracker, the points scattered below the diagonal of Figure 10-2 will be pushed upwards and the total water production will be correspondingly increased.

10.3 Product flow versus DC power

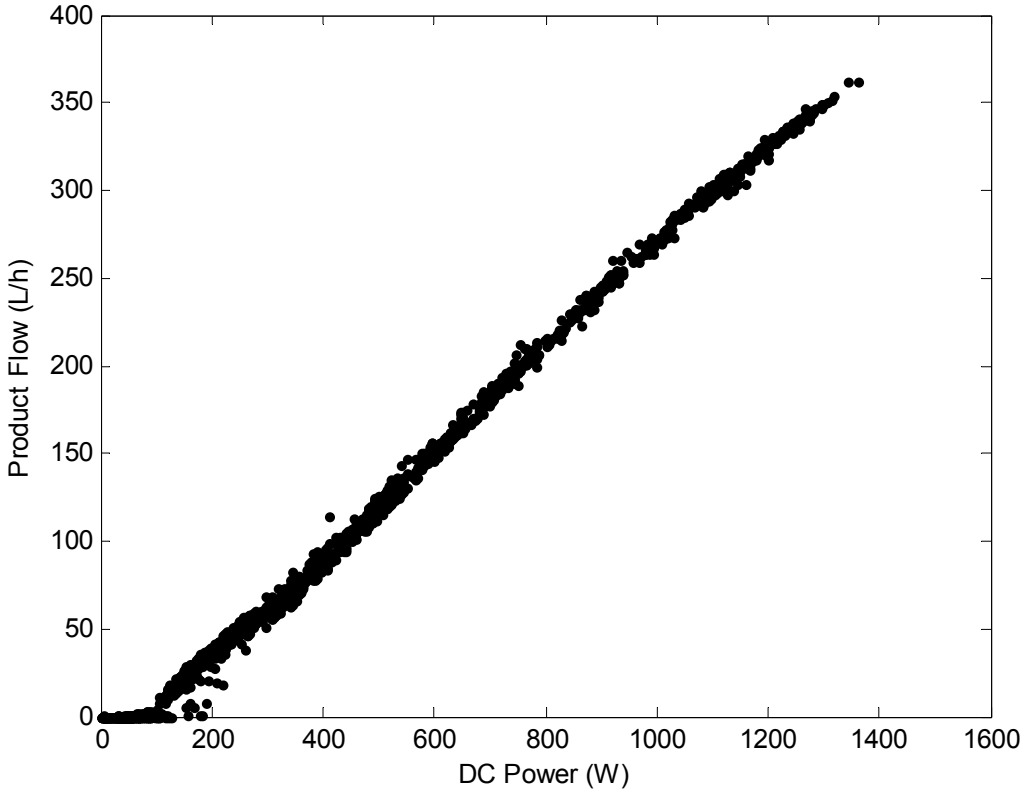

Figure 10-3 – Product flow versus DC power

In order to see the performance of the RO rig itself, Figure 10-3 shows the product flow against DC power coming from the PV array, measured at the input to the inverters. This graph and all subsequent graphs in this chapter use data averaged at 1-minute intervals, covering the whole of the two-day test.

Figure 10-3 shows that water production starts at just 100 W and then increases more or less proportionally to the available power.

10.4 Specific energy consumption (kWh/m^3)

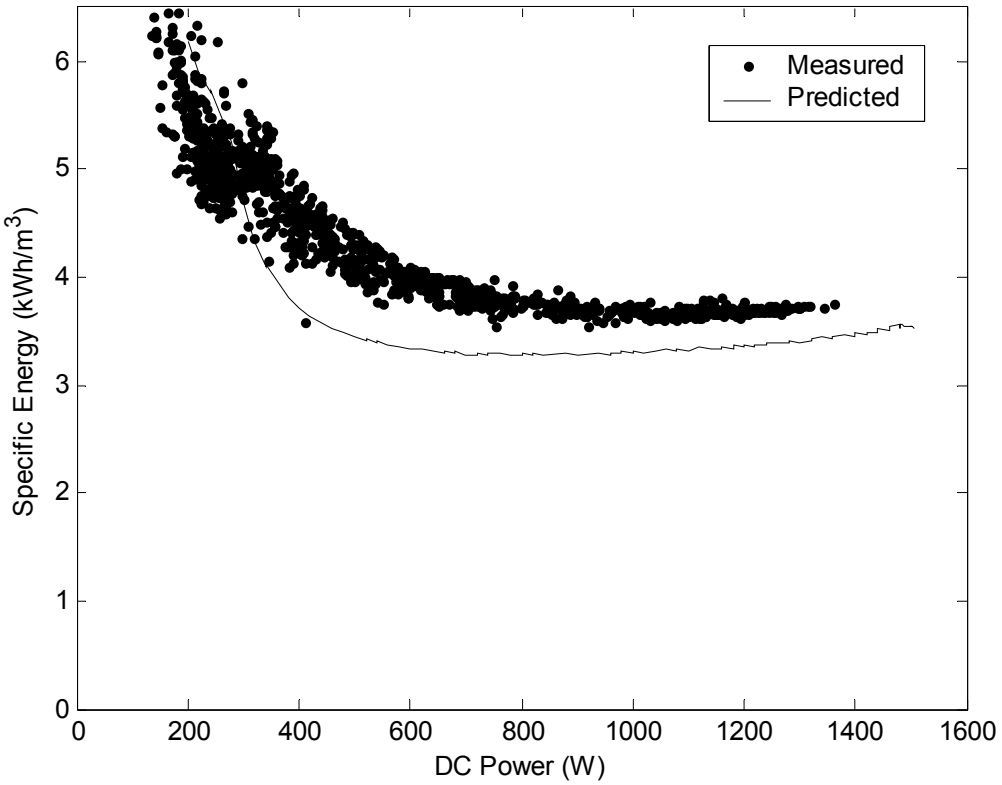

Figure 10-4 – Specific energy (kWh/m^3)

Plotting the same data, but this time as specific energy consumption, gives the *points* in Figure 10-4. The *line* is the predicted characteristic from the model described in section 6.5, and, in particular, from the data in Figure 6-19, but with the spread caused by temperature removed.

For perspective, bear in mind that a standard mains-powered RO unit would probably not even appear on this graph, and if it did, it would only offer a single fixed operating point.

At low input power (towards the left of Figure 10-4), it is apparent that the test rig is actually *more* efficient than was predicted. This is probably due to the membrane element models, which were extrapolated from measurements taken from slightly different elements. In particular, the measurements were taken from *high-rejection* elements; whereas the test rig is fitted with *high-flow* elements, see section 2.7.6.

At higher input power (moving to the right in Figure 10-4), it is apparent that the test rig becomes less efficient than was predicted. This is largely due to the plunger pump and its

motor, which do not match those in the design model. Recall that both the pump and motor were taken from the old test rig and that they are coupled by a toothed belt, as discussed in Chapter 7. As shown later in the chapter, the old motor has significantly lower efficiency than the new motor used on the Moineau pump, especially at low speeds.

10.5 Water recovery ratio

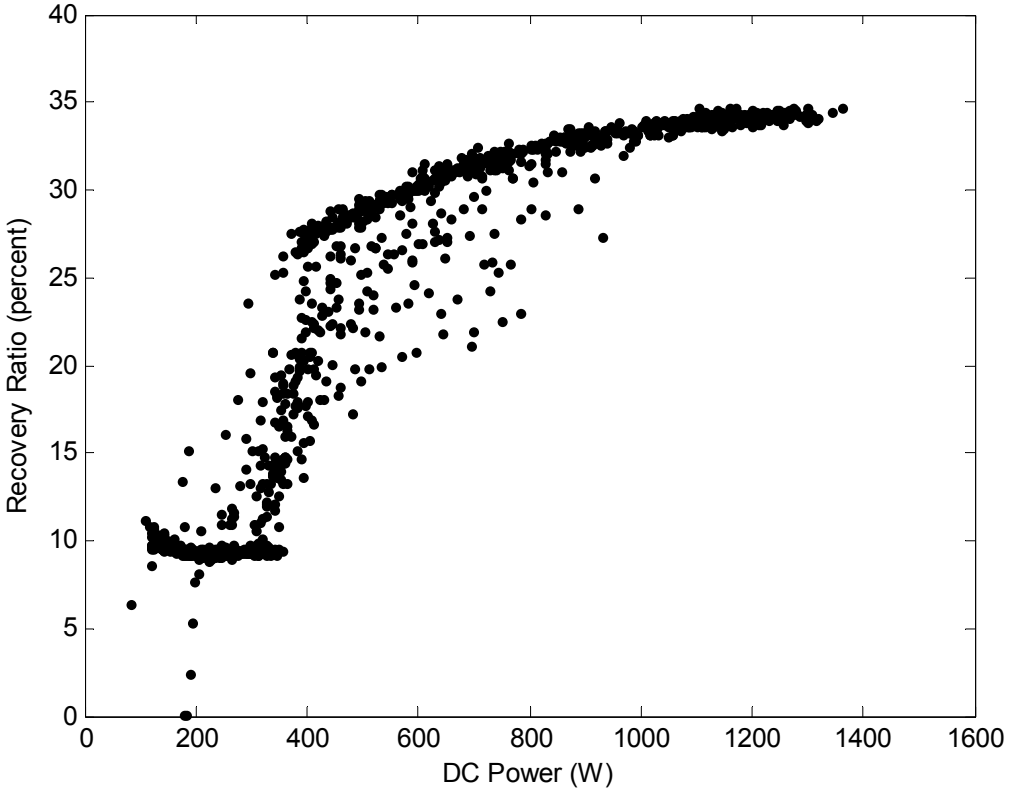

Figure 10-5 – Water recovery ratio

The variable recovery ratio discussed in Chapter 8 is clearly apparent in Figure 10-5. The section at the bottom left is where the Moineau pump only is running and the recovery ratio is around the fixed value of 10 % as determined by the Clark pump. The section across the top is where both motorised pumps are running. The scatter in the figure occurs because the recovery ratio varies rapidly in response to the varying irradiance, while the data used for this plot is averaged at 1-minute intervals.

Although the two modes of operation are very apparent in Figure 10-5, looking back at Figure 10-3 shows that the transition is in fact very smooth. In practice, the plunger pump was started and stopped and re-started very frequently with apparently no ill effect.

10.6 Product concentration

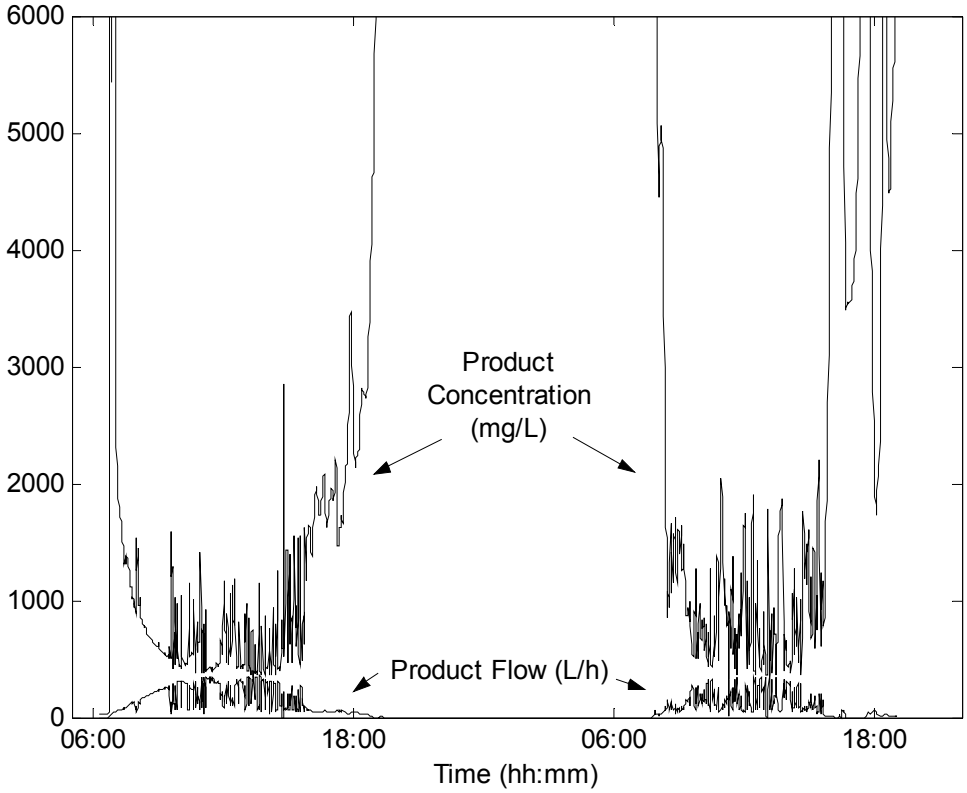

Figure 10-6 – Product concentration

The product concentration, measured via its conductivity as described in section 4.11 and averaged at 1-minute intervals, is shown in Figure 10-6. Recall, from section 2.1.3, that:

> *The palatability of water with a TDS level of less than 600 mg/litre is generally considered to be good; drinking-water becomes significantly unpalatable at TDS levels greater than 1200 mg/litre.* (WHO 2003)

Clearly, the concentration of product water from the PV-RO rig is, *at times*, greatly in excess of this. Fortunately, the high concentration generally coincides with low flow, and what matters is the average concentration of water in the product tank.

Of course, the test rig has no product tank, but the data has been aggregated to illustrate the volume and concentration that there would be.

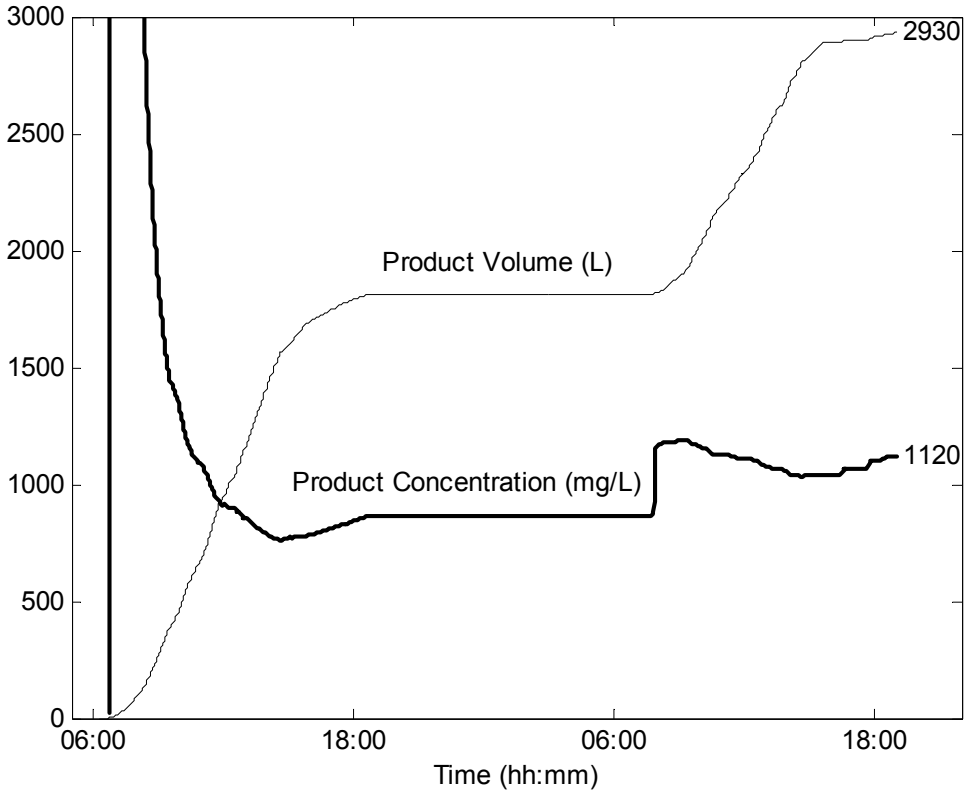

Figure 10-7 – Product tank volume and concentration, basic case

If all of the product water were directed to a tank, it would accumulate as shown in Figure 10-7, which is obtained simply by integrating the measured data shown in Figure 10-6. This shows the total production of 2.93 m^3 over the two days, as mentioned previously. It also shows that the concentration is getting close to the *significantly unpalatable* level.

A significant part of the total salt in the product tank is due to a small volume of very high concentration water coming from the membrane elements at startup (usually at sunrise). The salt is that which has diffused though the membranes while the pumps were stopped (overnight).

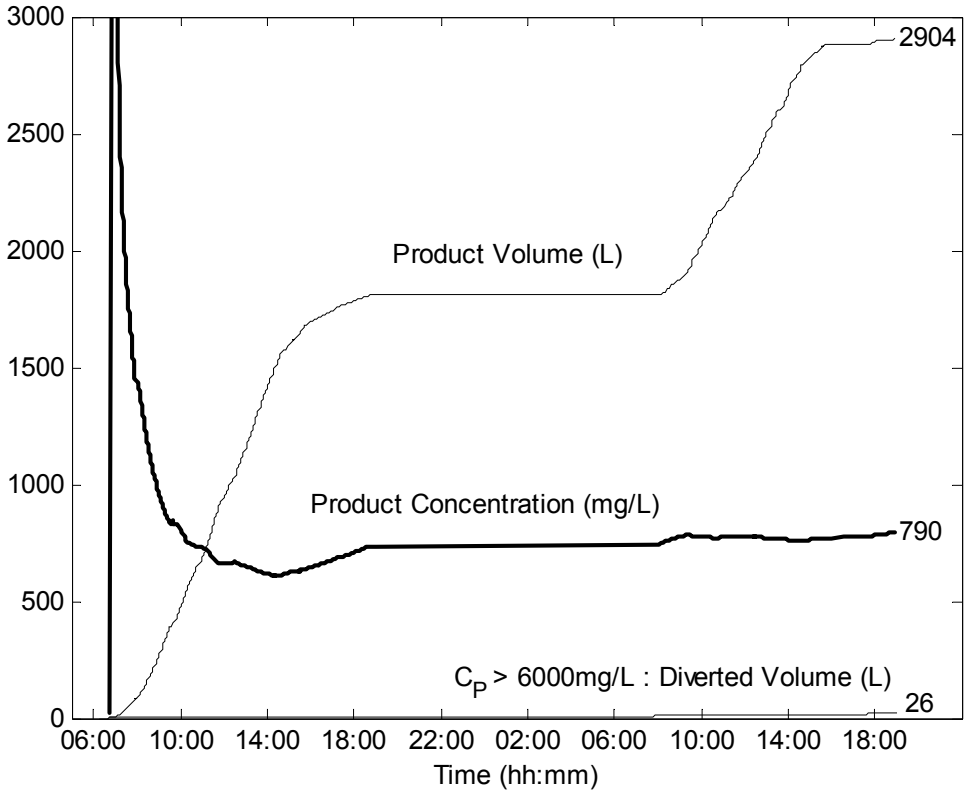

Figure 10-8 – Product tank volume and concentration, diverting > 6000 mg/L

A simple diverter valve, fitted in the product line prior to the tank, could be used to significantly reduce the concentration of the water in the tank. The valve would need to operate automatically and reject product water exceeding a chosen concentration threshold. The effect of such a valve, with a threshold set at 6000 mg/L, is illustrated in Figure 10-8. This discards less than 1 % of the product volume but brings the final concentration in the tank to below 800 mg/L.

The concentration of the product water actually delivered by the test rig is markedly higher than that predicted by the model. This is partly because the volume of production of good quality water is reduced by the small PV array and the passing clouds, but also because the model was based on measurements taken from membrane elements with *high-rejection*, whereas the test rig is fitted with *high-flow* elements, see section 2.7.6. High-rejection elements could certainly be used in the PV-RO system; they have similar cost and would improve the quality of the product, but at the expense of quantity.

10.7 Pressures

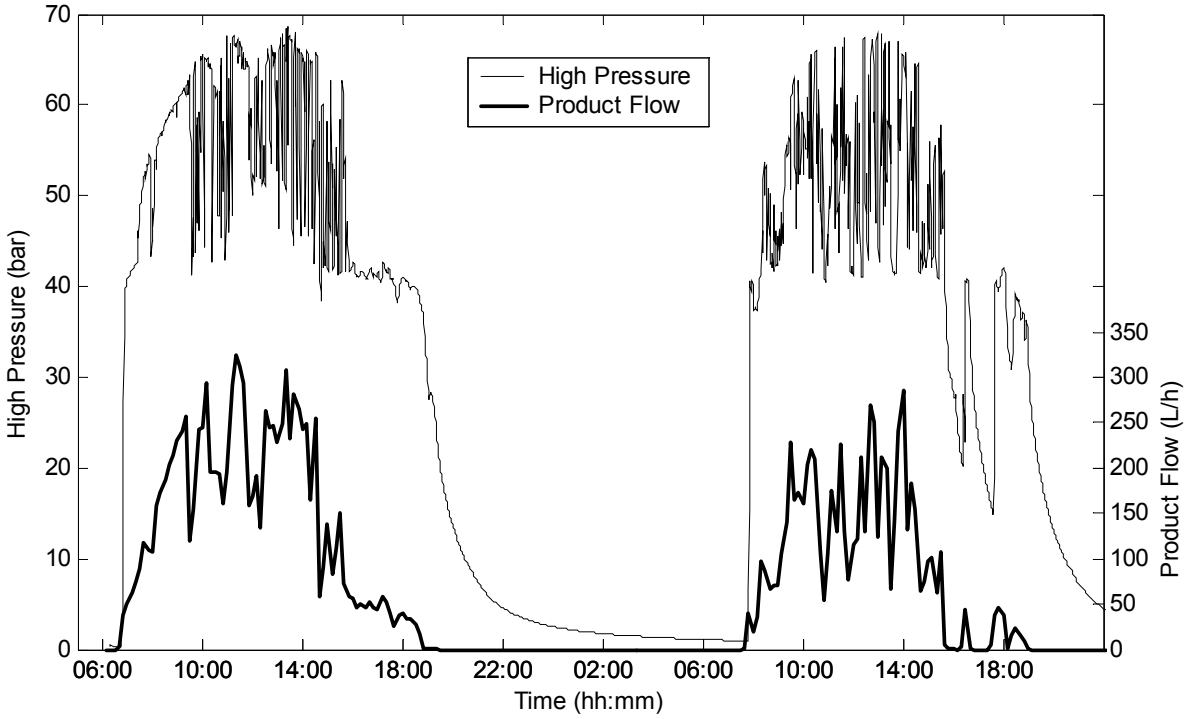

Figure 10-9 – Membrane feed pressure

The pressure of the feed water at the inlet of the first RO membrane element is shown in Figure 10-9. Production starts at around 40 bar and the pressure varies all the way up to the maximum 69 bar allowable by the membrane pressure vessels. Pressure is maintained during short interruptions (passing clouds), but decays almost to zero during the night.

The medium pressure, between the Moineau pump and the Clark pump, behaves similarly, but in the range 5 to 9.6 bar.

10.8 Pump efficiencies

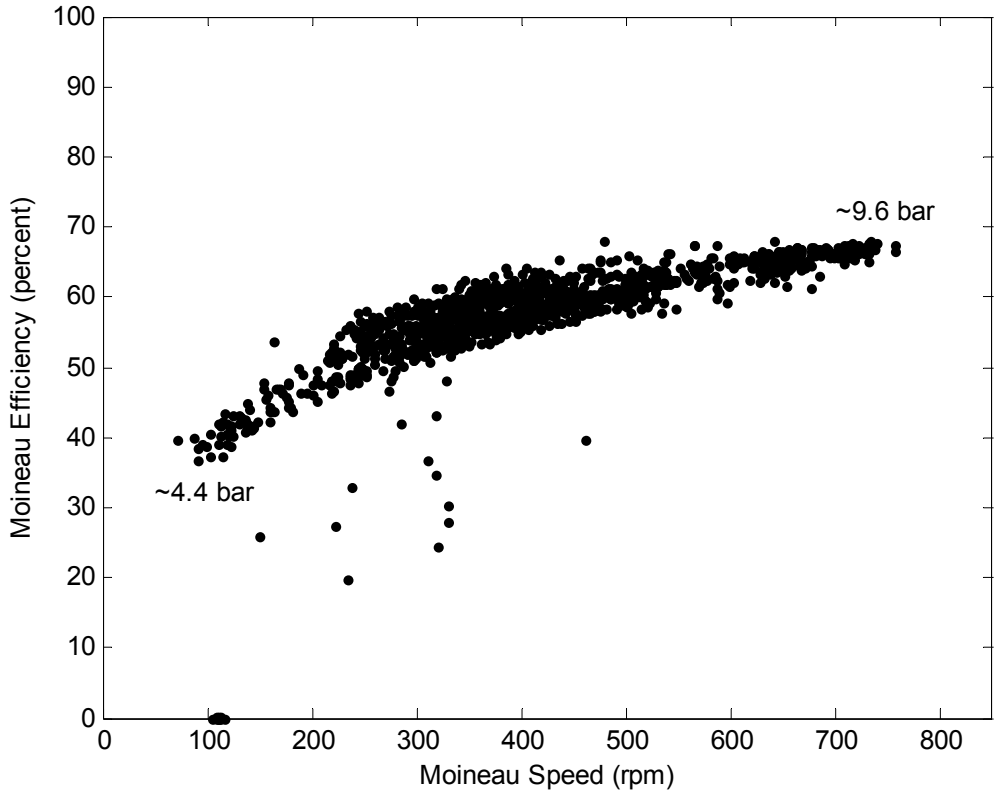

Figure 10-10 – Moineau pump efficiency

The Moineau pump meets its expectations. The efficiency shown in Figure 10-10 is certainly far higher than that attainable by a centrifugal pump of the same size. Vane pumps offer an alternative, but must be seawater compatible. Spectra Watermakers have had success with vane pumps. The scatter in Figure 10-10 occurs because the operating point of the pump varies rapidly in response to the varying irradiance, while the data used for this plot is averaged at 1-minute intervals.

The plunger pump efficiency measured between 75 and 85 % regardless of flow and pressure.

The energy losses in the Clark pump, while operating within the complete PV-RO system, were less than the data acquisition system could reliably measure. The Clark pump was tested in isolation, as described in section 5.2, and its efficiency has proved excellent throughout.

10.9 Inverter and motor efficiencies

The inverter and motor efficiencies are combined here because measurement of the high-frequency switched power between the two cannot readily be achieved with sufficient accuracy.

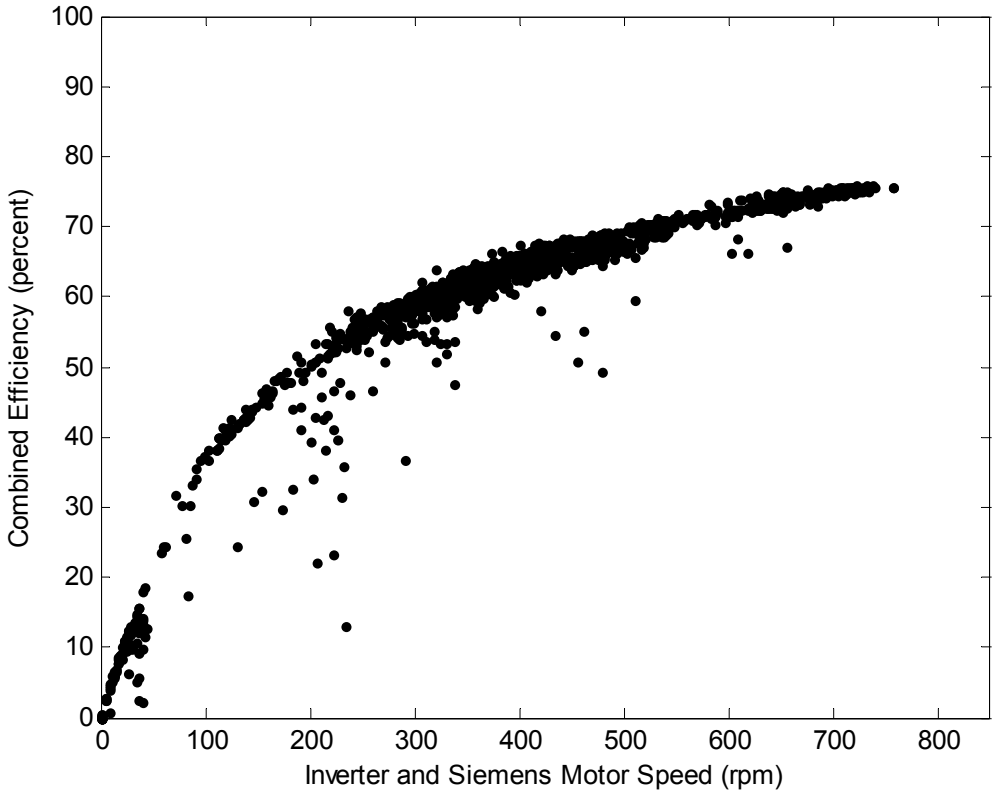

Figure 10-11 – Combined efficiency of inverter and motor driving the Moineau pump

Figure 10-11 shows the newer of the two motors, and its efficiency is very good considering that it is operating typically between 100 and 400 W shaft output power.

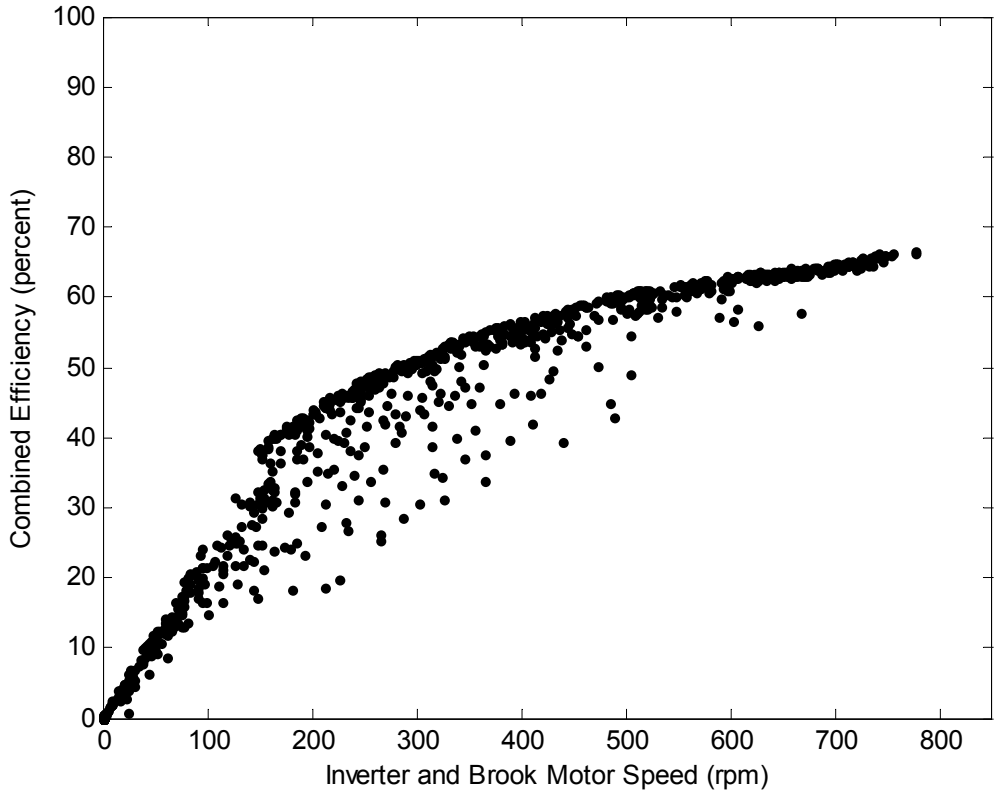

Figure 10-12 –Combined efficiency of inverter and motor driving the plunger pump

Figure 10-12 shows the combined efficiency for the older motor and its inverter, which is about 10 % lower than the new motor. Replacement of this motor and the associated plunger pump would bring significant improvement to the overall system performance.

Chapter 11 Practical considerations

11.1 Clark pump

The excellent energy efficiency of the PV-RO system reported in the previous chapter is due primarily to the Clark pump. The Clark pump is a *high-tolerance precision machine* (Spectra 2003), and will typically require more maintenance than a simple needle valve. Indeed, the Clark pump at CREST required some maintenance during the course of this project. Spectra, the manufacturers, provided excellent support and have altered the design over the years to improve the reliability of new Clark pumps.

11.2 Membrane fouling

Membrane fouling can cause a large reduction of product flow in an RO system, and a consequent increase in specific energy consumption. But, the effect can be compared to a reduction in temperature, and therefore, as discussed in section 6.2.4, the increase in specific energy consumption is very much less in systems with efficient brine-steam energy recovery.

Nonetheless, the main operating cost of the batteryless PV-RO system is expected to be the replacement of the RO membrane elements when they become excessively fouled and can no longer be effectively cleaned. And, as noted in section 2.9.3, there is concern that intermittent operation of an RO system will accelerate membrane fouling. Indeed, this is probable, but has not been quantified, and the relative costs of replacing batteries or membrane elements are not yet known.

Membrane life expectancy in a well-maintained 24-hour-a-day RO plant is around five years. The cost estimates presented in section 6.6 for the batteryless PV-RO system assumed that a complete new set of RO membrane elements would be required every 12 months. The membrane replacement rate in practice will be critically dependent upon feed-water quality, and this depends to a large extent on the feed water intake arrangement.

11.3 Feed water intake arrangement – beach wells

The Moineau pump in the PV-RO system can be above ground, as it is in the test rig, and suck water from a shallow well, or may be submersible and some distance from the main RO rig. The above-ground approach offers better energy efficiency because it allows use of a high-efficiency motor; submersible seawater-compatible motors are available but only at lower efficiency. On the other hand, sucking water from a well is limited to about 7 metres height, and provision must be made to ensure that the Moineau pump does not run dry.

Many large RO plants have *open-sea intakes*, which often provide feed water of poor quality that requires elaborate pre-treatment before it may be fed to the actual RO membranes. A far preferable arrangement is the use of a *beach well*, since this can provide pre-filtered water and greatly reduce pre-treatment requirements (Koch 2000; Schwarz 2000). Where a traditional beach well is not practical, alternative belowground intakes can be used to similar effect (Cansdale 2001; Kunczynski 2003).

A beach well intake or similar, providing very good quality feed water, may be considered an essential prerequisite for the PV-RO system described in this thesis, in order that it may operate intermittently and without chemical additives. The use of electrostatic pre-treatment in the form of a Zeta Rod (Romo et al. 1999) may also be worth considering.

11.4 Membrane flushing

Most RO systems include provision for flushing of the membranes at shut down. Often, this involves feeding product water, made earlier, through the membranes, which removes most of the salt and prevents precipitation. As an alternative, Koch Membrane Systems (2000) suggest use of seawater for the shutdown flush, in which case, the flush is simply a matter of reducing the recovery ratio to zero. The PV-RO system has no provision to automatically flush the membranes, but it does reduce the recovery ratio to just 10 % as the sun goes down. And, this 10 % is spread over a very generous membrane area, meaning that concentration polarisation is minimal. It is hoped, therefore, that the omission of a shutdown flush mechanism will not unduly affect membrane life. In its favour, the PV-RO system can be expected to run nearly every day, assuming it is located

in an area with a good solar resource. Thus, it should rarely stand still for much over 16 hours.

11.5 Product tank chlorination

At the time it is produced, the product water from an RO system should be almost free of biological activity, but it is very prone to re-infection, particularly in the storage tank. Modest chlorination is suggested to maintain safety in the tank and to provide a residual presence in the water, which will continue to be effective throughout any pipes, storage bottles or whatever.

11.6 Osmotic suck-back

When shutdown, most RO systems will suck water back from the product line because (forward) osmosis occurs. This can be used as a way to provide a shutdown flush, provided chlorine is not introduced, since chlorine will damage the membrane. But, suck-back does not occur in the PV-RO system, because the pumps are positive-displacement and do not release the pressure.

Chapter 12 Conclusions

This thesis has presented the design and demonstration of a photovoltaic-powered reverse-osmosis (PV-RO) seawater desalination system without batteries. The method of design, in particular the structure of the Matlab-Simulink model, was developed by the author and may be of value in the development of similar variable-flow/pressure RO systems. The use of variable recovery ratio to achieve energy efficiency over a wide range of input power has been demonstrated and serves to support the case that PV-RO systems can operate efficiently *without batteries*. Lastly, a novel maximum power point tracking algorithm has been developed, which, with further refinement, could be of value in PV-RO and other PV-pumping systems.

12.1 Renewable-energy powered desalination

The rapid worldwide uptake of desalination over the last thirty years, the expected continuation of this trend and the associated consumption of fossil fuel lead to considerable interest in renewable-energy powered desalination. The coupling of renewable energy and desalination technologies was reviewed in section 2.4, with reference to more comprehensive studies, and showed the significance of small-scale batteryless PV-RO, both in its own right and as a precursor to larger variable-flow RO systems for use in connection with PV and other intermittent renewable-energy sources.

12.2 Batteryless PV-RO

The case against using batteries in a PV-RO system was discussed in section 2.9.3 but not proven, since it relies on un-quantified reports of very poor battery performance in many other PV systems. The counter argument, that RO systems are best run at constant flow, was also presented, but again is un-quantified because of lack of documented experience of RO systems with intermittent or variable flow.

This thesis presents the design and testing of the batteryless approach, and provides estimates of performance and capital costs of such systems. Meanwhile, other researchers are developing PV-RO systems that do include batteries, and it would now be possible to compare cost estimates for the two approaches. Such a comparison would, however, be

critically reliant on assumptions regarding membrane lifetime under variable-flow conditions.

12.3 Variable-flow

The testing of RO membranes under variable-flow conditions, presented in Chapter 3 and Chapter 10, was successful and revealed no immediate problems. It was, however, very brief and used straight NaCl in place of seawater. The testing presented in Chapter 10 demonstrated energy efficiency over a broad range of operation, but did not provide any indication of membrane lifetime under real operating conditions. It is recommended, therefore, that long-term membrane testing under intermittent and variable flow conditions should now be conducted. This could be within a field trial of batteryless PV-RO or carried out under laboratory conditions at an established RO plant. The latter approach would perhaps yield better-calibrated data and a better comparison against traditional continuous operation. Such testing is also highly relevant to the coupling of RO with other intermittent renewable-energy sources, in particular windpower, and should take account of variable recovery ratio as discussed below.

12.4 Product concentration

Operation of RO membranes under variable-flow conditions generally implies a reduction in average flow, which in turn causes an increase in the concentration of the product water. The results of the initial testing (section 3.1) and the software modelling (section 6.5.2), both of which were based on high-rejection membrane elements, suggested that this increase would be perfectly acceptable. However, the results measured from the new test rig, which was fitted with high-flow membranes, did show rather high concentrations at times, particularly at dawn and dusk (Figure 10-6). This indicates the need for some caution in designing RO systems to operate with variable-flow but the problem is not insurmountable. Use of high-rejection membranes or a simple diverter valve to reduce product concentration is discussed in section 10.6.

Furthermore, the acceptable concentration of product water is primarily a matter of taste and depends greatly on who the consumers are. The 500-mg/L TDS limit, often stated in desalination literature, may not always be appropriate (section 2.1.3).

12.5 Energy recovery – The Clark pump

Brine-stream energy recovery is critical for the efficiency of seawater RO, but is often neglected in small systems because suitable mechanisms are only now becoming available. Testing of a hydraulic motor, presented in Chapter 3, showed that it gave a water-to-water efficiency of typically below 60 % and raised doubts regarding its seawater compatibility. The Clark pump was identified as an alternative and a theory defining its efficiencies was developed in section 5.2.1. A Clark pump was tested (section 5.2.2 and Appendix C) and showed water-to-water efficiency typically above 90 %. Furthermore, this efficiency was maintained over a very wide range of operation, making it well suited for a batteryless PV-RO system. The Clark pump is central to the design presented in this thesis.

12.6 Variable recovery ratio

In order to make best use of the Clark pump, a system design employing two motor-driven pumps was adopted (section 6.2.3), and, to provide efficient operation over a wide range of input power, use of a variable recovery ratio was proposed and modelled (Figure 6-6). The new test rig was commissioned with a variable recovery ratio as described in Chapter 8, and efficient operation over a wide range of input power was demonstrated (Figure 8-3).

The use of a variable recovery ratio is recommended for RO systems operating from variable energy sources. Use of a variable recovery ratio also has implications for the membrane lifetime, since operation at a very low recovery ratio is akin to a seawater flush (section 11.4). It is recommended that the membrane testing, suggested above, should also consider variable recovery ratio.

12.7 Maximum power point tracking and industrial inverters

A novel maximum power point tracking (MPPT) algorithm specifically for use with low-cost industrial drive inverters was proposed and demonstrated as discussed in Chapter 9. The algorithm appeared to perform well under steady sun, but needs further refinement to track unsteady conditions more rapidly. The algorithm could readily be applied to PV water pumping applications, and it would be interesting to compare its performance with existing MPPT techniques used with industrial inverters.

12.8 Batteryless PV-RO hardware demonstration

The design features outlined above were brought together in hardware, and seawater RO operating from a PV array *without* batteries was successfully demonstrated (Chapter 10).

The rate of water production varied according to the irradiance, as shown in Figure 10-1, and the variable recovery ratio can be seen in Figure 10-5. The overall water production was in line with expectations, given that the testing was performed in the UK, with many passing clouds, and that the PV array used was only 64 % of the design size. These factors are removed when one considers the specific energy consumption shown in Figure 10-4. It is a little higher than predicted because one pump and one motor were taken from the earlier test rig and do not quite match the design. Despite this, efficient operation is achieved over a wide range of input power, enabling the system to make good use of the available power from the PV.

12.9 System complexity and reliability

The energy-efficient operation of the system just described is achieved, in part, through the addition of components that undeniably increase its complexity and may adversely affect reliability. The Clark pump required some maintenance during the course of this project, and the implementation of variable recovery ratio introduces a second inverter, motor and pump to the system. Clearly, reliability is a critical factor for any desalination system intended to provide drinking water in remote locations, and it is recommended that reliability be treated as a priority alongside energy-efficiency in the future development of PV-RO.

12.10 Instrumentation

The instrumentation of the test rig centred on National Instruments' data-acquisition hardware and LabView software, both of which are excellent and are recommended for future work of this type. Turbine flow meters were found to be inadequate and were replaced by oval-gear flow meters, which are much more satisfactory. Concentration measurements were initially error prone but were improved as discussed in section 4.11. Torque measurements remain prone to electrical noise from the inverter-driven motors, and it is recommended that the load cells be mounted further from the motors in future.

12.11 Software modelling

The use of Matlab-Simulink for the modelling of the complete PV-RO system proved successful. The model includes everything from the solar irradiance striking the photovoltaic panels through to the water in the product tank. It models the variations of flows and pressures throughout the system with respect to variations in irradiance and feed-water temperature, and it can, for example, perform an hour-by-hour simulation of a whole year of operation. A critical feature of the model is its structure, described in sections 5.1 and 6.1, which allows the components, such as motors, pumps and RO modules, to be added, deleted and reconnected simply by manipulating the blocks and interconnections of the graphical interface.

The model was used to evaluate alternative system configurations and to minimise the *Capital cost per daily water production*, as shown in section 6.3. The components of the model were developed from in-house testing supplemented by manufacturer's data, and the performance predications it gave showed good agreement with measurements taken later from the test rig. The use of Simulink and the model structure described is recommended for future modelling of variable-flow RO systems.

12.12 Market identification

The system described in this thesis is one of many seawater PV-RO demonstrations worldwide, and it appears that the technology could soon be commercialised, as has already happened with brackish-water PV-RO. However, interest in PV-RO today seems dominated by *technology push*, with rather less evidence of *market pull*. A precise identification of the market for such systems is now required.

Published Papers

Desalination

Thomson, Murray, Marcos S. Miranda and David Infield (2003). A small-scale seawater reverse-osmosis system with excellent energy efficiency over a wide operating range. *Desalination* **153**(1-3): 229-236. Also available at: http://www.desline.com/articoli/4925.pdf (accessed: March 04)

Thomson, Murray and David Infield (2003). A photovoltaic-powered seawater reverse-osmosis system without batteries. *Desalination* **153**(1-3): 1-8. Also available at: http://www.desline.com/articoli/4895.pdf (accessed: March 04)

Thomson, Murray and David Infield (2003). A Reverse-Osmosis System for the Desalination OF Seawater Powered by Photovoltaics Without Batteries. *Proceedings of Renewable Energy Sources for Islands, Tourism and Water Desalination Conference*. Crete, Greece, May 2003, EREC (European Renewable Energy Council) page 551

Thomson, Murray, Jo Gwillim, Andrew Rowbottom, Ian Draisey and Marcos Miranda (2001). *Batteryless Photovoltaic Reverse-Osmosis Desalination System*, S/P2/00305/REP, ETSU, DTI, UK. Also available at: http://www.dti.gov.uk/energy/renewables/publications/pdfs/SP200305.pdf (accessed: March 04)

Others

Thomson, Murray (2000). Automatic voltage control relays and embedded generation – Part 1. *IEE Power Engineering Journal* **14**(2): 71-76

Thomson, Murray (2000). Automatic voltage control relays and embedded generation – Part 2. *IEE Power Engineering Journal* **14**(3): 93-99

References

Abufayed, A.A. (2003). Performance characteristics of a cyclically operated seawater desalination plant in Tajoura, Libya. *Desalination* **156**: 59-65

Al Suleimani, Zaher and V. Rajendran Nair (2000). Desalination by solar-powered reverse osmosis in a remote area of the Sultanate of Oman. *Applied Energy* **65**(1-4): 367-380

Alawaji, Saleh, Mohammed Salah Smiai, Shah Rafique and Byron Stafford (1995). PV-Powered Water Pumping and Desalination Plant for Remote Areas in Saudi Arabia. *Applied Energy* **52**(2-3): 283-289

Andrews, W. T., Wil F. Pergande and Gregory S. McTaggart (2001). Energy performance enhancements of a 950 m3/d seawater reverse osmosis unit in Grand Cayman. *Desalination* **135**(1-3): 195-204

Andrews, William T. and David S. Laker (2001). A twelve-year history of large scale application of work-exchanger energy recovery technology. *Desalination* **138**(1-3): 201-206

Arrindell, E. M. and J. D. Birkett (2002). Aruba's Early Experiences in Desalination. *International Desalination and Water Reuse Quarterly* **12**(3): 30-37

Assimacopoulos, D., R. Morris and A. Zervos (2001). Water, Water everywhere..: Desalination Powered by Renewable Energy Sources. *REFOCUS, Elsevier*. Also available at: http://www.re-focus.net/jul2001_4.html (accessed: March 04)

ASTM (1985). D4516-85 Standard Practice for Standardizing Reverse Osmosis Performance Data

ASTM (1998). D1141-98e1 Standard Practice for the Preparation of Substitute Ocean Water.

Avlonitis, S. A., I. Poulios, N. Vlachakis, S. Tsitmidelis, K. Kouroumbas, D. Avlonitis and M. Pavlou (2003). Water resources management for the prefecture of Dodekanisa of Greece. *Desalination* **152**(1-3): 41-50

BP-Solar (2002). *BP 585 photovoltaic module datasheet*, 02-3009-2B 6/02. Also available at: www.bpsolar.com (accessed: May 03)

Bray, D. T. (1966). Engineering of Reverse-Osmosis Plants. *Desalination by Reverse Osmosis*. U. Merten. Cambridge, Massachusetts, M.I.T. Press

Buros, O.K. (2000). *The ABCs of Desalting*. Topsfield, Massachusetts, USA, International Desalination Association. Also available at: http://www.idadesal.org/ABCs1.pdf (accessed: March 04)

Byrne, Wes (1995). *Reverse Osmosis - A practical guide for industrial users*. Littleton, CO, USA, Tall Oaks

Cabassud, Corinne and David Wirth (2003). Membrane distillation for water desalination: how to choose an appropriate membrane? *Desalination* **157**: 307-313

Cansdale, Richard (2001). The installation of a new sub-sand sea water intake for La Source, Grenada. *International Desalination and Water Reuse Quarterly* **11**(3): 40-43

Chamberlin, Charles E., Peter Lehman, James Zoellick and Gian Pauletto (1995). Effects of mismatch losses in photovoltaic arrays. *Solar Energy* **54**(3): 165-171

Childs, Willard D. and Ali E. Dabiri (1998). *Vari-Ro Desalting Pilot Plant Testing And Evaluation Final Technical Report*, Water Treatment Technology Program Report No. 30, Assistance Agreement No. 14255-FC-Sl-20410, U. S. Department of the Interior, May 1998, Science Applications International Corporation, San Diego, CA

Childs, Willard D. and Ali E. Dabiri (1999). Hydraulic Driven RO Pump & Energy Recovery System. *International Desalination and Water Reuse Quarterly* **9**(2): 21-29

Childs, Willard D. and Ali E. Dabiri (2000). *VARI-RO Solar-powered Desalting Study*, MEDRC Project: 97-AS-005a, March 2000, MEDRC: The Middle East Desalination Research Center, Muscat, Sultanate of Oman. Also available at: http://www.medrc.org/ (accessed: March 04)

Childs, Willard D., Ali E. Dabiri, Hilal A. Al-Hinai and Hussein A. Abdullah (1999). VARI-RO solar-powered desalting technology. *Desalination* **125**(1-3): 155-166

CRES (1998). *Desalination Guide Using Renewable Energies, THERMIE - DG XVII, European Commission Report*, ISBN 960-90557-5-3., CRES, Greece

Danfoss (2002). *Danfoss Water Pumps type APP 0.6/1.0 , APP 1.8/2.2 and APP 5.1/6.5/7.2/8.2*, Danfoss, Nordborg, Denmark

Delyannis, E. and V. Belessiotis (2001). Research and Technological Applications in Solar Desalination. *International Journal of Island Affairs - The Water-Energy Binomial* **10**(1): 7-11

Doman, D.G., Bowie G. Keefer and J.L. Richardson (1982). Performance of energy recovery triplex pumps developed for reverse osmosis desalination. *10th Annual Conference of the Water Supply Improvement Association*. Honolulu, July 1982

Doujak, Eduard and Bernhard List (2003). Application of PIV for the Design of Pelton Runners for RO-Systems. *Proceedings of Renewable Energy Sources for Islands, Tourism and Water Desalination Conference*. Crete, Greece, May 2003, EREC (European Renewable Energy Council) pp 533-540

DOW (1995). *FILMTEC Membrane Elements - Technical Manual*, April 1995, Dow Liquid Separations. Also available at: http://www.dow.com/liquidseps/lit/down_lit.htm (accessed: March 04)

DOW (2000). *ROSA, Version 4.2*. Dow Liquid Separations. Also available at: http://www.dow.com/liquidseps/design/rosa.htm (accessed: March 04)

Druck (1997). *PDCR 800 SERIES Datasheet*, 12/1997, Druck Limited, Fir Tree Lane, Groby, Leicester LE6 0FH England. Also available at: www.druck.com (accessed: March 04)

Dunlop, James P. and Brian N. Farhi (2001). Recommendations For Maximizing Battery Life In Photovoltaic Systems: A Review Of Lessons Learned. *Proceedings of Forum 2001, Solar Energy: The Power to Choose, Washington, DC*

El-Dessouky, Hisham T. and Hisham M. Ettouney (2002). *Fundamentals of Salt Water Desalination*. Amsterdam, Elsevier

El-Nashar, Ali M. (2001). The economic feasibility of small solar MED seawater desalination plants for remote arid areas. *Desalination* **134**(1-3): 173-186

EPA (2004). National Secondary Drinking Water Regulations, US Environmental Protection Agency. Also available at: http://www.epa.gov/safewater/mcl.html (accessed: March 04)

Espino, Tomas, Baltasar Penate, Gonzalo Piernavieja, Dirk Herold and Apostel Neskakis (2003). Optimised desalination of seawater by a PV powered reverse osmosis plant for a decentralised coastal water supply. *Desalination* **156**: 349-350

Fabre, Aurélie (2003). Wind turbines designed for the specific environment of islands case study: Experience of an autonomous wind powered water desalination system on the island of Therasia, Greece - Vergnet SA, France. *Proceedings of Renewable Energy Sources for Islands, Tourism and Water Desalination Conference*. Crete, Greece, May 2003, EREC (European Renewable Energy Council) pp 247-252

Garcia-Rodriguez, Lourdes (2002). Seawater desalination driven by renewable energies: a review. *Desalination* **143**(2): 103-113

Gocht, W., A. Sommerfeld, R. Rautenbach, Th. Melin, L. Eilers, A. Neskakis, D. Herold, V. Horstmann, M. Kabariti and A. Muhaidat (1998). Decentralized desalination of brackish water by a directly coupled reverse-osmosis-photovoltaic-system - A pilot plant study in Jordan. *Renewable Energy* **14**(1-4): 287-292

Gotor, Antonio Gomez, gnacio De la Nuez and Celso Argudo Espinoza (2003). Optimization of RO desalination systems powered by renewable energies. *Desalination* **156**: 351-351

Gottschalg, Ralph (2001). Module/Cell Performance Evaluation. *Photovoltaic Technology for Bangladesh*. A. K. M. S. Islam and D. G. Infield, Bangladesh University of Engineering and Technology, Dhaka

Green, Donna (2003). Thailands solar white elephants an analysis of 15yr of solar battery charging programmes in northern Thailand. *Energy Policy*

Green, Martin A. (1995). *Silicon Solar Cells - Advanced Principles and Practice*. Sydney, Australia, Centre for Photovoltaic Devices and Systems, Univeristy of New South Wales

Gwillim, Jo (1996). *Village Scale Photovoltaic Powered Reverse Osmosis*, March 1996, Dulas Limited, Machynlleth, Wales

Gwillim, Jo (2001). Pesonal Communication. Dulas Limited, Machynlleth, Wales

Hasnain, Syed M. and Saleh A. Alajlan (1998). Coupling of PV-powered RO brackish water desalination plant with solar stills. *Desalination* **116**(1): 57-64

Herold, D., V. Horstmann, A. Neskakis, J. Plettner-Marliani, G. Piernavieja and R. Calero (1998). Small scale photovoltaic desalination for rural water supply-demonstration plant in Gran Canaria. *Renewable Energy* **14**(1-4): 293-298

Herold, Dirk and Apostolos Neskakis (2001). A small PV-driven reverse osmosis desalination plant on the island of Gran Canaria. *Desalination* **137**(1-3): 285-292

IEA (1999). *Lead acid battery guide for stand alone photovoltaic systems*, IEA-PVPS 3-06:1999, December 1999, International Energy Agency Photovoltaic Power Systems Programme

IEA (2002). *Testing of batteries used in Stand Alone PV Power Supply Systems*, IEA PVPS T3-11: 2002, October 2002, International Energy Agency Photovoltaic Power Systems Programme

IPCC (2001). Climate Change 2001: The Scientific Basis. Contribution of Working Group I to the Third Assessment Report of the Intergovernmental Panel on Climate Change. J. T. Houghton, Y. Ding, D.J. Griggs, M. Noguer, P.J. van der Linden, X. Dai, K. Maskell, and C.A. Johnson (eds.), Cambridge University Press

Jensen, Thomas Lynge (2000). *Renewable Energy on Small Islands*, Forum for Energy and Development (FED)

Johnson, James S., Lawrence Dresner and Kurt A. Kraus (1966). Hyperfiltration (Reverse Osmosis). *Principles of Desalination*. K. S. Spiegler. New York, Academic Press

Kalogirou, Soteris (1997). Survey of solar desalination systems and system selection. *Energy* **22**(1): 69-81

Kapp, Gisbert (1888). *Society of Telegraph Engineers and Electricians*

Keefer, Bowie G. (1980). *Reverse osmosis method and apparatus*. United States Patent 4,187,173

Keefer, Bowie G. (1984). *Multi-cylinder reverse osmosis apparatus and method*. United States Patent 4,434,056

Keefer, Bowie G., R. D. Hembree and F. C. Schrack (1985). Optimized matching of solar photovoltaic power with reverse osmosis desalination. *Desalination* **54**: 89-103

Koch (2000). *Seawater Design Guide - Reverse Osmosis Membrane Systems*. Wilmington, Koch Membrane Systems

Koch-ROPRO (2000). *ROPRO Version 6.1*. Fluid Systems, Koch Membrane Systems, .

Kolhe, Mohanlal, Sunita Kolhe and J. C. Joshi (2002). Economic viability of stand-alone solar photovoltaic system in comparison with diesel-powered system for India. *Energy Economics* **24**(2): 155-165

Koschikowski, Joachim, Matthias Rommel and Marcel Wieghaus (2003). Solar thermal-driven desalination plants based on membrane distillation. *Desalination* **156**: 295-304

Kunczynski, Yan (2003). Development and Optimization of 1000-5000 GPD Solar Power SWRO. *IDA World Congress on Desalination and Water Reuse*. Bahamas, Sept 28-Oct 3 2003

Laborde, H. M., K. B. Franca, H. Neff and A. M. N. Lima (2001). Optimization strategy for a small-scale reverse osmosis water desalination system based on solar energy. *Desalination* **133**(1): 1-12

Lührs, I. (2003). ENERCON Desalination: Sustainable solutions for drinking water production. *Proceedings of Renewable Energy Sources for Islands, Tourism and Water Desalination Conference*. Crete, Greece, May 2003, EREC (European Renewable Energy Council) pp 221-222

MacHarg, John P. (2001). Exchanger Tests Veryfy 2.0 kWh/m^3 SWRO Energy Use. *International Desalination and Water Reuse Quarterly* **11**(1): 42-46

MacHarg, John P. (2002). The Evolution of SWRO Energy-Recovery Systems. *International Desalination and Water Reuse Quarterly* **11**(4): 48-53

Manth, Thomas, Michael Gabor and Eli Oklejas Jr. (2003). Minimizing RO energy consumption under variable conditions of operation. *Desalination* **157**: 9-21

Markvart, Tomas (1999). *Solar electricity*. Chichester, Wiley

Maslin, Anthony, David Annandale and Marc Saupin (2003). Decentralised water solutions Island infrastructure project. *Proceedings of Renewable Energy Sources for Islands, Tourism and Water Desalination Conference*. Crete, Greece, May 2003, EREC (European Renewable Energy Council) pp 287-294

Mathew, Kuruvilla, Stewart Dallas, Goen Ho and Martin Anda (2001). Innovative Solar-Powered Village Potable Water Supply. *Women Leaders on the Uptake of Renewable Energy Seminar*. Perth, Australia, June 2001. Also available at: http://acre.murdoch.edu.au/unep/papers/Mathew.pdf (accessed: March 04)

Merten, Ulrich and (Editor) (1966). *Desalination by Reverse Osmosis*. Cambridge, Massachusetts, M.I.T. Press

Millero, F.J. (1996). *Chemical Oceanography*, CRC Press. Also available at: http://fig.cox.miami.edu/~lfarmer/MSC215/216major.htm (accessed: March 04)

Miranda, Marcos S. (2003). *Small-Scale Wind-Powered Seawater Desalination Without Batteries*, Ph.D Thesis (Forthcoming), Loughborough University

Norris, W. T. (1999). The hundred year hunt. *Power Engineering Journal* **13**(3): 184

Oklejas, Eli (2002). Energy Efficiency Considerations for RO plants: A Method for Evaluation. *International Desalination and Water Reuse Quarterly* **11**(4): 26-39

Oldach, Rolf (2001). *Matching renewable energy with desalination plants*, MEDRC Project: 97-AS-006a, September 2001, IT Power Ltd. Sponsored by MEDRC: The Middle East Desalination Research Center, Muscat, Sultanate of Oman. Also available at: http://www.medrc.org/ (accessed: March 04)

Parish, Oliver (1999). Economic aspects. *Stand-Alone Photovoltaic Applications: Lessons Learned*. G. Loois and B. V. Hemert. London, James and James pp 10-13

Permar, Clark (1995). *Liquid treatment apparatus for providing a flow of pressurized liquid*. United States Patent 5,462,414

Pinkerton, Harry E. (1979). *Fluid handling system*. United States Patent 4,178,240

Rahal, Zeina (2001). *Wind powered desalination*, Ph.D Thesis, Loughborough University

Reid, C. E. (1966). Principles of Reverse Osmosis. *Desalination by Reverse Osmosis*. U. Merten. Cambridge, Massachusetts, M.I.T. Press

Richards, Bryce S. and Andrea I. Schafer (2003). Photovoltaic-powered desalination system for remote Australian communities. *Renewable Energy* **28**(13): 2013-2022

Roberts, Simon (1991). *Solar electricity : a practical guide to designing and installing small photovoltaic systems*. New York, Prentice Hall International

Rodriguez-Girones, R J., Miriam Rodriguez Ruiz and Jose M. Veza (1996). *Experience on Desalination with Renewable Energy Sources, Work Package 1, EURORED*,

APAS RENA-CT94-0063, March 1996, Universidad de Las Palmas de Gran Canaria

Romo, Rodrigo F. V. and M. Michael Pitts (1999). Application of Electrotechnology for Removal and Prevention of Reverse Osmosis Biofouling. *Environmental Progress* **18**(2): 107

Sardi, L. (1996). R.O. Deslainators Powered by PV Systems for Small/Medium Italian Islands. *Proceedings of the Mediterranean Conference on Renewable Energy Sources for Water Production*. Santorini, Greece, June 1996 pp 36-44

Sauer, D. U., M. Bachler, G. Bopp, W. Hohe, J. Mittermeier, P. Sprau, B. Willer and M. Wollny (1997). Analysis of the performance parameters of lead/acid batteries in photovoltaic systems. *Journal of Power Sources* **64**(1-2): 197-201

Schwarz, Joshua (2000). *Beach well intakes for small seawater reverse osmosis plants*, MEDRC 97-BS-015, August 2000, TAHAL Consulting Engineers Ltd, Tel Aviv, Israel. Also available at: http://www.medrc.org/ (accessed: March 04)

Smith, David (2000). Battery-powered desalter relies on unique pressure pump. *International Desalination and Water Reuse Quarterly* **10**(3): 18-22

Snoke, J. A. (2002). GEOL 4104: Properties of Seawater Physical Oceanography. Also available at: http://www.geol.vt.edu/profs/jas/pdf/4104-properties.pdf (accessed: March 04)

Snyder, A. E. (1966). Freezing Methods. *Principles of Desalination*. K. S. Spiegler. New York, Academic Press

Spectra (2003). *Clark Pump Field Repair & Rebuild Manual*, 22/08/03, Spectra Watermakers, San Rafael, California. Also available at: http://www.spectrawatermakers.com/documents/Repair3.pdf (accessed: March 04)

Spiegler, K.S. and Y.M. El-Sayed (1994). *A Desalination Primer Introductory book for studcms and newcomers to desalination*, Balaban Desalination Publications

Stewart, Robert H. (2002). *Introduction To Physical Oceanography*, Department of Oceanography

Texas A & M University. Also available at: http://oceanworld.tamu.edu/resources/ocng_textbook/PDF_files/book_pdf_files.html (accessed: March 04)

Thomson, Murray, Jo Gwillim, Andrew Rowbottom, Ian Draisey and Marcos Miranda (2001). *Batteryless Photovoltaic Reverse-Osmosis Desalination System*, S/P2/00305/REP, ETSU, DTI, UK. Also available at: http://www.dti.gov.uk/energy/renewables/publications/pdfs/SP200305.pdf (accessed: March 04)

Tonner, Jodie (1999). *Standard Seawater*, 13 April, 1999, World Wide Water. Also available at: http://www.world-wide-water.com/PDFs/Std%20SW%20ions%20xls.pdf (accessed: March 04)

Tzen, Eftihia and Marios Sigalas (2003). Design and Development of a Hybrid Autonomous System for Seawater Desalination. *Proceedings of Renewable Energy Sources for Islands, Tourism and Water Desalination Conference*. Crete, Greece, May 2003, EREC (European Renewable Energy Council) pp 231-238

UNESCO (2003). *The United Nations World Water Development Report - Water for People - Water for Life (Executive Summary)*, UNESCO Publishing / Berghahn Books

Wagner, Jørgen (2001). *Membrane Filtration Handbook - Practical Tips and Hints*, Osmonics. Also available at: http://www.osmonics.com/library/mfh.htm (accessed: March 04)

Wangnick, Klaus (2002). *IDA Worldwide Desalination Plants Inventory*, Report No. 17, Wangnick Consulting GmbH

Weber-Shirk, Monroe L. (2003). *Laboratory Measurements and Procedures*. Also available at: http://ceeserver.cee.cornell.edu/mw24/cee453/Lab_Manual/pdf/Lab%20Measurements.pdf (accessed: June 03)

Weiner, Dan, David Fisher, Eduard J. Moses, Baruch Katz and Giora Meron (2001). Operation experience of a solar- and wind-powered desalination demonstration plant. *Desalination* **137**(1-3): 7-13

Wenham, Stuart R., Martin A. Green and Muriel. E. Watt (1994). *Applied Photovoltaics*, Centre for Photovoltaic Devices and Systems, Australia

WHO (2003). *Guidelines for Drinking-Water Quality (Draft) 3rd Edition*, 17 February 2003, World Health Organization

Wilamowski, Bogdan M and Xiangli Li (2002). Fuzzy System Based Maximum Power Point Tracking for PV System. *IEEE*

Wilson, Leslie P. S. (1983). *Reverse osmosis liquid purification apparatus*. United States Patent 4,367,140

Wiseman, Robin (2002). IDA Desalination Inventory: Installed capacity doubles in less than two years. *International Desalination and Water Reuse Quarterly* **12**(3): 10-13

Appendix A Details of testing carried out using the initial test rig

This appendix provides details of the testing outlined in Chapter 3.

A.1 Instrumentation and data-acquisition

The instrumentation and data-acquisition system used with the initial test rig was based on National Instruments hardware and LabView software as described in Chapter 4. Analogue signals were sampled at 1 kHz and then averaged and logged at 1 Hz. Pulse signals were converted to frequency and also logged at 1 Hz. The sensors were broadly as described in Chapter 4, though the following details should be noted.

Electrical input power to the inverter was measured using a Elcontrol VIP96-APQ power meter, which has an integral digital display of real and reactive power and provides analogue outputs representing each. These were connected to analogue inputs of the LabView-based data-acquisition system, which was calibrated simply to match the digital display on the Elcontrol power meter. Unfortunately, the calibration of the Elcontrol meter itself was undermined by the fact that the current drawn by the inverter is non-sinusoidal and thus the collected data should be viewed with a degree of caution. This matter was addressed later by dispensing with the Elcontrol power meter and replacing it with instantaneous voltage and current sensors, sampled at 10-kHz directly into LabView, as described in section 4.16.

The flow meters used for this testing were the turbine flow meters detailed in section B.1, which were found to be problematic and were later replaced by the oval-gear flow meters.

Thus, the data presented in this appendix should be viewed with caution. Nonetheless, the testing revealed various matters that were valuable in the design of the new test rig and its instrumentation, as discussed below.

A.2 Procedure and results

The data shown in Table 3-1 was collected from a single run, 3¾ hours long, during which the speed setpoint was ramped up and down three times in steps of 30 rpm, as shown in Figure A-1.

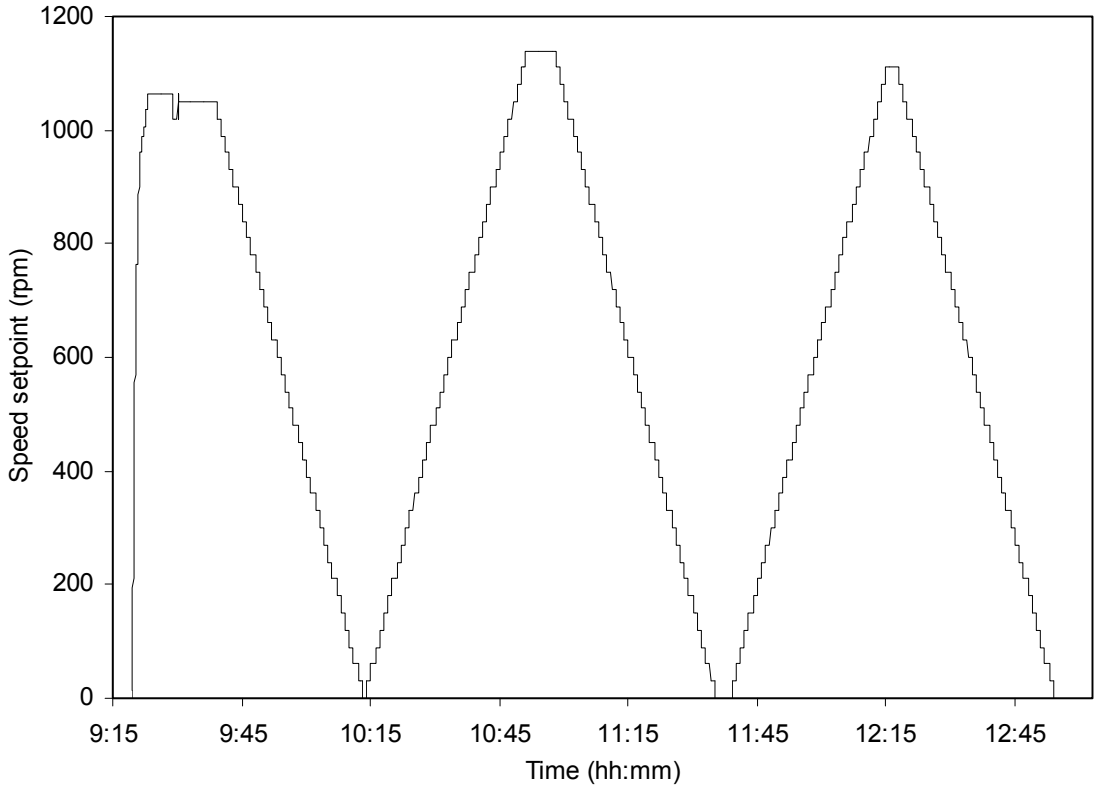

Figure A-1 – Speed setpoint profile

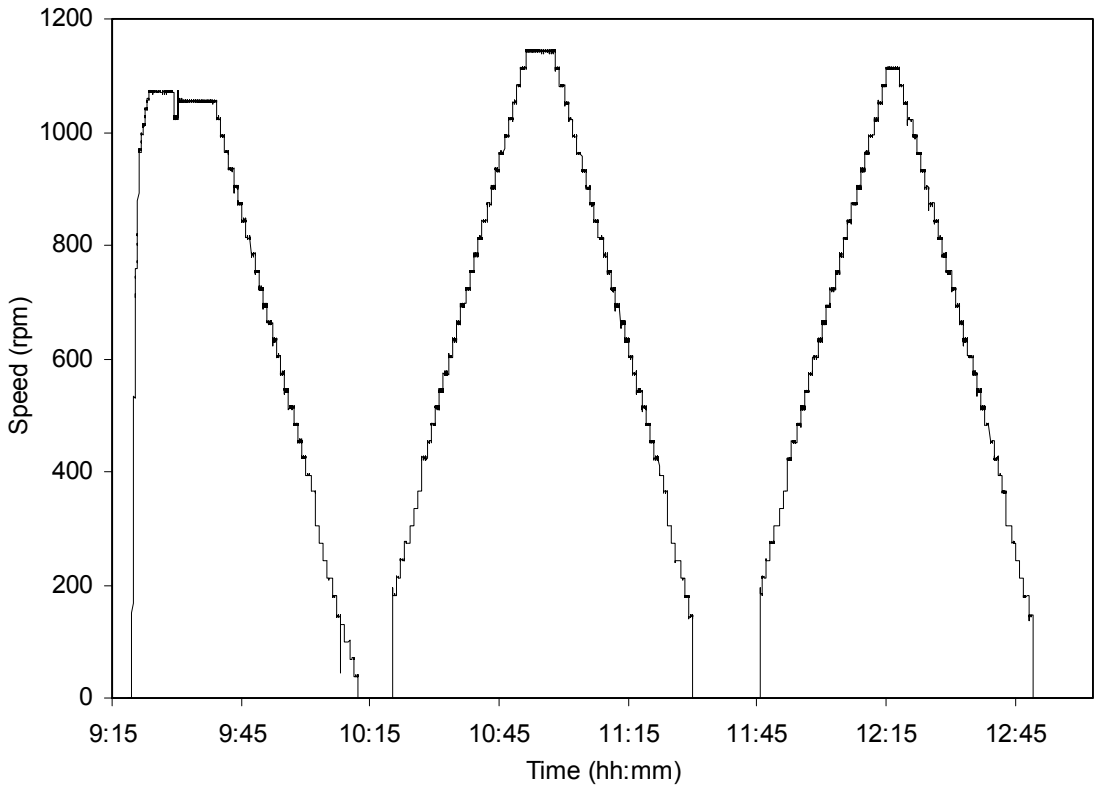

Figure A-2 – Measured speed

The measured speed shown in Figure A-2 closely matches the setpoint shown in Figure A-1, except for the irregular steps between 300 and 400 rpm. These are due to a mode change within the inverter software.

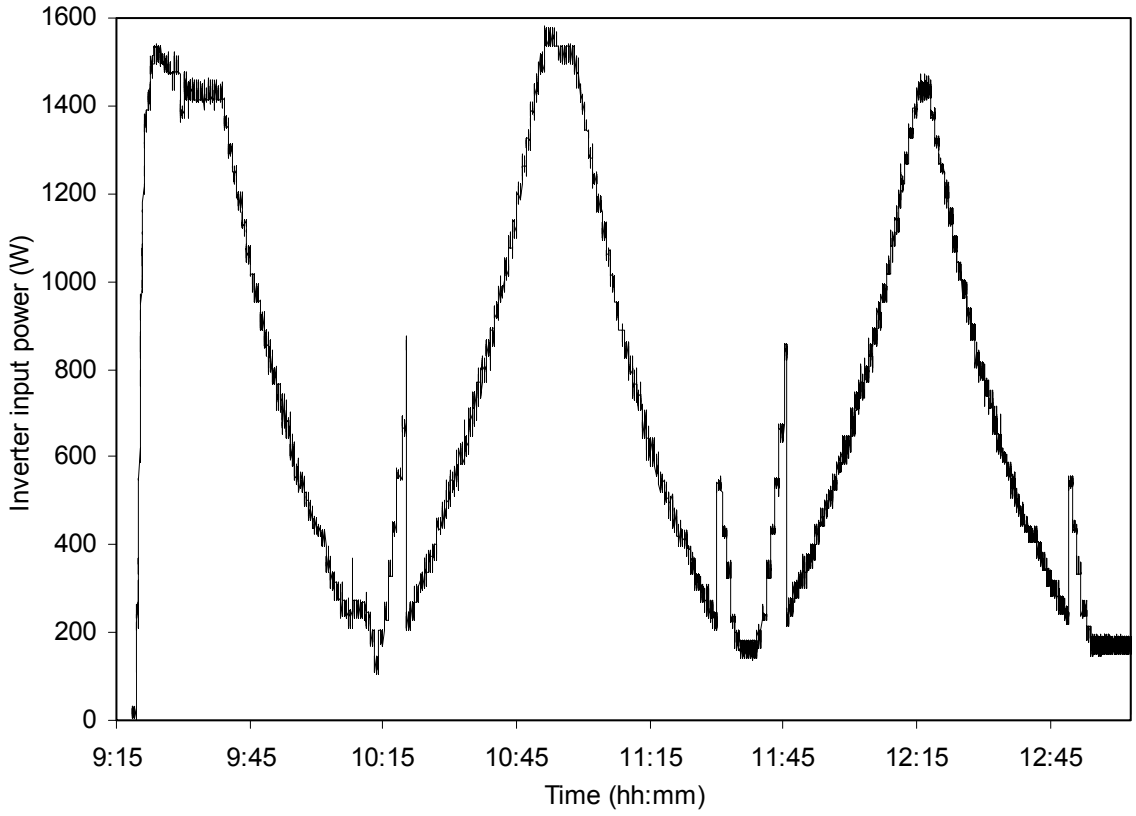

Figure A-3 – Measured inverter input power consumption

Figure A-3 shows the input power to the inverter, and shows the aforementioned mode change more markedly. The inverter in use during this test was a Siemens Micromaster standard industrial drive, which has one mode for normal operation and another for low-speed operation. This improves the performance of the drive in normal industrial applications, where the addition power drawn in the low-speed mode would normally go unnoticed. But for operation direct from a PV array, as discussed in this thesis, it would considerably complicate maximum power point tracking. The inverters used later, with the new test rig, were FKI brand, as described in section 5.7, and did not exhibit any mode-change affects.

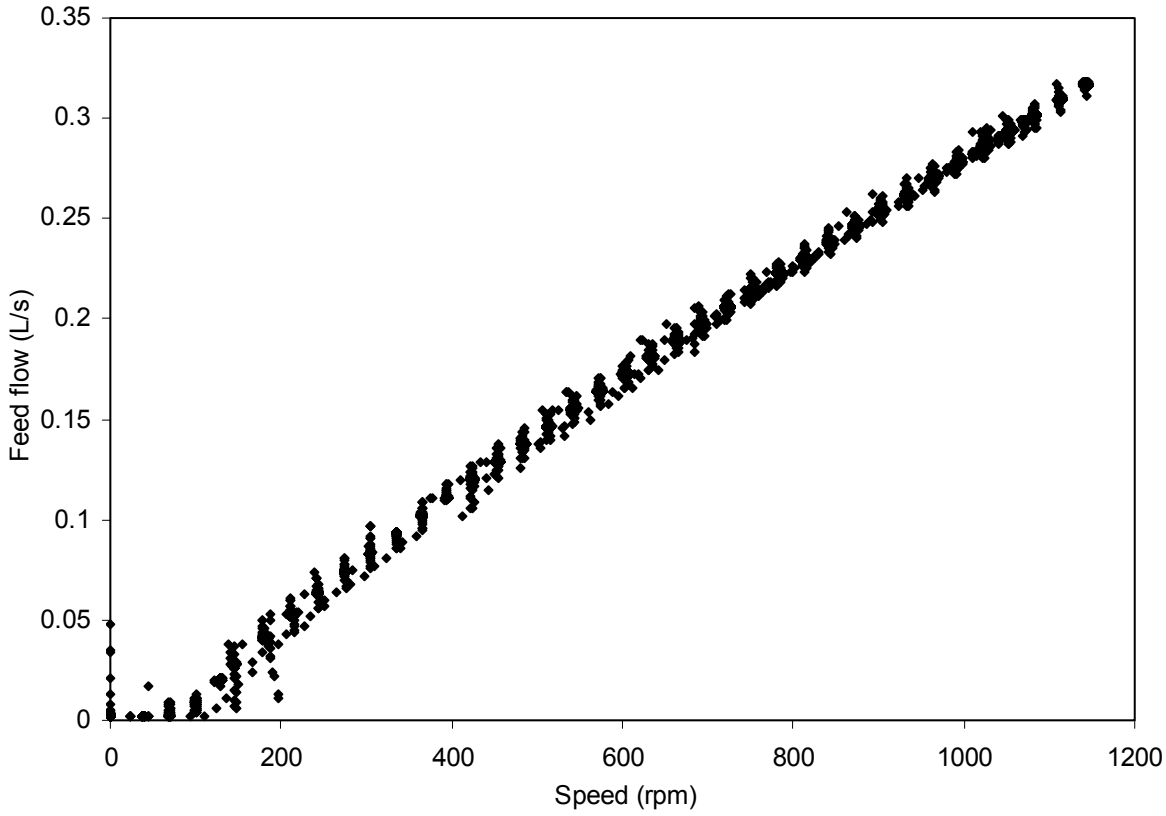

Figure A-4 – Measured feed flow versus pump speed

Figure A-4 shows that the feed flow through the plunger pump is approximately equal to its shaft speed, as expected with a positive displacement pump. The scatter in the figure is due primarily to the inaccuracy of the turbine flow meter in use at the time.

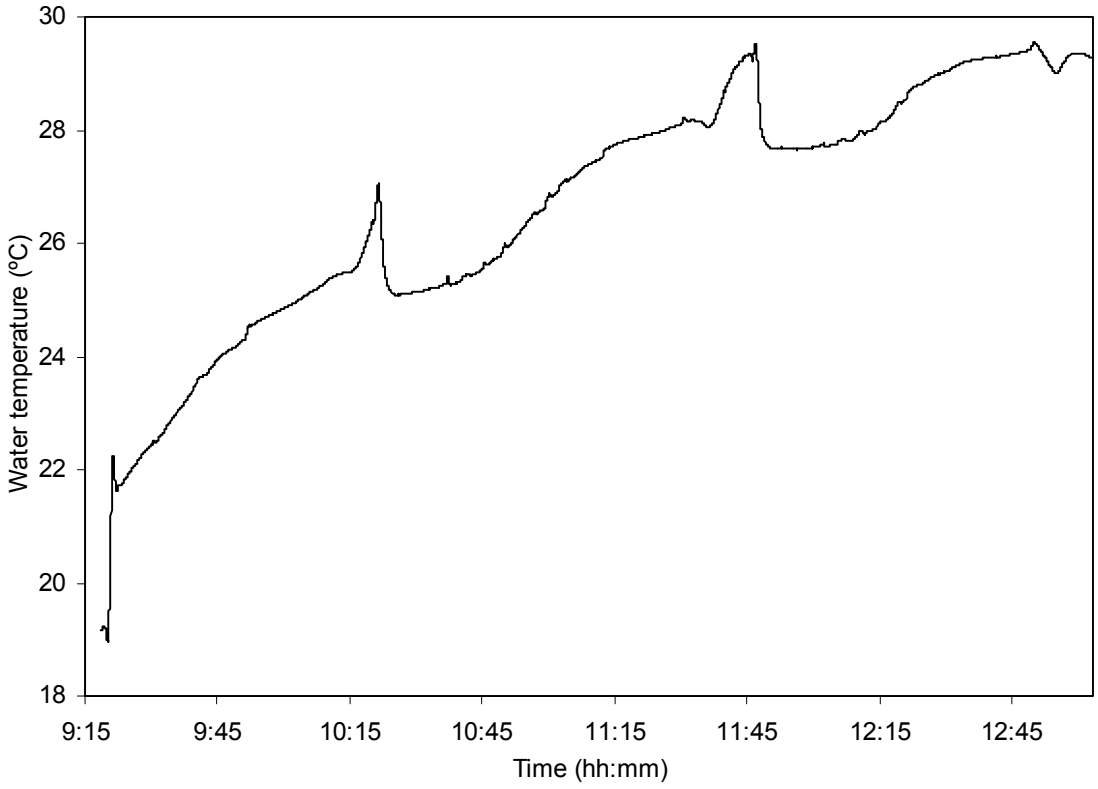

Figure A-5 – Measured water temperature

The water for the test rig is circulated through the tank as shown in Figure 3-1and heats up by virtue of the energy introduced by the two pumps. At the time of the testing described here, there was no cooling mechanism and water temperature rose as shown in Figure A-3. The peaks around 10:20 and 11:45 are where the water is starting to flow again after being stationary for while, see Figure A-2, and yet being heated by the constant-speed centrifugal pump.

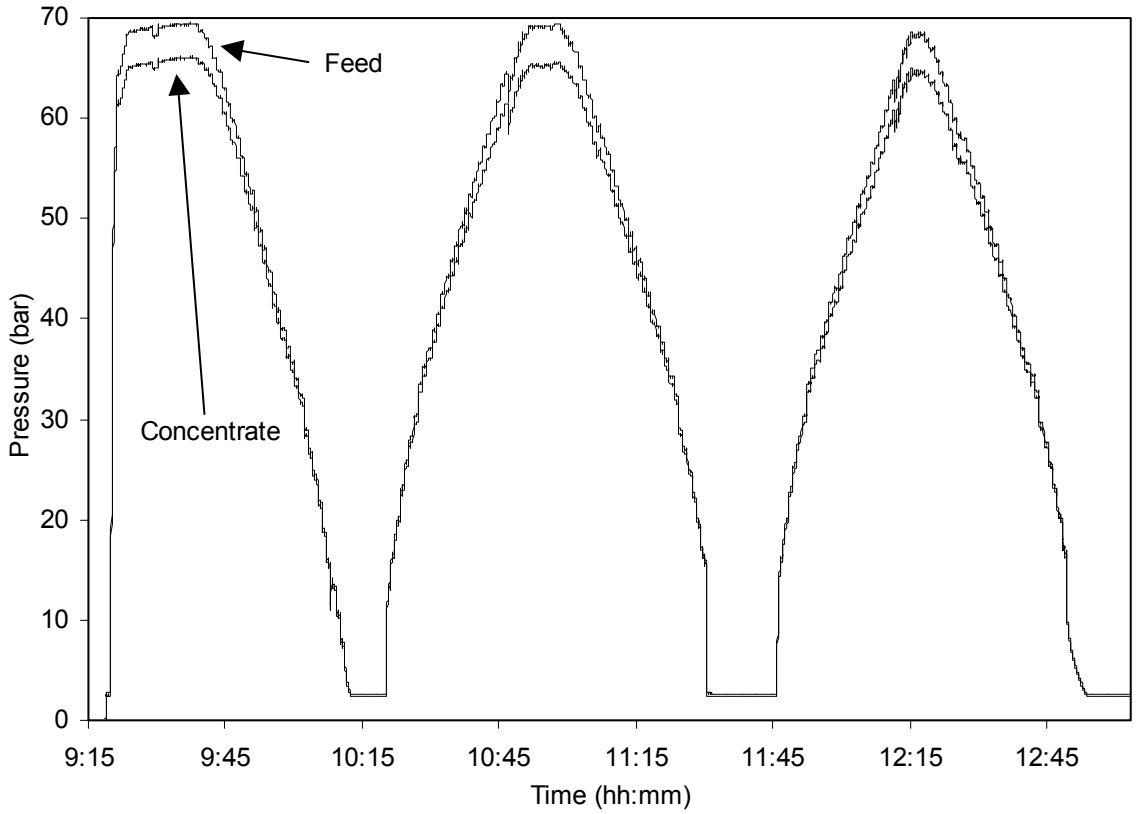

Figure A-6 – Measured feed and concentrate pressures

The measured pressures in Figure A-6 indicate a delta pressure of up to 4 bar, which is unusually high and was caused partly the poor condition of the membranes and partly because they are small-diameter (2½-inch) membrane elements.

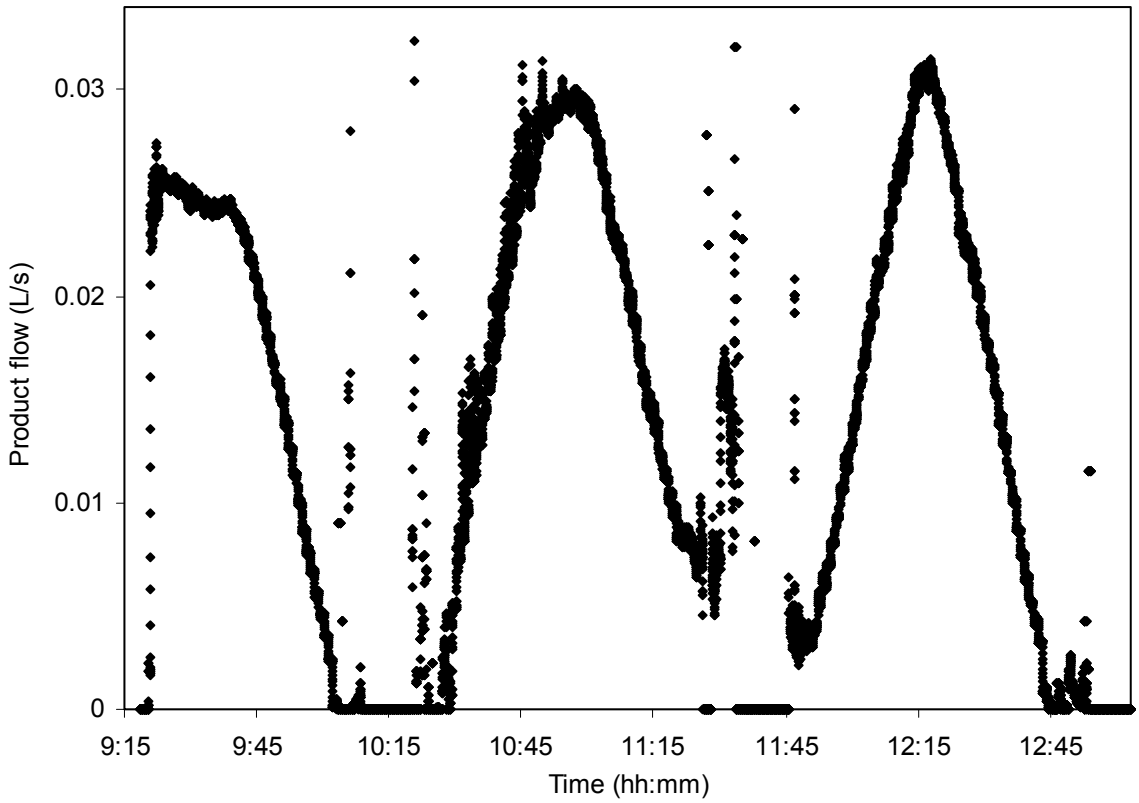

Figure A-7 – Measured product flow

The three main peaks, shown in Figure A-7 (9:30, 10:55 and 12:15), are progressively higher, due to the rising water temperature, shown in Figure A-3.

The periods of virtually no product flow, shown in Figure A-7, from 10:00 until 10:30, from 11:25 to 11:50 and after 12:40 are where the feed pressure, shown in Figure A-6, is below the osmotic pressure ~23 bar. The random product flow recorded during these periods is due primarily to *osmotic suck-back*: the product being sucked back through the membranes by (forward) osmosis. This introduced air in to the product flow pipe and meter, which then gave erratic data until the air was expelled by positive product flow when the feed pressure returned above the osmotic pressure.

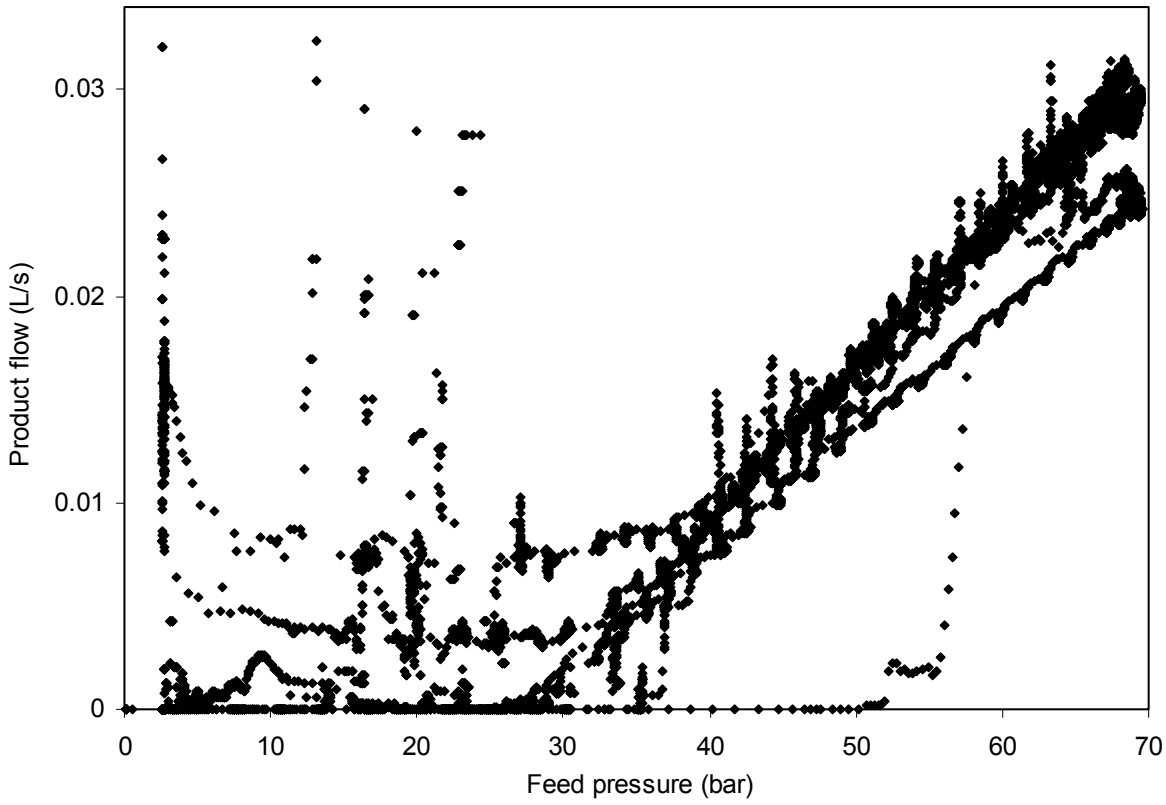

Figure A-8 – Measured product flow versus feed pressure

Figure A-8 illustrates, as expected, that the product flow is roughly proportional to the net driving pressure (the feed pressure less the osmotic pressure). It also highlights the aforementioned affects of water temperature and osmotic suck-back and is marred overall by the errors introduced by the turbine product flow meter, discussed in section B.1.1. Recognition of these problems led to the introduction of the temperature control system discussed in section 4.13 and the oval-gear flow meters.

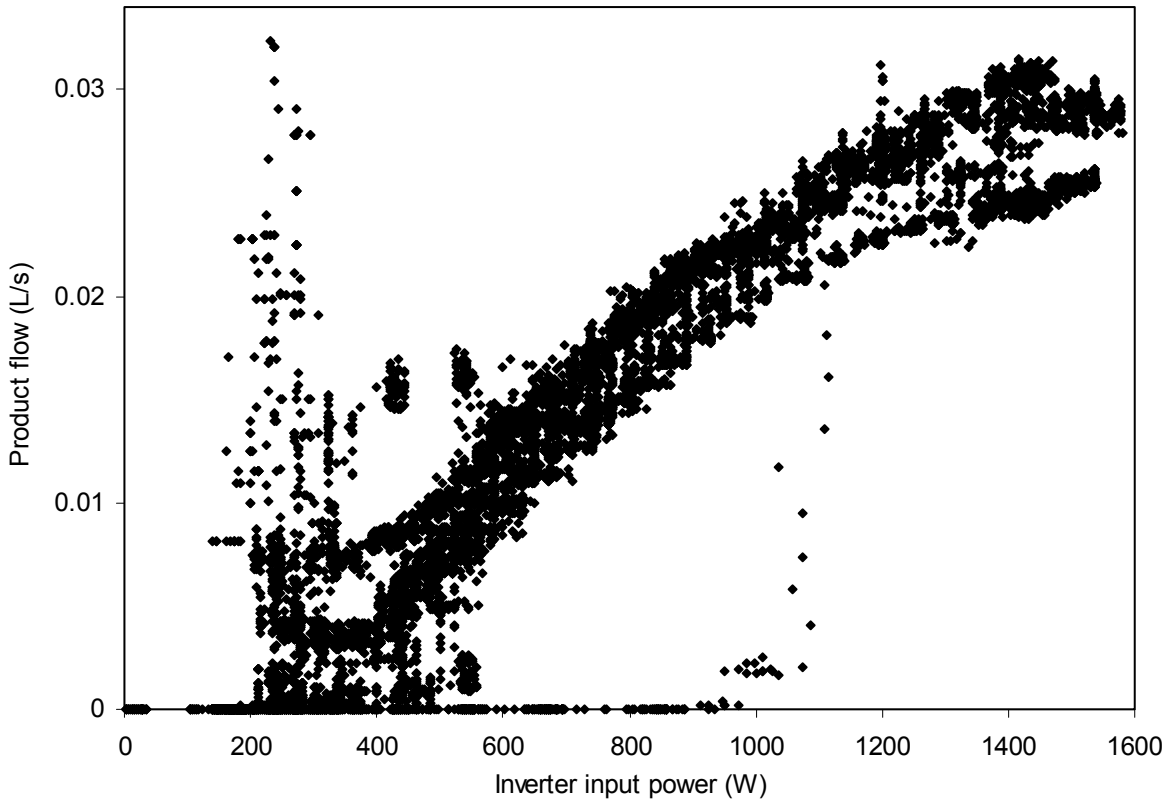

Figure A-9 – Measured product flow versus inverter input power consumption

Figure A-9 again shows the spurious product flow due to suck-back between 200 and 300 W. Ignoring this, it can be seen that water production starts below 400 W and increases to a maximum of ~0.029 L/s at around 1500 W.

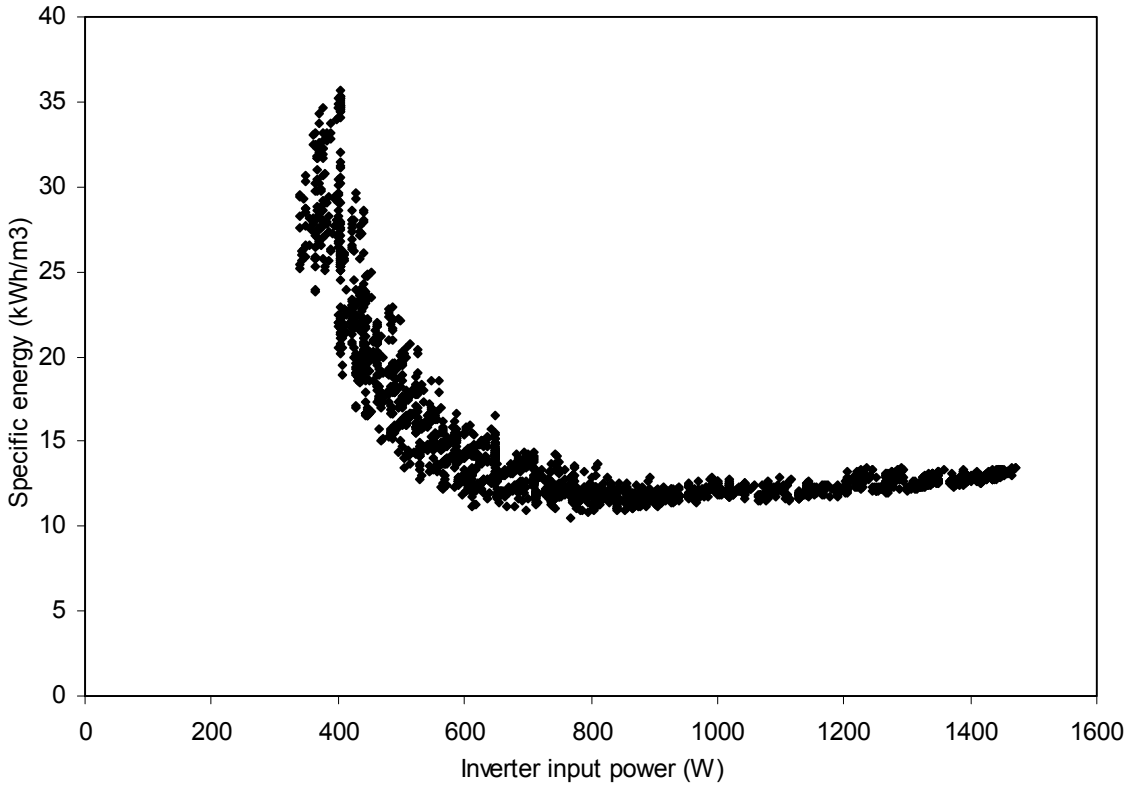

Figure A-10 – Specific energy versus inverter input power

$$specific\ energy\ (\mathrm{kWh/m^3}) = \frac{input\ power\ (\mathrm{W})}{product\ flow\ (\mathrm{L/s})\ \times 3600}$$

Figure A-10 shows the specific energy consumption during the third ramp-up/ramp-down, in particular, between 11:50 and 12:43. This data was selected in order to eliminate spurious data caused by the osmotic suck-back described earlier.

It is apparent that the specific energy is roughly constant between 600 W and 1500 W. This was encouraging in the design of the system intended to operate at variable power directly from a PV array.

The average specific energy across this band is around 13 kWh/m^3, which is very high, perhaps more typical of system without energy recovery, and is caused primarily by the use of very old membranes, during this testing.

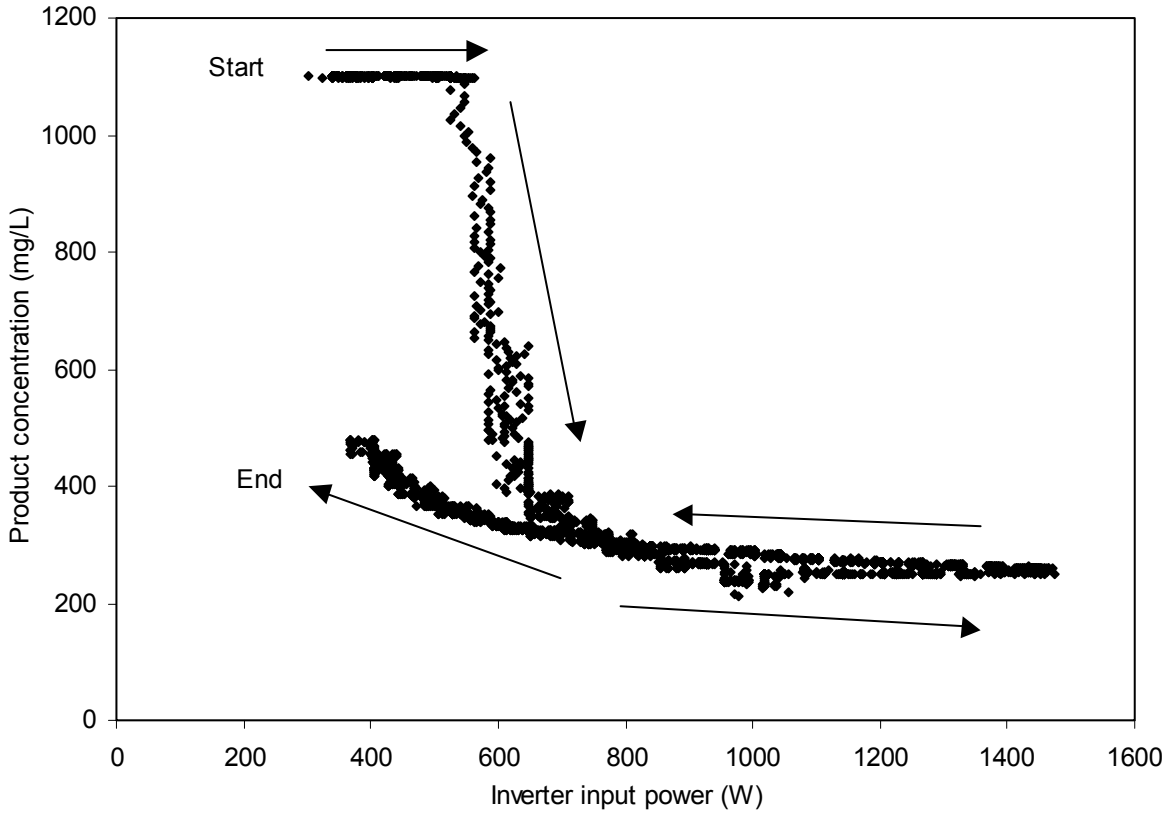

Figure A-11 – Measured product concentration versus inverter input power

Figure A-11 shows the concentration of the product during the same period: between 11:50 and 12:43. Again this data was selected in order to eliminate spurious data caused by osmotic suck-back; in particular, the concentration sensor was affected by the air introduced.

At the start (11:50), the pressure is increasing and the product starts to flow. Initially, it has very high concentration, exceeding the range of the conductivity meter and the recorded data is limited to ~1100 mg/L. The excessive concentration is due to the salt that diffused through the membranes while there was no flow.

As the product flow increases, the concentration falls rapidly to about 400 mg/L at 700 W. Thereafter, the concentration falls to below 300 mg/L at full power.

As the power is reduced, the concentration starts to rise again, and is a little higher than shown at the same power on the ramp-up; this is due to the water temperature being higher, as shown in Figure A-5.

Finally, the concentration rises to around 500 mg/L at 400 W.

A.2.1 Results data summary table

In order to summarise the data presented in the preceding graphs, three nominal input powers were chosen: 500 W, 1,000 W and 1,500 W, and the data was binned at these powers +/– 50 W. The data in these three bins was then averaged to produce Table 3-1.

Electrical input power (W)	502	997	1515
Speed (rpm)	494	864	1130
Electric motor torque (Nm)	6.9	8.7	10.3
Feed pressure (bar)	38.7	58.9	68.9
Concentrate pressure (bar)	37.7	56.4	65.1
Feed concentration (mg/L)	29000	29000	29000
Product concentration (mg/L)	550	283	262
Feed flow (L/s)	0.134	0.233	0.300
Product flow (L/s)	0.0075	0.022	0.0291
Specific energy (kWh/m3)	18.6	12.6	14.4

Table 3-1 – Repeated here for convenience

A.3 Power flow and efficiency calculations for Sankey diagram

The power flows and efficiencies shown on the Sankey diagram of Figure 3-2, are calculated from Table 3-1, as follows. The values shown below correspond to the middle column of Table 3-1.

$$electric\ motor\ shaft\ power = speed \times torque$$

$$= 864\,\text{rpm} \times \frac{2\pi\ \text{rad/s}}{60\,\text{rpm}} \times 8.7\,\text{Nm}$$

$$= 787\,\text{W}$$

$$inverter\ \&\ motor\ losses = electrical\ input\ power - electric\ motor\ shaft\ power$$

$$= 997\,\text{W} - 787\,\text{W}$$

$$= 210\,\text{W}$$

$$feed\ power = feed\ flow \times feed\ pressure$$

$$= 0.233\,\mathrm{L/s} \times \frac{\mathrm{m}^3}{1000\,\mathrm{L}} \times 58.9\,\mathrm{bar} \times \frac{10^5\ \mathrm{Pa}}{\mathrm{bar}}$$

$$= 1372\,\mathrm{W}$$

$$concentrate\ flow = feed\ flow - product\ flow$$

$$= 0.233\,\mathrm{L/s} - 0.022\,\mathrm{L/s}$$

$$= 0.211\,\mathrm{L/s}$$

$$crossflow\ loss = concentrate\ flow \times delta\ pressure$$

$$= concentrate\ flow \times (feed\ pressure - concentrate\ pressure)$$

$$= 0.211\,\mathrm{L/s} \times \frac{\mathrm{m}^3}{1000\,\mathrm{L}} \times (58.9\,\mathrm{bar} - 56.4\,\mathrm{bar}) \times \frac{10^5\ \mathrm{Pa}}{\mathrm{bar}}$$

$$= 53\,\mathrm{W}$$

$$concentrate\ \ power = concentrate\ flow \times concentrate\ pressure$$

$$= 0.211\,\mathrm{L/s} \times \frac{\mathrm{m}^3}{1000\,\mathrm{L}} \times 56.4\,\mathrm{bar} \times \frac{10^5\ \mathrm{Pa}}{\mathrm{bar}}$$

$$= 1190\,\mathrm{W}$$

From section 5.11.6, NaCl solution at 32,800 mg/L has an osmotic pressure of 25.8 bar. The testing described here used NaCl solution at 29,000 mg/L:

$$osmotic\ pressure = 25.8\,\mathrm{bar} \times \frac{29000\ \mathrm{mg/L}}{32800\ \mathrm{mg/L}}$$

$$= 23\ \mathrm{bar}$$

$$desalination\ power = product\ flow \times osmotic\ pressure$$

$$= 0.022\,\mathrm{L/s} \times \frac{\mathrm{m}^3}{1000\,\mathrm{L}} \times 23\,\mathrm{bar} \times \frac{10^5\,\mathrm{Pa}}{\mathrm{bar}}$$

$$= 51\,\mathrm{W}$$

$$throughflow\ loss = feed\ power - crossflow\ loss - concentrate\ power - desalination\ power$$

$$= 1372\,\mathrm{W} - 53\,\mathrm{W} - 1190\,\mathrm{W} - 51\,\mathrm{W}$$

$$= 78\,\mathrm{W}$$

Returning to the plunger pump, an efficiency of 85% is assumed, see section 5.3.

$$pump\ shaft\ power = \frac{feed\ power}{pump\ efficiency}$$

$$= \frac{1372\,\mathrm{W}}{0.85}$$

$$= 1614\,\mathrm{W}$$

$$pump\ loss = pump\ shaft\ power - feed\ power$$

$$= 1614\,\mathrm{W} - 1372\,\mathrm{W}$$

$$= 242\,\mathrm{W}$$

$$recoverd\ power = pump\ shaft\ power - electric\ motor\ shaft\ power$$

$$= 1614\,\mathrm{W} - 787\,\mathrm{W}$$

$$= 827\,\mathrm{W}$$

$$saving\ given\ by\ energy\ recovery = \frac{recoverd\ power}{pump\ shaft\ power}$$

$$= \frac{827\,\mathrm{W}}{1614\,\mathrm{W}}$$

$$= 51\,\%$$

The toothed belt is assumed to have an efficiency of 95%.

$$hydraulic\ motor\ output\ \ power = \frac{recoverd\ power}{belt\ efficiency}$$

$$= \frac{827\,\mathrm{W}}{0.95}$$

$$= 871\,\mathrm{W}$$

$$hydraulic\ motor\ efficiency = \frac{hydraulic\ motor\ output\ \ power}{concentrate\ \ power}$$

$$= \frac{871\,\mathrm{W}}{1190\,\mathrm{W}}$$

$$= 73\,\%$$

$$water\text{-}to\text{-}water\ efficiency = hydraulic\ motor\ efficiency \times belt\ efficiency \times pump\ efficiency$$

$$= 73\,\% \quad \times \quad 95\,\% \quad \times \quad 85\,\%$$

$$= 59\,\%$$

The results of the above calculations are summarised in Table A-1, along with those for the other columns of Table 3-1.

Electrical input power (W)	502	997	1515
Motor shaft power (W)	357	787	1219
Inverter & motor losses (W)	145	210	296
Inverter & motor efficiency	71%	79%	80%
Feed water power (W)	519	1372	2067
Crossflow loss (W)	13	53	103
Concentrate power (W)	477	1190	1764
Desalination power (W)	17	51	67
Throughflow loss (W)	12	78	133
Pump shaft power (W)	611	1614	2432
Pump loss (W)	92	242	365
Recovered power (W)	254	827	1213
Saving given by energy recovery	42%	51%	50%
Hydraulic motor output power	267	871	1277
Belt loss (W)	13	44	64
Hydraulic motor efficiency	56%	73%	72%
Water-to-water efficiency	45%	59%	58%

Table A-1 – Caluclated powers and efficeincies

Appendix B Sensor details and calibration

B.1 Turbine flow meters

The initial test rig, described in Chapter 3, was fitted with turbine flow meters, which are described in this section.

(Oval-gear flow meters, see sections 4.9.2 and B.2, were used for the testing of the Clark pump and are fitted to the new test rig.)

B.1.1 Product-flow turbine flow meter

- RS part number 257-149
- Pulse output

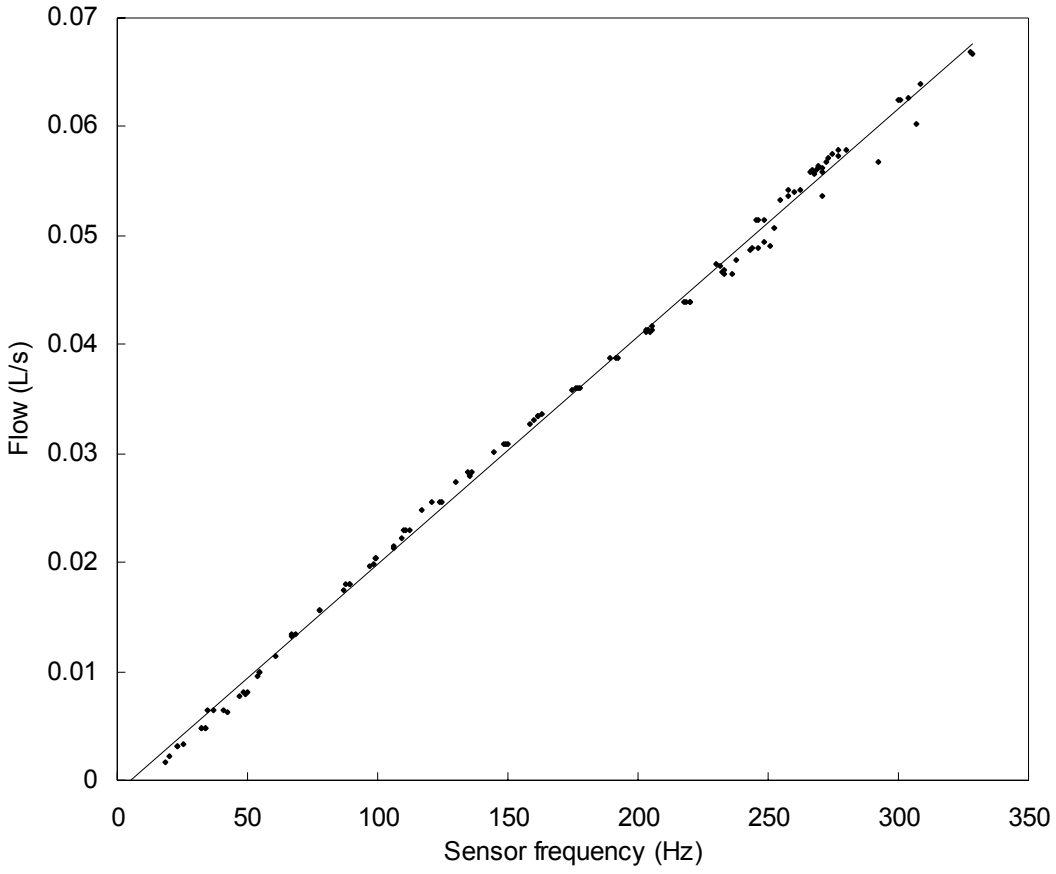

Figure B-1 – Product-flow turbine flow meter calibration

The product-flow turbine flow meter was calibrated using a "bucket and stopwatch". The flow was adjusted across the range of interest by means of the variable-speed drive on the pump and a total of 120 measurements were made. The stopwatch was implemented in LabView and operated manually, and the time taken to fill bucket ranged from 25 to 695 seconds. The "bucket" was actually a flask with a narrow neck; its volume was 1.665 L. The sensor frequency was measured in LabView. Figure B-1, shows the calibration results and the fitted straight line:

$$flow = 0.000210 \times frequency - 0.00117$$

This straight line was compared against the original data and the normalised error calculated:

$$Normalised\ error = \frac{\mathrm{RMS}\,(errors)}{\mathrm{RMS}\,(original\ values)} = 2.4\%$$

where RMS is root-mean-square. A normalised error of 2.4% was considered excessive, but worse than this, a subsequent spot check of the calibration revealed a drift of 13%, which renders the data useless for the study of efficiencies etc. and instigated the replacement of the turbine flow meters with oval-gear flow meters.

B.1.2 Feed flow

- RS part number 257-026
- Internal pulse-to-analogue converter
- Manufacturer's claimed accuracy +/– 2%

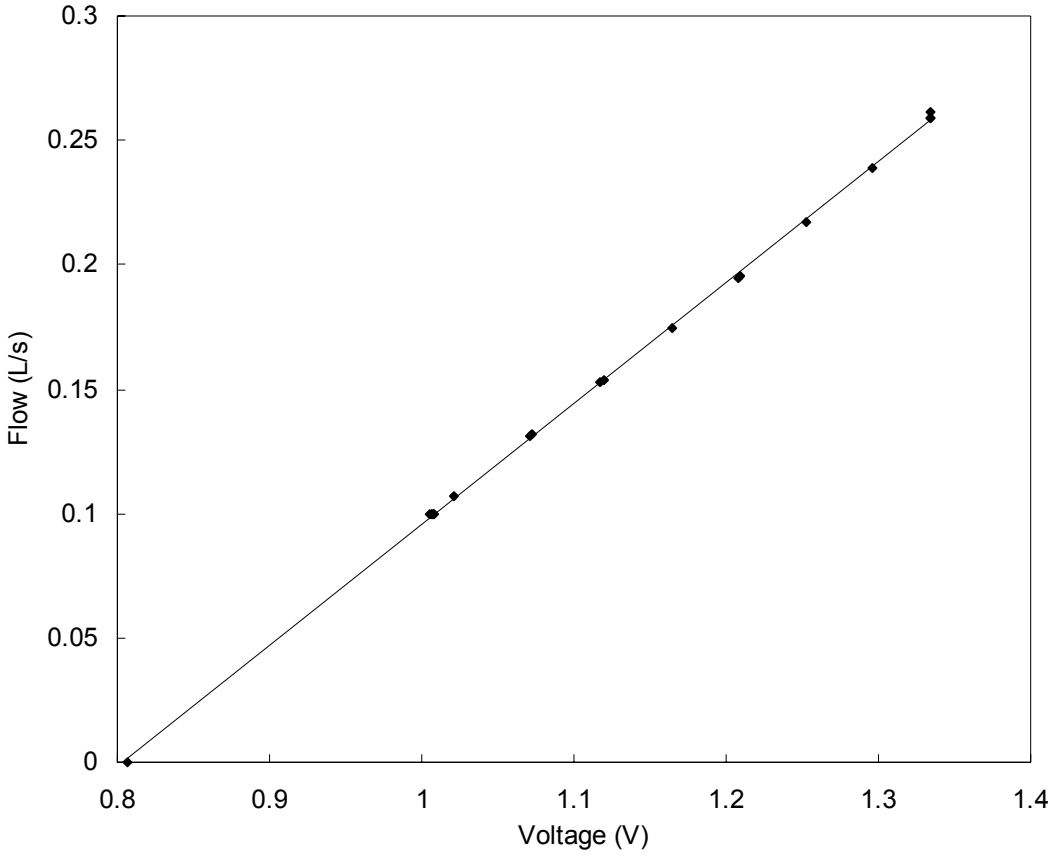

Figure B-2 – Feed-flow turbine flow meter calibration

The feed-flow turbine flow meter was also was calibrated using a bucket and stopwatch. Twenty measurements were made and a straight line fitted:

$$flow = 0.4862 \times voltage - 0.3903$$

which gave a normalised error of less than 1%. However, a subsequent spot check revealed a drift of 4%, which was not considered acceptable, and lead to this meter also being replaced.

B.2 Oval-gear flow meter calibration sheets

Titan Enterprises, Ltd.

MECHANICAL DATASHEET

29010R

Customer: Crest-Amrel
Meter Model: PD1350 St.Steel/Peek
Meter Serial: 29010
Elec Model :

End Fitting: 3/4" BSPF
Bearing Type: St.Steel/Peek
Pickoff Type: Hall effect
Pickoff P/N:
NOTE: No 10K Resistor Fitted
NOTE:

Job: R878
Meter Tag: 130-051
Elec Tag :
Elec Serial :
Ambient Temp:
Calib. Media: WATER @ 14.7 PSIA
Fluid Visc: 1.06 cSt
Fluid Temp: 20.11 °C
Fluid Dens: 0.997 kg/l

Meter Flow Rate (LPM)	Meter Freq (Hz)	Meter K Factor (1)	Meter Temp (°C)
0.9975	1.655	99.57	20.08
1.7222	2.862	99.71	20.09
2.9843	4.961	99.74	20.09
5.4202	9.024	99.89	20.08
9.8911	16.426	99.64	20.08
16.7364	27.706	99.33	20.08
31.6501	52.121	98.81	20.21
52.3062	85.627	98.22	20.21

Signal Output : Pulse(TTL)
K Factor : 98.5

Calibrated by: J Thorne
Date: 5/2/01

Figure B-3 – Clark-pump-inlet oval-gear flow meter calibration

Titan Enterprises, Ltd.

MECHANICAL DATASHEET

29011

Customer:	Crest-Amrel	Job:	4070
Meter Model:	PD1200 St.Steel/Peek	Meter Tag:	120-025
Meter Serial:	29011	Elec Tag :	
Elec Model :		Elec Serial :	
		Ambient Temp:	
End Fitting:	3/4" BSPF	Calib. Media:	WATER @ 14.7 PSIA
Bearing Type:	St.Steel/Peek	Fluid Visc:	1.01 cSt
Pickoff Type:	Hall effect	Fluid Temp:	21.95 °C
Pickoff P/N:		Fluid Dens:	0.997 kg/l

NOTE: No 10K Resistor Fitted

NOTE:

Meter Flow Rate (LPM)	Meter Freq (Hz)	Meter K Factor (1)	Meter Temp (°C)
1.0070	6.779	403.90	21.94
1.4025	9.469	405.09	21.94
2.0190	13.635	405.20	21.95
2.8136	19.030	405.83	21.95
3.9019	26.363	405.38	21.95
5.3629	36.090	403.77	21.94
7.1138	47.813	403.27	21.95
9.5250	63.789	401.82	21.95

Signal Output : Pulse(TTL)
K Factor : 402.9

Calibrated by: J Thorne
Date: 20/04/00

Figure B-4 – Plunger-pump-inlet oval-gear flow meter calibration

Titan Enterprises, Ltd.

MECHANICAL DATASHEET

pd35246

Customer:	Crest-Amrel	Job:	4909
Meter Model:	PD1200 St St\PEEK	Meter Tag:	126-S-2HM-V-50
Meter Serial:	PD35246	Elec Tag :	
Elec Model :		Elec Serial :	
		Ambient Temp:	
End Fitting:	1/2" BSP F	Calib. Media:	WATER @ 14.7 PSIA
Bearing Type:		Fluid Visc:	1.01 cSt
Pickoff Type:	Hall effect	Fluid Temp:	21.94 °C
Pickoff P/N:		Fluid Dens:	0.997 kg/l
NOTE:	No internal 10K ohm resistor		
NOTE:			

Meter Flow Rate (LPM)	Meter Freq (Hz)	Meter K Factor (1)	Meter Temp (°C)
1.0019	6.730	403.02	21.94
1.4321	9.627	403.35	21.94
1.9542	13.140	403.44	21.94
2.8036	18.833	403.04	21.94
3.5862	24.060	402.54	21.94
5.3037	35.499	401.60	21.93
7.3372	48.968	400.43	21.93
9.9931	66.480	399.15	21.93

Signal Output : Pulse(TTL)
K Factor : 401.5

Calibrated by: G Bown. G.Bown
Date: 30/4/01

Figure B-5 – Product-flow oval-gear flow meter calibration

B.3 Medium-pressure sensor specification and calibration sheet

Druck

SPECIFICATION

Date	10-MAY-2000
Sales Number	T00301.1.4
Transducer Type	PDCR 810-0799
Serial Number	1297310
Part No.	D810-0799-12
Pressure Range	15 barg
Supply Voltage	10 V
Zero Offset	0 +/- 3 mV
Span	100 +/- 3 mV
Non-Linearity & Hysteresis	max +/- 0.10 % BSL
Temperature Error Band	max +/- 0.50 % FRO
Compensated Temperature Range	+0°C to +50 °C
Pressure Connection	G1/4B-60 Int Cone
Electrical Connection	
Cable Length	1 m
Positive Supply	Red
Negative Supply	White
Positive Output	Yellow
Negative Output	Blue
Screen	See Application Data
Mounting Torque	20 Nm

Calibration Traceable To National Standards

APPLICATION DATA

1 Supply voltage may be up to a maximum of 12 volts. Transducer sensitivity and current consumption will be proportional to supply voltage.

2 Current consumption will not exceed 10 mA for stated supply voltage.

3 Zero offset can be nulled using a 250 Kohm potentiometer across the output terminals with the wiper connected to the negative supply via a 250 Kohm resistor.

4 For best temperature stability, the transducer must be operated into a load impedance of > 50 Kohm.

5 A shunt calibration resistor may be connected between the negative supply and the negative terminal to produce a positive output. The output obtained may be temperature sensitive. In case of difficulty, refer to the manufacturer.

6 If a power supply earth is to be used, then the positive side should be earthed.

7 Following conventional practice, the cable screen is not connected to the transducer body.

CALIBRATION DATA

Full Range Output(FRO) 100.24 mV at 23°C

Deviations from Best Straight Line

Pressure	(barg)	0.00	0.00	3.03	6.07	9.10	9.10	12.13	15.17	15.17
	(psig)	0.00	0.00	44.00	88.00	132.00	132.00	176.00	220.00	220.00
% FRO		0.02	0.00	0.00	-0.01	-0.02	-0.01	-0.01	0.01	0.02

Thermal Zero Shift

Temperature (°C)	0.0	23.0	50.0
% FRO	-0.10	0.00	-0.02

Thermal Span Shift

Temperature (°C)	0.0	23.0	50.0
% FRO	-0.11	0.00	0.01

Temperature Error Band +/- 0.11 % FRO

D 276

Druck Limited, Fir Tree Lane, Groby, Leicester LE6 0FH. Telephone:(0116) 2317100, Telex: 341743 Druck G, Facsimile:(0116) 2317101.

Figure B-6 – Medium-pressure sensor specification and calibration

B.4 Concentration from conductivity

µS/cm	ppm	µS/cm	ppm	µS/cm	ppm	µS/cm	ppm	µS/cm	ppm	µS/cm	ppm	µS/cm	ppm
10	5	610	302	1400	702	3200	1644	8200	4430	18750	10708	44000	26357
20	9	620	307	1420	713	3250	1671	8300	4486	19000	10852	45000	27035
30	14	630	312	1440	723	3300	1699	8400	4542	19250	11015	46000	27713
40	19	640	317	1460	733	3350	1726	8500	4598	19500	11169	47000	28391
60	28	650	323	1480	743	3400	1753	8600	4654	19750	11323	48000	29069
70	33	660	328	1500	754	3450	1781	8700	4710	20000	11476	49000	29747
80	38	670	333	1525	766	3500	1808	8800	4767	20250	11630	50000	30425
90	42	680	338	1550	770	3550	1835	8900	4823	20500	11784	51000	31103
100	47	690	343	1575	792	3600	1863	9000	4879	20750	11937	52000	31781
110	52	700	348	1600	805	3650	1899	9100	4935	21000	12091	53000	32459
120	57	710	353	1625	817	3700	1917	9200	4991	21250	12245	54000	33137
130	61	720	358	1650	830	3750	1945	9216	5000	21500	12399	55000	33815
140	66	730	363	1675	843	3800	1972	9300	5047	21750	12552	56000	34493
150	71	740	368	1700	856	3850	1999	9400	5103	22000	12705	57000	35171
160	75	750	373	1725	868	3900	2027	9500	5159	22250	12860	58000	35849
170	80	760	378	1750	881	3950	2054	9600	5215	22500	13013	59000	36527
180	85	770	383	1775	894	4000	2081	9700	5271	22750	13167	60000	37205
190	90	780	388	1800	907	4100	2136	9800	5327	23000	13321	61000	37883
200	95	790	393	1825	920	4200	2191	9900	5383	23250	13474	62000	38561
210	100	800	399	1850	932	4300	2245	10000	5439	23500	13628	63000	39239
220	105	810	404	1875	945	4400	2300	10200	5551	23750	13782	64000	39917
230	110	820	409	1900	958	4500	2356	10400	5664	24000	13936	65000	40595
240	115	830	414	1925	971	4600	2412	10600	5776	24250	14089	66000	41273
250	120	840	419	1950	983	4700	2468	10800	5888	24500	14243	67000	41961
260	125	850	424	1975	996	4800	2524	11000	6000	24750	14397	68000	42629
270	130	860	429	2000	1000	4900	2580	11200	6122	25000	14550	69000	43307
280	135	870	434	2025	1022	5000	2636	11400	6243	25500	14858	70000	43985
290	140	880	439	2050	1034	5100	2692	11600	6364	26000	15165	71000	44663
300	145	890	444	2075	1047	5200	2748	11800	6485	26500	15473	72000	45341
310	150	900	449	2125	1073	5300	2805	12000	6607	27000	15780	73000	46091
320	155	910	454	2150	1085	5400	2861	12200	6728	27500	16087	74000	46697
330	160	920	459	2175	1098	5500	2917	12400	6843	28000	16395	76000	48053
340	165	930	464	2200	1111	5600	2973	12600	6970	28500	16702	77000	48731
350	171	940	469	2225	1124	5700	3029	12800	7091	29000	17010	78000	49409
360	176	950	474	2250	1137	5800	3085	13000	7213	29500	17317	79000	50087
370	181	960	480	2275	1140	5900	3141	13200	7334	30000	17624	80000	50765
380	186	970	485	2300	1162	6000	3197	13400	7455	30500	17932	81000	51443
390	191	980	490	2325	1175	6100	3253	13600	7576	31000	18239	82000	52121
400	196	990	495	2350	1188	6200	3309	13800	7898	31500	18547	83000	52799
410	201	1000	500	2375	1200	6300	3365	14000	7819	32000	18854	84000	53477
420	206	1020	510	2400	1213	6400	3421	14200	7940	32500	19161	85000	54155
430	211	1040	520	2425	1226	6500	3477	14400	8061	33000	19469	86000	54833
440	216	1080	540	2450	1239	6600	3533	14600	8182	34000	20084	87000	55511
450	221	1100	550	2475	1251	6700	3589	14800	8304	34500	20391	88000	56130
460	226	1120	561	2500	1264	6800	3645	15000	8425	35000	20698	89000	56867
470	231	1140	571	2550	1290	6900	3701	15250	8576	35500	21006	90000	57545
480	236	1160	581	2600	1315	7000	3758	15500	8728	36000	21313	91000	58223
490	241	1180	591	2650	1344	7100	3814	15750	8879	36500	21621	92000	58901
500	247	1200	601	2700	1371	7200	3870	16000	9031	37000	21928	93000	59579
510	252	1220	611	2750	1398	7300	3926	16250	9182	37500	22235	94000	60257
520	257	1240	621	2800	1426	7400	3982	16500	9334	38000	22543	95000	60935
530	262	1260	632	2850	1453	7500	4038	16750	9486	38500	22850	96000	61613
550	272	1280	642	2900	1480	7600	4094	17000	9637	39000	23158	97000	62291
560	277	1300	652	2950	1508	7700	4150	17500	9940	39500	23465	98000	62969
570	282	1320	662	3000	1535	7800	4206	17750	10092	40000	23773	99000	63647
580	287	1340	672	3050	1562	7900	4262	18000	10247	41000	24387	100000	64325
590	292	1360	682	3100	1589	8000	4318	18250	10400	42000	25002		
600	297	1380	692	3150	1617	8100	4374	18500	10554	43000	25679		

Table B-1 – Conductivity (µS/cm) and concentration (ppm) data for sodium chloride solution (DOW 1995 section 10.2)

The conductivity of sodium chloride solution increases with the concentration but the relationship is not linear. DOW (1995) provide the data shown in Table B-1 as a means of converting from one to the other. In order to program the conversion in LabView (or any programming language) a mathematical function is more convenient than a look up table.

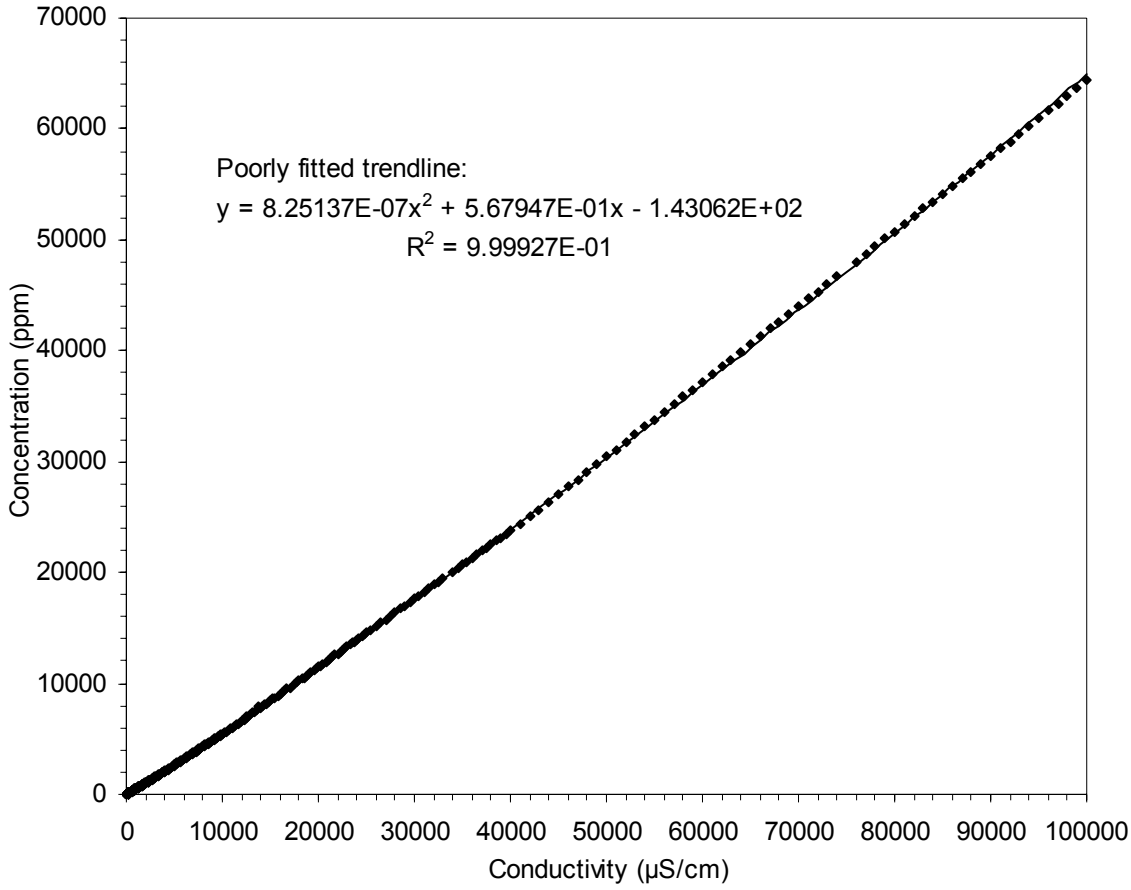

Figure B-7 – Concentration versus conductivity – linear scales

Figure B-7 shows the data from Table B-1 and a second-order polynomial trendline. The trendline appears to be a very good fit and this is supported by the R^2 value. However, close inspection below 1000 ppm reveals that the fit is actually very poor in this critical region, as illustrated in Figure B-8.

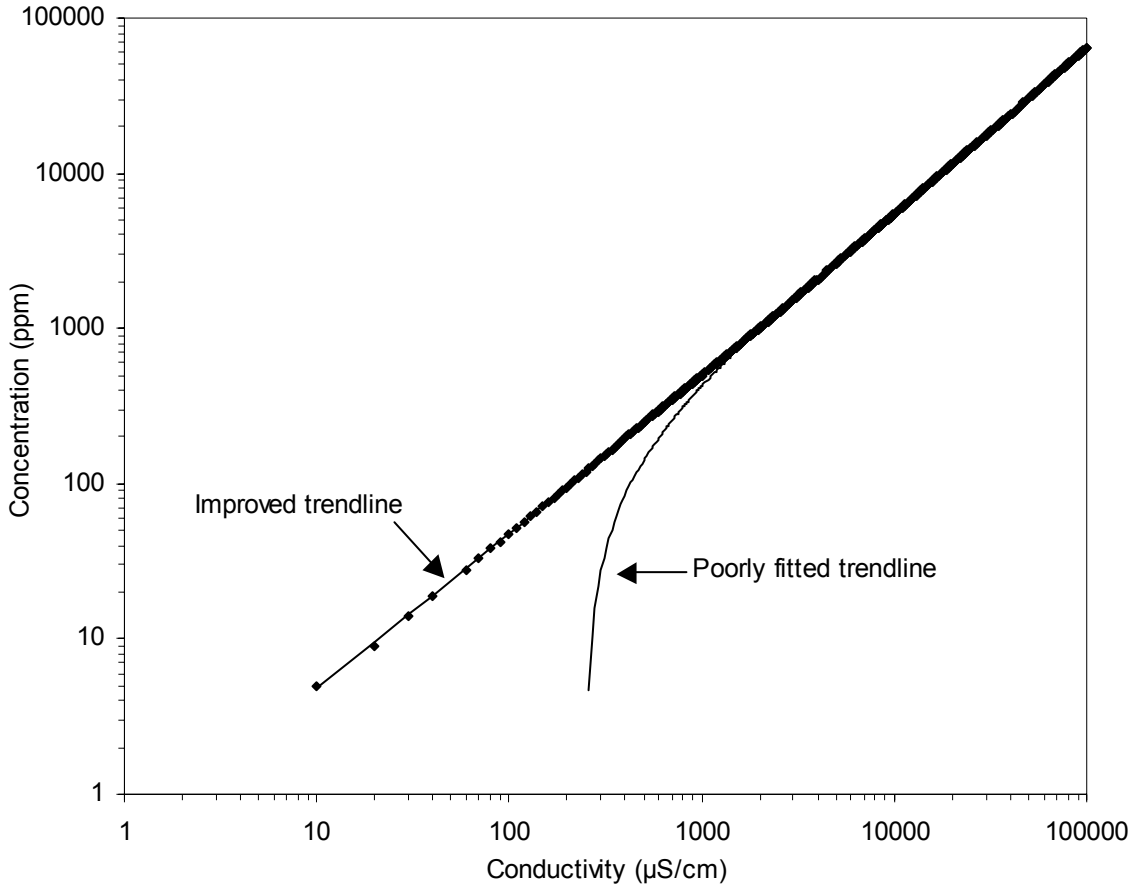

Figure B-8 – Concentration versus conductivity – logarithmic scales

The improved trendline, shown in Figure B-8 was obtained by taking the logarithm of both concentration and conductivity prior to fitting a second-order polynomial. The equation of the improved trendline is:

$$y = \exp\left(0.00565 \times (\ln x)^2 + 0.952 \times \ln x - 0.642\right)$$

where y is the concentration in ppm, and x is conductivity in µS/cm.

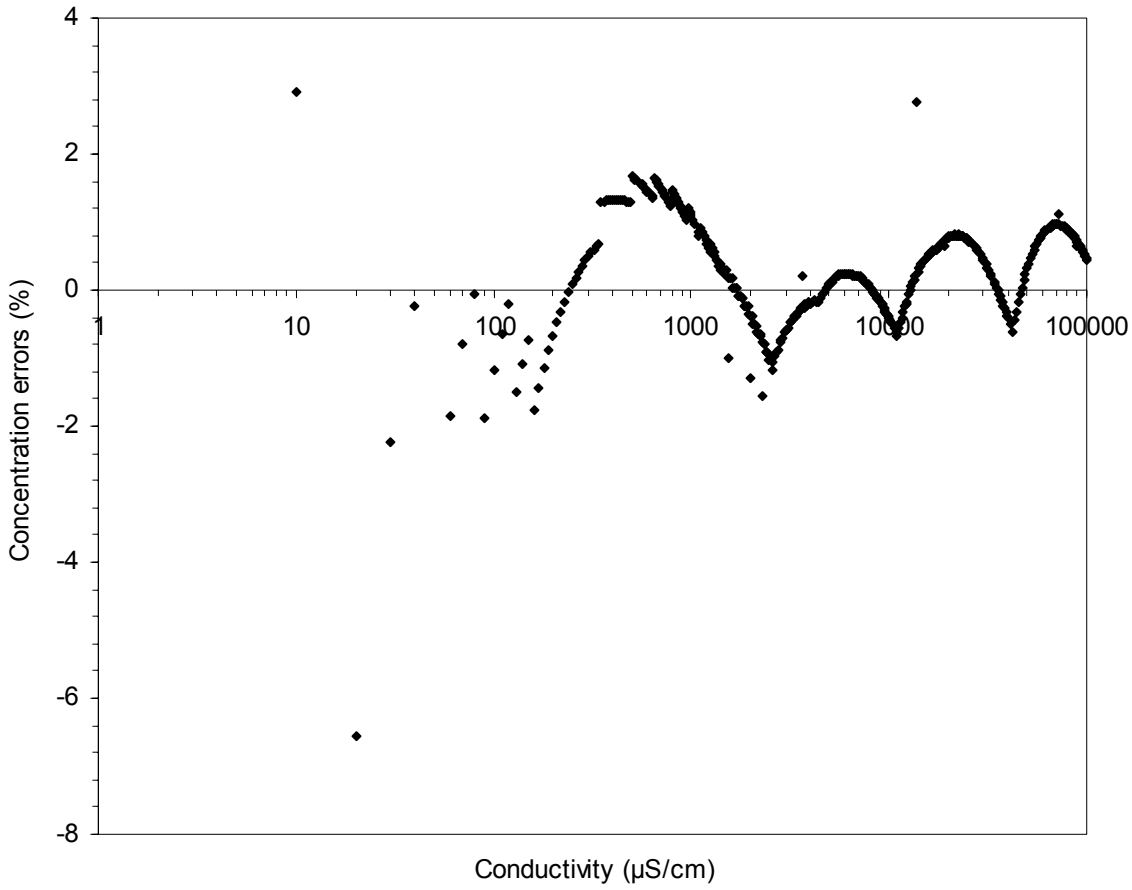

Figure B-9 – Concentration trendline errors

Figure B-9 shows the percentage error between the improved trendline and the original data. It suggests that the original data is itself a collection of four or five segments, and that no further refinement of the trendline would be profitable.

B.5 Torque load-cell and calibration

B.5.1 Load-cell datasheet

Amber Instruments Ltd

LOAD CELL TEST DATA SHEET

~~~~~~~~~~~~~~~~~~~~~~~~~~~~~~~~~~ General Data ~~~~~~~~~~~~~~~~~~~~~~~~~~~~~~~~~~

Serial Number	*17373*	*Calibration Mode :-*	*Compression*
Model	*355 (Stainless Steel)*	*Input Impedance*	*380 +/-10 Ohms*
Capacity (kg)	*20*	*Output Impedance*	*350 +/-3 Ohms*
Thread Type	*NONE*	*Insulation Resistance*	*> 1000 MOhms*
Grade	*C4*	*Test Excitation*	*10 V dc*

~~~~~~~~~~~~~~~~~~~~~~~~~~~~~~~~~~ Metrology Data ~~~~~~~~~~~~~~~~~~~~~~~~~~~~~~~~~~

Zero Balance	*0.66*	*% Rated Load*
Output @ Rated Load	*2.001*	*mV/V*
Total Error	*< 0.015*	*% Rated Load*
Non Repeatablity	*< 0.010*	*% Rated Load*
Zero Return	*< 0.012*	*% Rated Load*

Temperature Effect on Zero Balance	*< 0.010 % Rated Load / 10 Degree C*
Temperature Effect on Span	*< 0.007 % Rated Load / 10 Degree C*
Compensated Temperature Range	*- 10 To + 40 Degree C*
Safe Temperature Range	*- 30 To + 90 Degree C*

~~~~~~~~~~~~~~~~~~~~~~~~~~~~~~~~~~ Notes / Wiring Diagram ~~~~~~~~~~~~~~~~~~~~~~~~~~~~~~~~~~

Notes :-

1. *Total Error is the Maximum Deviation from a straight line drawn between the No Load and Rated Load Outputs for both increasing and decreasing loads.*
2. *Zero Return is measured using rated load.*
3. *This Load Cell is Hermetically sealed.*
4. *Changes in Barometric pressure have NO effect on this type of Load Cell.*

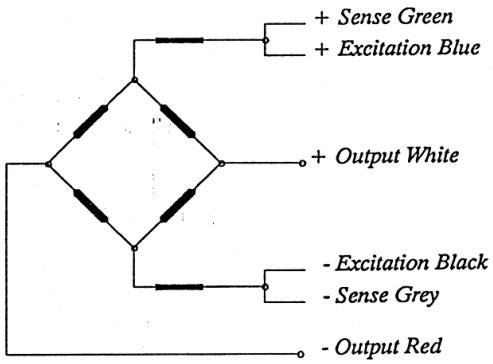

Figure B-10 – Torque load-cell manufacturer's test datasheet

B.5.2 Torque measurement calibration

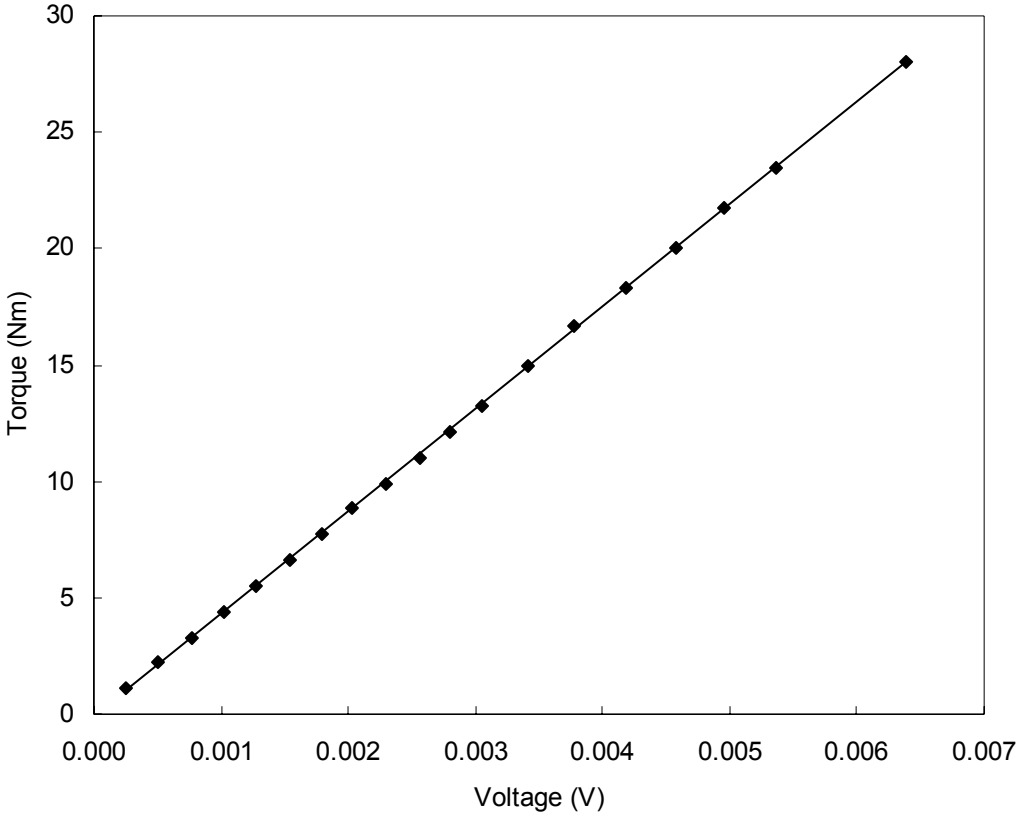

Figure B-11 – Torque measurement calibration

Torque (Nm)	Voltage (V)
1.10	0.00025
2.20	0.00051
3.31	0.00077
4.41	0.00103
5.51	0.00128
6.61	0.00154
7.72	0.00179
8.82	0.00203
9.92	0.00229
11.02	0.00256
12.13	0.00280
13.23	0.00305
14.93	0.00342
16.64	0.00378
18.34	0.00419
20.04	0.00457
21.74	0.00496
23.45	0.00536
27.99	0.00639

Table B-2 – Data for Figure B-11

Figure B-11 shows the torque measurement calibration results and the fitted straight line:

$$torque = 4396 \times voltage - 0.1049$$

The linearity is good: the largest error from the straight line was 0.12 Nm, which was considered acceptable.

B.6 Irradiance pyranometer calibration certificate

Kipp & Zonen B.V.
Röntgenweg 1 2624 BD Delft
P.O. Box 507 2600 AM Delft
The Netherlands
T +31-(0)15-2698000
F +31-(0)15-2620351
E info.holland@kippzonen.com
Website www.kippzonen.com

CALIBRATION CERTIFICATE

PYRANOMETER

PYRANOMETER MODEL	:	CM11
SERIAL NUMBER	:	027700
SENSITIVITY (± 0.5%) at normal incidence on horizontal pyranometer	:	5,16 μV/W/m^2

CALIBRATION PROCEDURE : The reference and test pyranometers are mounted horizontally on a table which can rotate to exchange the positions of both instruments.. A 1000W Tungsten-halogen filament lamp produce a directed vertical beam (divergence 3.5°). The irradiance at the pyranometers is approx. 500 W/m². The indoor procedure is based on a sequence of simultaneous readings. The Kipp & Zonen procedure is described in the International Standard ISO 9847, Annex A.3.1

REFERENCE PYRANOMETER : Kipp & Zonen CM11 913550 active from 11-jan-02.

hierarchy of traceability:

This pyranometer has been compared with the "reference pyranometer" at the World Radiation Center (WRC) in Davos. All measurements were performed under mainly clear sky conditions, using the sun and sky radiation as source. The reference pyranometer is periodically calibrated against the World Standard Group (WSG). The readings are referred to the World Radiometric Reference (WRR) as stated in the WMO Technical Regulations. The Davos site is 1590m above sea level at latitude 46°48' N and longitude 9°49' E.

For this calibration, the inclination of the receiver surfaces versus their horizontal position were set to 00 degrees, the instrument signal wire to the north. During the comparisons, the instrument received global radiation intensities from 622 to 944 with a mean of 812 W/m^2. The angle between the solar beam and the normal of the receiver surface varied from 29 to 50 with a mean of 38 degrees. The instrument's temperature ranged from +13,0 to +24,8 with a mean of +20,1°C. The sensitivity calculation and its standard deviation is based on 963 individual measurements.
Sensitivity in Davos was: 4,7 ± 0,02 μV/W/m^2 (but is corrected by Kipp & Zonen to 4,71 μV/W/m². See "correction applied" below.)
The testing was done July 31 and August 1,2,7,14,15,16 and 22, 2001.

Global radiation data were obtained with the absolute cavity pyrheliometer PMO-2 (member of the WSG, WRR-Factor: 0,99955, based on the last International Pyrheliometer Comparison IPC-2000) and a continuous disk shaded pyranometer Eppley PSP-20655F3.

correction applied : -0,4 %
This correction was necessary to correct for the mean directional errors of the reference CM 11 in Davos. This error is estimated at Kipp & Zonen measuring the cosine error for the mean angle of incidence (55°) at azimuth SE and SW.
The reference CM 11 now measures the vertical directed beam of the indoor calibration facility more correctly.

IN CHARGE OF TEST: G. v/d Wilt, 14-jan-02, Kipp & Zonen, Delft, Holland

Figure B-12 – Kipp and Zonen CM11 pyranometer calibration certificate

Appendix C Clark pump details, test results and analysis

C.1 Specification

Spectra Watermakers Inc. supply complete desalination systems that incorporate Clark pumps; they do not normally supply Clark pumps separately, and so do not normally supply detailed specifications of the Clark pump in isolation. The data used in this thesis is a follows.

Maximum flow	3.5 US gallons per minute	0.22 L/s
Maximum pressure	950 psi	65 bar
Piston diameter	2.75 inches	69.8 mm
Rod diameter	0.875 inches	22.2 mm

Table C-1 – Clark pump specification

From the rod and the piston diameters, the theoretical recovery ratio $R_t = 0.10124$.

C.2 Test procedure

As outlined in section 5.2.2, the Clark pump was tested at a total of 55 discrete test points. These were the 45 permutations of:

- feed flow: 0.042, 0.127 and 0.211 L/s,
- high pressure: 20, 30, 40, 50 and 60 bar,
- delta pressure: 0, 2 and 4 bar,

plus the 10 permutations of:

- feed flow: 0.085and 0.17 L/s,
- high pressure: 20, 30, 40, 50 and 60 bar,
- delta pressure: 0 bar.

These test points were the nominal targets for the manual adjustment of the valves, shown in Figure 5-6, and the speed of the feed-pump motor. (The target motor speeds were round numbers, which accounts for the odd choice of nominal feed flows.) Once the adjustments were made (for each of the 55 discrete test points) and steady operation had

been achieved, data logging (via the LabView data acquisition system) was enabled for a period of at least a minute. The data was then averaged over this test period and each test provides one row in Table C-2. Of course, the manual adjustment of the valves was not perfect and motor speed of the feed pump reduced slightly with pressure, and so the measured values do differ slightly form the nominal targets; the measured values were used for the analysis and modelling.

C.3 Measured data

Feed Flow (L/s)	High Pressure (bar)	Concentrate Pressure (bar)	Delta Pressure (bar)	Product Flow (L/s)	Feed Pressure (bar)
0.04318	20.065	20.056	0.009	0.004182	2.597
0.04233	29.840	29.834	0.006	0.004029	3.655
0.04238	39.802	39.795	0.008	0.003966	4.733
0.04239	49.930	49.922	0.008	0.003884	5.821
0.04240	60.075	60.066	0.009	0.003794	6.895
0.08491	19.842	19.795	0.046	0.008240	2.966
0.08487	30.011	29.964	0.047	0.008034	4.013
0.08467	39.787	39.728	0.059	0.007895	5.051
0.08488	49.905	49.852	0.053	0.007727	6.067
0.08489	60.171	60.114	0.057	0.007614	7.153
0.12742	19.812	19.784	0.027	0.012417	3.500
0.12742	29.907	29.875	0.031	0.012120	4.533
0.12741	40.094	40.061	0.033	0.011859	5.580
0.12746	49.997	49.971	0.026	0.011573	6.562
0.12738	59.917	59.895	0.022	0.011452	7.531
0.16930	20.093	19.997	0.096	0.016718	4.181
0.16932	30.105	30.002	0.103	0.016195	5.220
0.16925	39.818	39.708	0.111	0.015878	6.173
0.16934	50.142	50.027	0.115	0.015429	7.163
0.16930	59.897	59.781	0.117	0.015245	8.133
0.21101	19.775	19.704	0.071	0.021093	4.970
0.21093	30.174	30.096	0.078	0.020296	6.051
0.21082	40.024	39.949	0.074	0.019927	7.036
0.21082	49.845	49.758	0.087	0.019302	7.927
0.21078	59.763	59.670	0.093	0.019130	8.896
0.04245	19.773	17.729	2.043	0.004115	4.529
0.04244	29.782	27.765	2.017	0.004042	5.602
0.04239	39.716	37.585	2.131	0.003963	6.779
0.04248	49.882	47.951	1.931	0.003907	7.661
0.04247	59.882	57.833	2.049	0.003799	8.799
0.12734	19.913	17.874	2.039	0.012334	5.347
0.12737	29.965	27.993	1.972	0.012099	6.361
0.12733	40.012	38.052	1.961	0.011904	7.409
0.12743	49.973	48.009	1.965	0.011658	8.436
0.12727	60.029	58.059	1.970	0.011479	9.436
0.21086	19.859	17.803	2.056	0.020901	6.825
0.21128	29.607	27.536	2.071	0.020274	7.861
0.21072	40.171	38.125	2.046	0.019848	8.935
0.21079	49.968	47.910	2.057	0.019328	9.828
0.21071	59.436	57.508	1.927	0.019045	10.600
0.04241	20.014	15.921	4.094	0.004156	6.546
0.04247	29.794	25.884	3.910	0.004070	7.440
0.04234	39.737	35.640	4.097	0.003979	8.712
0.04251	49.537	45.668	3.869	0.003881	9.534
0.04249	59.831	55.952	3.879	0.003865	10.627
0.12740	19.877	15.872	4.005	0.012371	7.242
0.12739	29.871	25.832	4.039	0.012181	8.349
0.12739	40.032	36.006	4.026	0.011947	9.431
0.12736	49.948	45.919	4.029	0.011686	10.404
0.12727	59.863	55.832	4.031	0.011552	11.438
0.21056	19.919	15.808	4.111	0.020964	8.759
0.21083	29.773	25.635	4.138	0.020335	9.796
0.21075	39.699	35.543	4.157	0.019962	10.854
0.21064	49.868	45.705	4.163	0.019452	11.855
0.21066	60.343	56.195	4.148	0.019183	12.885

Table C-2 – Clark pump test results data

The first four columns of Table C-2 represent the test conditions, while the last two columns are the results.

With the exception of the delta pressure, the data in each column is that from an individual sensor as shown in Figure 5-6.

C.4 Analysis

The data shown in Table C-2 was analysed in order to quantify leakages, pressure losses and efficiencies, according to the definitions of these quantities given in sections 5.2.1 and 5.2.4.

In particular:

		Cross-references to sections 5.2.1 and 5.2.4
Leakages	$Q_L = Q_F R_t - Q_P$	Combining and rearranging equations 17 and 19
Pressure losses	$P_L = P_F - P_H - (1 - R_t)(P_E - P_C)$	Rearranging equation 35
Volumetric efficiency	$\eta_V = 1 - \frac{Q_L}{Q_F R_t}$	Equation 22
Mechanical efficiency	$\eta_M = 1 - \frac{P_L}{P_F - P_E(1 - R_t)}$	Equation 34
Overall efficiency	$\eta_{Clark} = \frac{Q_H P_H - Q_F P_F}{Q_C P_C - Q_E P_E}$	Equation 38

Table C-3 – Clark pump analysis equations

Where:

Q_F is feed flow
Q_H is high-pressure flow
Q_P is product flow
Q_C is concentrate flow
Q_E is exhaust flow (discharge)
Q_L is leakage flow
P_F is feed pressure (medium pressure)
P_H is high pressure

P_C is concentrate pressure
P_E is exhaust pressure (discharge)
ΔP is delta pressure = $P_H - P_C$
R_t is theoretical recovery ratio = 0.10124, see section C.1.

The exhaust pressure P_E was taken as a constant 0.1 bar, corresponding to 1 metre head of water between that Clark pump and the water recirculation tank.

The high-pressure flow Q_H and the concentrate flow Q_C could not be measured because the oval-gear flow meters on the test rig are limited to 20 bar. Instead, it was assumed that $Q_H = Q_F$, and therefore, by virtue of equation 25: $Q_F + Q_C = Q_H + Q_E$, that $Q_C = Q_E$. Fortunately, this assumption only affects the last equation in Table C-3: the overall efficiency: $\eta_{Clark} = \frac{Q_H P_H - Q_F P_F}{Q_C P_C - Q_E P_E}$, and it affects it very little:

In practice, Q_H would be slightly less than Q_F, but, again by equation 25, Q_C would also be less than Q_E by exactly the same amount. And, because $P_H \approx P_C$ and $P_F \approx P_E$, the error in the numerator will be largely cancelled out by a very similar error in the denominator.

Leakages (L/s)	Pressure Losses (bar)	Volumetric Efficiency	Mechanical Efficiency	Overall Efficiency
0.000189	0.467	95.7%	81.4%	96.9%
0.000256	0.539	94.0%	84.9%	97.3%
0.000324	0.607	92.4%	86.9%	97.5%
0.000407	0.669	90.5%	88.3%	97.5%
0.000499	0.715	88.4%	89.5%	97.4%
0.000356	0.825	95.9%	71.3%	94.9%
0.000558	0.843	93.5%	78.5%	96.2%
0.000676	0.880	92.1%	82.3%	96.7%
0.000867	0.878	89.9%	85.3%	96.9%
0.000980	0.920	88.6%	87.0%	97.0%
0.000483	1.380	96.3%	59.5%	91.8%
0.000780	1.387	94.0%	68.8%	94.2%
0.001040	1.401	91.9%	74.5%	95.2%
0.001331	1.387	89.7%	78.6%	95.8%
0.001444	1.355	88.8%	81.8%	96.3%
0.000422	1.971	97.5%	51.8%	88.7%
0.000947	1.989	94.5%	61.2%	92.0%
0.001257	1.952	92.7%	67.9%	93.7%
0.001714	1.894	90.0%	73.2%	94.7%
0.001895	1.874	88.9%	76.7%	95.3%
0.000269	2.815	98.7%	42.3%	83.9%
0.001059	2.837	95.0%	52.4%	89.0%
0.001416	2.827	93.4%	59.3%	91.4%
0.002042	2.713	90.4%	65.4%	92.9%
0.002210	2.672	89.6%	69.7%	93.9%
0.000183	0.601	95.7%	86.5%	95.7%
0.000255	0.685	94.1%	87.6%	96.6%
0.000328	0.753	92.4%	88.7%	96.9%
0.000394	0.785	90.8%	89.6%	97.2%
0.000500	0.806	88.4%	90.7%	97.2%
0.000558	1.408	95.7%	73.2%	90.7%
0.000796	1.465	93.8%	76.6%	93.5%
0.000987	1.506	92.3%	79.4%	94.8%
0.001243	1.521	90.4%	81.8%	95.4%
0.001406	1.499	89.1%	84.0%	95.9%
0.000446	2.877	97.9%	57.3%	81.7%
0.001116	2.912	94.8%	62.5%	87.7%
0.001485	2.940	93.0%	66.8%	90.7%
0.002012	2.830	90.6%	70.9%	92.4%
0.002288	2.761	89.3%	73.7%	93.5%
0.000137	0.750	96.8%	88.4%	94.4%
0.000230	0.820	94.7%	88.8%	95.9%
0.000308	0.917	92.8%	89.4%	96.3%
0.000422	0.951	90.2%	89.9%	96.6%
0.000437	0.994	89.8%	90.6%	96.9%
0.000527	1.541	95.9%	78.5%	88.7%
0.000715	1.605	94.5%	80.6%	92.5%
0.000949	1.670	92.6%	82.1%	94.0%
0.001207	1.637	90.6%	84.1%	95.0%
0.001333	1.664	89.7%	85.3%	95.6%
0.000353	2.958	98.3%	65.9%	78.9%
0.001009	2.972	95.3%	69.4%	86.6%
0.001374	3.009	93.6%	72.0%	89.9%
0.001873	2.976	91.2%	74.7%	91.8%
0.002144	2.958	89.9%	76.9%	93.1%

Table C-4 – Clark pump analysis results data (ordered to match Table C-2)

C.5 Graphs and discussion

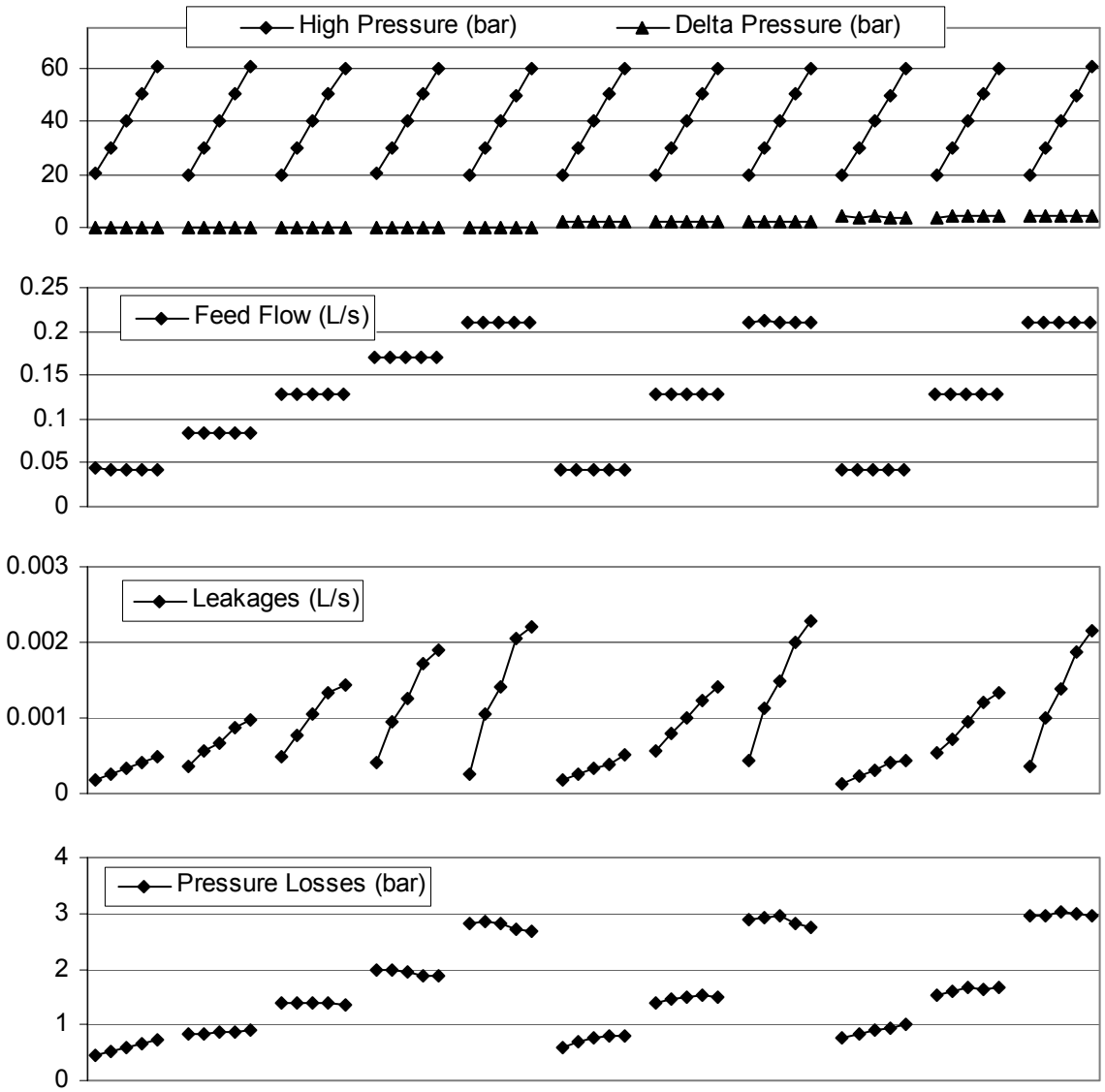

Figure C-1 – Clark pump leakages and pressure losses

In Figure C-1, the top two charts (high pressure, delta pressure and feed flow) show the *input* conditions of the tests, taken from Table C-2. The bottom two charts show the resulting leakages and pressure losses, taken from Table C-4.

Inspection suggests that the leakages are dependent mainly on the *product* of the high-pressure and the feed flow. The expectation had been that the leakages would increase with the *sum* of pressure and flow components. However, regression calculations (see later) confirm that the product is indeed the dominant term. The delta pressure (up to 4 bar) has little effect on leakages.

Inspection of the bottom chart, in Figure C-1, suggests the pressure losses are dependent on the feed flow and the feed flow squared. This was anticipated, since this "pressure" loss includes frictional and viscous effects. Also, a relationship to delta pressure is apparent.

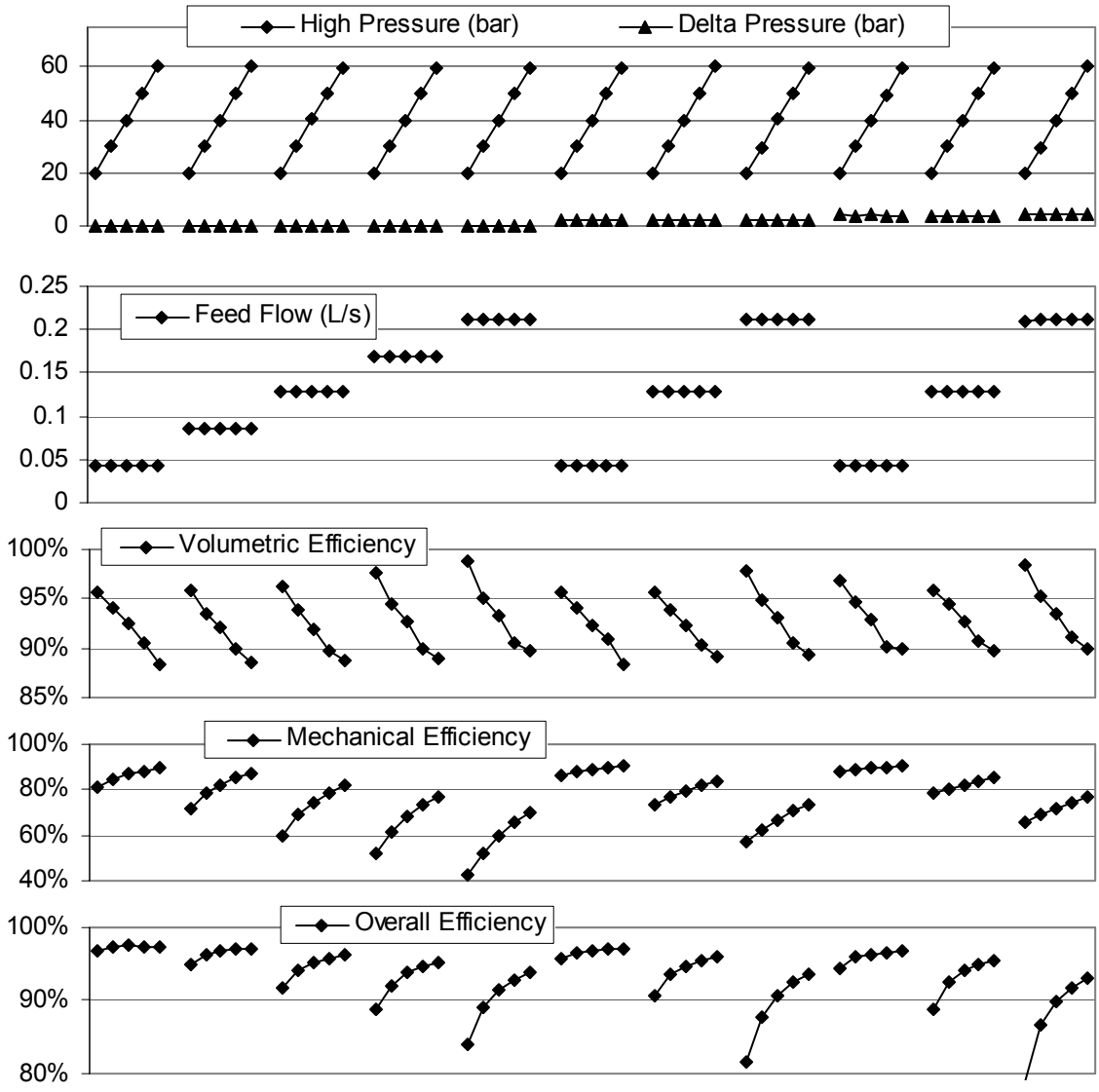

Figure C-2 – Clark pump efficiencies

In Figure C-2, the top two charts are the same as those in Figure C-1 and represent the *input* conditions, taken from Table C-2. The bottom the charts show the resulting efficiencies, taken from Table C-4.

NB: ***volumetric efficiency*** × ***mechanical efficiency*** ≠ ***overall efficiency***

With rotary pumps (those converting mechanical shaft power to hydraulic power) and with hydraulic motors (those converting power the other way), it is common to define the volumetric efficiency and the mechanical efficiency such that the product of the two equals the overall efficiency. This is natural and desirable in systems in which the components are all in series (for example an inverter, driving a motor, driving a pump) since it maintains the condition that the system efficiency equals the product of the component efficiencies. However, in systems with branches and loops (such as a reverse osmosis system with brine-stream energy recovery), this condition cannot be achieved. It is therefore not essential that the product of volumetric and mechanical efficiencies should equal the overall efficiency. Certainly, this is not achieved by the efficiency definitions set out for the Clark pump in Table C-3, as is clearly illustrated in Figure C-2.

From Figure C-2, it is apparent that the volumetric efficiency is very high throughout and that the overall efficiency is dominated by the mechanical efficiency (pressure and frictional losses).

C.6 Modelling

In order to construct a mathematical model of the Clark pump, for implementation in Simulink, expressions were sought for the leakages Q_L and the pressure losses P_L, in terms of the input variables: feed flow Q_F, high pressure P_H and delta pressure ΔP. The eight formulas shown in Table C-5 were considered.

Formula under consideration	Normalised Error
$Q_L = 7.68\times10^{-3}\times Q_F + -1.51\times10^{-5}$	37 %
$Q_L = 6.80\times10^{-3}\times Q_F + 2.74\times10^{-5}\times P_H + -1.02\times10^{-3}$	19 %
$Q_L = -2.33\times10^{-3}\times Q_F + -2.69\times10^{-6}\times P_H + 2.17\times10^{-4}\times Q_F P_H + 2.18\times10^{-4}$	8 %
$Q_L = 1.78\times10^{-4}\times Q_F P_H + 1.56\times10^{-5}$	10 %
$P_L = 12.7\times Q_F + 0.0399$	11 %
$P_L = 1.83\times Q_F + 42.2\times Q_F^2 + 0.570$	8 %
$P_L = 1.43\times Q_F + 43.9\times Q_F^2 + 7.06\times10^{-2}\times \Delta P + 0.454$	3 %
$P_L = 49.2\times Q_F^2 + 7.09\times10^{-2}\times \Delta P + 0.528$	3 %

Table C-5 – Alternative formula considered for modelling leakages Q_L and pressure losses P_L

For each formula in Table C-5, the coefficients were determined by multiple linear regression (least squares). Each formula was then tested with the original data set by comparing its predictions against the original measured values. The errors, for each formula, were then averaged and normalised using:

$$Normalised\ error = \frac{\mathrm{RMS}(errors)}{\mathrm{RMS}(original\ values)}$$

where RMS is root-mean-square. The errors (residuals) were also examined at each stage, in order to identify what components should be added to the formula for consideration.

The fourth and eighth formula in Table C-5:

$$Q_L = 1.78\times10^{-4}\times Q_F P_H + 1.56\times10^{-5}$$

$$P_L = 49.2\times Q_F^2 + 7.09\times10^{-2}\times \Delta P + 0.528$$

in which, the units are litres/second and bar, were considered to offer a good balance of precision and simplicity, and were used in the Simulink model of the Clark pump, presented in section 5.2.3.

C.7 Testing of the Simulink model

The competed Simulink model of the Clark pump was presented in section 5.2.3. It was tested by using the feed flow, high pressure and concentrate pressure data collected during the original hardware testing (Table C-2) as inputs to the model. The output data from the model was then compared against the original test results: product flow and feed pressure, as shown in Table C-6.

Comparing Table C-6 against Table C-2 illustrates, as hoped, that the model closely matches the measured data. The normalised errors for the product flow and feed pressure are 0.95% and 0.85% respectively.

Modelled Feed Pressure (bar)	Error (bar)		Modelled Product Flow (L/s)	Error (L/s)
0.0042	0.0000		2.750	0.153
0.0040	0.0000		3.733	0.078
0.0040	0.0000		4.743	0.010
0.0039	0.0000		5.769	-0.052
0.0038	0.0000		6.797	-0.098
0.0083	0.0001		3.026	0.060
0.0082	0.0002		4.056	0.042
0.0080	0.0001		5.055	0.005
0.0078	0.0001		6.075	0.008
0.0077	0.0001		7.119	-0.034
0.0124	0.0000		3.449	-0.051
0.0122	0.0001		4.475	-0.058
0.0120	0.0001		5.508	-0.072
0.0118	0.0002		6.504	-0.058
0.0115	0.0000		7.504	-0.028
0.0165	-0.0002		4.155	-0.026
0.0162	0.0000		5.176	-0.044
0.0160	0.0001		6.166	-0.007
0.0156	0.0002		7.216	0.053
0.0153	0.0001		8.205	0.073
0.0206	-0.0005		4.879	-0.091
0.0202	-0.0001		5.938	-0.114
0.0198	-0.0001		6.929	-0.107
0.0194	0.0001		7.936	0.009
0.0191	0.0000		8.944	0.049
0.0042	0.0001		4.689	0.160
0.0040	0.0000		5.677	0.075
0.0040	0.0000		6.793	0.014
0.0039	0.0000		7.629	-0.032
0.0039	0.0001		8.755	-0.044
0.0124	0.0001		5.409	0.062
0.0122	0.0001		6.362	0.001
0.0119	0.0000		7.368	-0.041
0.0117	0.0000		8.381	-0.055
0.0115	0.0000		9.402	-0.034
0.0206	-0.0003		6.810	-0.016
0.0203	0.0000		7.820	-0.041
0.0198	0.0000		8.854	-0.082
0.0195	0.0002		9.858	0.030
0.0191	0.0001		10.689	0.089
0.0041	-0.0001		6.702	0.156
0.0041	0.0000		7.514	0.074
0.0039	-0.0001		8.701	-0.011
0.0039	0.0000		9.473	-0.060
0.0038	-0.0001		10.525	-0.103
0.0124	0.0000		7.312	0.070
0.0122	0.0000		8.357	0.008
0.0120	0.0001		9.373	-0.058
0.0118	0.0001		10.379	-0.025
0.0115	-0.0001		11.384	-0.054
0.0206	-0.0004		8.802	0.043
0.0202	-0.0001		9.832	0.036
0.0198	-0.0002		10.853	-0.001
0.0194	-0.0001		11.886	0.031
0.0191	-0.0001		12.933	0.048

Table C-6 – Simulink model output data and errors (ordered to match Table C-2)

Appendix D Netzsch 021 Moineau pump datasheet

NM021*2S

Förderkennlinie
Performance Curve

NETZSCH

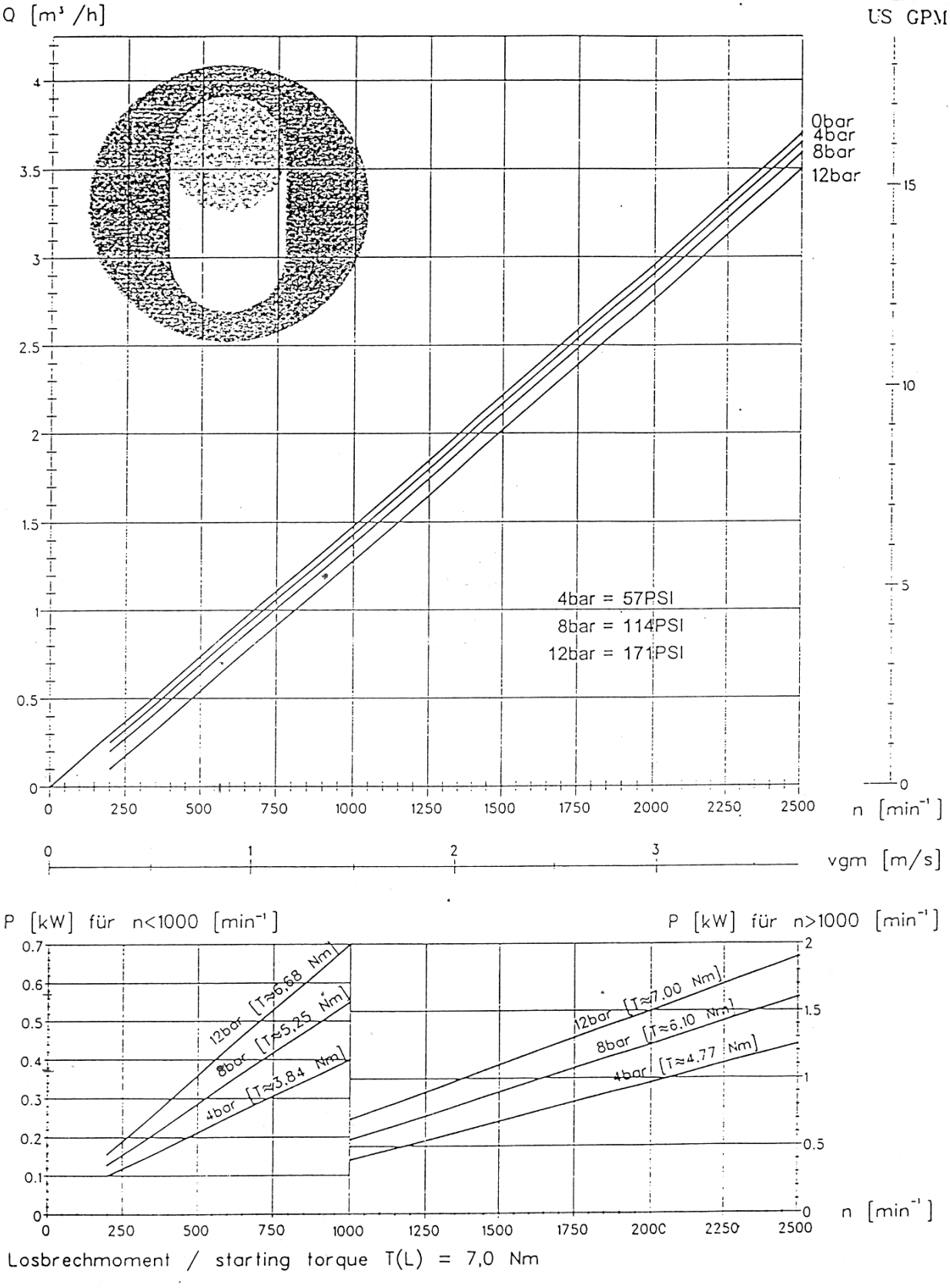

Appendix E Excerpt from (Thomson et al. 2001)

E.1 Cost of water over the lifetime of the equipment

A maintenance programme was devised in order to estimate the cost per cubic metre of product water over the expected lifetime of the equipment. A 20-year life was chosen to reflect the expectancy of the PV array. This figure is a little pessimistic for a high-quality installation, but reflects the possibility of harsh environmental conditions in a tropical maritime climate. The major points of the maintenance schedule are shown in Table E-1.

Frequency	**Action**
Every day	• Inspect installation for signs of malfunction
Every month	• Clean PV array
Every 3 months	• Dismantle RO modules and clean membranes • Perform general maintenance
Every year	• Replace RO membranes • Replace inlet filters • Maintain pumps and couplings
Every 5 years	• Replace Clark pump
Every 10 years	• Replace Moineau pump

Table E-1 – Outline maintenance schedule

The dominant yearly cost is the replacement of the membranes. It is possible that they will not need to be replaced so frequently, but as the effect of the proposed cyclic mode of operation has not been characterised, caution has been applied.

The average annual expenditure on replacement parts and consumables is estimated at £1643. The annual labour costs are much lower, £293 based on an hourly wage of £3. This is probably higher than expected in developing countries but the difference in cost between this and a more likely rate is small, and allows some contingency.

The Net Present Value (NPV) of the maintenance costs is calculated using an 8% discount rate. The calculations of the cost per cubic metre of product are show below.

Life cycle costs based on 20 years of operation	
Annual product volume (m^3)	1,424
Total amount of water produced (m^3)	28,480
Initial hardware cost	£23,055
Estimated shipping and installation costs	£5,500
NPV of maintenance costs	£28,446
NPV of Total investment	£57,001
Cost per cubic metre	**£2.00**

Table E-2 – Calculation of cost per cubic metre